

Simulation of Microelectromechanical Systems

by

Gary Keith Fedder

S.B., Massachusetts Institute of Technology (1982)  
S.M., Massachusetts Institute of Technology (1984)

A dissertation submitted in partial satisfaction of the  
requirements for the degree of

Doctor of Philosophy

in

Engineering-Electrical Engineering and Computer Sciences

in the

GRADUATE DIVISION

of the

UNIVERSITY of CALIFORNIA at BERKELEY

Committee in charge:

Professor Roger T. Howe, Chair  
Professor Paul R. Gray  
Professor Roberto Horowitz

1994

The dissertation of Gary Keith Fedder is approved:

---

Chair

Date

---

Date

---

Date

University of California at Berkeley

1994

**Simulation of Microelectromechanical Systems**

**© 1994**

**by**

**Gary Keith Fedder**

## Errata

G. K. Fedder, Simulation of Microelectromechanical Systems, Ph.D. Thesis, U.C.Berkeley, 1994.  
Revised: February 21, 2000 by fedder@ece.cmu.edu

This document is a list of corrections to the original Ph.D. Thesis filed in September 1994. If you find other items which may need correcting, please bring them to my attention via email, so I can log the corrections here.

- p. 18     Figure 2.6: y-axis units should be mΩ-cm
- p. 74     First paragraph: units of “ $B_z = 0.024 \text{ Pa-s}$ ” should be N-s/m
- p. 115    Eq. 3.145: “mechanical work” should be “mechanical power”
- p. 115    Footnote 11: “ $j$ th conductor” should be “ $j$ th mechanical terminal pair”
- p. 118    Eq. 3.156 should be:  $F_{e,z} = -\frac{\gamma}{(1 - \Delta z/z_o)^2} V^2$   
Note:  $\gamma$  is the force factor in units of N/V<sup>2</sup>
- p. 135    Table 3.5: analytic dc gain = 0.9976, HSPICE dc gain = 0.9965
- p. 136    Eq. 3.188: exponent in equation should be +1/2, not -1.
- p. 138    Eq. 3.192: Noise is generated by only the diode photocurrent and not the ac current.  
This correction must be propagated through the noise analysis.
- p. 174    Sec. 5.2.1, 2nd paragraph: “in section sec:eqn-of-motion.” should read “in section 3.2.”
- p. 198-9   In footnote 5: “in chapter chp:results.” should read “in chapter 6.”
- p. 203    Eq. 5.51 should be:  $L(z_1, 0) = \frac{2F_{ext}\cos(0.5\pi F_{ext}/F_o)}{k_z z_1 \sin(\pi F_{ext}/F_o)} - 1$
- p. 203    Eq. 5.52 should be:  $\frac{2F_o}{\pi k_z z_1} - 1 \leq L(z_1, 0) \leq \frac{F_o}{k_z z_1} - 1$
- p. 203    Figure 5.21, the plot should be shifted down by 2 to reflect the change in Eq. (5.51)
- p. 204    Eq. 5.56 should be:  $F_{fb} = \begin{cases} +F_{fbo}(t)/(1 - \Delta z/z_o)^2 & ; \text{upper actuator} \\ +F_{fbo}(t)/(1 + \Delta z/z_o)^2 & ; \text{lower actuator} \end{cases}$
- p. 205    Eq. 5.59 is incorrect - more on this later...
- p. 212    Eq. 5.83 should be:  $a_1 = c_1 = \zeta\omega_n - \omega_n\sqrt{\zeta^2 - 1}$
- p. 212    Eq. 5.84 should be:  $a_2 = c_2 = \zeta\omega_n + \omega_n\sqrt{\zeta^2 - 1}$
- p. 213    Top line should read: “...the gain at the frequency,  $\frac{f_N}{2} = \frac{1}{4T_s}$ , will be -1 if  $K_n = \pi/2$ .”
- p. 263    In buffer HSPICE file: rout=10000x

## Abstract

### **Simulation of Microelectromechanical Systems**

by

Gary Keith Fedder

Doctor of Philosophy in Engineering-Electrical Engineering  
and Computer Sciences

University of California at Berkeley

Professor Roger T. Howe, Chair

This thesis describes a general system simulation of microelectromechanical systems (MEMS) based on lumped-parameter modeling. First-order analytic models are derived for mechanical equations of motion of a suspended plate, squeeze-film damping, fixed-fixed, crab-leg, folded-flexure, and serpentine spring constants, parallel-plate and comb-finger electrostatic actuators, and capacitive position sensors. The models are implemented in a circuit simulation program (SPICE) and in a numerical simulation program (MATLAB<sup>TM</sup>).

Verification of the models and simulations motivated creation of an integrated testbed for research in multi-mode digital control of MEMS: a suspended polysilicon plate having four capacitive-bridge vertical position sensors, each with an integrated CMOS buffer amplifier, four differential electrostatic feedback actuators on the plate's corners, and an interdigitated comb for lateral force input. Sigma-delta ( $\Sigma$ - $\Delta$ ) force-balance control is implemented for each corner of the plate. The testbed is configured with a 0.25 N/m spring constant, 0.47  $\mu$ g mass, and a vertical resonance of 3.7 kHz. In air, vertical displacement and tilt of the plate in two axes are controlled within  $\pm 25$  nm and  $\pm 0.03^\circ$ , respectively. Measured noise acceleration is 19 milli-G with -69 dB dynamic range in a 50 Hz bandwidth. When operating in a low-pressure ambient, the mechanically underdamped system experiences limit-cycle oscillations, which are bounded through the use of digital lead compensation. An analytic model of the  $\Sigma$ - $\Delta$  loop, as well as simulation, successfully predicts the limit-cycle behavior.

In a separate part of this thesis, thermal microassembly techniques are demonstrated which extend the capabilities of surface micromachining technology. Polysilicon

fuses act as temporary anchors that can be cleanly severed by application of a single 300 mA, 1  $\mu$ s pulse. Fuse applications include configurable springs and frequency trimming of microresonators. Welding technology is used to pre-stress springs and actively align structures. An aluminum microbridge is used to form a robust weld, connecting two polysilicon structures. The surface tension of the molten aluminum produces a force of approximately 15  $\mu$ N, which is about 100 times larger than electrostatic comb-drive forces. A series of current pulses is used to melt the aluminum without destroying the weld joint.

Approved by \_\_\_\_\_  
Committee Chairman

To my parents  
and to my wife Cheryl.

# Contents

<b>List of Figures</b>	<b>viii</b>
<b>List of Tables</b>	<b>xv</b>
<b>1 Introduction</b>	<b>1</b>
<b>2 Thermal Assembly of Polysilicon Microstructures</b>	<b>6</b>
2.1 Introduction . . . . .	6
2.2 Fabrication . . . . .	8
2.3 Heating of Microbridges . . . . .	10
2.3.1 Analytic Thermal Analysis . . . . .	11
2.3.2 Finite-Element Thermal Analysis . . . . .	16
2.4 Resistive Cutting . . . . .	21
2.4.1 Introduction: Tee-Bridge Fusible Supports . . . . .	21
2.4.2 Current Sink for Fuse Cutting . . . . .	23
2.4.3 Fusible Support Designs . . . . .	24
2.4.4 Fuse-Cutting Energy . . . . .	29
2.4.5 Fuse-Cutting Time . . . . .	33
2.4.6 Parallel Fuse Cutting . . . . .	37
2.5 Resistive Welding . . . . .	41
2.5.1 Silicon–Silicon Welding . . . . .	41
2.5.2 Aluminum–Silicon Welding . . . . .	44
2.5.2.1 Description of Welding Structure . . . . .	44
2.5.2.2 Analysis of Surface-Tension Force . . . . .	47
2.5.2.3 Finite-Element Analysis of Welding Structures . . . . .	50
2.5.2.4 Weld Structure Fabrication Issues . . . . .	53
2.5.2.5 Welding of Flipped Microstructures . . . . .	55
2.6 Narrow-Gap Comb-Drive Microactuator . . . . .	57
2.7 Trimmable Microresonators . . . . .	59
2.7.1 Frequency Trimming With Fuses . . . . .	60
2.7.2 Frequency Trimming With Weld Structures . . . . .	64

<b>3 Lumped-Parameter Modeling</b>	<b>67</b>
3.1 Introduction . . . . .	67
3.2 Mechanical Equations of Motion . . . . .	67
3.3 Squeeze-Film Damping . . . . .	71
3.3.1 Simplifying Assumptions for Viscous Flow . . . . .	71
3.3.2 One-Dimensional Analysis . . . . .	73
3.3.3 Damping of Rotational Modes . . . . .	74
3.4 Polysilicon Flexure Design . . . . .	76
3.4.1 Spring Constants for Simple Beams . . . . .	76
3.4.2 Nonlinear Effects . . . . .	78
3.4.3 Design Limitations . . . . .	81
3.4.3.1 Limitations on Beam Length . . . . .	82
3.4.3.2 Limitations on Beam Width and Thickness . . . . .	83
3.4.4 Flexure Spring Constants . . . . .	84
3.4.4.1 Overview of Flexures . . . . .	84
3.4.4.2 Linear Spring-Constant Analytic Method . . . . .	86
3.4.4.3 Spring Constants for the Fixed-Fixed Flexure . . . . .	87
3.4.4.4 Spring Constants for the Crab-Leg Flexure . . . . .	90
3.4.4.5 Spring Constants for the Folded Flexure . . . . .	97
3.4.4.6 Spring Constants for the Serpentine Flexure . . . . .	104
3.5 Electrostatic Actuators . . . . .	115
3.5.1 Electrostatic Force . . . . .	115
3.5.2 Parallel-Plate Actuators . . . . .	117
3.5.3 Comb-Finger Actuators . . . . .	118
3.5.3.1 Comb-Drive Lateral Force . . . . .	118
3.5.3.2 Comb-Drive Levitation Force . . . . .	122
3.6 Capacitive Position Sensing . . . . .	125
3.6.1 Capacitive Position Sensing Using a Unity-Gain Buffer . . . . .	126
3.6.1.1 Single-Capacitor Sensor . . . . .	127
3.6.1.2 Balanced Capacitive Divider With Driven Shield . . . . .	128
3.6.1.3 Unity-Gain Buffer . . . . .	130
3.6.1.4 Buffer Test Circuit . . . . .	139
3.6.2 Capacitive Position Sensing Using a Transresistance Amplifier . . . . .	144
3.6.2.1 Balanced Capacitive Divider . . . . .	144
3.6.2.2 Transresistance Amplifier . . . . .	146
3.6.2.3 Transresistance Amplifier Test Circuit . . . . .	151
3.6.3 Sensor Noise and Minimum Detectable Signal . . . . .	152
3.6.3.1 Interconnect Noise . . . . .	152
3.6.3.2 Electronic Sensor Noise . . . . .	153
3.6.3.3 Brownian Noise . . . . .	156

<b>4 Integrated Micromechanical Testbed</b>	<b>158</b>
4.1 Introduction . . . . .	158
4.2 Sigma-Delta Architecture . . . . .	159
4.3 Testbed Description . . . . .	161
4.4 Fabrication . . . . .	166
4.4.1 Second Structural Polysilicon Layer . . . . .	166
4.4.2 Rapid-Thermal Annealing of Residual Stress . . . . .	168
4.4.3 TiSi <sub>2</sub> Contacts . . . . .	171
4.4.4 Testbed Fabrication Results . . . . .	171
<b>5 System Simulation and Analysis</b>	<b>173</b>
5.1 Introduction . . . . .	173
5.2 System Modeling . . . . .	173
5.2.1 Testbed Plate Model . . . . .	174
5.2.2 Position-Sensor Model . . . . .	177
5.2.3 Electrostatic Actuator Model . . . . .	179
5.3 SPICE Simulation . . . . .	179
5.3.1 Equivalent Circuit Model of a Mass-Spring-Damper . . . . .	181
5.3.2 Time-Varying Capacitor Model . . . . .	182
5.3.3 Micromechanical Capacitor Model . . . . .	183
5.3.4 Testbed Simulation . . . . .	184
5.4 MATLAB Simulation . . . . .	187
5.5 Limit-Cycle Analysis . . . . .	191
5.5.1 Describing Function of the Feedback Path . . . . .	191
5.5.2 Describing Function of Only the Quantizer . . . . .	195
5.5.3 Non-Zero External Force . . . . .	199
5.5.4 Feedback Nonlinearity With Position . . . . .	204
5.6 Noise Analysis . . . . .	207
5.6.1 Brownian Noise . . . . .	207
5.6.2 Sigma-Delta Quantization Noise . . . . .	209
5.6.2.1 Sampled-Data Representation . . . . .	209
5.6.2.2 Equivalent Output-Referred Quantization Noise . . . . .	211
5.6.2.3 Equivalent Quantization Noise Acceleration . . . . .	213
5.6.3 Equivalent Noise Force from Interconnect Resistance . . . . .	214
5.6.4 Total Noise Acceleration for the Testbed . . . . .	215
<b>6 Testbed Experimental Results</b>	<b>216</b>
6.1 Introduction . . . . .	216
6.2 Experimental Setup . . . . .	216
6.3 Position-Sensor Characterization . . . . .	217
6.4 Capacitive Feedthrough . . . . .	220
6.5 Open-Loop Step Response . . . . .	222
6.6 Comb-Drive Levitation Force . . . . .	224
6.7 Closed-Loop Step Response . . . . .	225
6.8 Accelerometer Testing . . . . .	227

6.9 Underdamped Operation at Low Pressure . . . . .	232
<b>7 Conclusions</b>	<b>235</b>
7.1 Future Work . . . . .	236
<b>Bibliography</b>	<b>238</b>
<b>A Testbed Technical Information</b>	<b>246</b>
A.1 Testbed Parameter Data . . . . .	246
A.2 External Testbed Electronics . . . . .	252
A.2.1 Schematics . . . . .	252
A.2.2 Card-Cage Layout . . . . .	260
A.2.3 Test Setup . . . . .	262
<b>B HSPICE Input Files</b>	<b>263</b>
B.1 CMOS Unity-Gain Buffer HSPICE File . . . . .	263
B.2 Testbed HSPICE File . . . . .	268
<b>C MICS Fabrication Process</b>	<b>281</b>

# List of Figures

1.1	Pictoral representation of the lumped-parameter modeling and simulation process for a microaccelerometer. . . . .	2
2.1	Cross-sections of the nine-mask process flow to fabricate fusing and welding structures. . . . .	9
2.2	Schematic drawing of a polysilicon microbridge used for I-V measurements.	11
2.3	I-V characteristics of several microbridges. (a) Different values of length. (b) Different values of width. . . . .	14
2.4	SEM of an open-circuited 10 $\mu\text{m}$ -wide, 20 $\mu\text{m}$ -long microbridge. . . . .	15
2.5	I-V characteristics of 2 $\mu\text{m}$ -wide, 20 $\mu\text{m}$ -long bridges on adjacent dice, showing insensitivity to ambient conditions. . . . .	16
2.6	Resistivity versus temperature model, determined by fitting finite-element results to measured data. . . . .	18
2.7	Measured I-V characteristics of several microbridges, compared with finite-element results. . . . .	20
2.8	Temperature distribution of the 10 $\mu\text{m}$ -wide by 20 $\mu\text{m}$ -long microbridge as current is varied from 10 mA to 50 mA. . . . .	21
2.9	Resistivity distribution of the 10 $\mu\text{m}$ -wide by 20 $\mu\text{m}$ -long microbridge as current is varied from 10 mA to 50 mA. . . . .	22
2.10	SEM of a polysilicon tee bridge. (a) Before resistive cutting. (b) After resistive cutting. . . . .	22
2.11	SEM of the polysilicon cantilever beam, released by the tee bridge. . . . .	23
2.12	Schematic of voltage-controlled current sink used to cut fuses. . . . .	24
2.13	Layout of five fusible support designs. . . . .	25
2.14	SEM of a 2 $\mu\text{m}$ -wide, 12 $\mu\text{m}$ -long, 2 $\mu\text{m}$ -thick polysilicon fuse. (a) Before cutting. (b) After cutting. . . . .	26
2.15	SEM of a 2 $\mu\text{m}$ -wide, 12 $\mu\text{m}$ -long, 4000 Å-thick polysilicon fuse. (a) Before cutting. (b) After cutting. . . . .	26
2.16	SEM showing a structure stuck to the substrate because of inadequate fuse spacing. . . . .	27
2.17	SEM showing a structure stuck to the substrate because of inadequate fuse thickness. . . . .	28

2.18 SEM of 2 $\mu\text{m}$ -wide, 12 $\mu\text{m}$ -long, 2000 Å-thick polysilicon fuses supporting a serpentine spring. (a) Before cutting. (b) After cutting. . . . .	28
2.19 SEM of 2 $\mu\text{m}$ -wide, 12 $\mu\text{m}$ -long, 2 $\mu\text{m}$ -thick polysilicon fuses that are cut. (a) Too much current (260 mA). (b) Too little current (100 mA). . . . .	29
2.20 Circuit for capacitive cutting of fuses. . . . .	30
2.21 Layout of parallel fuses used in the measurement of cutting energy. . . . .	31
2.22 Capacitor voltage, capacitor current, and circuit resistance waveforms for one, two, and three fuses cut in parallel. . . . .	32
2.23 A current-monitor voltage waveform from cutting a 2 $\mu\text{m}$ -wide, 10 $\mu\text{m}$ -long, 2 $\mu\text{m}$ -thick polysilicon fuse. . . . .	35
2.24 Time required to cut a 2 $\mu\text{m}$ -wide, 10 $\mu\text{m}$ -long, 2 $\mu\text{m}$ -thick polysilicon fuse as a function of applied current (log-log scale). . . . .	36
2.25 Time required to cut four different-size fuses. . . . .	37
2.26 Layout of four parallel fuses supporting a beam. . . . .	38
2.27 SEMs of parallel-fuse structures. . . . .	39
2.28 Current-monitor waveform of four fuses being cut in parallel. . . . .	40
2.29 Schematic of the first-generation welding test structure. . . . .	42
2.30 SEM of a first-generation welding test structure. (a) Before welding. (b) A similar structure, after welding. . . . .	42
2.31 Close-up view of the lower joint, showing a clean weld and out-of-plane alignment. . . . .	43
2.32 Schematic drawing of an aluminum–silicon welding structure. . . . .	45
2.33 SEM of a weld joint. (a) Before welding. (b) After welding. . . . .	46
2.34 SEM of a structure used to measure weld strength, showing the fracture of a 2 $\mu\text{m} \times 2\mu\text{m}$ beam and the intact weld joint. . . . .	47
2.35 SEM of welding structure used to measure lateral force. (a) Before welding. (b) After welding. . . . .	49
2.36 Differential volume of a polysilicon structure suspended over the substrate. . . . .	50
2.37 Two-dimensional finite-element analysis of the welding structure. . . . .	52
2.38 Cross-sections of the original and revised weld-structure process. . . . .	54
2.39 SEM of an inoperable aluminum microbridge which was to be used for welding. . . . .	55
2.40 Schematic of the vertical weld structure. . . . .	56
2.41 Vertical welding test structure. (a) Movable plate before welding. (b) Heating filament before welding. . . . .	56
2.42 Vertical welding test structure after welding. . . . .	57
2.43 Schematic of conventional and narrow-gap electrostatic comb drive designs. . . . .	58
2.44 Partially assembled microactuator. (a) Before assembly. (b) After assembly. . . . .	58
2.45 Fuse with a grounded shield to reduce electrostatic force. . . . .	60
2.46 Folded-flexure trimmable resonator. Fuses are used to adjust the folded-flexure's beam length. . . . .	61
2.47 Magnified view of the fuse array for adjusting beam length. . . . .	61
2.48 “Centipede” trimmable resonator. . . . .	63
2.49 Laser-trimmable resonator. (a) Before laser cutting. (b) After laser cutting. . . . .	63

2.50	Schematic of a modified fixed-fixed resonator with weld structures used to trim frequency. . . . .	64
2.51	Trimmable fixed-fixed resonator. Weld structures are used to adjust tension in the suspension. . . . .	65
2.52	Magnified view of weld structures used for tensioning the suspension. . . . .	66
3.1	Schematic of a rigid rectangular plate suspended by four springs located at the plate's corners. . . . .	69
3.2	Cross-section schematic of a plate with an air gap, $z_o$ , above the substrate, illustrating the squeeze-film damping arising from vertical motion of the plate with velocity, $v$ . . . . .	71
3.3	Schematic of a plate for one-dimensional analysis of squeeze-film damping. .	73
3.4	Schematic of a plate for one-dimensional analysis of squeeze-film damping of the $\phi$ rotational mode about the $y$ -axis. . . . .	75
3.5	Various beams with concentrated load, $F$ , or distributed load, $f$ . Only the $y$ -components of force are shown. . . . .	77
3.6	Comparison of small deflection theory (linear theory) with exact theory for cantilever beams [1]. . . . .	79
3.7	Displacement versus force for two fixed-fixed beams. . . . .	80
3.8	Spring constant versus residual strain of three fixed-fixed beams ( $2\ \mu\text{m}$ -wide by $2\ \mu\text{m}$ -thick). . . . .	81
3.9	Various flexure designs. (a) fixed-fixed flexure. (b) folded flexure. (c) crab-leg flexure. (d) serpentine spring. . . . .	85
3.10	Flow-chart for spring constant analysis using energy methods. . . . .	86
3.11	Fixed-fixed flexure . . . . .	88
3.12	(a) Crab-leg flexure. (b) Free-body diagram of a crab-leg beam. . . . .	91
3.13	Free-body diagram of a crab-leg beam with an applied force in the $z$ direction. .	94
3.14	Plot of $J/I_p$ versus the aspect ratio of the rectangular beam cross-section. .	95
3.15	Comparison of analytic crab-leg spring constants with finite-element analysis	96
3.16	(a) Folded-flexure schematic. (b) Free-body diagram. . . . .	97
3.17	Folded-flexure free-body diagram for calculation of the $z$ -directed spring constant. . . . .	100
3.18	Comparison of analytic folded-flexure spring constants with finite-element analysis . . . . .	103
3.19	Serpentine spring schematic. . . . .	104
3.20	Free-body diagram of a serpentine spring. . . . .	105
3.21	Free-body diagram of a serpentine spring with an applied force in the $z$ direction. . . . .	108
3.22	Comparison of analytic serpentine spring constants (solid lines) with finite-element analysis (points). . . . .	110
3.23	Layout of ten microresonators, each with a different serpentine flexure. . . . .	112
3.24	Schematic of two charged conductors . . . . .	115
3.25	Path of integration in the $x$ - $V$ variable space used to calculate coenergy. . . . .	116
3.26	Parallel-plate microactuator. (a) Top view. (b) Side view. . . . .	117
3.27	Electrostatic comb drive (a) Top view. (b) Side view. . . . .	119

3.28	Cross-section of one rotor finger between two stator fingers, showing the partitioning of capacitance for comb-drive force evaluation. . . . .	120
3.29	Path of integration in the $x$ - $V_s$ - $V_r$ variable space used to calculate the comb-drive coenergy. . . . .	120
3.30	Comb-drive schematics for evaluation of lateral force. (a) Comb-drive layout, showing the three comb-finger regions: 1. unengaged rotor fingers, 2. engaged fingers, and 3. unengaged stator fingers. (b) Cross section of engaged comb fingers. (c) Cross section of unengaged stator fingers. . . . .	121
3.31	Finite-element calculations of capacitance and lateral force for a common comb-drive geometry. (a) Cross section of comb-finger geometry. (b) Plots of capacitance and lateral force versus the rotor's vertical displacement. . .	123
3.32	Plot of vertical force, $f_{e,z}$ , versus the rotor's vertical displacement, $\Delta z$ , for the comb-drive geometry of Figure 3.31(a), where $w = t = g = z_o = 2 \mu\text{m}$ . . .	124
3.33	Schematic views of a micromechanical parallel-plate capacitor. (a) Top view. (b) Side view. . . . .	125
3.34	Equivalent circuit of the micromechanical capacitor. . . . .	126
3.35	Capacitive divider circuit using a single micromechanical capacitor. . . . .	127
3.36	Schematic cross-section of a micromechanical parallel-plate sense capacitor with a driven shield. . . . .	129
3.37	Balanced capacitive divider circuit. . . . .	129
3.38	CMOS unity-gain buffer circuit. . . . .	131
3.39	Low-frequency, small-signal model of buffer circuit. . . . .	133
3.40	Noise model of buffer circuit. . . . .	137
3.41	Typical buffer noise voltage spectral density. . . . .	139
3.42	Schematic of the capacitive position-sense test circuit with a unity-gain buffer. . . . .	140
3.43	SEM of the capacitive position-sense test circuit with a unity-gain buffer. . . . .	141
3.44	Plot of unity-gain buffer output voltages versus input voltage. . . . .	142
3.45	Measured voltage waveforms from the position-sense test-circuit. . . . .	143
3.46	Balanced capacitive divider circuit with displacement current-sense using a transresistance amplifier. . . . .	145
3.47	Transresistance amplifier circuit schematic. . . . .	147
3.48	Low-frequency, small-signal equivalent circuit of the two-stage CMOS operational amplifier, where $C_c$ sets the dominant pole. . . . .	147
3.49	Plot of position-sensor gain versus modulation frequency for two values of feedback resistance, $R_f=200 \text{ k}\Omega$ and $1 \text{ M}\Omega$ . . . . .	149
3.50	Noise models of the transresistance amplifier. (a) Model including equivalent noise voltage of the transresistance amplifier. (b) Equivalent input-referred noise current model. . . . .	150
3.51	SEM of the capacitive position-sense test circuit with a transresistance amplifier. . . . .	151
3.52	Equivalent circuit models, illustrating interconnect noise sources. (a) Unity-gain-buffer sensor. (b) Transresistance-amplifier sensor. . . . .	153
4.1	Block diagram of a conventional $\Sigma$ - $\Delta$ modulator. . . . .	159
4.2	Block diagram of a micromechanical $\Sigma$ - $\Delta$ loop. . . . .	160

4.3	Block diagram of a micromechanical $\Sigma$ - $\Delta$ loop with digital compensation in the feedback path. . . . .	161
4.4	Schematic drawing of one quarter of the integrated testbed. . . . .	162
4.5	Optical photograph of the multi-project MICS chip. . . . .	163
4.6	Die photograph of the integrated testbed. The dashed rectangle delimits the area shown in Figure 4.7. . . . .	164
4.7	Expanded view of the polysilicon plate and serpentine springs. The white dashed rectangle delimits the area shown in Figure 4.10. . . . .	165
4.8	Block diagram of one corner of the integrated testbed. . . . .	165
4.9	MICS process cross-section. . . . .	166
4.10	SEM of one corner of the movable plate, suspended below the upper actuator cantilever. . . . .	167
4.11	Composite of two SEMs of a cross-section of a comb drive, showing the poly-3 stringers between comb fingers. . . . .	168
4.12	Polymer stringers after microstructure release. . . . .	169
4.13	Strain-gauge design used to measure residual stress in microstructural polysilicon films. (a) Layout showing the 1 mm-long, 16 $\mu\text{m}$ -wide beam that releases its built-in axial stress. (b) Enlargement of displacement vernier with 0.2 $\mu\text{m}$ resolution. . . . .	170
5.1	Simplified layout of the testbed, where the plate's suspension is configured with one fuse cut on each spring. . . . .	175
5.2	Illustration of the eight lowest mechanical modes of the testbed. . . . .	176
5.3	Simplified testbed layout, identifying the position-sensor electrodes and lower-actuator electrodes. . . . .	178
5.4	Simplified testbed layout, identifying the upper-actuator electrodes. . . . .	180
5.5	Electrical analogy to a second-order mechanical system. (a) Mechanical mass-spring-damper. (b) Equivalent LCR circuit. . . . .	181
5.6	Time-varying capacitor (TVC) model in SPICE. (a) Circuit instance. (b) Subcircuit. . . . .	182
5.7	Parallel-plate micromechanical capacitor macro-model in SPICE. . . . .	183
5.8	Block diagram of the testbed, modeled in SPICE. . . . .	185
5.9	SPICE simulation of the testbed closed-loop step response in air. . . . .	186
5.10	SPICE simulation of the testbed under vacuum, with a mechanical Q of 50. . . . .	188
5.11	Block diagram of the testbed, modeled in MATLAB. . . . .	189
5.12	Loop model of the $\Delta z$ mode, modeling the entire feedback path as a describing function. . . . .	192
5.13	Limit-cycle waveforms of linearized feedback force with no compensation (solid line), and vertical plate displacement (dashed line). . . . .	192
5.14	Limit-cycle waveforms of linearized feedback force with compensation (solid line), and vertical plate displacement (dashed line). . . . .	193
5.15	Alternative loop model of the $\Delta z$ mode for limit-cycle analysis. . . . .	195
5.16	Minimum lead-compensation gain for stability versus the ratio of sampling frequency to resonant frequency . . . . .	197

5.17	Limit cycle amplitude and frequency versus lead-compensation gain, $G_v$ , with $T_d = 5/12T_s, T_s, 17/12T_s$ . $f_s = 100$ kHz. (a) Amplitude, $z_1$ . (b) Frequency, $\omega$ .	198
5.18	Limit cycle amplitude and frequency versus lead-compensation gain, $G_v$ , with $T_d = 5/12T_s, T_s, 17/12T_s$ . $f_s = 1$ MHz. (a) Amplitude, $z_1$ . (b) Frequency, $\omega$ .	200
5.19	Limit cycle amplitude and frequency versus sampling frequency, $f_s$ with various damping factors. (a) Amplitude, $z_1$ . (b) Frequency, $\omega$ .	201
5.20	Limit-cycle waveforms of linearized feedback force with compensation (solid line), and vertical plate displacement (dashed line). The external force is balanced by feedback with duty cycle, $D$ .	202
5.21	DC loop gain versus external force normalized to the full-scale force.	203
5.22	Limit-cycle waveforms of nonlinear feedback force with compensation (solid line), and vertical plate displacement (dashed line).	205
5.23	Limit cycle amplitude and frequency versus sampling frequency, $f_s$ , with various damping factors. Actuator nonlinearity is included in the calculations. (a) Amplitude, $z_1$ . (b) Frequency, $\omega$ .	206
5.24	Single-loop representation of the testbed. (a) Continuous-time block diagram. (b) Sampled-data version of (a).	210
6.1	Custom mounting assembly for testing on the wafer probe-station.	217
6.2	Custom probe card for testing in the vacuum probe-station (shown in the background).	218
6.3	Photograph of the experimental test setup.	218
6.4	One period of the modulated sensor voltage, for various position reference input values.	219
6.5	Measured and calculated peak-to-peak sensor voltage versus plate displacement.	220
6.6	Waveforms of an actuator voltage and the demodulator output voltage during closed-loop operation with $f_m = 50$ kHz.	221
6.7	Open-loop responses to 30 Hz square-wave levitation force varying in amplitude from 1 V to 7 V.	223
6.8	Comb-drive levitation force versus comb-drive voltage. Points are calculations from measured data and the line is the best-fit analytic calculation.	225
6.9	Closed-loop response to an 150 Hz square-wave position reference input.	226
6.10	Spectrum of one digital bitstream, showing the $\approx 1$ G acceleration signal at 1.6 Hz. (a) manual shaking along z-axis. (b) manual shaking along lateral axis.	228
6.11	Averaged output signals from the three working channels, with the device tilted 90° from horizontal.	229
6.12	Enlargement of the averaged output signals from Figure 6.11. (a) Comparison of the left-channel signals. (b) Comparison of the upper-right signal and the sum of the left-channel signals.	230
6.13	Accelerometer signals for differing tilt angles.	231
6.14	Accelerometer tilt test results, displaying sensor acceleration output versus external acceleration input.	232

6.15	Measured, simulated, and theoretical peak-to-peak sensor voltage waveforms during underdamped operation at three different pressure values: 10 T, 1 T, and 0.1 T. . . . .	233
A.1	Layout of the testbed's micromechanical plate and springs. . . . .	247
A.2	Testbed layout dimensions. . . . .	248
A.3	Layout of one serpentine spring, showing the 6 fuses that can be cut to set the spring constant. . . . .	249
A.4	Timing board, schematic #1: digital control logic . . . . .	252
A.5	Timing board, schematic #2: voltage references and balanced modulation source. . . . .	253
A.6	Photograph of the timing board, identifying the functional blocks and test points. . . . .	254
A.7	Feedback board, schematic #1: input demodulator (1 of 4). . . . .	255
A.8	Feedback board, schematic #2: feedback logic (1 of 4). . . . .	256
A.9	Photograph of one of the feedback boards (board #2), identifying the functional blocks and test points. . . . .	257
A.10	Schematic of the opto-isolation board. . . . .	258
A.11	Photograph of the opto-isolation board. . . . .	259
A.12	External electronics, housed in a standard card cage. (a) Front view. (b) Rear view. . . . .	260
A.13	Schematic of the experimental test setup. . . . .	262

# List of Tables

2.1	Effective pad conductance width over length ratio . . . . .	18
2.2	Scaling factors of cutting time and energy with fuse width and length. . . . .	36
2.3	Measured deflection for lateral force test structures. . . . .	48
2.4	Values of spring constant and resonant frequency for the fuse-trimmable resonator . . . . .	62
3.1	Displacement equations derived from small displacement theory [2] . . . . .	77
3.2	Geometrical parameters of serpentine microresonators. . . . .	111
3.3	Measured comb-drive voltage and lateral position of serpentine microresonators.	113
3.4	Measured lateral resonant frequency of serpentine microresonators. . . . .	114
3.5	Values of buffer performance specifications, calculated from analytic analysis and HSPICE [3] simulation. . . . .	135
3.6	Description of each capacitive divider configuration and corresponding measured peak-to-peak output voltage, $V_{pp}$ , for the waveforms in Figure 3.45. .	142
4.1	Experimental results of <i>in situ</i> phosphorous-doped polysilicon stress annealing using RTA. . . . .	170
6.1	Measured peak-to-peak feedthrough between different actuators and the lower-left testbed sensor. The actuator drive is a 4 V p-p square wave. . . . .	221
6.2	Open-loop risetime and falltime measurements. . . . .	223
A.1	Testbed geometric parameters. . . . .	249
A.2	Testbed spring configurations. (a) Static spring constants (four-spring suspension). (b) System resonant frequencies. . . . .	250
A.3	Capacitance definitions, dimensions and calculated values. . . . .	251
A.4	Pin assignments for working testbed chip in a 24-pin dual-inline package. .	251
A.5	Backplane assignments. . . . .	261

## Acknowledgements

I thank my research advisor and friend, Professor Roger T. Howe, for introducing me to the micromechanics field, for guiding my research, for providing my research funding, and for helping me land a great job. Many thanks to my other two thesis committee members, Professor Paul R. Gray and Professor Roberto Horowitz, for reviewing the manuscript, to Professor Bernhard Boser for discussions on quantization noise, and to Professor Richard S. Muller, Professor Richard M. White, Professor Albert P. Pisano, and Professor Ping K. Ko for their help, encouragement, and discussions.

I thank Weijie Yun, whose microaccelerometer research was a springboard for my work. Thanks to William A. Clark and Sang Won Son for helping construct the external testbed electronics. More thanks to Bill Clark and Patrick Cheung for discussions and reviewing portions of the manuscript. Ron Wilson, Richard Hsu, and V. Wong are responsible for most of the great-looking SEM photos, thank you. My research on polysilicon fuses was aided by discussions with Carlos H. Mastrangelo and by his doctoral work on thermal applications of microbridges. Jeff Chang, Dave Chan, and Young Shin directly contributed to the thermal assembly work; it was a privilege to work with each of them.

Device fabrication was made possible through the efforts of Katalin Voros, Robert Hamilton, Evan Stateler, James Parrish, David and Debra Hebert, Maria Perez, Marilyn Kushner, Phillip Guillory, Mike Linan, Rosemary Spivey, and the rest of the staff of the U. C. Berkeley Microfabrication Laboratory. Special thanks to Shengqing Fang for completing the CMOS process steps, to James M. Bustillo, who helped with sensor processing and developed the spin-on-glass process sequence, to Weijie Yun and Clark T.-C. Nguyen who are responsible for much of the MICS process development, and to Greg Mulhern for performing the supercritical CO<sub>2</sub> drying steps.

Thanks to the BSAC administrative staff: Joel Nice, Barbara Barnes, and especially Sheila Kelly, who went the extra mile and beyond. I thank Jeff Chang, Robert Freeman, Rob McNicholas, and all the system administrators for keeping the computers running, especially while writing this manuscript.

My time spent at Berkeley was made special through the social and academic interactions with my fellow students (not mentioned elsewhere): Rod Alley, Reid “Turtle” Brennen, Savior Charles, Michael Cohn, Ben Costello, Robert Freeman, Jack Judy, Chris Keller, Peter Krulevitch, Amit Lal, Martin Lim, David Loconto, Crist Lu, Dave Monk,

Richard Moroney, Annabel Nickles, Steve Parke, Robert Ried, Dennis Sinitsky, William Tang, Amy Wang, Stewart Wenzel, and Kirt Williams. Jim Bustillo and Charles E. Bradley made the arduous task of thesis writing more tolerable by engaging me in painful runs over steep terrain followed by invigorating lunchtime conversation. Thanks to Leslie Field for sharing her processing expertise and for the relaxing walks together through North Berkeley. Extra-special thanks to my friends, Michael and Grace Judy, for all of the fun, support, and conversation.

Last, I declare my deepest debt of gratitude to my wife, Cheryl, who has persevered countless nights and weekends alone while I studied, and who has fully supported me. I look forward to spending much more time together with her and love her very, very much.

This research was funded by the Berkeley Sensor & Actuator Center (an NSF/Industry/University Research Center), by a grant from the Emerging Technologies Initiative of the U. S. National Science Foundation, by an Analog Devices Career Development Professorship, by an IBM Graduate Fellowship, and by ARPA.

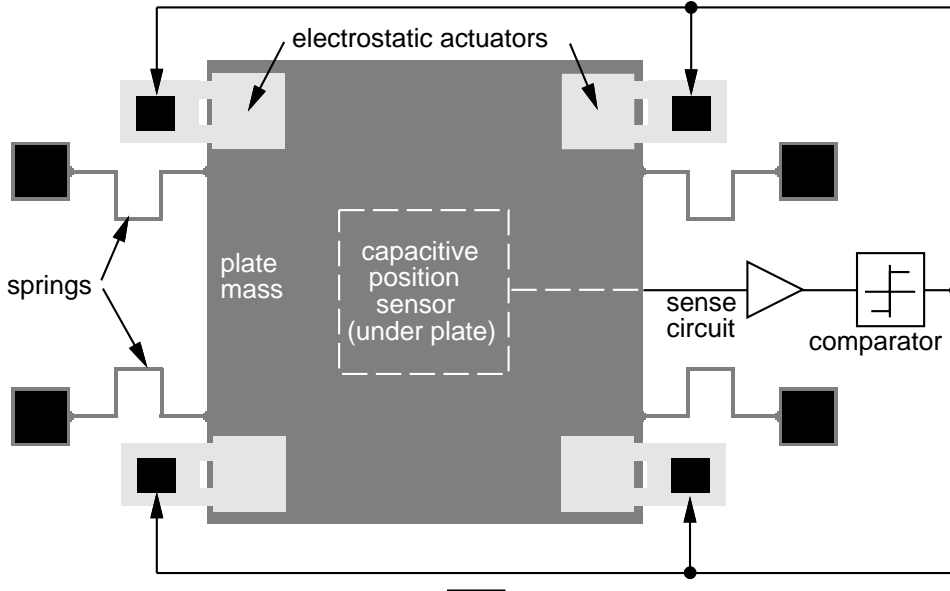
# Chapter 1

## Introduction

Microelectromechanical systems (MEMS) technology is capable of producing very complex systems, such as accelerometers and gyroscopes, that integrate micromechanical parts, analog circuits, and digital logic. Hand design of these systems is extremely difficult because of the interdisciplinary nature of the systems, and because of the large number of system interactions. Currently, no system-level computer-aided design (CAD) tools exist that can be used to design and synthesize MEMS effectively, although several research thrusts are making progress in the CAD area [4–11]. Availability of CAD software that integrates micromechanical models and system simulation would provide a quantum leap in MEMS design productivity. Design time is decreased and quality improved by incorporating practical and theoretical MEMS knowledge in parameterized macro-models. System functionality and performance are verified before committing to silicon, thereby minimizing, or even eliminating, layout iterations.

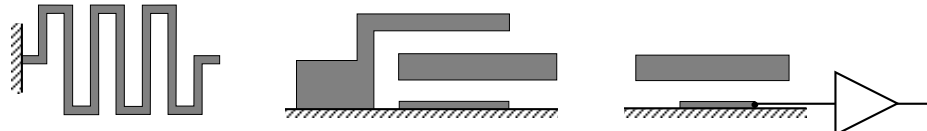
Simulations that successfully predict measured results require proper identification and construction of the micromechanical component models. In this thesis, we identify and analyze micromechanical components that are used in a broad class of surface microsystems, such as accelerometers, gyroscopes, and microresonator oscillators and filters. Behavioral information about each component is embodied in a “macro-model”, and implemented in a circuit simulation program, such as SPICE [3] or a numerical simulation program, such as MATLAB<sup>TM</sup> [12]. Figure 1.1 illustrates the modeling and simulation procedure for a closed-loop microaccelerometer. The accelerometer is a plate suspended by four springs and controlled at the corners by four electrostatic actuators. A circuit senses the plate’s vertical position via a capacitor electrode located under the plate, a comparator determines

**System layout:**



**Parameterized modeling:**

- springs
- electrostatic actuators
- position sensors



**System simulation:**

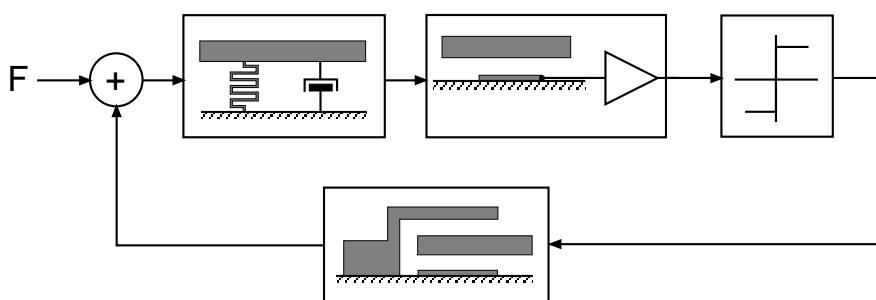


Figure 1.1: Pictoral representation of the lumped-parameter modeling and simulation process for a microaccelerometer.

whether the plate should be pulled up or down, and the digital signal is fed back to the actuators. The system is partitioned into a set of parameterized models, consisting of the mass-spring-damper, the electrostatic actuator, and the capacitive position sensor. After the model parameters are extracted from the layout, the model instances are assembled in a system simulation program.

In order to verify our modeling and simulation approach, we have designed, fabricated, and tested a micromechanical testbed that exhibits multi-mode digital control of a suspended microstructure. The testbed consists of a suspended polysilicon plate having four capacitive-bridge vertical position sensors, each with an integrated CMOS buffer amplifier, four differential electrostatic feedback actuators on the plate's corners, and an interdigitated comb for lateral force input.

In parallel to our research efforts on modeling and simulation, we have developed theory and produced experimental results for the thermal assembly of polysilicon microstructures, which is presented in chapter 2. Fusible polysilicon microbridges (fuses) support delicate microstructures to prevent breakage and sticking to the substrate or each other during final rinsing and drying process steps after microstructure release. Other fuse applications include adjustment of mechanical response in accelerometers and gyroscopes, and frequency trimming of resonators and mechanical filters. Analytic and finite-element analysis of resistive heating in short microbridges is performed to determine the fuse I-V characteristics and the time and energy required to cut a fuse. Several practical fuse designs are presented along with interconnection schemes that allow simultaneous cutting of many fuses in parallel. Next, we describe a novel welding structure design, made from an aluminum microbridge that connects two polysilicon microstructures. By resistively heating the aluminum to the melting point, relatively large lateral surface-tension forces are produced which join the polysilicon structures together to form a strong, permanent weld joint. To demonstrate thermal microassembly, a combination of welding and fusing techniques are used to construct a narrow-gap comb-drive microactuator. Another thermal assembly application, frequency trimming of microresonators, uses weld structures or fuses to adjust the stiffness of the resonator's suspension.

In chapter 3, we develop general lumped-parameter models of surface-micromachined components, including the micromechanical equations of motion, squeeze-film damping, spring constants, electrostatic actuation, and capacitive position sensing. An effort is made to derive analytic models whose parameters can be extracted from the layout of an

arbitrary surface microsystem. Expressions are given for spring constants of fixed-fixed, crab-leg, folded-flexure, and serpentine geometries, for squeeze-film damping coefficients, and for electrostatic forces generated by parallel-plate and comb-finger microactuators. In the last section, we analyze two methods of capacitive position detection — voltage sensing with a unity-gain buffer and displacement-current sensing with a transresistance amplifier — and compare their performance in sensing position and acceleration of a micromechanical plate. Brownian noise (thermal noise of the structure) is compared with electronic noise of the position sensor to determine which mechanism limits the signal sensitivity.

The micromechanical testbed is introduced in chapter 4. We start with a background discussion of the conventional, second-order sigma-delta ( $\Sigma$ - $\Delta$ ) feedback loop, and then describe the analogous micromechanical  $\Sigma$ - $\Delta$  architecture that is used in the testbed. Four independent  $\Sigma$ - $\Delta$  feedback loops control the vertical position and out-of-plane rotation of the testbed’s suspended polysilicon plate. Digital compensation in the feedback path allows operation at low pressures, when the mechanical system is underdamped. Several fabrication problems, some encountered while extending the process to two structural polysilicon layers, are documented with their solutions: inter-polysilicon spin-on-glass planarization, rapid-thermal-annealing to reduce residual stress, and sputtering of thin titanium/titanium-nitride films to form robust contacts.

Chapter 5 details the simulation and analysis of the testbed. Geometric parameters are extracted for the testbed’s mass-spring-damper, parallel-plate electrostatic actuators, and capacitive position sensors. Then, the micromechanical component models, described in chapter 3, are implemented in the SPICE and MATLAB simulation software. The remaining sections deal with analytic analysis of limit cycles and quantization noise in a micromechanical  $\Sigma$ - $\Delta$  loop. Contributions from Brownian noise, quantization noise, electronic noise, and interconnect noise are compared for the testbed, and a theoretical value for total noise acceleration is calculated.

Chapter 6 begins with a description of the testbed experimental setup, followed by a report on several experimental results. First, position-sensor output voltage as a function of plate position is experimentally characterized by measuring displacement with laser interferometry. We then measure the capacitive feedthrough from the feedback actuators to the position-sense capacitors. The value of squeeze-film damping in air is determined by measuring the open-loop step response to an electrostatic comb-drive force. Expected closed-loop behavior is demonstrated through a comparison of the measured and simulated

response to an external square-wave position reference. Static accelerometer tests provide a measured noise acceleration value that is compared with the theoretical result. Our final results illustrate the bounded limit cycle behavior during underdamped operation at low pressure.

In the final chapter, we form conclusions about our lumped-parameter modeling approach to simulating MEMS and discuss the performance of the multi-mode  $\Sigma$ - $\Delta$  testbed. We then outline some future research in thermal assembly, modeling, simulation, and surface microsystems.

The appendices contain detailed information about the testbed layout and extracted parameters, schematics and pictures of the external testbed electronics, input files for the HSPICE simulations, and the process flow that resulted in successful testbed fabrication. Information in the appendices (and elsewhere in this thesis) will be accessible on the World Wide Web (WWW) through a hypertext viewer, such as Mosaic, by specifying the Universal Resource Locator (URL) for the Berkeley Sensor & Actuator Center home page: "<http://nitride.eecs.berkeley.edu>". From that location, browse to find the link to my research home page (look for "Gary Fedder"). Good luck!

## Chapter 2

# Thermal Assembly of Polysilicon Microstructures

### 2.1 Introduction

A key feature of surface micromachining is that micromechanical systems, consisting of flexures, linkages, and bearings can be fabricated *in situ* on the silicon substrate, thereby eliminating painstaking and costly microassembly steps [13]. Since these structures are fabricated from deposited thin films, their mechanical behavior can be altered by run-to-run variations in thickness, mechanical properties, and patterning of the structural layer. Residual strain in the structural layer is an important design constraint in sensitive structures, such as resonators with clamped suspensions. For the case of polysilicon films, considerable work has been done over the last several years to control residual strain for specific applications [14–16]. It is not possible, however, to have functional microstructures with arbitrarily large lateral dimensions. For example, fixed-fixed microbridges, which are useful for resonant strain gauges [17–19] require extremely tight control of the average residual strain. In the case of heavily phosphorus-doped (coarse grain) polysilicon films (which are useful for electrostatically driven and sensed microbridges), such precise control of residual strain has not been achieved to date. For certain applications, it may be possible to select flexure designs which allow release of the average residual strain [20].

Surface micromachining involves the selective etching of a sacrificial layer surrounding a patterned microstructural layer. After rinsing and drying, free-standing mi-

cromechanical elements are produced. For many microstructures, this basic process suffices for their *in situ* fabrication. However, microstructures with highly compliant suspensions are susceptible to breakage, or to attachment to the substrate, or attachment to each other, due to surface tension forces in the final rinse and drying step [21, 22]. Release of microstructures using supercritical CO<sub>2</sub> methods [23] or freeze-drying methods [16, 24] relieves the surface tension forces during drying, but does not address breakage during rinsing. A dry-release method that uses polymer columns to temporarily support microstructures [25] is a processing alternative to using fuses.

Given the limitations of thin films as mechanical materials, how can surface micromachining be modified or extended to fabricate microstructures that are free of residual stress and that survive the rinsing and drying process? One avenue is to implement some form of post-fabrication trimming procedure. In this chapter, we investigate resistive heating to separate, weld, or deform polysilicon microstructures, subsequent to release from the substrate [26, 27]. The techniques are based on the ability to heat polysilicon microstructures to high temperatures with little power [28–30]. As we will describe, these thermal microassembly procedures are accomplished under electrical control, without the need for micromanipulation; costly adjustment or assembly of wafers at a wafer probe station is eliminated.

Additional motivations for post-micromachining assembly are the control or elimination of clearances in microbearings, pre-stressing springs, and active alignment of critical elements. Micromechanical systems with sub-micron spacing between elements are difficult to fabricate using conventional lithography and etching. For example, it is desirable to design sub-micron gaps between the stator and movable comb in a lateral resonator to increase the electrostatic force for a given applied voltage. Pre-biased lateral flexures have been described by Judy [31] that also have application to post-micromachining adjustment and assembly. Self-adjusting microstructures and thermal microassembly are both aimed at enhancing the capabilities of surface micromachining technology by means of adjustments and modification to the microstructure after its release from the substrate.

After outlining the fabrication process for the polysilicon welding and cutting test structures, we develop models for the resistive heating of polysilicon microbridges up to the melting point. Resistive welding and cutting on the macro scale provides some qualitative insight into these processes with polysilicon microbridges. Resistive heating can raise the temperature of polysilicon bridges above the melting point while dissipating less

than 100 mW of power. Experimental measurements of I-V characteristics for polysilicon microbridges are presented, which are in general agreement with the model. We describe several applications of thermal microassembly: the severing of temporary support beams which stabilize a large, delicately suspended microstructure during etching of the sacrificial phosphosilicate glass (PSG) layer, the assembly of a comb-drive with sub-micron gaps between its fingers, bonding of flipped structures to anchor points, and frequency trimming for microresonators.

## 2.2 Fabrication

Micromechanical structures, thin polysilicon fusible supports, and aluminum welding structures are integrated in a nine-mask process (Figure 2.1). The initial processing steps are similar to the first comb-drive resonator process [20]. Different versions of fusing and welding test structures are made from separate process runs. Some of the runs omit or modify the steps outlined here; these process alterations will be presented with the experimental results associated with each run. After each processing step is discussed, the corresponding part of Figure 2.1 will be stated in parenthesis.

Our processing starts with 4", prime, n-type,  $<100>$  silicon wafers. Silicon nitride is deposited over thermal silicon dioxide to isolate the structures from the silicon substrate. A 3000 Å *in situ* doped polysilicon film is deposited and plasma etched in  $\text{CCl}_4$  to form an interconnect layer. Next, 2  $\mu\text{m}$ -thick PSG is deposited as a sacrificial spacer for the polysilicon microstructures. Dimples are fabricated on the underside of the structural polysilicon by patterning openings over the sacrificial PSG and doing a timed wet etch in 5:1 BHF. Contact cuts are made to the underlying polysilicon layer using a  $\text{CHF}_3/\text{CF}_4$  plasma etch. An undoped, 2  $\mu\text{m}$ -thick film of LPCVD polysilicon is deposited at 605 °C, 250 sccm  $\text{SiH}_4$ , and 550 mTorr, producing a slightly tensile film (a). This deposition pressure is higher than the 320 mTorr used for very low strain films at 605 °C in previous work on undoped polysilicon deposited on PSG [32]. Results for undoped films deposited on thermal oxide are consistent with a tensile film [33]. An additional 0.5  $\mu\text{m}$  of PSG is deposited and annealed for one-hour at 950 °C to dope the polysilicon and reduce stress gradients in the film. After stripping the top layer of PSG, trenches in the polysilicon structural layer are formed (b). Thin fusible supports and aluminum microbridges will be placed in these trenches. The photoresist mask is ashed in  $\text{O}_2$  plasma for 7 minutes at 50 W to ensure sloped sidewalls.

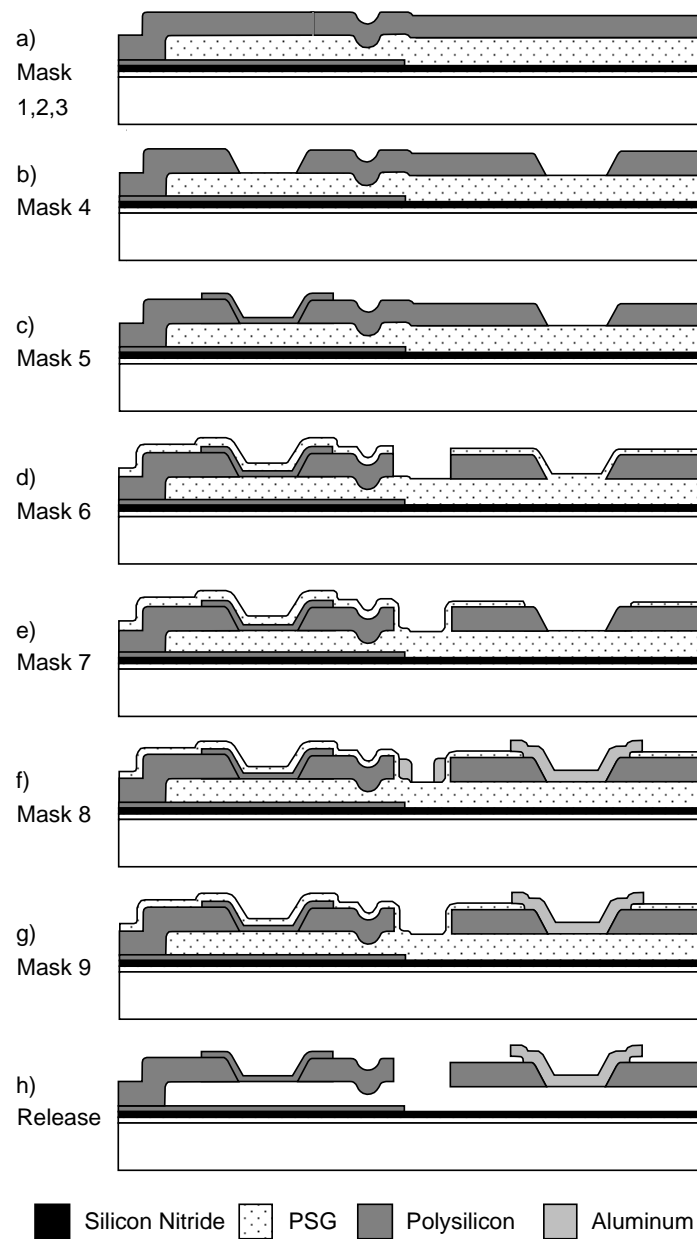


Figure 2.1: Cross-sections of the nine-mask process flow to fabricate fusing and welding structures.

A  $\text{CCl}_4$  plasma etch transfers the sidewall pattern to the polysilicon trench. Next, 2000 Å–4000 Å of *in situ* doped polysilicon is deposited directly on top of the structural polysilicon. Thin polysilicon fuses, made from the second polysilicon film, attach directly to the thick structural layer without the need for an extra contact-cut module. A timed  $\text{CCl}_4$  plasma etch defines the fusible supports in the trenches (c). Another 0.5  $\mu\text{m}$ –0.8  $\mu\text{m}$  of PSG is deposited and densified using rapid thermal annealing (RTA) at 1050 °C for 1 minute. The PSG is patterned and used as a mask for the structural polysilicon etch. Structural etching was deferred until after etching the fusible supports, so the thin polysilicon fuse layer does not conformally coat the structures and affect their mechanical integrity. Plasma etching combined with the PSG mask results in vertical sidewalls on the mechanical microstructures (d). After an additional 3000 Å of PSG is deposited, the PSG is patterned and wet etched to form contact cuts for the subsequent aluminum layer (e). The sputtered 1.5  $\mu\text{m}$ -thick aluminum, used in the welding structures, is etched in a  $\text{Cl}_2$  plasma (f). A final mask is used to protect the aluminum weld joints during wet etch of aluminum sidewalls (g). A 1 minute concentrated (49%) HF etch releases the microstructures without attacking the aluminum (h) [34].

## 2.3 Heating of Microbridges

Resistive heating of polysilicon microbridges has been used in flowmeters, pressure sensors [30], light sources [35], electrical fuses for trimming, and temporary mechanical supports for microstructures [26]. These applications require a qualitative understanding of the thermal and electrical properties of polysilicon at very high temperatures. However, micromechanical structures which rely on the melting of polysilicon, such as welding and stress-relief structures, require more detailed knowledge of polysilicon resistivity and thermal conductivity at temperatures around the melting point. A quantitative model of the temperature distribution in polysilicon microbridges during melting is a first step toward optimal design of these micromechanical structures. In this section, we will first present the analytic one-dimensional thermal analysis of microbridges. Next, we extend the microbridge analysis by solving a one-dimensional finite-element formulation that includes nonlinear temperature dependence of polysilicon resistivity. Analytic and finite-element calculations are compared with experimental results.

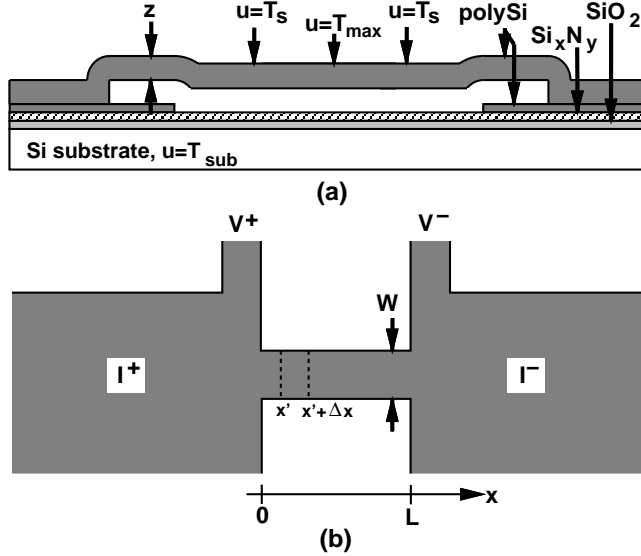


Figure 2.2: Schematic drawing of a polysilicon microbridge used for I-V measurements. (a) Side view. (b) Top view. Current is applied from  $I^+$  to  $I^-$ . Voltage is sensed from  $V^+$  to  $V^-$ .

### 2.3.1 Analytic Thermal Analysis

Little previous work could be found about modeling of polysilicon microbridges at temperatures up to the melting point. The analysis of polysilicon fuses in integrated circuits is a different problem, since conduction to the substrate under the resistor dominates the heat transfer [36]. A one-dimensional model, including heat conduction and convection through air, has been used to explain thermal characteristics of polysilicon microbridges [30]. For sufficiently short bridges in air, heat is conducted primarily out the ends of the bridge to the supporting structure. Conduction and convection through the ambient atmosphere and radiative terms can be neglected. The temperature distribution in the bridge is approximated as one-dimensional, varying lengthwise.

A schematic drawing of the microbridge used in our experiments is shown in Figure 2.2. The one-dimensional heat flow equation is derived by examining a differential element of the bridge of width  $w$ , thickness  $z$ , and length  $\Delta x$  (Figure 2.2(b)). Under steady-state conditions, ohmic power generated in the element is equal to heat conduction out of the element.

$$\kappa_p A \left( \frac{\partial u}{\partial x} \Big|_x - \frac{\partial u}{\partial x} \Big|_{x+\Delta x} \right) = J^2 \rho A \Delta x \quad (2.1)$$

where  $A = wz$  is the cross-sectional area of the bridge,  $\kappa_p$  is the thermal conductivity of polysilicon,  $u(x)$  is the temperature of the bridge,  $J$  is the current density, and  $\rho(u)$  is the electrical resistivity of the bridge. The resistivity is assumed to have a linear temperature coefficient,  $\xi$ , such that  $\rho(T_o) = \rho_o$ .

$$\rho = \rho_o (1 + \xi (u - T_o)) \quad (2.2)$$

The resistivity of degenerately-doped n-type polysilicon exhibits a positive temperature coefficient at temperatures below 300 °C [30,37]. The potential barrier at the grain boundaries is reduced in heavily-doped polysilicon, producing behavior in resistivity similar to single-crystal silicon [38,39]. Combining Equations (2.1) and (2.2) and taking the limit as  $\Delta x \rightarrow 0$  produces the following second-order differential equation.

$$\kappa_p \frac{\partial^2 u}{\partial x^2} = -J^2 \rho_o (1 + \xi (u - T_o)) \quad (2.3)$$

Solving Equation (2.3) and using the boundary conditions,  $u|_{x=0} = u|_{x=L} = T_s$  gives the temperature along the length of the bridge.

$$u(x) = \left( T_s - T_o + \frac{1}{\xi} \right) \frac{\cos(\gamma(2x/L - 1))}{\cos \gamma} + T_o - \frac{1}{\xi} \quad (2.4)$$

where  $\gamma \triangleq 0.5JL\sqrt{\rho_o\xi/\kappa_p}$ .

The maximum temperature,  $T_{\max}$ , is found at the center of the bridge.

$$T_{\max} = \frac{T_s - T_o + \frac{1}{\xi}}{\cos \gamma} + T_o - \frac{1}{\xi} \quad (2.5)$$

The total resistance of the bridge is found by integrating the differential resistance,  $(\rho/A)dx$  across the bridge.

$$R = \frac{\rho_o L}{A} (1 + \xi (T_s - T_o)) \frac{\tan \gamma}{\gamma} + R_s \quad (2.6)$$

$R_s$  is a constant series resistance term, which is present because the voltage sense leads ( $V^+$  and  $V^-$  in Figure 2.2(b)) do not physically contact the bridge at  $x = 0$  and  $x = L$ . Placing sense leads at the end of the bridge would have altered the temperature distribution of the bridge.

The voltage across the bridge is simply the ohmic drop,  $V = IR$ .

$$V = \frac{I\rho_o L}{A} (1 + \xi (T_s - T_o)) \frac{\tan \gamma}{\gamma} + IR_s \quad (2.7)$$

It is interesting to note that voltage as a function of maximum temperature can also be found by an alternative derivation [40] if  $R_s$  is neglected.

$$V = \sqrt{8\kappa_p\rho_o \left( (1 - \xi T_o) (T_{\max} - T_s) + \frac{\xi}{2} (T_{\max}^2 - T_s^2) \right)} \quad (2.8)$$

Since the anchor pads are not perfect conductors of heat, the temperature at the ends of the bridge,  $T_s$ , will not be constant;  $T_s$  varies with bridge geometry and power dissipation. Heat lost,  $\dot{Q}_{\text{loss}}$ , through conductive flow out the ends of the bridge is modeled with a linear relationship:

$$\dot{Q}_{\text{loss}} = \alpha(T_s - T_{\text{sub}}) \quad (2.9)$$

where  $\alpha$  is the effective thermal conductance of the pad (with units of W/°K) and  $T_{\text{sub}}$  is the substrate temperature. In steady-state, total heat flow out the ends of the bridge must equal heat flow through the pads, giving an equation for  $T_s$ .

$$T_s = \frac{\alpha T_{\text{sub}}/A + J \sqrt{\rho_o \kappa_p / \xi} (1 - \xi T_o) \tan \gamma}{\alpha/A - J \sqrt{\rho_o \kappa_p \xi} \tan \gamma} \quad (2.10)$$

Current versus voltage (I-V) characteristics in air are shown for several values of bridge length (Figure 2.3(a)) and bridge width (Figure 2.3(b)). As applied current is increased, the differential resistance monotonically increases, because of the positive temperature coefficient of resistivity. At a sufficiently high voltage, however, the current rises dramatically and eventually the bridge becomes an open-circuit. Figure 2.4 shows a bridge that has melted. The bridge visibly starts to melt when the large increase in current begins to occur. Presumably the melting decreases the resistance, either from deformation or a decrease in resistivity [41, 42]. Larger values of open-circuit voltage are observed for long, narrow bridges.

Good general agreement is observed between the theoretical curves and the measured data. An experimental value for thermal conductivity of degenerately doped polysilicon has been found to be 32 W/m/°K [29]. A measured value for the temperature coefficient at low temperatures ( $\xi = 8.3 \times 10^{-4} \text{ }^{\circ}\text{C}^{-1}$ ) is used in Equation (2.7) to generate these curves. Values for resistivity, measured for each die, are nominally  $3.7 \times 10^{-5} \Omega\text{-m}$  at  $T_o=27 \text{ }^{\circ}\text{C}$ . The substrate is at room temperature,  $T_{\text{sub}}=27 \text{ }^{\circ}\text{C}$ . The sense lead resistance and pad conductance are estimated to be constant:  $R_s=8 \Omega$  and  $\alpha=64 \mu\text{W}/\text{°K}$ , respectively. In Figure 2.3, the theoretical curves end when the middle of the bridge reaches the melting

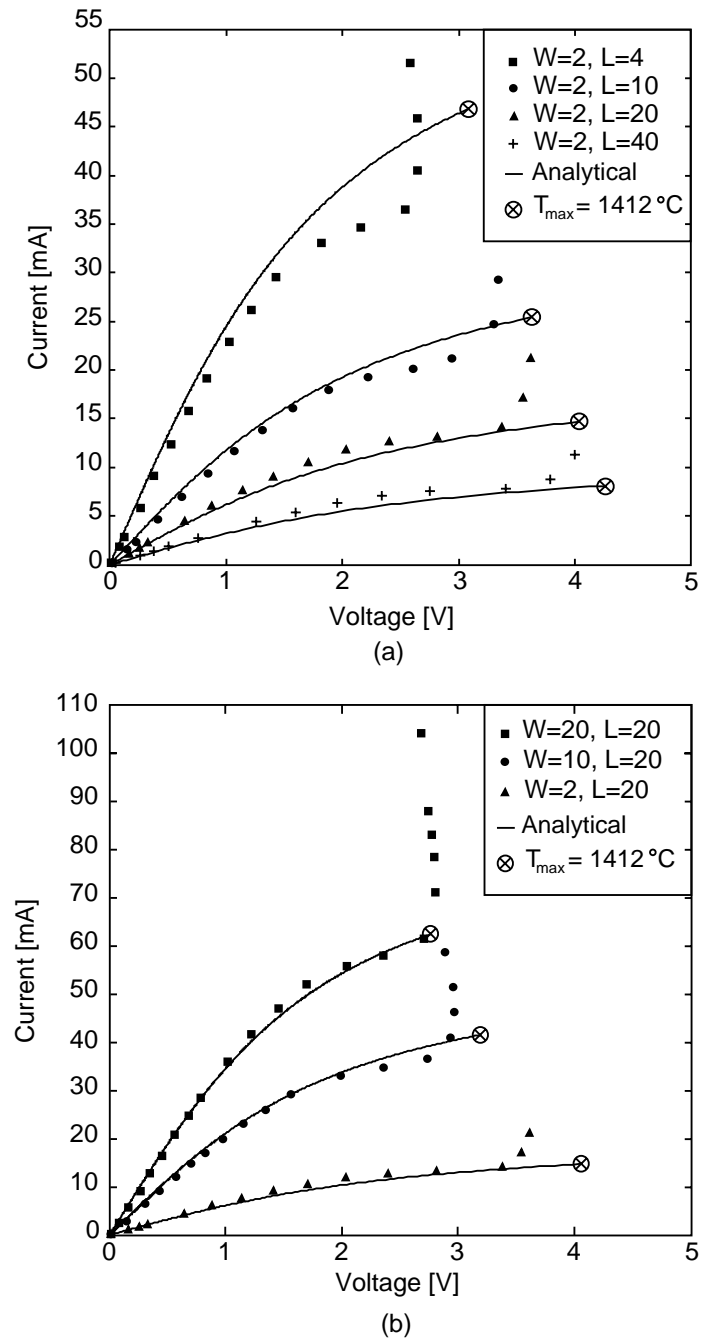


Figure 2.3: I-V characteristics of several microbridges. (a) Different values of length.  
(b) Different values of width.

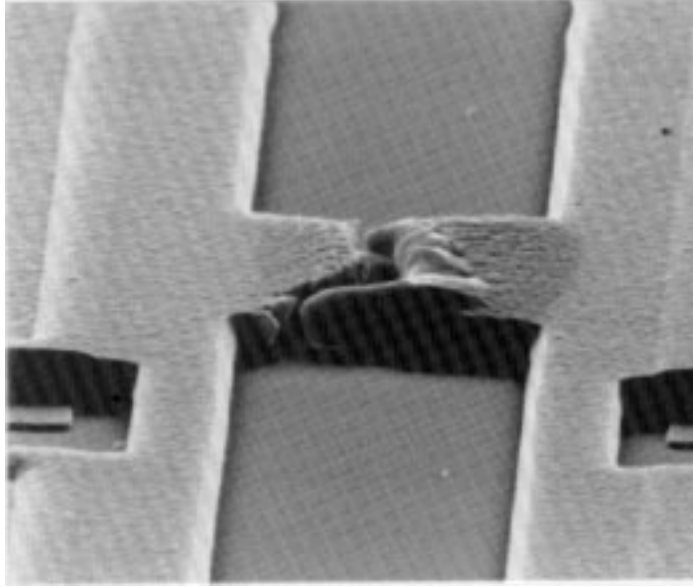


Figure 2.4: SEM of an open-circuited  $10 \mu\text{m}$ -wide,  $20 \mu\text{m}$ -long microbridge.

point ( $1412^\circ\text{C}$ ), which will be interpreted as the point when the bridge becomes an open-circuit. The finite thermal conductance of the pads accounts for the observed dependence of the open-circuit voltage on bridge geometry.

The measured I-V data in Figure 2.3 was recorded manually; it took several seconds to log each data point. Resistance of polysilicon microbridges has been shown to change with time when operated at high constant temperature [35]. These effects are omitted in the present analysis and may account for some of the differences between the model and data at higher temperatures. However, we believe that most of the discrepancies between measured and theoretical results are due to the nonlinear resistivity changes at high temperatures.

Figure 2.5 shows I-V curves for three  $20 \mu\text{m}$ -long bridges on three adjacent dice of the same wafer. Two of the bridges were measured in air, while the third bridge was measured in a vacuum probe station pumped down to  $3 \times 10^{-4}$  Torr. Each of the three bridges has a slightly different resistance value, due to process parameter variations across the wafer. Since the values of the open-circuit voltage of each bridge are nearly the same, effects of heat conduction and convection through air are shown to be small. A large increase in current was not observed prior to the open-circuit for the bridge in vacuum; however, increases were seen with other bridges tested in a vacuum.

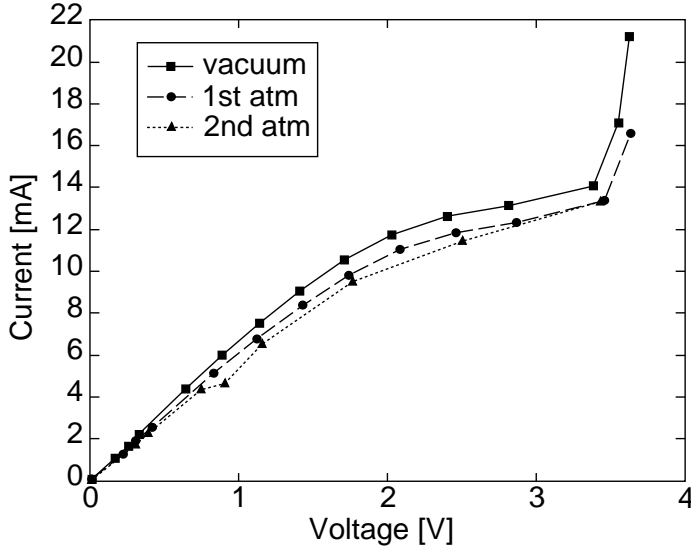


Figure 2.5: I-V characteristics of 2  $\mu\text{m}$ -wide, 20  $\mu\text{m}$ -long bridges on adjacent dice, showing insensitivity to ambient conditions.

### 2.3.2 Finite-Element Thermal Analysis

An analytic solution does not exist for the temperature distribution in the micro-bridge at high current levels, because of the nonlinear resistivity variation with temperature. In this section, nonlinear resistivity is modeled using finite-element thermal analysis.

The temperature dependence of silicon resistivity at very high temperatures is not well understood. Below 600  $^{\circ}\text{C}$ , positive values of temperature coefficient for heavily doped silicon resistivity have been measured [43], and negative values of temperature coefficient have been reported above 400  $^{\circ}\text{C}$  [41]. Localized melting of grain boundary layers has been suggested as a mechanism for the decrease in resistivity at sufficiently high temperatures [42].

Temperature variation in single-crystal silicon thermal conductivity [44] suggests that polysilicon thermal conductivity also has a significant temperature dependence at high temperatures. However, we assume a constant thermal conductivity in the finite-element analysis.

Referring to Figure 2.2, the temperature distribution in the bridge can be approximated as one-dimensional, varying lengthwise.

$$\kappa_p \frac{\partial^2 u}{\partial x^2} = -J^2 \rho(u) \quad (2.11)$$

where the resistivity is a function of temperature, which varies with position.

The resistivity is given by Equation (2.2) at temperatures below  $T_m$ . A different linear temperature coefficient,  $\xi_m$ , models resistivity variation at intermediate temperatures. Above a crossover temperature,  $T_c$ , resistivity is modeled as exponentially decreasing with temperature [41].

$$\begin{aligned}\rho_L &= \rho_o(1 + \xi(u - T_o)) \quad ; \quad u \leq T_m \\ \rho_M &= \rho_L(u = T_m)(1 + \xi_m(u - T_m)) \quad ; \quad T_m < u \leq T_c \\ \rho_H &= \rho_M(u = T_c)\left((1 - A_m)e^{-(u-T_c)/T_r} + A_m\right) \quad ; \quad u > T_c\end{aligned}\quad (2.12)$$

where  $\rho_o = \rho_L(u = T_o)$  and  $T_r$  determines how fast the resistivity will drop with temperature.  $T_m$ ,  $T_c$  and  $T_r$  are used as fitting parameters in the numerical analysis. The finite-element results are not sensitive to the exact value of  $A_m$ , which determines the high temperature resistivity limit. The three regimes are stitched together using a Fermi-Dirac smoothing function, given by

$$f(u, T) = \frac{1}{1 + e^{(u-T)/T_a}} \quad (2.13)$$

where  $T_a$  is a measure of the transition between regimes, and is fixed at 100 °C. The complete resistivity equation is

$$\rho = f(u, T_m)\rho_L + (1 - f(u, T_m))f(u, T_c)\rho_M + (1 - f(u, T_c))\rho_H \quad (2.14)$$

Model parameters for polysilicon resistivity are determined by fitting the finite-element results to the measured I-V data. The resulting resistivity curve is shown in Figure 2.6, where the fitting parameters are set to  $\xi = 4 \times 10^{-4} \text{ } ^\circ\text{C}^{-1}$ ,  $\xi_m = 8 \times 10^{-4} \text{ } ^\circ\text{C}^{-1}$ ,  $A_m = 0.35$ ,  $T_m = 600 \text{ } ^\circ\text{C}$ ,  $T_c = 1100 \text{ } ^\circ\text{C}$ ,  $T_r = 400 \text{ } ^\circ\text{C}$ . A sharp decrease in resistivity occurs when the polysilicon melts, but this effect is not included in our analysis. Modeling high-temperature effects with the decreasing exponential function is adequate in fitting to the measured I-V data.

The total resistance of the bridge is found by integrating the differential resistance,  $(\rho/A)dx$  across the bridge. The voltage across the bridge is the ohmic drop,  $V = IR$ .

$$V = J \int_0^L \rho(x)dx \quad (2.15)$$

The pad thermal conductance is a function of the fuse cross-section and the pad geometry.

$$\alpha = \kappa z \left(\frac{W}{L}\right)_{\text{pad}} \quad (2.16)$$

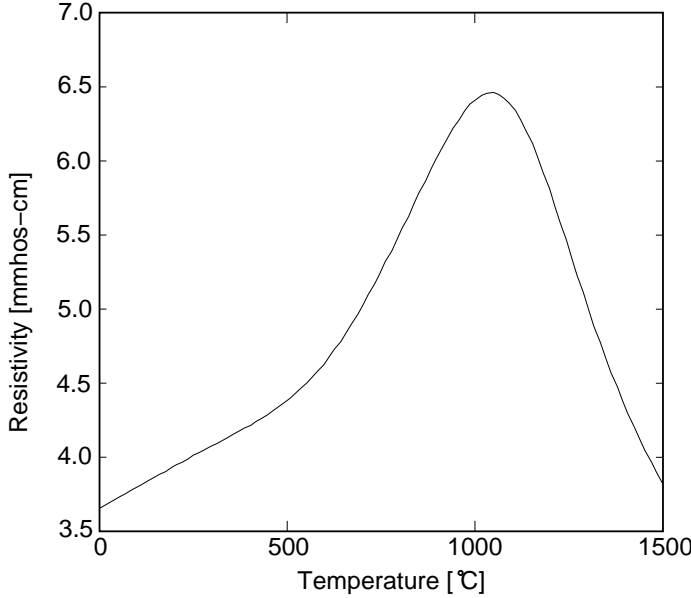


Figure 2.6: Resistivity versus temperature model, determined by fitting finite-element results to measured data.

w [μm]	(W/L) <sub>pad</sub>	α [μW/°K]
2	0.8	51
10	1.0	64
20	1.2	77

Table 2.1: Effective pad conductance width over length ratio fitted to make measured I-V results and finite-element I-V results match.  $z=2 \mu\text{m}$ .

where  $(W/L)_{\text{pad}}$  is the effective width over length ratio of the heat conductance path out through the pad. We have fit the conductance as a function of fuse width, the values are given in Table 2.1. The fitted pad thermal conductivity does not scale linearly with fuse width.

The microbridge is divided into 10 elements of equal length, using cubic shape functions and four-point Gaussian integration. General natural boundary conditions model the pad conductance. The low-temperature solution, Equation (2.4), provides a first prediction of the temperature profile. An iterative technique is then used to find a solution for the nonlinear differential equation. If the previous solution were used to calculate coefficients for the next step, a bistable state would be obtained, with no convergence. Instead, the estimated temperature profile is found by averaging the last two iterative solutions. Resis-

tivity values, for use in the next iteration, are calculated using the estimated temperature values. Less than 20 iterations are required for adequate convergence of each solution.

Voltage across the bridge must be calculated to compare numerical results with experimental I-V curves. Resistance across the bridge is calculated using four-point Gaussian integration of the resistivity of each element along the bridge.

I-V characteristics from experimental measurements, analytic calculations, and finite-element simulations for several microbridges are given in Figure 2.7. Since we are interested in modeling the high-temperature resistivity, we reduce the effects of parameter errors at low temperatures by fitting the analytic calculations to the data. Therefore, the room-temperature resistivity,  $\rho_0$ , is fitted for each bridge and the temperature coefficient at low temperatures is fixed at  $\xi = 4 \times 10^{-4} \text{ }^{\circ}\text{C}^{-1}$ . At low voltages, the analytic and finite-element solutions match, validating the finite-element code. The finite-element solution and measured data are in general agreement, displaying a rapid rise in current when the bridge temperature rises above the crossover temperature. The steep resistivity increase with temperature over 600  $^{\circ}\text{C}$  shows up as a downward bend in the curves at intermediate current values. At high temperatures, the calculated I-V results depend strongly on the resistivity, pad heat conduction, and sense lead resistance parameters. In particular, placement of the kink in the finite-element I-V curve is strongly dependent on the pad heat conduction model. Also, thermal conductivity may not be constant with temperature, affecting the calculated I-V characteristics at higher current levels. Experimental testing of many samples must be done to provide confidence in the model parameters. Polysilicon resistivity models will vary with doping levels and deposition parameters; our results are limited to polysilicon deposited at 605  $^{\circ}\text{C}$  and doped by high-temperature diffusion from PSG.

Assuming the finite-element thermal modeling is adequate, bridge temperature can be predicted for various bridge geometries. Figure 2.8 shows temperature distributions of the 10  $\mu\text{m}$ -wide by 20  $\mu\text{m}$ -long bridge as current is varied from 10 mA to 50 mA. For currents up to 30 mA, the temperature profile varies as the square of the current, approximately. At higher currents, the rate of increase in temperature is retarded; however, the profile keeps the same sinusoidal shape. Note that much of the bridge has temperature values above the melting point (1412  $^{\circ}\text{C}$ ) at a current of 50 mA. Long bridges have relatively low temperatures at the ends of the bridge, while short bridges have very high temperatures throughout the bridge. For example, when the temperature at the center of the bridge is 1412  $^{\circ}\text{C}$ , the temperature at the ends is  $T_s = 352 \text{ }^{\circ}\text{C}$  for a 2  $\mu\text{m}$ -wide by 40  $\mu\text{m}$ -long bridge

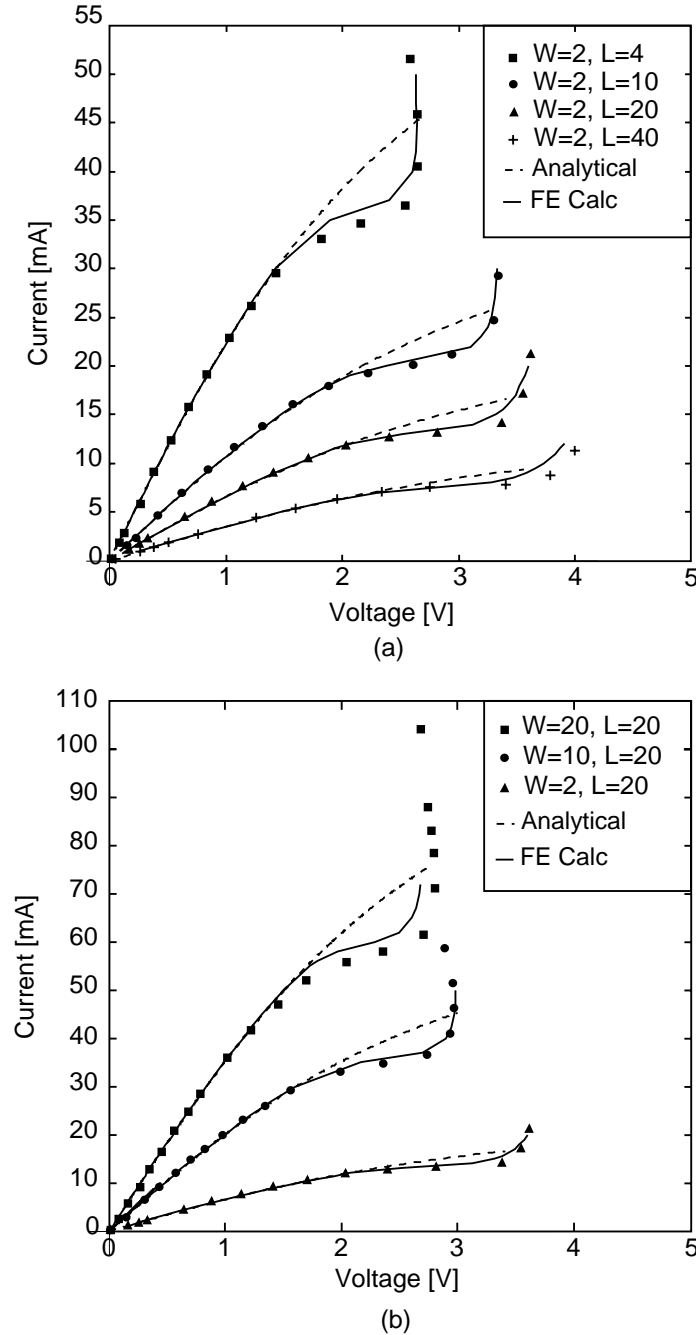


Figure 2.7: Measured I-V characteristics of several microbridges, compared with finite-element results. (a) Different values of length. (b) Different values of width.

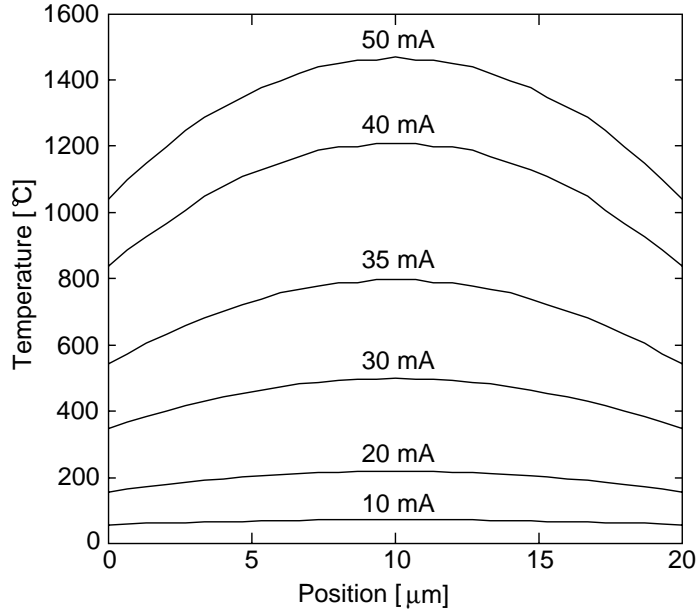


Figure 2.8: Temperature distribution of the  $10 \mu\text{m}$ -wide by  $20 \mu\text{m}$ -long microbridge as current is varied from  $10 \text{ mA}$  to  $50 \text{ mA}$ .

and  $T_s = 1087^\circ\text{C}$  for a  $2 \mu\text{m}$ -wide by  $4 \mu\text{m}$ -long bridge. Clearly, the temperature of the entire pad cannot be assumed to be at a constant, low value. Further increases in current widen the molten area while limiting the temperature rise of the bridge.

Resistivity distributions along the  $10 \mu\text{m}$ -wide by  $20 \mu\text{m}$ -long bridge are shown in Figure 2.9. Lower current levels produce a sinusoidal resistivity profile. At high current levels, a peak value is reached near the ends of the bridge, with lower values in the middle, where the temperature is greatest. Although less power is generated in the middle of the bridge, the temperature will not decrease because heat can only flow out through the ends of the bridge.

## 2.4 Resistive Cutting

### 2.4.1 Introduction: Tee-Bridge Fusible Supports

Resistive cutting allows the electrical removal of temporary micromechanical supports. Temporary supports are used to hold delicate microstructures in place during a wet etch of sacrificial PSG, and away from the substrate while drying. One microstructure designed for this application, a “tee” bridge, is shown in Figure 2.10(a). Current flows

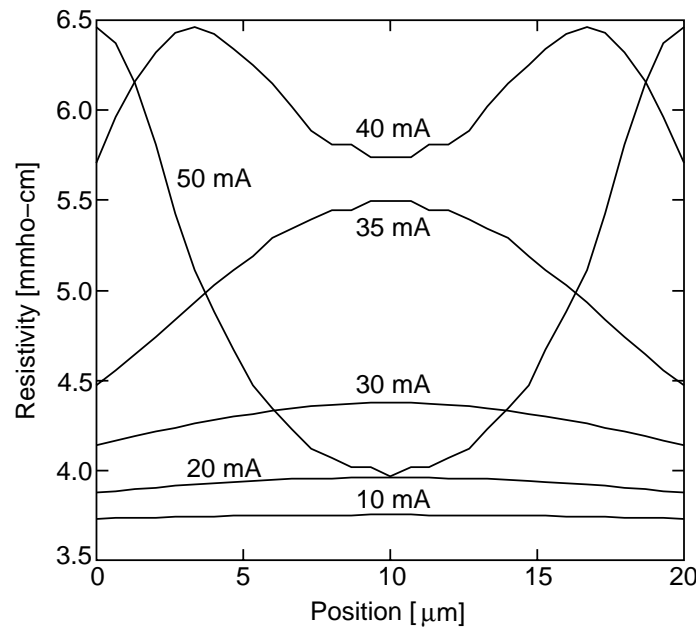


Figure 2.9: Resistivity distribution of the  $10\text{ }\mu\text{m}$ -wide by  $20\text{ }\mu\text{m}$ -long microbridge as current is varied from  $10\text{ mA}$  to  $50\text{ mA}$ .

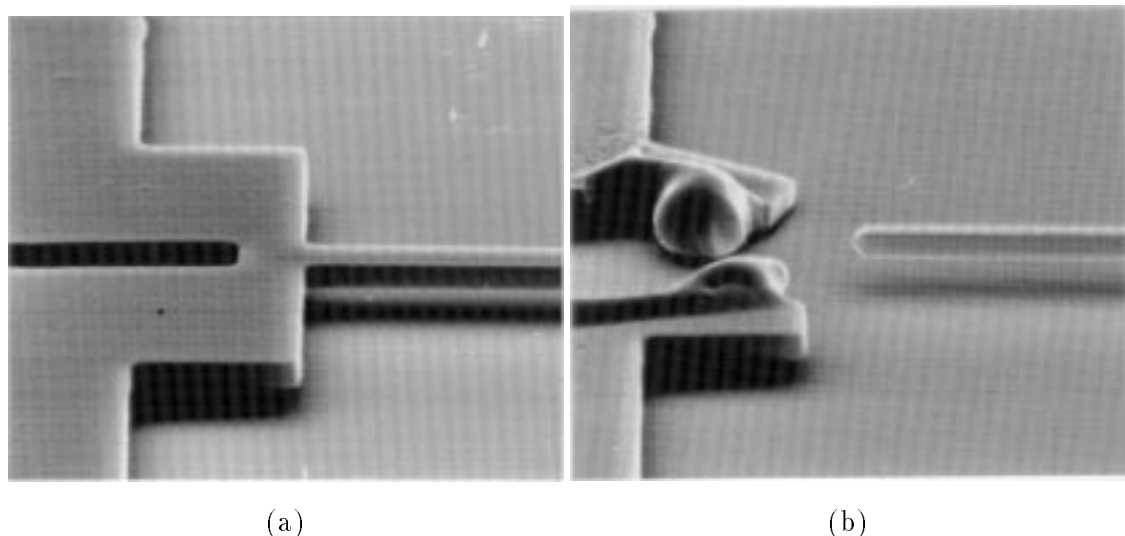


Figure 2.10: SEM of a polysilicon tee bridge. (a) Before resistive cutting. (b) After resistive cutting.

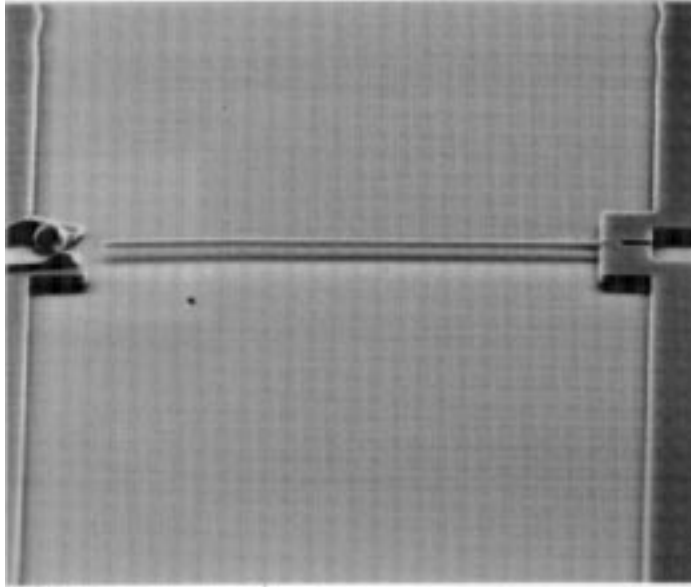


Figure 2.11: SEM of the polysilicon cantilever beam, released by the tee bridge.

through the supporting bridge, which melts the polysilicon and frees the attached beam. Figure 2.10(b) shows the severed tee bridge after application of a single  $100 \mu\text{s}$ ,  $300 \text{ mA}$  pulse. The bridge actually cuts in around  $1 \mu\text{s}$ , opening the circuit for the remaining duration of the pulse. Current does not pass through the  $2 \mu\text{m}$ -wide suspension beam, leaving the released microstructure undamaged by resistive heating. No residual material is deposited on the substrate from the cutting operation. Material from the polysilicon bridge melts and wicks to the ends of the bridge during cutting. A view of the entire microstructure (Figure 2.11) shows the cantilever beam created by cutting the support.

#### 2.4.2 Current Sink for Fuse Cutting

Although voltages from  $3\text{--}5 \text{ V}$  are sufficient to melt a bridge and create an open-circuit, much larger voltages are needed to form a wider gap and reliably sever a bridge. A current source is preferred for resistively cutting bridges, so that ohmic drops across contacts, pads, and interconnect do not affect the input power. In a series-connected array of bridges, one bridge will electrically open first, removing the power source from the circuit. Therefore, only one cut can be made reliably at a time. Voltage sources can produce many cuts in parallel, but it is difficult to control the input power and produce clean cuts.

A schematic of the voltage-controlled current sink used to cut the fuses is shown in

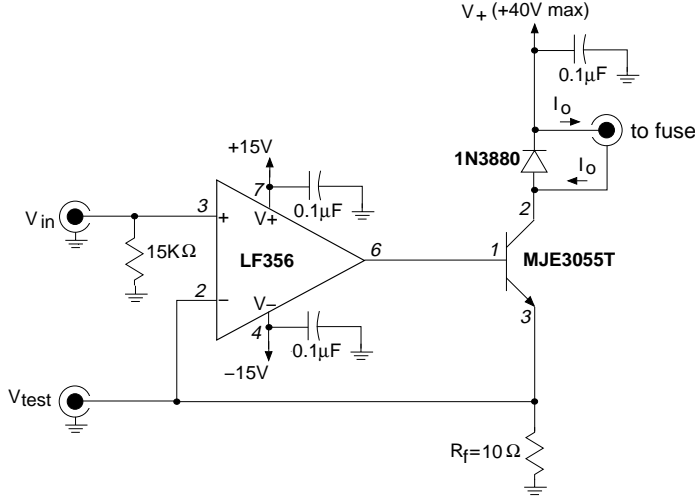


Figure 2.12: Schematic of voltage-controlled current sink used to cut fuses.

Figure 2.12. Current feedback to the LF356 operational amplifier ensures that the output current tracks the input voltage with the relation:

$$I_o = \frac{V_{in}}{R_f} = 0.1 V_{in} \quad (2.17)$$

The MJE3055T npn power transistor switches the large currents necessary to cut the fuses. We connected fuses through micromanipulators on a wafer probe-station. Low-inductance leads (less than 17" of twisted-pair wire) that connect the current sink to the micromanipulators are necessary to suppress ringing of the output voltage during switching transients. The fast diode reduces inductive voltage spikes at the collector after turn-off. A test-point connection,  $V_{test}$ , is available to monitor the applied current.

### 2.4.3 Fusible Support Designs

Practical fusible supports must be designed as a loop to avoid passing current through the microstructure. Layout of five different fusible supports are shown in Figure 2.13 to illustrate some design issues. The tee bridge (a) was the first design that we considered in our study (see Figure 2.10). Although the structure cuts cleanly, the released microstructure has a limited range of motion in the  $x$  direction. The long tee bridge (b) allows more lateral clearance for the cut microstructure than the initial tee bridge design. The tapered tee bridge (c) is a modified version of the long tee bridge. Its tapered width minimizes molten silicon wicking onto the released microstructure; instead, surface tension pulls most of the

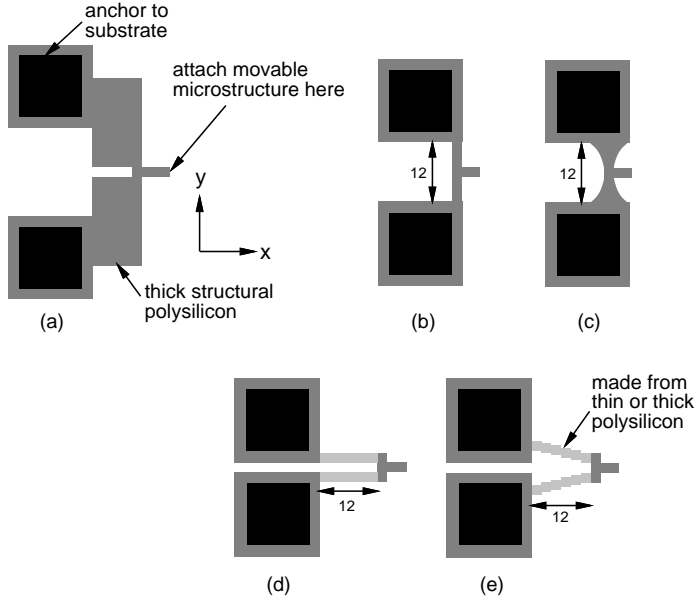


Figure 2.13: Layout of five fusible support designs. (a) tee bridge. (b) long tee bridge. (c) tapered tee bridge. (d) U-bridge. (e) V-bridge.

molten silicon onto the anchors. The U-bridge design (d) moves the microstructure further away from the support anchors, providing clearance in both  $x$  and  $y$  directions. This fuse design can be made from either the thin fuse polysilicon layer or the thick structural polysilicon layer. The close spacing between the legs of the fuse is a design flaw; the legs can melt together, short out the fuse, and cause catastrophic destruction of the surrounding area. The V-bridge design (e) has an increased distance between the leg attachment points to the anchors, eliminating the shorting problem. The attachment point to the microstructure is made as small as possible to reduce extraneous mass on the movable structure.

Figure 2.14 shows a  $2 \mu\text{m}$ -wide by  $12 \mu\text{m}$ -long by  $2 \mu\text{m}$ -thick polysilicon V-bridge fuse before and after resistive cutting. The fuse was cut in  $0.9 \mu\text{s}$  with  $260 \text{ mA}$  of current. Surface tension of the molten silicon pulls the mass to the two anchored ends. A substantial amount of the bridge's mass has been left attached to the movable structure after cutting. A thin V-bridge fuse,  $2 \mu\text{m}$ -wide,  $12 \mu\text{m}$ -long, and  $4000 \text{ \AA}$ -thick, is shown before and after resistive cutting in Figure 2.15. The molten silicon freezes into balls on both sides of the bridge. The fuse was cut in  $520 \text{ ns}$  with  $80 \text{ mA}$  of current, faster and with less current than the  $2 \mu\text{m}$ -thick fuse. No silicon residue is left on the substrate under the fuse.

The fuses shown in Figure 2.16 are used to support very compliant serpentine

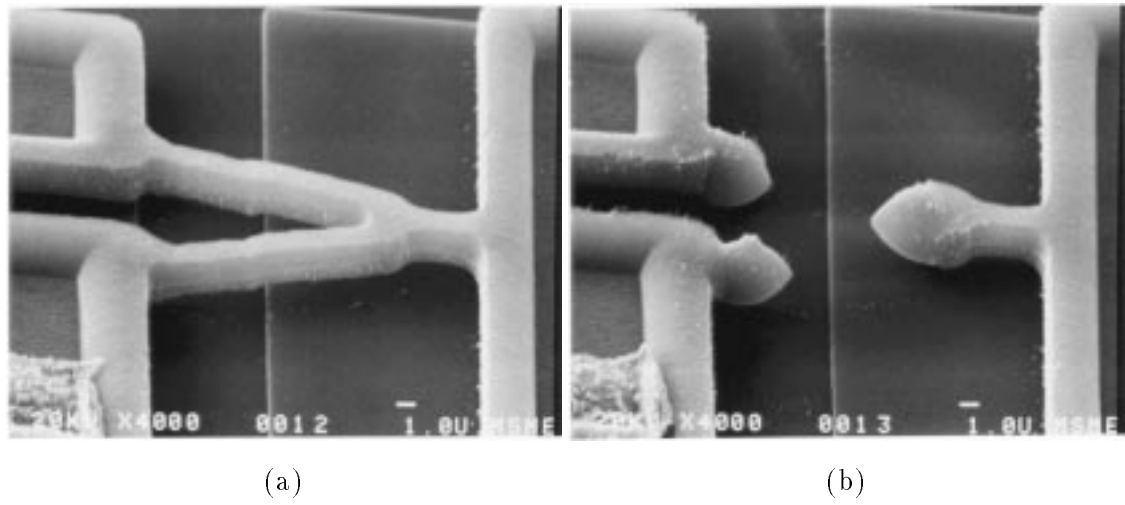


Figure 2.14: SEM of a  $2 \mu\text{m}$ -wide,  $12 \mu\text{m}$ -long,  $2 \mu\text{m}$ -thick polysilicon fuse. (a) Before cutting. (b) After cutting.

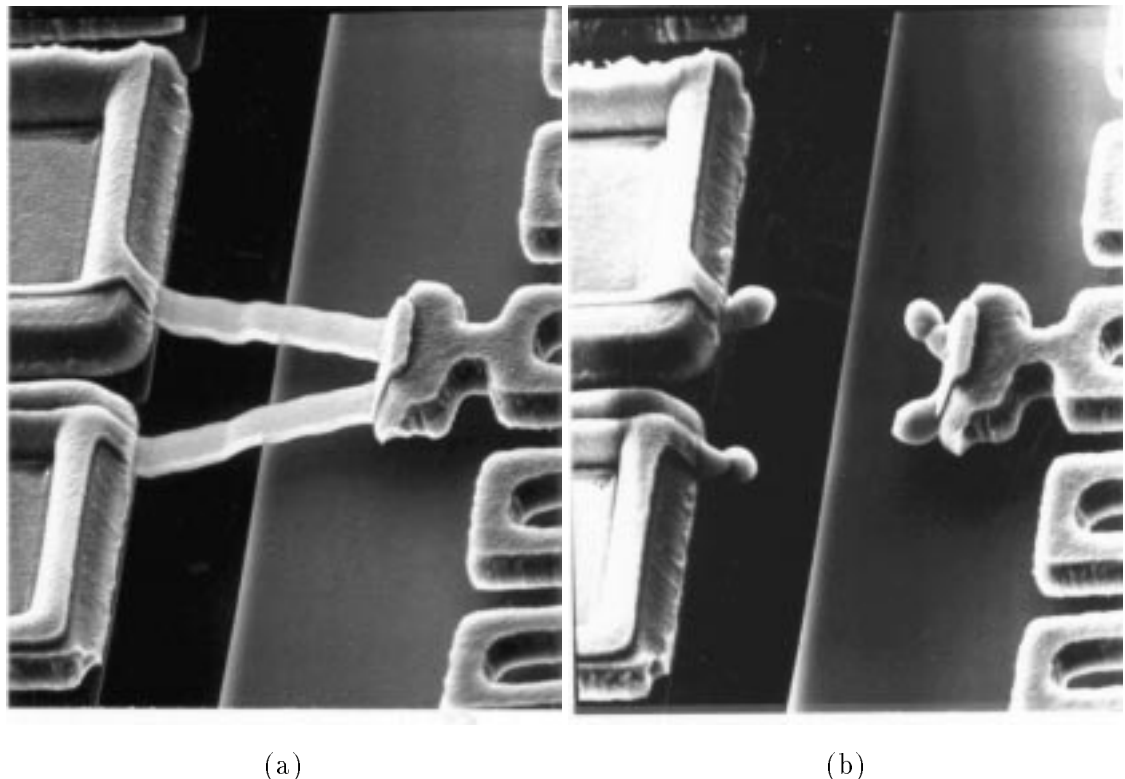


Figure 2.15: SEM of a  $2 \mu\text{m}$ -wide,  $12 \mu\text{m}$ -long,  $4000 \text{\AA}$ -thick polysilicon fuse. (a) Before cutting. (b) After cutting.

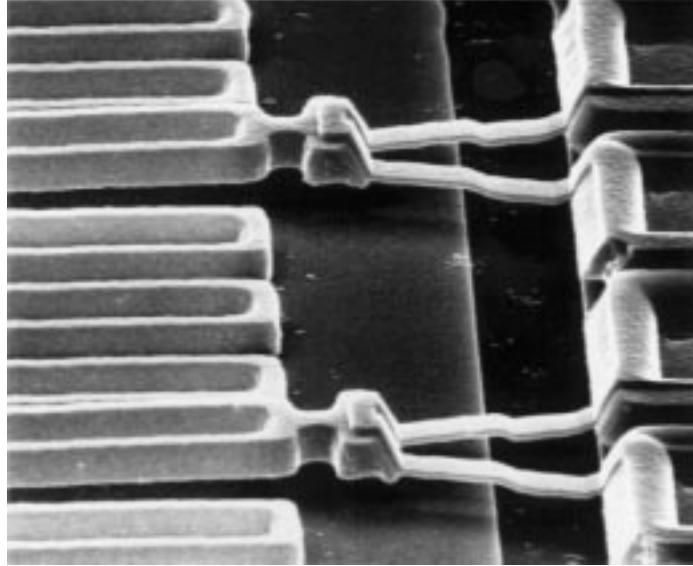


Figure 2.16: SEM showing a structure stuck to the substrate because of inadequate fuse spacing.

springs. The 4000 Å-thick fuses keep the structure from moving, and possibly breaking, during the sacrificial wet etch and rinse. The serpentine spring is stuck to the substrate because the unsupported beam length between fuses is very long (824 μm). Fuses should be placed every 300 μm along the beam length to support the structure during the heat-lamp drying step. If the fuses are too thin, they will be unable to balance the surface tension force during drying, as illustrated by the 2000 Å-thick fuses stuck down to the substrate in Figure 2.17.

Four 2000 Å-thick V-bridge fuses which support a serpentine spring are shown in Figure 2.18. A current pulse of 140 mA was used to cut each fuse. Polysilicon residue, left on the substrate after cutting, is a result of cylindrical instability of the molten filament during cutting [45]. If we assume the bridge forms a cylindrical molten filament, an aspect ratio,  $R$ , can be defined as the bridge length divided by the filament diameter.

$$R = \frac{l}{2} \sqrt{\frac{\pi}{tw}} \quad (2.18)$$

where  $l$ ,  $w$ , and  $t$  are the bridge length, width, and thickness, respectively. The molten-drop instability occurs somewhere between aspect ratios of 12 and 17, which are the values for the 4000 Å-thick fuse and 2000 Å-thick fuse, respectively. Bridges that are 2 μm wide, 2 μm thick and greater than 27 μm long leave residue on the substrate after cutting.

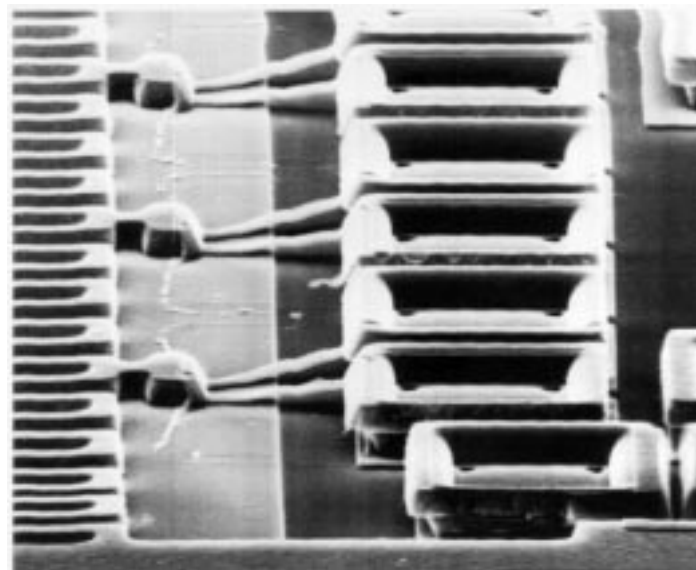


Figure 2.17: SEM showing a structure stuck to the substrate because of inadequate fuse thickness.

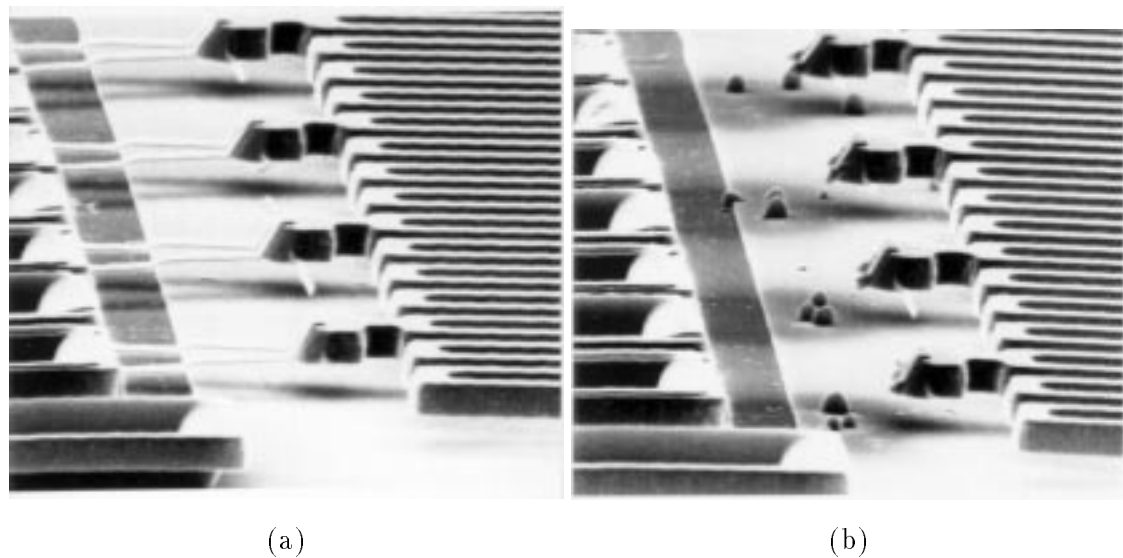


Figure 2.18: SEM of 2  $\mu\text{m}$ -wide, 12  $\mu\text{m}$ -long, 2000 Å-thick polysilicon fuses supporting a serpentine spring. (a) Before cutting. (b) After cutting.

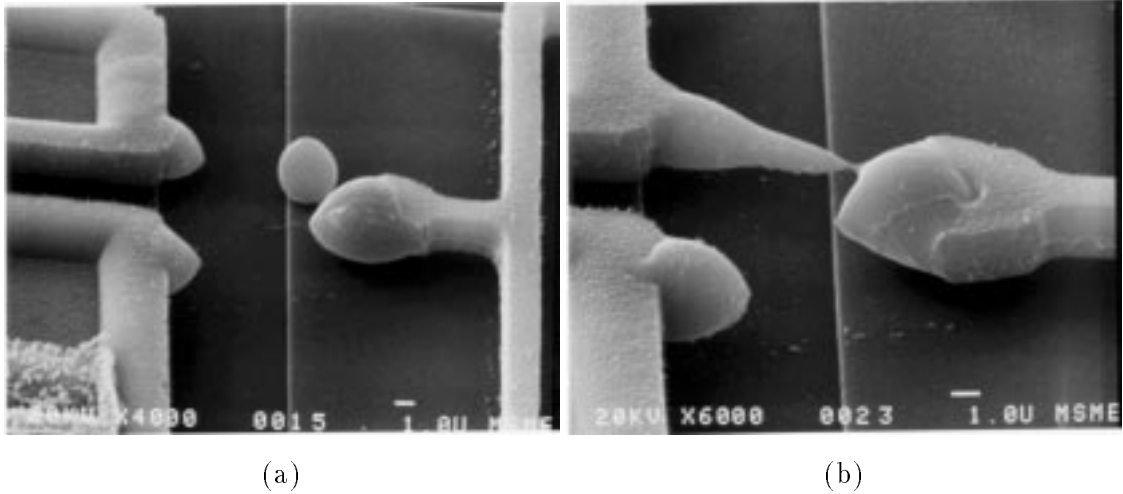


Figure 2.19: SEM of 2  $\mu\text{m}$ -wide, 12  $\mu\text{m}$ -long, 2  $\mu\text{m}$ -thick polysilicon fuses that are cut. (a) Too much current (260 mA). (b) Too little current (100 mA).

Residue from short fuses can be deposited on the substrate by cutting with too much current. Figure 2.19(a) shows the silicon residue a 2  $\mu\text{m}$ -thick fuse that was cut with a 260 mA current pulse. In this case, a 2  $\mu\text{m}$ -diameter molten silicon ball was ejected from the fuse. We have seen silicon balls similar in size jettisoned more than 10  $\mu\text{m}$  from the fuse. The fuse in Figure 2.19(a) was connected to a structural beam, which provided a moderate heat sink to the substrate. In contrast, the fuse previously shown in Figure 2.14(b) was directly connected to an anchor point. The same current level used to cut the beam-connected fuse (260 mA) cleanly cut the well-anchored fuse. Heat conduction out of the fuse connection affects the optimal cutting current value and must be accounted for in fuse design.

Using too little current can result in cutting only one leg of the fuse, as shown in Figure 2.19(b). The thermoelectric effect in polysilicon causes the fuse leg closest to the anode to be hotter than the other leg. At intermediate current levels, one leg is hot enough to cut before the other leg can cut. Once the circuit is opened, the leg near the cathode freezes and forms a conical filament. The filament in Figure 2.19(b) necks down to about 1000 Å in diameter.

#### 2.4.4 Fuse-Cutting Energy

Another way to cut a fuse is by discharging a capacitor through the fuse. We use the circuit shown in Figure 2.20 to measure the voltage across the fuse during the discharge

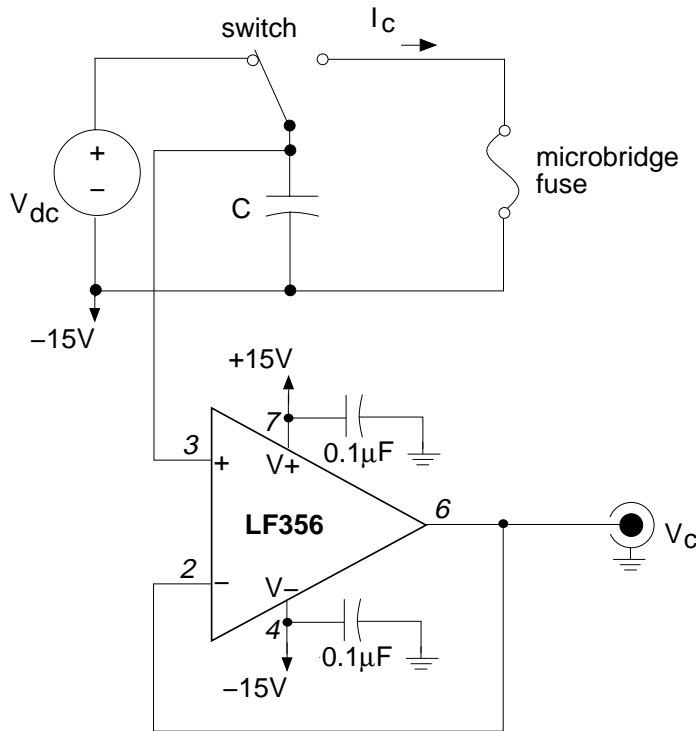


Figure 2.20: Circuit for capacitive cutting of fuses.

transient. The capacitor voltage is monitored with an op-amp buffer. The dc voltage source which charges the capacitor is referenced to the  $-15\text{ V}$  supply so the full range of the op-amp output is used. A mechanical switch provides a low-resistance connection to the fuse. Although the switch bounces, the fuses cut within several microseconds — well before the first bounce occurs.

The energy required to cut a fuse can be estimated by cutting different numbers of fuses in parallel. Some energy is dissipated in interconnect and the contact pads, but an incremental amount of energy is needed to cut an additional fuse in parallel. Layout of  $2\text{ }\mu\text{m}$ -wide,  $10\text{ }\mu\text{m}$ -long,  $2.1\text{ }\mu\text{m}$ -thick fuses for this experiment is shown in Figure 2.21. The measured value of polysilicon resistivity for the samples is  $6.3 \times 10^{-5}\Omega\cdot\text{m}$ . Four-point resistance values at room temperature were measured from pad to pad:  $248\text{ }\Omega$  for one fuse,  $133\text{ }\Omega$  for two fuses in parallel, and  $90\text{ }\Omega$  for three fuses in parallel. About  $80\text{ }\Omega$  of resistance in series with each fuse is attributed to the pads.

Figure 2.22 shows the capacitor voltage, capacitor current, and circuit resistance waveforms for  $2\text{ }\mu\text{m}$ -wide,  $10\text{ }\mu\text{m}$ -long,  $2.1\text{ }\mu\text{m}$ -thick fuses cut with a  $0.48\text{ }\mu\text{F}$  capacitor

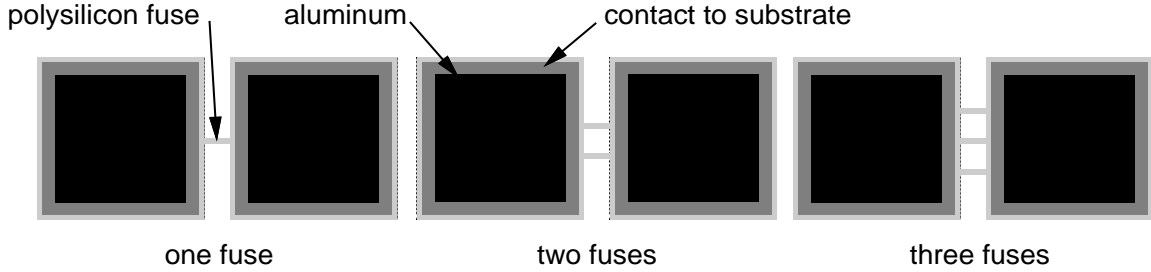


Figure 2.21: Layout of parallel fuses used in the measurement of cutting energy.

initially charged to 12 V. We measured capacitor voltage with a digitizing oscilloscope and reduced noise and ringing in the signal using a 600 ns-wide sinc<sup>3</sup> finite-impulse-response filter. The ringing is caused by impedance mismatch in the interconnect. Current is found from  $C dV/dt$ , where a quadratic approximation to the derivative is computed. The circuit resistance waveform is the instantaneous ratio of voltage to current.

After the capacitor is switched to the fuses, the circuit resistance drops from the room-temperature values to between 10 and 30  $\Omega$  within 200 ns. An expression for the thermal time constant,  $\tau$ , for polysilicon microbridges has been derived by Mastrangelo<sup>1</sup> [30]:

$$\tau = \frac{L^2}{\alpha_p \pi^2} \quad (2.19)$$

where  $\alpha_p$  is the thermal diffusivity of polysilicon, equal to  $1.85 \times 10^{-5}$  m<sup>2</sup>/s. For a 10  $\mu\text{m}$ -long bridge, the thermal time constant is 550 ns. Current levels during the capacitive discharge are much greater than the levels used in the I-V analysis. Therefore, if the polysilicon resistivity was constant, the steady-state temperature of the fuse would be much greater than the melting point of silicon. The change in temperature with time is the ratio of the target steady-state temperature over the thermal time constant — about 480 °C/ns. After the capacitor is connected across the fuse, the fuse temperature rises in about 3 ns to the point where the polysilicon resistivity begins to decrease. At the melting point, the polysilicon resistivity drops to nearly zero. Further reduction in fuse resistance occurs when the melt zone starts to grow in size. It takes about 200 ns for the 2  $\mu\text{m}$ -wide, 10  $\mu\text{m}$ -long fuses to melt completely, leaving only the pad resistance in the circuit. The pad is also at a high temperature and has lowered resistance. After a molten filament has formed, an

---

<sup>1</sup>We have neglected the effects of conduction through air, along with other heat-loss mechanisms on the thermal time constant. Also, resistivity variation with temperature is neglected.

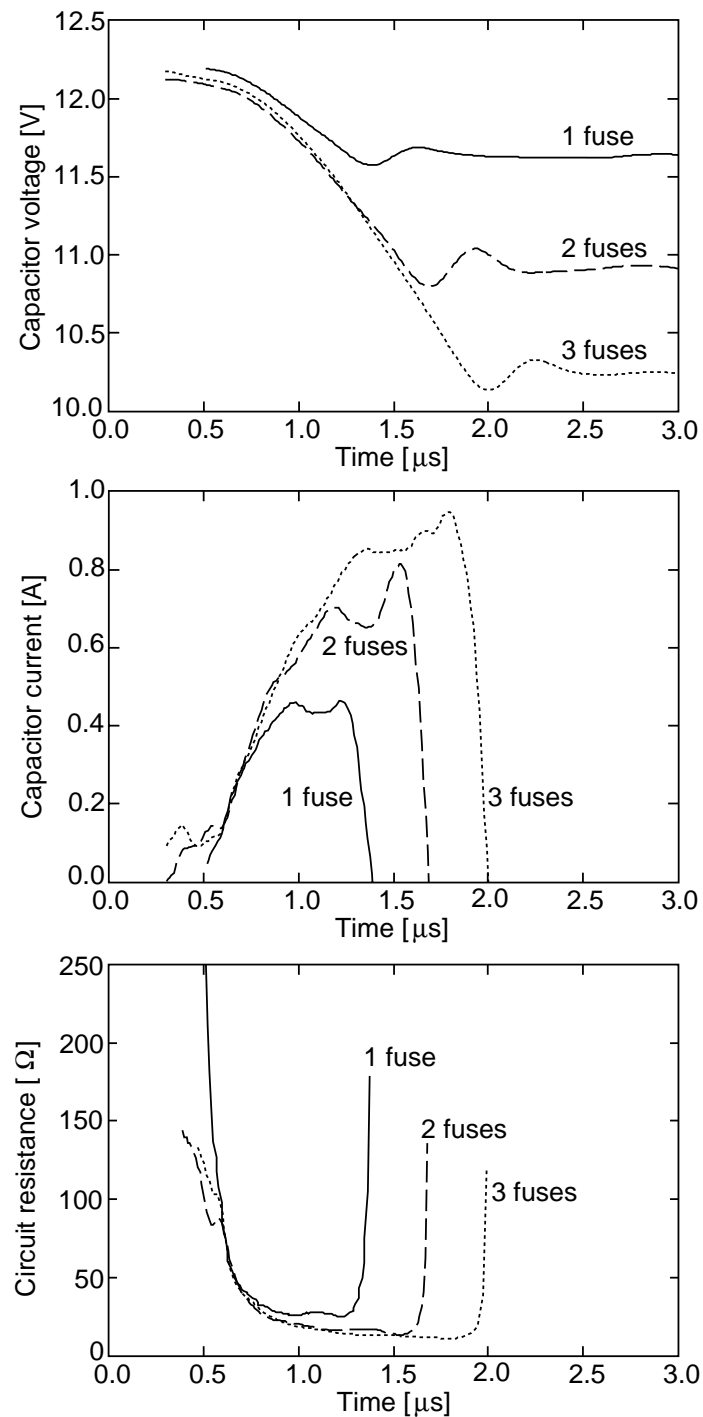


Figure 2.22: Capacitor voltage, capacitor current, and circuit resistance waveforms for one, two, and three fuses cut in parallel.

additional amount of time is needed for surface tension forces to pull the filament apart and create an open-circuit (about 500 ns for the 2  $\mu\text{m}$ -wide, 10  $\mu\text{m}$ -long fuses).

The energy to raise a mass,  $M$ , of polysilicon from room temperature to the melting point is

$$Q_m = M (c_p(1412^\circ\text{C} - 27^\circ\text{C}) + \Delta H_m) \quad (2.20)$$

where  $c_p$  is the specific heat and  $\Delta H_m$  is the heat of solid-to-liquid transition. We use values for single-crystal silicon [46]:  $c_p=0.72 \text{ J/g}/^\circ\text{K}$  and  $\Delta H_m=1655 \text{ J/g}$ . For a 2  $\mu\text{m}$ -wide, 10  $\mu\text{m}$ -long, 2.1  $\mu\text{m}$ -thick fuse, the mass is 0.097 ng and the energy,  $Q_m$ , is 256 nJ. Heat loss out the ends of the fuse, assuming the temperature at the ends is at the melting point, is about 0.18 W. If the fuse cuts in about 1  $\mu\text{s}$ , the total energy required is 436 nJ.

Experimentally, we determine the energy required to cut the fuse,  $Q_c$ , by measuring values of capacitor voltage before and after cutting, and then calculating the capacitor energy expended.

$$Q_c = \frac{1}{2}C (V_i^2 - V_f^2) \quad (2.21)$$

where  $V_i$  is the initial capacitor voltage and  $V_f$  is the final capacitor voltage. Energy values for the test structures in Figure 2.21 are: 3.07  $\mu\text{J}$  for one fuse, 6.62  $\mu\text{J}$  for two fuses in parallel, and 10.3  $\mu\text{J}$  for three fuses in parallel. The measured energy values are significantly larger than the theoretical values, because most of the energy is dissipated in the pad resistance.

#### 2.4.5 Fuse-Cutting Time

We have developed a simple model of fuse heating to predict the time required to cut fuses as a function of applied current. Interconnect and pad resistance do not affect heat generation in the fuse, since the current is held constant. Ohmic power generated in the fuse is given by

$$\dot{Q}_{\text{gen}} = I^2 R(\bar{u}) \quad (2.22)$$

where  $Q_{\text{gen}}$  is the energy generated and  $\bar{u}$  is the average temperature of the fuse. We have seen from the microbridge I-V analysis that the resistance is a complex function of temperature. For our analysis of cutting time, the resistance is approximated as constant for temperatures below the melting point and zero above the melting point.

$$R = \begin{cases} R_o & ; u < 1412^\circ\text{C} \\ 0 & ; u \geq 1412^\circ\text{C} \end{cases} \quad (2.23)$$

The average temperature of the fuse is assumed to rise with an effective time constant,  $\tau_c$ , whose value is determined empirically.

$$\bar{T} = T_{\text{sub}} + (T_{\infty} - T_{\text{sub}})(1 - e^{-t/\tau_c}) \quad (2.24)$$

where  $T_{\infty}$  is the target steady-state temperature at the fuse ends when the current is first applied. Reduction in the resistance and, hence, ohmic power when the temperature nears the melting point causes the effective time constant to be larger than the thermal time constant. Heat flow out the ends of the fuse,  $\dot{Q}_{\text{loss}}$ , is found by substituting Equation (2.24) into Equation (2.9).

$$\dot{Q}_{\text{loss}} = \alpha T_{\infty}(1 - e^{-t/\tau_c}) \quad (2.25)$$

where we can neglect the effect of the substrate temperature. Steady-state occurs when the heat generation equals the heat loss,  $\alpha T_{\infty} = I^2 R_o$ .

Subtracting Equation (2.25) from Equation (2.22), we find that the net heat flow into the fuse,  $\dot{Q}_{\text{net}}$ , decreases exponentially with time.

$$\dot{Q}_{\text{net}} = \dot{Q}_{\text{gen}} - \dot{Q}_{\text{loss}} = I^2 R_o e^{-t/\tau_c} \quad (2.26)$$

The energy required to melt the fuse,  $Q_c$ , is calculated from the integral of the net heat flow, and is assumed to be constant.

$$\int_0^{t_m} \dot{Q}_{\text{net}} dt = Q_c \quad (2.27)$$

Solving Equation (2.27) gives an expression for the time required to melt the entire fuse,  $t_m$ .

$$t_m = \tau_c \ln \left[ \frac{1}{1 - \left( \frac{I_c}{I} \right)^2} \right] \quad (2.28)$$

where  $I_c \triangleq \sqrt{Q_c/\tau_c/R_o}$  is the current required to melt the entire fuse. For  $I < I_c$ , the time to melt becomes infinite. When  $I \gg I_c$ , the conductive heat loss is negligible compared to the heat generation, and  $t_m \approx \tau_c (I_c/I)^2$ . In the preceding section, we theorized that extra time is required for surface tension forces to pull the fuse apart (about 500 ns for a 2  $\mu\text{m}$ -wide by 10  $\mu\text{m}$ -long fuse). Therefore, the time required to cut the fuse,  $t_c$ , is

$$t_c = t_w + \tau_c \ln \left[ \frac{1}{1 - \left( \frac{I_c}{I} \right)^2} \right] \quad (2.29)$$

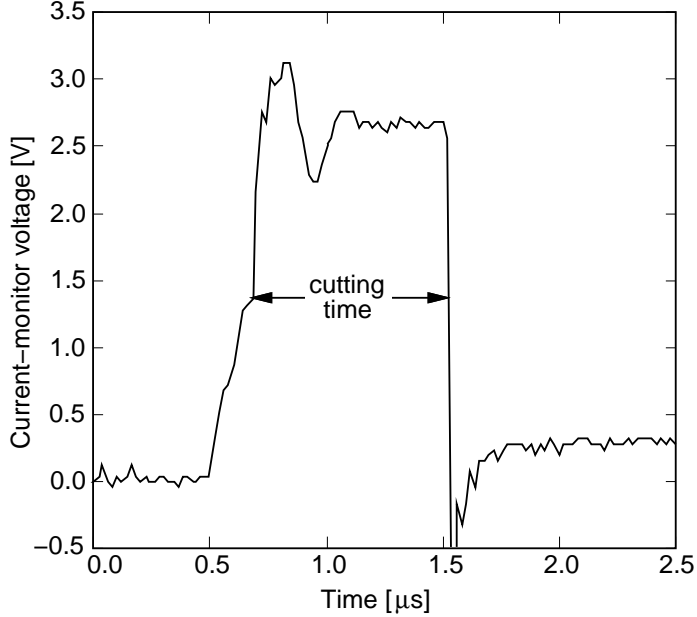


Figure 2.23: A current-monitor voltage waveform from cutting a  $2 \mu\text{m}$ -wide,  $10 \mu\text{m}$ -long,  $2 \mu\text{m}$ -thick polysilicon fuse.

where  $t_w$  is the extra time to wick the fuse mass to the anchors.

Time to cut a fuse is measured by connecting the current-monitor output of the current sink (see Figure 2.12) to a digitizing oscilloscope operating in single-shot mode. A typical waveform of the current-monitor voltage is shown in Figure 2.23. The monitor voltage to current scaling factor is  $0.1 \text{ S}$ . The current sink used in the measurements is limited in bandwidth to  $1 \text{ MHz}$ , so the current is not constant for values of cutting time less than several microseconds. Measurements at or below  $1 \mu\text{s}$  may be inaccurate because of the bandwidth limitation. Cutting time is measured at the  $50\%$  risetime and falltime points of the waveform. After the fuse is cut and until the input voltage is turned off, the op-amp in the current sink sources about  $30 \text{ mA}$  of current through the sense resistor.

A log-log plot of cutting time versus applied current for  $2 \mu\text{m}$ -wide,  $10 \mu\text{m}$ -long fuses is given in Figure 2.24. Equation (2.29) is fit to the measured data using  $I_c = 60 \text{ mA}$  and  $\tau_c = 17 \mu\text{s}$ . The slope of the plot is nearly  $-2$  for large values of current. Values of cutting time level out below  $1 \mu\text{s}$  because of the extra time required to wick the fuse to the anchors. For smaller currents above  $I_c$ , the heat loss becomes significant, and it takes longer to cut the fuse. At very low currents, the fuse does not melt and will not cut. A portion of the fuse melts at currents between  $20$  and  $60 \text{ mA}$ . At these low current levels,

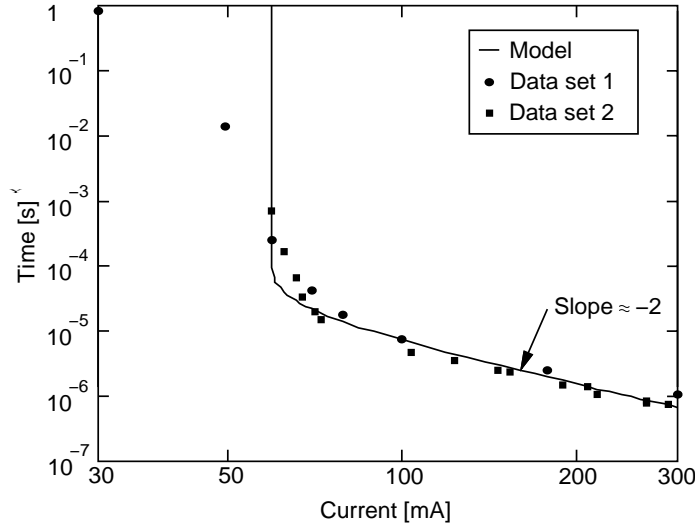


Figure 2.24: Time required to cut a  $2 \mu\text{m}$ -wide,  $10 \mu\text{m}$ -long,  $2 \mu\text{m}$ -thick polysilicon fuse as a function of applied current (log–log scale).

w × L change [μm]	mass scale factor	$t_c$ scale factor	$Q_{\text{gen}}$ scale factor
$2 \times 10 \rightarrow 2 \times 20$	2	0.56	1.1
$2 \times 10 \rightarrow 4 \times 10$	2	4.5	2.3
$4 \times 10 \rightarrow 4 \times 20$	2	0.77	1.5
$2 \times 20 \rightarrow 4 \times 20$	2	6.0	3.0

Table 2.2: Scaling factors of cutting time and energy with fuse width and length.

instability from surface tension, mass diffusion, and oxidation eventually forms a fissure, causing an open circuit. The cutting time is not well defined in this low-current regime.

Cutting time versus current is plotted for four different-size fuses in Figure 2.25. In all cases, the cutting time varies approximately as  $I^{-2}$ . Measured scale factors of cutting time and ohmic energy, estimated from the data in Figure 2.25, are given in Table 2.2. Scaling of cutting time is tabulated assuming a fixed cutting current. Notice that the ohmic energy does not scale linearly with the fuse mass, although the energy does increase with increasing fuse dimensions. Cutting time and energy are more sensitive to changes in width than length, because of the increase with width of heat flow out the fuse ends.

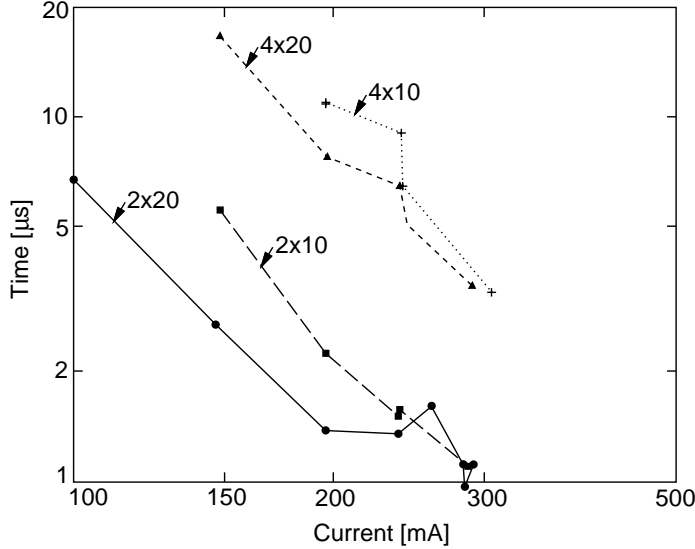


Figure 2.25: Time required to cut four different-size fuses: (a)  $2 \mu\text{m}$ -wide  $\times 10 \mu\text{m}$ -long, (b)  $2 \mu\text{m}$ -wide  $\times 20 \mu\text{m}$ -long, (c)  $4 \mu\text{m}$ -wide  $\times 10 \mu\text{m}$ -long, (d)  $4 \mu\text{m}$ -wide  $\times 20 \mu\text{m}$ -long. All of the fuses are  $2 \mu\text{m}$ -thick. (log-log scale).

#### 2.4.6 Parallel Fuse Cutting

In many applications, it is desirable to cut more than one fuse at a time. Cutting fuses individually is a laborious process; there may be hundreds of fuses attached to microstructures on a single die. Also, by synchronizing the fuse cutting, transient surface-tension forces generated by the cutting process and acting on the structures can be balanced.

We have investigated cutting fuses that are connected in parallel. Series-connected fuses can also be cut, but the method fails if one fuse cuts before the rest. If series-connected fuses are attached to a single microstructure, current will pass through the structure, possibly destroying it. A parallel arrangement of fuses solves both of these problems.

The main difficulty with parallel cutting is survival of the interconnect, which must carry large currents. An example of a parallel-fuse layout is shown in Figure 2.26. We use  $3000 \text{ \AA}$ -thick,  $14 \mu\text{m}$ -wide, polysilicon lines to carry current to the fuses. Most of the interconnect is in contact with the substrate, but  $2 \mu\text{m}$ -thick bridges are used for crossovers. Resistance of each interconnect loop is matched so equal current flows through each fuse. A dc current of  $300 \text{ mA}$  will melt the polysilicon interconnect — even the traces that make thermal contact with the substrate. The interconnect survives if the current flow lasts less than about  $8 \mu\text{s}$ . Since the fuses cut in about  $1 \mu\text{s}$ , the interconnect is left intact.

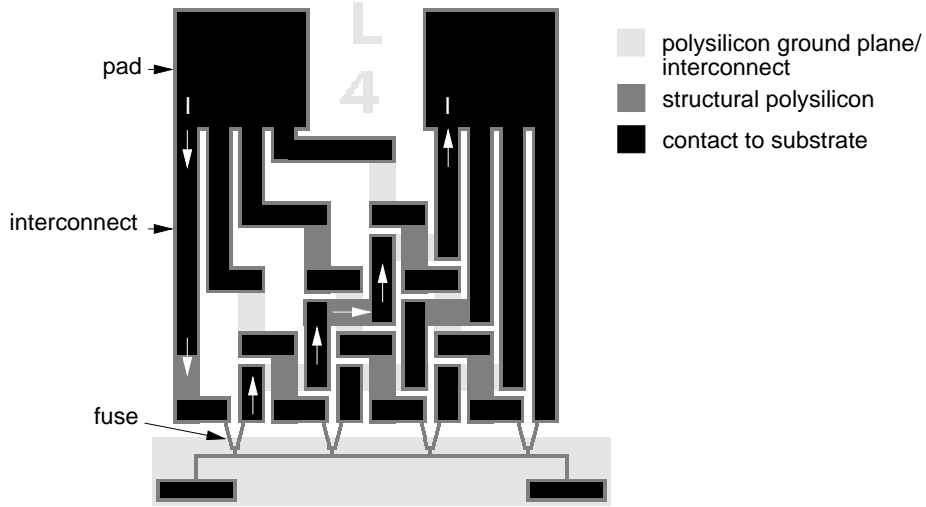


Figure 2.26: Layout of four parallel fuses supporting a beam. The direction of current,  $I$ , carried by one interconnect loop is indicated by the white arrows.

Interconnect resistance has limited successful cutting to four fuses in parallel. Two versions of parallel-fuse circuits were made to examine the effects of interconnect resistance: one version has polysilicon interconnect, the other version includes a layer of aluminum on top of the polysilicon. Aluminum can not be deposited on the traces below a crossover, so some polysilicon interconnect remains on the aluminum version. Four scanning electron micrographs of parallel-fuse structures with aluminum interconnect are shown in Figure 2.27: (a) four uncut fuses supporting a beam, (b) a partly-cut version of the same structure, (c) four cut fuses connected to separate structures, and (d) eight fuses that are unsuccessfully cut. Staging the cutting of multiple fuses is important when compliant structures are involved. We believe the top fuse in (b) did not cut cleanly because the beam pulled in while the fuses were cutting. Bending of the beam is evident in the photograph. The other fuse legs cut before the uncut leg could separate into two pieces. It is also possible that current in the top loop was lower than the other loops (due to a resistance mismatch), contributing to the failure. The partly-cut fuses in (d) experienced low current levels because the compliance limit of the current-sink circuit was reached. This current-drive limitation will now be discussed.

Room-temperature resistance of the parallel-fuse circuit in Figure 2.26 is  $246 \Omega$  for the polysilicon version and  $183 \Omega$  for the aluminum version. Each fuse has a room-temperature resistance of  $360 \Omega$ . Current-monitor waveforms for both versions while being

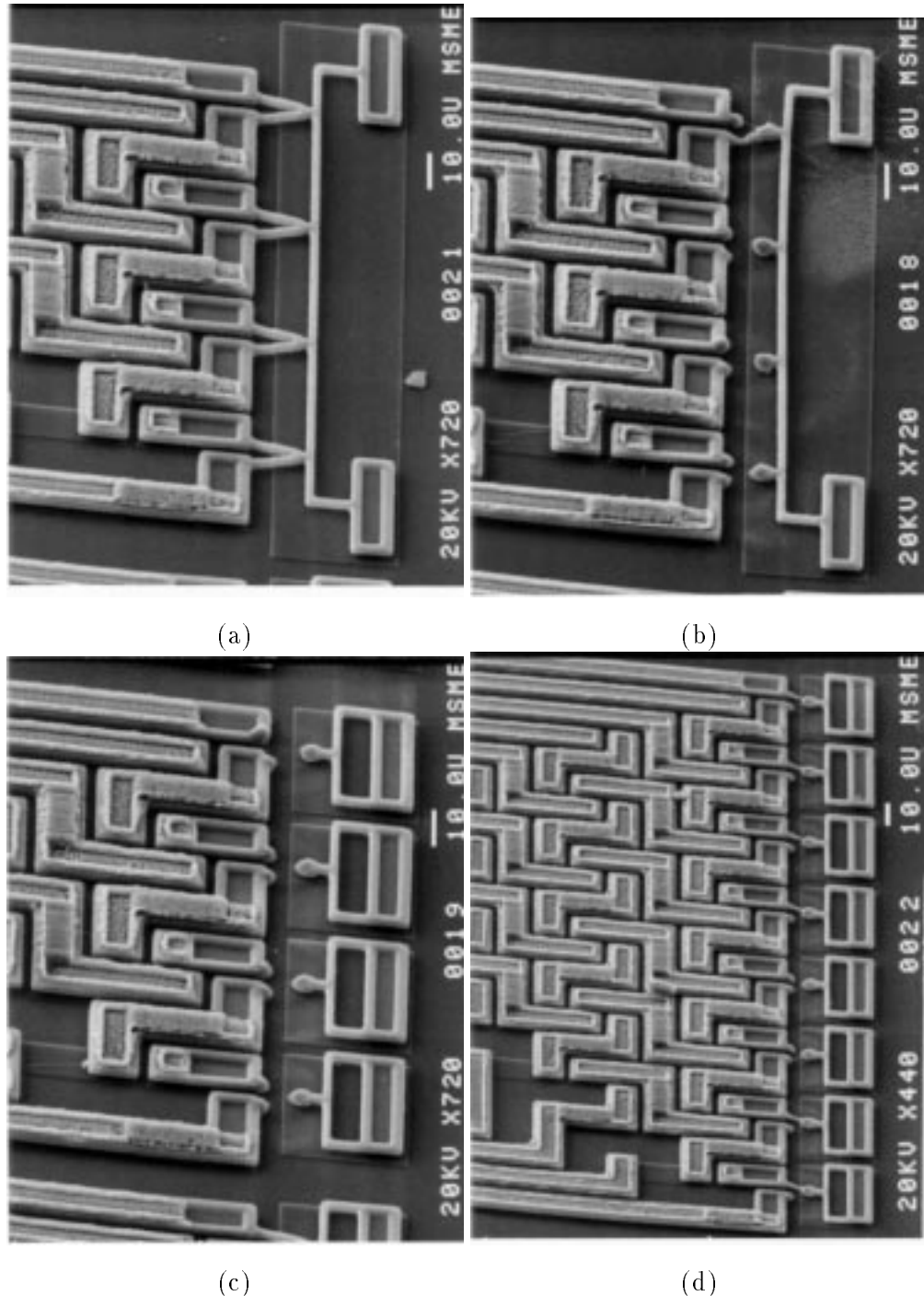


Figure 2.27: SEMs of parallel-fuse structures. (a) Four uncut fuses supporting a beam. (b) A partly-cut version of the same structure. (c) Four cut fuses connected to separate structures. (d) Eight fuses that are unsuccessfully cut.

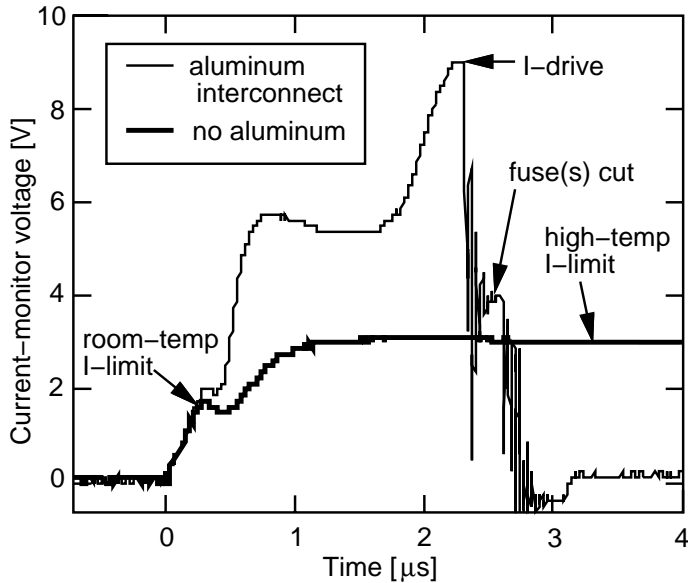


Figure 2.28: Current-monitor waveform of four fuses being cut in parallel. The thick line is the circuit with polysilicon interconnect, the thin line is the circuit with aluminum interconnect.

cut are shown in Figure 2.28. The current-sink was set with an 880 mA pulse drive and a 40 V compliance limit. (The maximum compliance limit of the current-sink is around 50 V, being set by the voltage breakdown of the power transistor in the circuit.) The fuses with the aluminum interconnect cut in about  $2.3 \mu\text{s}$ , while the fuses with the polysilicon interconnect did not cut. If the circuit resistance maintained its room-temperature value throughout the cutting transient, the current would be limited by the compliance to 156 mA and 207 mA for the polysilicon and aluminum versions, respectively. This current limit is seen as the first kink in the waveforms. When the fuses melt, their resistance is nearly zero and the circuit resistance reduces to the interconnect resistance: 156  $\Omega$  (polysilicon) and 93  $\Omega$  (aluminum). In the measured waveform, the current limit for the polysilicon version is around 300 mA, corresponding to a circuit resistance of 123  $\Omega$ . Although the fuses melt with just 75 mA/fuse, a clean cut is not obtained. The current limit for the aluminum version has an intermediate level at around 550 mA, then the current rises to the drive value of 880 mA. The drive-current level corresponds to a circuit resistance of 35  $\Omega$ ; the aluminum in the interconnect must have formed a low-resistance eutectic during cutting to produce such a low resistance value. Note the step down in current when the fuses start to

cut, because the fuses do not all cut at the same time. Once one fuse is cut, the compliance limit is again reached.

Problems with melting and resistance of interconnect need to be resolved before massive-parallel cutting of fuses is viable. The cutting current can be reduced by using thin fuses, at the cost of increased process complexity. Low-resistance metal interconnect that is embedded under oxide may survive the high current levels and reduce the voltage needed to cut many fuses.

## 2.5 Resistive Welding

Micromechanical resistive welding is the process of joining two conductive structures, passing current through the mechanical interface, generating heat through ohmic dissipation, and melting the interface to form a welded joint. In this section, we will discuss the design, modeling, and finite-element simulation of two kinds of welding: silicon–silicon welding, where two polysilicon structures are brought together and welded, and aluminum–silicon welding, where an aluminum microbridge is used as “solder” to weld together two polysilicon structures.

### 2.5.1 Silicon–Silicon Welding

Structures used for resistive welding must provide maximum temperature at the interface, otherwise the structure will be destroyed prior to creating a welded joint. In particular, designs should be avoided which pass welding current through mechanical flexures. A schematic of the silicon–silicon welding test structure is shown in Figure 2.29. The movable plate is to be welded to the rigid cantilevered supports by forcing the plate into contact with the supports and melting silicon at the interface. A fixed-fixed flexure is used to support the plate prior to welding. Welding current is supplied externally through micromanipulator probes to two anchored pads. The current path is symmetric, beginning at one anchored pad, through a cantilevered support which contacts the structural plate, and then back through a second contact to the other pad. A SEM of one of the welding test structures is shown in Figure 2.30. A plunger, shown on the right side of Figure 2.30, allows a micromanipulator probe tip to close the  $2 \mu\text{m}$  gap separating the contacts and to supply sufficient force for welding. The two cantilever supports are  $40 \mu\text{m}$ -wide by  $60 \mu\text{m}$ -long, with four pointed teeth at the end of the beams. Several other designs, with different

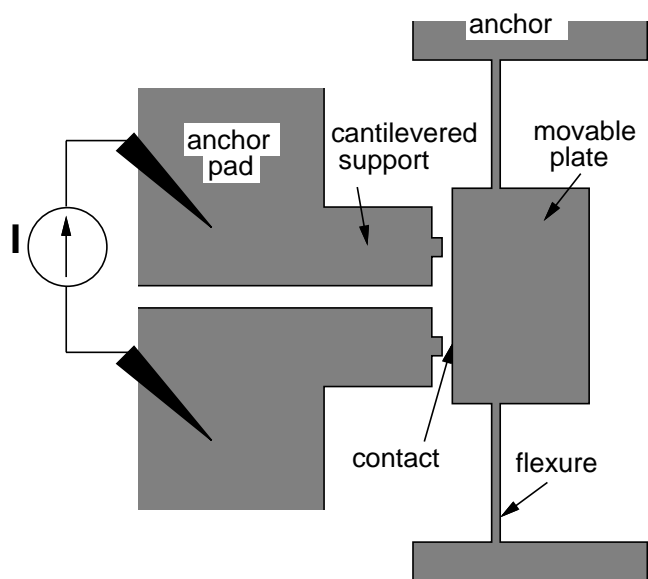


Figure 2.29: Schematic of the first-generation welding test structure.

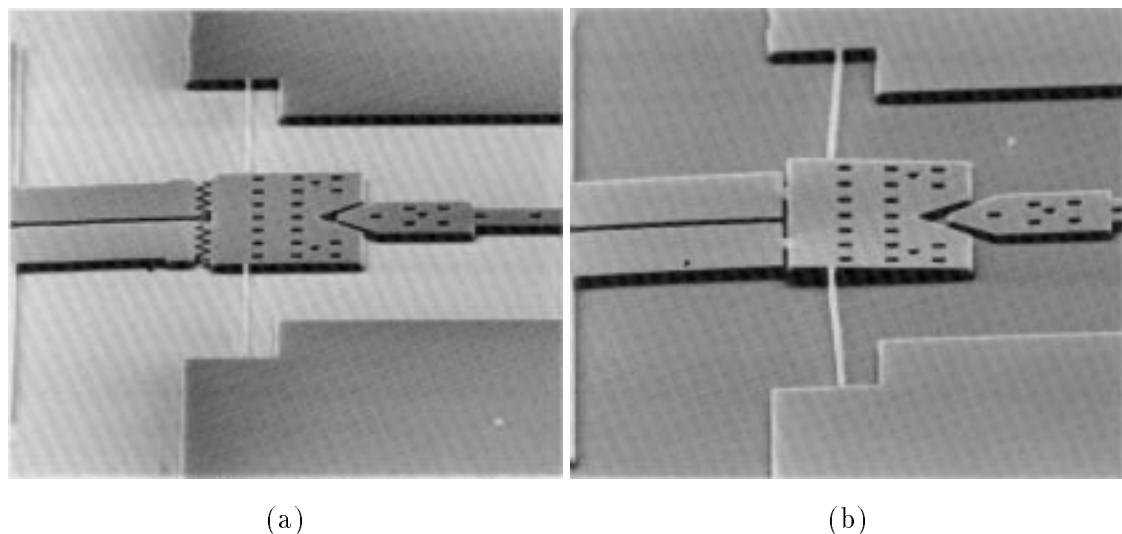


Figure 2.30: SEM of a first-generation welding test structure. (a) Before welding. (b) A similar structure, after welding. The structural plate in the center is welded to the 40  $\mu\text{m}$ -wide, 60  $\mu\text{m}$ -long cantilever supports, located on the left.

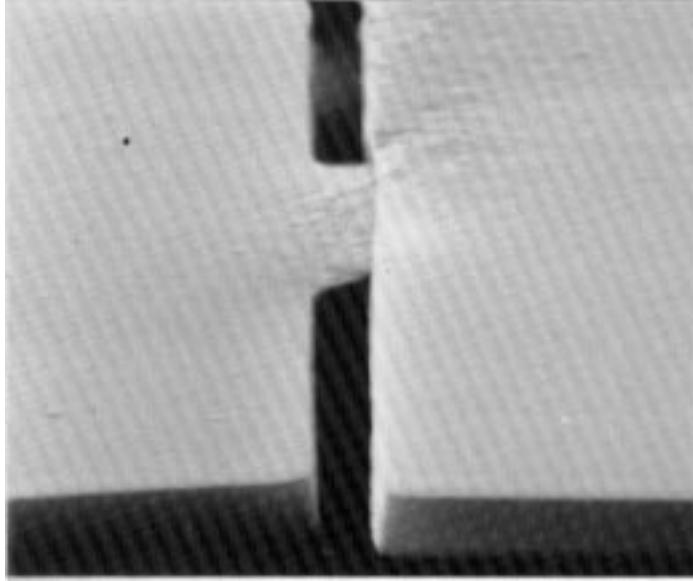


Figure 2.31: Close-up view of the lower joint, showing a clean weld and out-of-plane alignment.

cantilever support dimensions and number and type of teeth, were fabricated.

Delicate microstructures can be attached to the structural plate without being subjected to high temperatures. Unlike short microbridges, conduction through air under the plate is significant. Much of the plate experiences a low current density, allowing the outer regions of the plate to sink heat from hotter areas. The cantilever supports extend the contact away from the pad, which would otherwise act to reduce temperature at the contact. Contact width should be small relative to the support width, both to increase power generation near the contact and to avoid melting of the supports. Contact area should be maximized, to provide current flow across the junction with a minimal amount of applied force.

Figure 2.30(b) shows a completed welding structure after 30 mA of current was applied for several minutes in air. The resulting structure is bonded to the anchored supports. A close-up view of the lower joint (Figure 2.31) shows a clean weld, but out-of-plane alignment. A large force is required to create an electrical connection through the joint, making perfect alignment impossible. A thin layer of native oxide, covering the polysilicon contacts, acts as a barrier to conduction. Even with the highly anisotropic plasma etch, the polysilicon sidewalls have a slight slope, which reduces the contact area. We believe that

the large applied force is necessary to penetrate this oxide layer. Electrostatic forces produced by micromechanical actuators are not large enough to initiate the polysilicon welding process reliably.

Both flexures supporting the structural plate were broken by a probe tip without affecting the welded joints. A probe tip was then used to break the welded joints by pushing on the plate. The upper joint in Figure 2.30(b) did not fail. Instead, a large section of the structural plate was broken. The lower joint was marginal, since a break occurred near the weld. The applied current was raised slightly higher on other samples, resulting in uncontrollable deformation of the structure which lasted until the electrical connection was cut. The butted-end contact was the only design to provide a welded joint. In contrast with the large-tooth contact in Figure 2.30, the butted-end contact constricts the current path at the interface, which concentrates heat generation at the desired location.

The absence of oxygen may improve the weld quality, since no thermal oxidation of the polysilicon can take place. However, when operating in a vacuum, the entire structure becomes unacceptably hot, making welding impossible without first destroying the structure. Experiments have shown that the location of maximum temperature can be adjusted by changing pressure in the vacuum chamber. Nitrogen was used to raise the pressure. An inert gas, such as argon, may be better suited for such experiments, since a thin film of silicon nitride can form on polysilicon in a nitrogen ambient at elevated temperatures.

## 2.5.2 Aluminum–Silicon Welding

### 2.5.2.1 Description of Welding Structure

A schematic of an aluminum–silicon welding structure is shown in Figure 2.32. The current path is symmetric, beginning at one anchored pad, through a 8  $\mu\text{m}$ -wide by 12  $\mu\text{m}$ -long polysilicon filament, to another anchored pad. In contrast to the silicon–silicon welding structure, the aluminum–silicon welding structure does not require an external force to complete the electrical connection for welding. A tab on the movable microstructure is connected to the polysilicon filament by an aluminum microbridge. When sufficient current is applied, the heated filament melts the aluminum and a permanent weld joint is formed. Silicon and aluminum mix to form an eutectic with a minimum melting point of 577 °C. A 4  $\mu\text{m}$ -wide anchored beam, connected to the center of one side of the filament, acts as a heat sink to reduce the temperature of the filament area opposite the movable

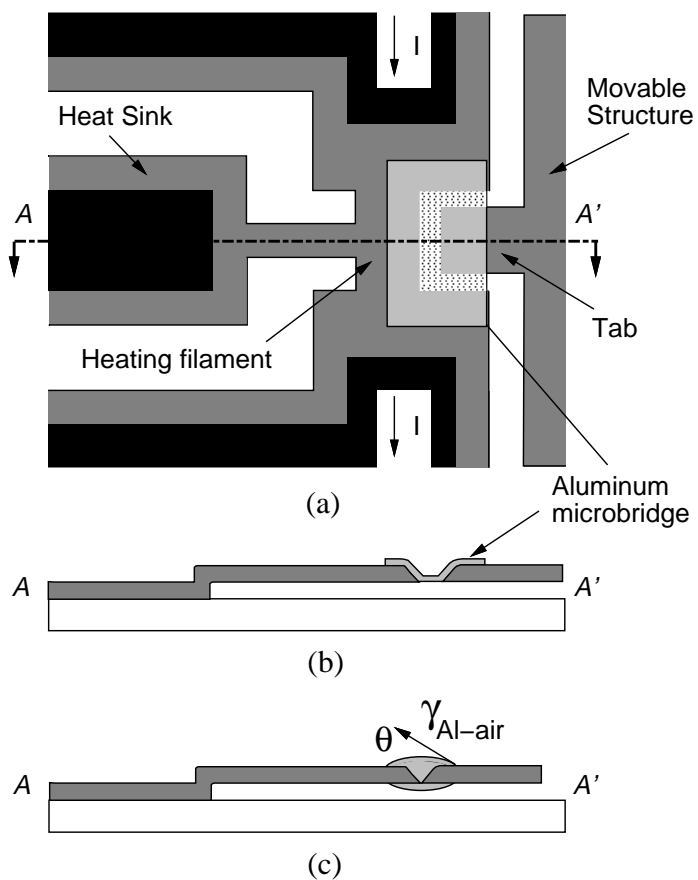


Figure 2.32: Schematic drawing of an aluminum–silicon welding structure. (a) Top view. (b) Side view before welding. (c) Side view before welding.

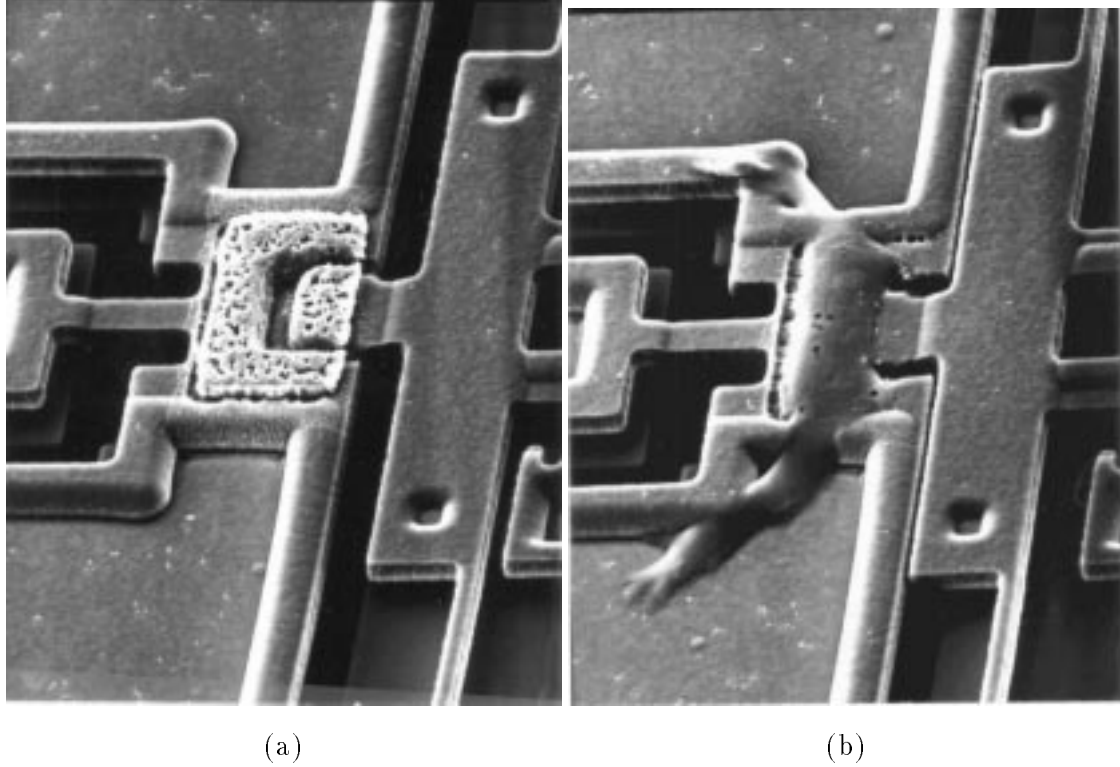


Figure 2.33: SEM of a weld joint. (a) Before welding. (b) After welding.

microstructure. Related work has involved formation of aluminum filaments in polysilicon bridges by diffusion of metal from contact pads [47].

Aluminum–silicon welding is more robust than silicon–silicon welding. The aluminum–silicon welding structure does not have the problems associated with making electrical contact between two silicon surfaces. Melting is localized to the aluminum area, because of the large difference in the melting point of silicon and the aluminum–silicon eutectic.

A weld joint, before and after application of current, is shown in Figure 2.33. The aluminum microbridge starts melting at an applied dc current of 100 mA. Welding with dc current produces uncontrolled melting and migration of the aluminum, resulting in poor quality welds or destroyed structures. Instead, a robust welding procedure, using pulsed current, is arrived at empirically. For the most common welding structure, sixty, 5  $\mu$ s-wide, 50 %-duty-cycle, 500 mA current pulses are used to produce the best quality weld joints. Different welding structure layouts require separate optimization of the current waveform. The largest deflection observed is 6  $\mu$ m.

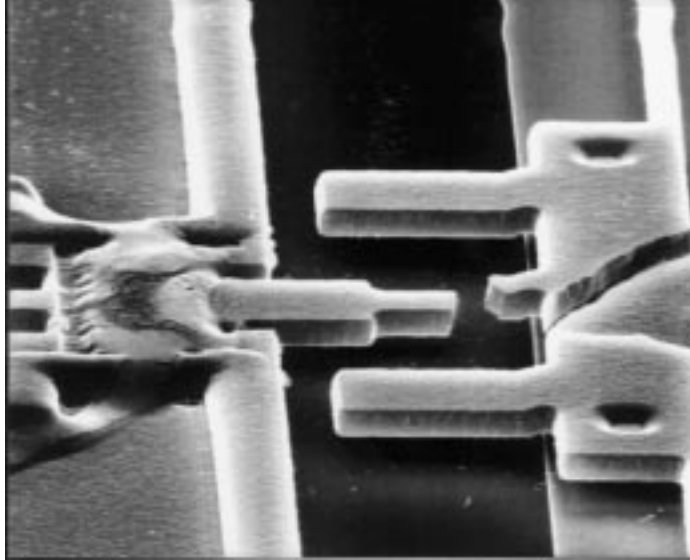


Figure 2.34: SEM of a structure used to measure weld strength, showing the fracture of a  $2 \mu\text{m} \times 2 \mu\text{m}$  beam and the intact weld joint.

Several structures, one of which is shown in Figure 2.34, have been fabricated to test weld joint strength. A micromanipulator probe tip provides the force to pull on the weld joint. The  $2 \mu\text{m} \times 2 \mu\text{m}$  beam fractured at an estimated axial force of 6 mN, based on 1 % fracture strain for polysilicon [48]. The large puller cracked in half on structures with  $2 \mu\text{m} \times 4 \mu\text{m}$  and  $2 \mu\text{m} \times 6 \mu\text{m}$  beams. Forces at least 1000 times greater than typical electrostatic forces are required to fracture the weld joint.

### 2.5.2.2 Analysis of Surface-Tension Force

Surface tension of the molten aluminum provides a lateral force which is strong enough to pull the movable microstructure into contact with the polysilicon filament. The lateral force has components due to surface tension,  $F_{st}$ , and Laplace pressure,  $F_p$  [45]. Assuming that the molten aluminum surrounds the movable tab, the lateral component of surface tension is integrated around the beam to obtain the first force component.

$$F_{st} = 2(w + z_o)\gamma_{\text{Al-air}} \cos(\theta) \quad (2.30)$$

where  $w$  and  $z_o$  are the width and thickness of the movable tab,  $\gamma_{\text{Al-air}}$  is the surface tension of aluminum in air, and  $\theta$  is the contact angle (see Figure 2.32(c)).

The Laplace pressure difference between the molten aluminum and air contributes

#	$k_x$ [N/m]	$\Delta x$ [ $\mu\text{m}$ ]	$F$ [ $\mu\text{N}$ ]	normalized $F$
1	$0.27 \pm 0.08$	$3.8 \pm 0.1$	$0.95 \pm 0.20$	$0.063 \pm 0.002$
2	$0.53 \pm 0.15$	$3.8 \pm 0.1$	$1.9 \pm 0.39$	$0.13 \pm 0.004$
3	$1.3 \pm 0.39$	$3.8 \pm 0.1$	$4.8 \pm 0.98$	$0.32 \pm 0.095$
4	$2.7 \pm 0.77$	$3.8 \pm 0.1$	$9.5 \pm 2.0$	$0.63 \pm 0.019$
5	$5.3 \pm 1.6$	$3.0 \pm 0.1$	$15 \pm 3.1$	1
6	$13 \pm 3.9$	$1.6 \pm 0.1$	$20 \pm 4.2$	$1.3 \pm 0.067$
7	$27 \pm 7.7$	$1.0 \pm 0.1$	$25 \pm 5.4$	$1.7 \pm 0.12$
8	$53 \pm 15$	$0.6 \pm 0.1$	$30 \pm 7.1$	$2.0 \pm 0.24$
9	$133 \pm 39$	$0.4 \pm 0.1$	$50 \pm 14$	$3.3 \pm 0.59$

Table 2.3: Measured deflection for lateral force test structures.

a second component of force. The pressure difference is found by equating the work done by expansion of the molten liquid to the increase in total surface energy.

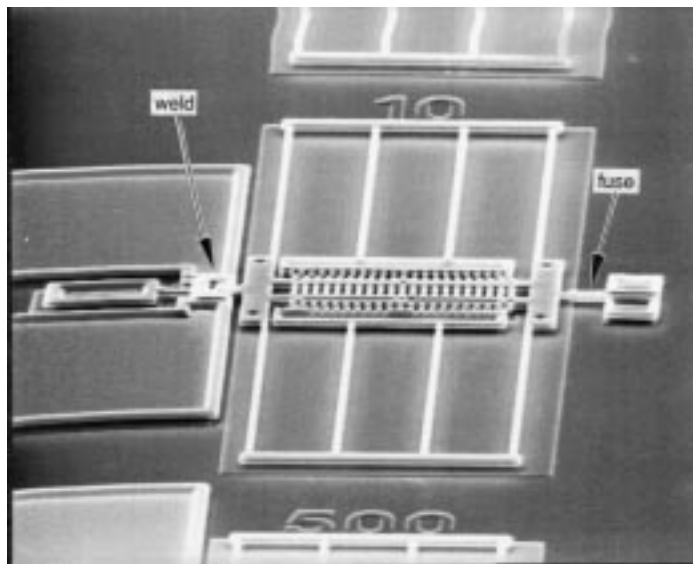
$$F_p = wz\sigma \frac{\gamma_{\text{Al}}}{R} \quad (2.31)$$

where  $\gamma_{\text{Al}}$  is the surface tension of aluminum in vacuum, and  $R$  is the radius of curvature of the molten aluminum.

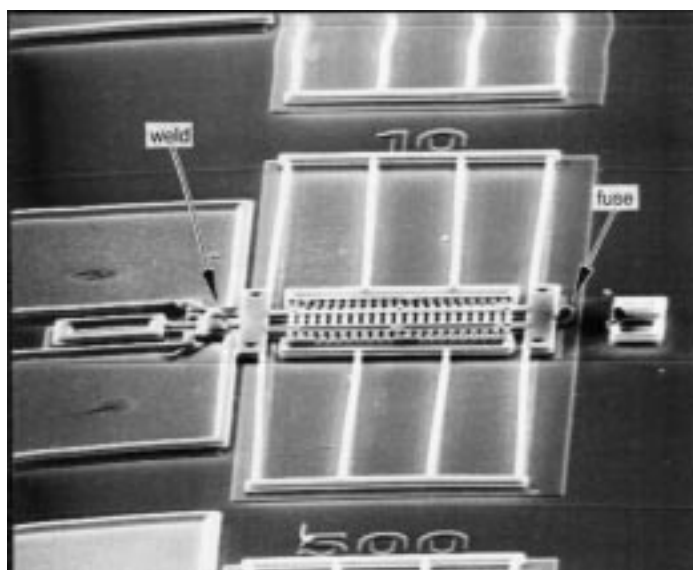
An experimental value for surface tension of aluminum in argon, and in vacuum, has been found to be 0.865 N/m [46]. This value is assumed to be valid in air. The measured contact angle of different welding structures varies between  $0^\circ$  to  $45^\circ$ . The movable tab connected to the aluminum is 8  $\mu\text{m}$ -wide and 2  $\mu\text{m}$ -thick. When the weld gap is zero, the measured radius of curvature is greater than 12  $\mu\text{m}$ . Adding Equations (2.30) and (2.31) gives a value between 11 and 17  $\mu\text{N}$  for lateral force. The Laplace pressure accounts for about 10% of the total calculated force. For comparison, a comb drive with twenty 2  $\mu\text{m}$ -thick fingers, a 2  $\mu\text{m}$  gap, and 20 V applied to the fingers generates 88 nN. The welding structure provides a force which is 100 times larger.

A series of nine test structures are used to measure the lateral force,  $F$ , of the molten aluminum weld joint. One of the welding test structures, before and after welding, is shown in Figure 2.35. Each structure is suspended by a folded flexure with a different spring constant,  $k_x$ . Measured lateral deflection,  $\Delta x$ , after each structure is welded into place, is given in Table 2.3.

For  $k_x < 5.3$  N/m, the movable structure hits a mechanical stop, which is designed to allow up to a 4  $\mu\text{m}$  deflection. Measurement errors of beam width and thickness account for the error bounds for the spring constant values. Deflection is measured with a 0.2  $\mu\text{m}$



(a)



(b)

Figure 2.35: SEM of welding structure used to measure lateral force. (a) Before welding.  
(b) After welding.

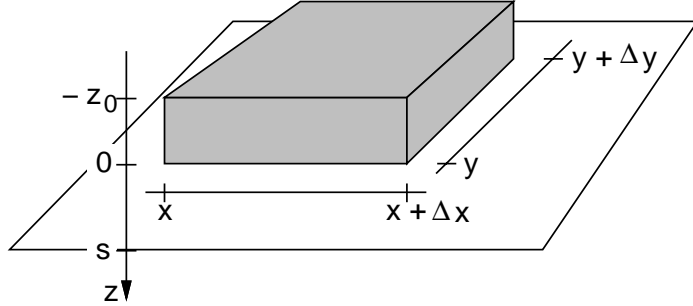


Figure 2.36: Differential volume of a polysilicon structure suspended over the substrate.

vernier, giving error bounds of  $\pm 0.1 \mu\text{m}$ . Values of normalized force have smaller error bounds, since the dimensional errors are not included.

Measured and calculated values of force agree for structure #5. The lateral force becomes larger for smaller deflections. As shown schematically in Figure 2.32(b), the aluminum microbridge starts out as a  $1.5 \mu\text{m}$  film. As the movable structure deflects, the gap between the movable structure and the polysilicon anchor decreases. When the gap is large, there is not enough aluminum to fill completely the gap region. A negative radius of curvature of the aluminum in the gap would lower the Laplace pressure and increase the lateral force.

### 2.5.2.3 Finite-Element Analysis of Welding Structures

In section 2.3.2, a one-dimensional finite-element model is used to explain thermal characteristics of polysilicon microbridges. This model is easily expanded to two dimensions. Convection and radiative terms are neglected; conduction is the dominant mode of heat transport. The temperature distribution of the welding structure is approximated as two-dimensional, with no variation in the vertical dimension.

A section of a polysilicon structure is shown, schematically, in Figure 2.36. The structure has thickness,  $z_0$ , and is raised above the substrate surface by a distance,  $s$ . The heat flow equation is derived by examining a differential element of volume  $z \Delta x \Delta y$ . Under steady-state conditions, ohmic power generated in the element is equal to heat conduction

out of the element.

$$\begin{aligned} \kappa z_o \left[ \Delta y \left( \frac{\partial u}{\partial x} \Big|_x - \frac{\partial u}{\partial x} \Big|_{x+\Delta x} \right) + \Delta x \left( \frac{\partial u}{\partial y} \Big|_y - \frac{\partial u}{\partial y} \Big|_{y+\Delta y} \right) \right] - \kappa_a \Delta x \Delta y \frac{\partial u}{\partial z} \Big|_{z=0} \\ = |\mathbf{J}|^2 \rho z_o \Delta x \Delta y \end{aligned} \quad (2.32)$$

where  $u(x, y)$  is the temperature of the bridge,  $\mathbf{J}$  is the current density,  $\rho$  is the electrical resistivity of the bridge,  $\kappa$  is the thermal conductivity of the microstructure, and  $\kappa_a$  is the thermal conductivity of air. Heat flow by conduction through the air is approximated by a linear gradient.

$$-\frac{\partial u}{\partial z} \Big|_{z=0} = \frac{u - T_{\text{sub}}}{s} \quad (2.33)$$

where  $T_{\text{sub}}$  is the substrate temperature. Combining Equations (2.32) and (2.33) and taking the limit as  $\Delta x \rightarrow 0$  and  $\Delta y \rightarrow 0$  produces the following second-order differential equation:

$$\nabla \cdot \kappa \nabla u - \frac{\kappa_a}{s z_o} (u - T_{\text{sub}}) = -|\mathbf{J}|^2 \rho \quad (2.34)$$

Since the anchor pads are not perfect conductors of heat, the temperature at the anchored ends of the bridge will not be constant. We model heat conducted out the ends of the bridge by Equation (2.9). Heat flow out the free sides and top of the plate is neglected.

We find the current density from charge continuity and the constitutive relationship,  $\mathbf{J} = \sigma \mathbf{E}$ .

$$\nabla \cdot \mathbf{J} = \nabla \cdot \sigma \mathbf{E} = -\nabla \cdot \sigma \nabla \Phi = 0 \quad (2.35)$$

$$\mathbf{J} = -\sigma \nabla \Phi \quad (2.36)$$

where  $\sigma = 1/\rho$  is the electrical conductivity,  $\mathbf{E} = -\nabla \Phi$  is the electric field and  $\Phi$  is the electrostatic potential.

Equations (2.34) and (2.35) are coupled through the temperature dependence of the resistivity. To simplify the present analysis of welding structures, a constant resistivity is assumed. Constant thermal conductivities of polysilicon and the ambient are also assumed.

We use the finite-element method to solve Equations (2.34) and (2.35), including general natural boundary conditions to model the thermal conductance of the anchor pad. The welding structure is divided into 146 quadratic triangular elements as shown in Figure 2.37(a). Only half of the structure is modeled, exploiting symmetry. Boundary conditions for the heat flux,  $\mathbf{Q}$ , and current density are identified at some edges of the structure in Figure 2.37(a). The edges with no boundary conditions labeled are set to  $\mathbf{Q}=0$  and  $\mathbf{J}=0$ .

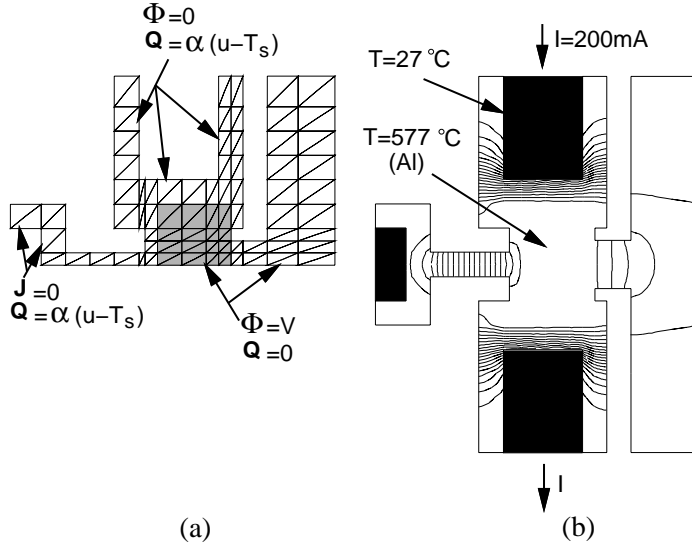


Figure 2.37: Two-dimensional finite-element analysis of the welding structure. (a) Discretization into 146 quadratic triangular elements. Shaded elements are aluminum, unshaded elements are polysilicon. (b) Temperature distribution. Isotherms are spaced  $27.4^{\circ}\text{C}$  apart.

A constant applied voltage,  $V$ , is specified between the edge of the pad and the axis of symmetry. The movable plate is placed in complete contact with the cantilever support. Two  $\times$  two point Gaussian integration is used to calculate element entries.

Calculation of the temperature distribution is a three-step process. First, the electrostatic potential is solved using Equation (2.35). Second, the current density is calculated directly from Equation (2.36). Third, Equation (2.34) is solved using the current density field, giving the temperature distribution in the structure. The total current applied is found by integrating the current density at the edge of the pad.

Values for the model parameters have been determined experimentally:

$$z_0=2 \text{ } \mu\text{m}$$

$s=2.5 \mu\text{m}$

$$\kappa(\text{polysilicon}) = 32 \text{ W/m/}^\circ\text{K} [29]$$

$$\kappa(\text{Al}) = 237 \text{ W/m}^{\circ}\text{K} [46]$$

$\kappa_a = 0.051 \text{ W/m}^\circ\text{K}$  at  $400^\circ\text{C}$  [46]

$$\rho = 3.7 \times 10^{-5} \text{ } \Omega\text{-m}$$

$$T_{\text{sub}} = 27^\circ\text{C}$$

Figure 2.37(b) shows the thermal distribution of the welding structure for an applied current of 200 mA. For this case, the temperature of the aluminum is 577 °C. The finite-element value of current is larger than the measured value (100 mA), probably because current spreading in the polysilicon underneath the aluminum is not modeled. Although a three-dimensional analysis would be more appropriate, the two-dimensional analysis does help in designing the welding structures.

#### 2.5.2.4 Weld Structure Fabrication Issues

Cross-sections of the original process and a revised process for aluminum–silicon weld structures are shown in Figure 2.38. For simplicity, the thin oxide and silicon nitride films that isolate the substrate are not shown. Wet etching of the contact cut for the aluminum microbridge is a critical step in the original process. The etch must be timed properly so a layer of PSG remains under the aluminum. The problem is exacerbated by the difficulty in wetting the photoresist openings with HF. We solved the wetting problem by adding a surfactant (Triton X-100) to the 5:1 BHF and by etching with ultrasonic agitation. However, agitation increases the etch rate, so the PSG etches down to the substrate in less than 2 minutes. Improper timing of this etch step led to the demise of many process runs. Aside from the initial welding-process run, we have not produced working weld structures with the original process. One of the inoperable aluminum microbridges is shown in Figure 2.39. The viewing angle is about 60° from vertical, looking from the movable structure toward the aluminum microbridge. Aluminum in the trench, which was to form a microbridge connecting the polysilicon structures, is separated from the polysilicon. Two process problems contributed to the failure. First, aluminum is sputtered in the trench too far below the structural polysilicon, due to overetching of the aluminum contact cut. Second, the trench sidewalls are vertical instead of sloping, due to photoresist erosion during the polysilicon etch step. The sputtered aluminum cannot coat the vertical sidewalls.

The revised process represents a better approach to making aluminum microbridges that avoids the timed contact etch. Both vertical-wall and sloped-wall polysilicon etches are performed with the same etch step. The resulting sloped-wall trenches are ready for aluminum deposition without a timed contact cut. It is necessary to use a very thick photoresist layer to define the polysilicon etch, since the resist must withstand several minutes of oxide and polysilicon plasma etching. Elimination of the timed BHF etch also eliminates

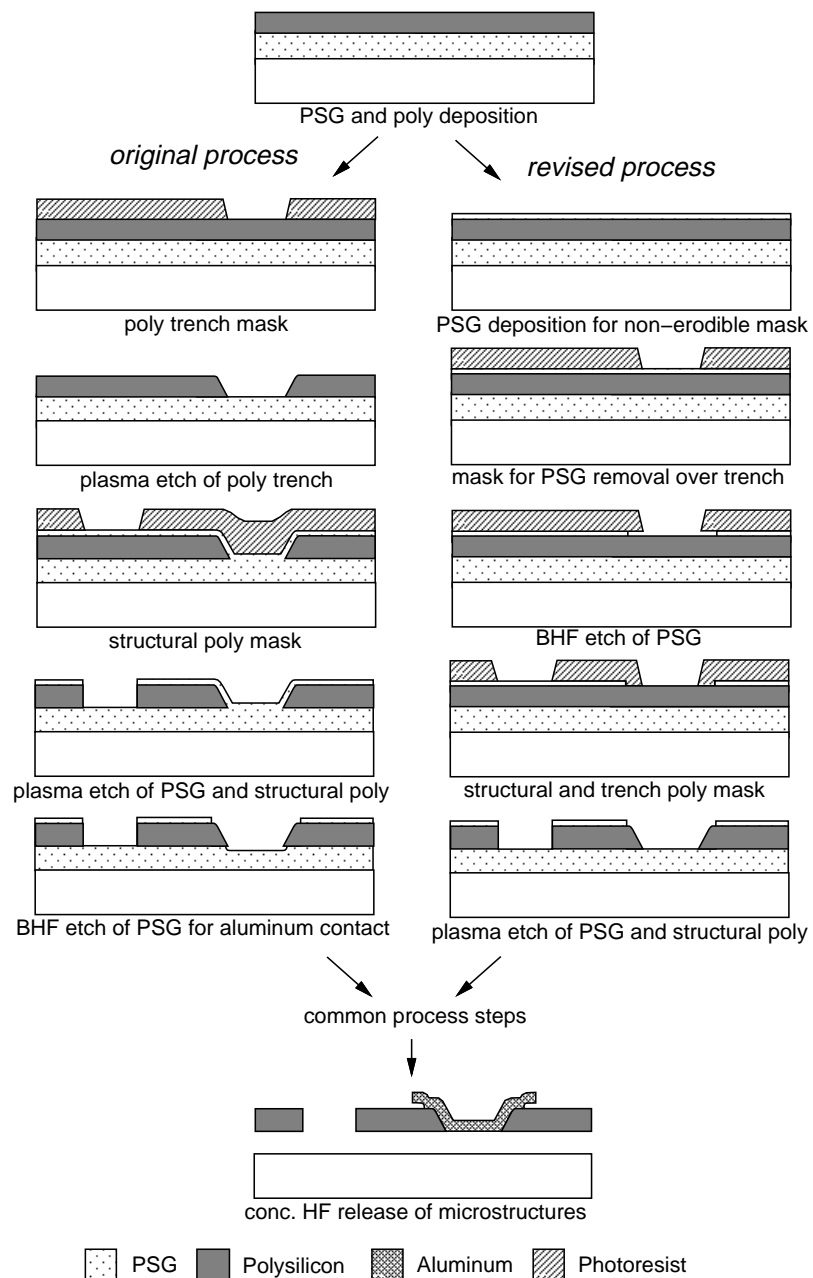


Figure 2.38: Cross-sections of the original and revised weld-structure process.

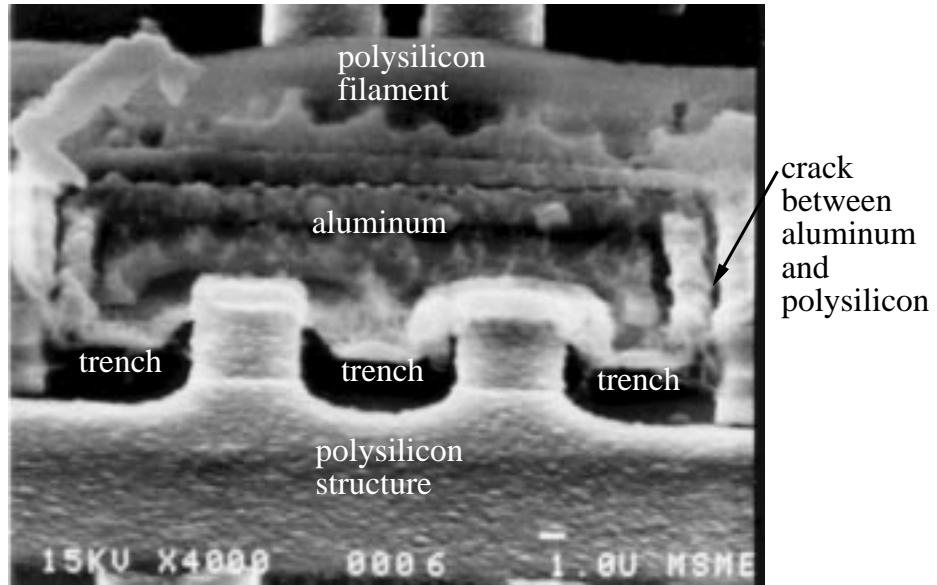


Figure 2.39: SEM of an inoperable aluminum microbridge which was to be used for welding. The viewing angle is about  $60^\circ$  from vertical.

the oxide on the structural sidewalls which acts as an etch stop during the aluminum plasma etch. Since we wet etch the aluminum sidewall stringers, an aluminum plasma overetch is unnecessary and should be avoided to prevent erosion of the structural polysilicon.

#### 2.5.2.5 Welding of Flipped Microstructures

The aluminum–silicon weld structures presented in the preceding sections are used to assemble lateral moving structures. Aluminum–silicon can also be used to assemble vertical stacks of structures. Figure 2.40 illustrates the vertical weld structure. A rigid plate is constrained on one side by a pair of hinges and is temporarily held in place on two other sides with fuses. Surface-micromachined hinges were first developed by Pister [49]. An upper polysilicon layer is used to form the top of the hinge, surrounding the axle. On the open side of the plate, a small tab with an aluminum pad extends out from the edge. After the fuses are cut, the plate is flipped over using a micromanipulator probe. The aluminum pad on the tab mates with a similar pad on a polysilicon filament. We then pass a current pulse through the filament, heat the aluminum pads, and weld the flipped structure to the anchored filament. These kind of weld joints can be used to construct surface-micromachined structures out of the plane of the substrate.

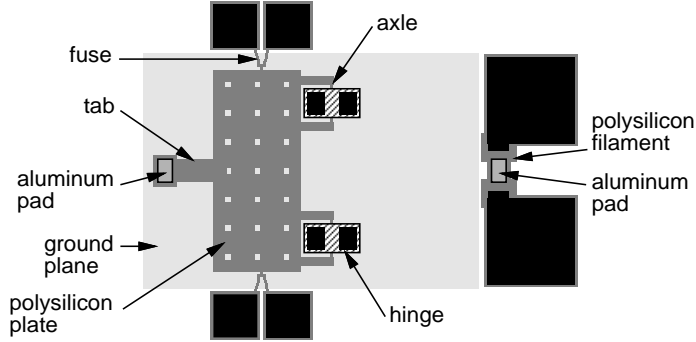


Figure 2.40: Schematic of the vertical weld structure.

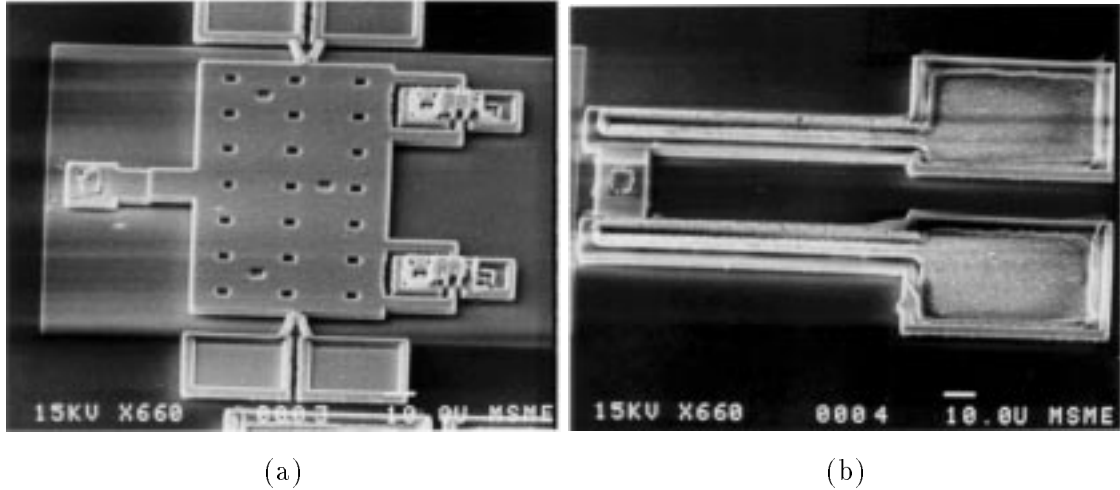


Figure 2.41: Vertical welding test structure. (a) Movable plate before welding. (b) Heating filament before welding.

An SEM of the test structure is shown in Figure 2.41, and the welded structure is shown in Figure 2.42. The weld joint is clean, with the melt zone sandwiched between the tab and the filament. The structure shifts slightly while the current is applied, aligning the tab's pad to the filament's pad. We use the structure's dimple etch to lower the height of the tab. When the structure is flipped over, the plate height from the substrate is reduced. Problems with polysilicon stringers cause the axles in the hinges to bind and break. Processing problems related to the stringers are discussed in section 4.4.1.

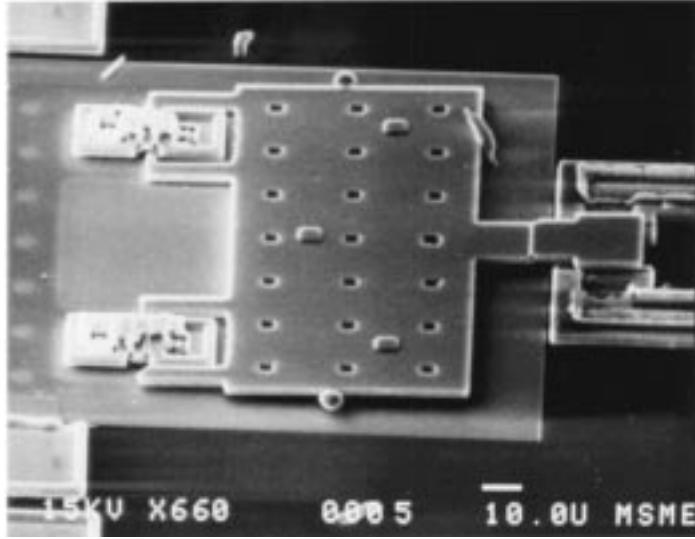


Figure 2.42: Vertical welding test structure after welding.

## 2.6 Narrow-Gap Comb-Drive Microactuator

Interdigitated comb drives are widely used in microresonator design, providing a lateral electrostatic force that is independent of lateral position. Comb drives are made from the same polysilicon layer as the resonator's shuttle mass, so no complexity is added to the processing. Usually, comb drives are made by defining the interdigitated fingers on the layout, as shown in Figure 2.43(a). The air gap between the fingers is limited in size by conventional photolithography and plasma etching to around  $2\text{ }\mu\text{m}$ . Narrow gaps (less than  $2\text{ }\mu\text{m}$ ) can be formed by defining unengaged comb fingers and assembling the fingers after release, as shown in Figure 2.43(b)–(c). We use aluminum–silicon welding to pull the comb fingers into place, and to provide strong, permanent connections. Comb fingers are fabricated unengaged, so the wide gaps can be easily etched. The finger width is defined such that a sub-micron gap forms when the fingers are engaged. This assembly method is similar to the oxidation machining process [50], however, we do not use oxidation to adjust the size of the comb finger gap.

We have fabricated several narrow-gap comb-finger microactuators; the designs have various comb-finger gaps and suspensions. A microactuator suspended by four very compliant serpentine springs is shown in Figure 2.44. Thin polysilicon fuses, which hold the springs in place during sacrificial etch, are cut to release the shuttle mass. Narrow-gap comb

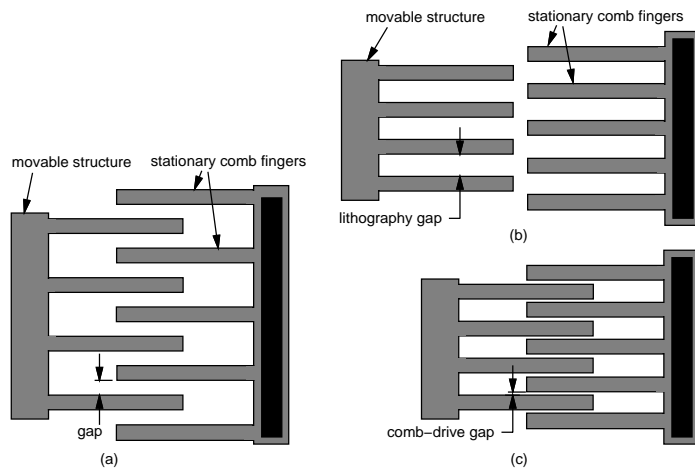


Figure 2.43: Schematic of the electrostatic comb drive. (a) Conventional design. (b) Narrow-gap design before assembly. (c) Narrow-gap design after assembly.

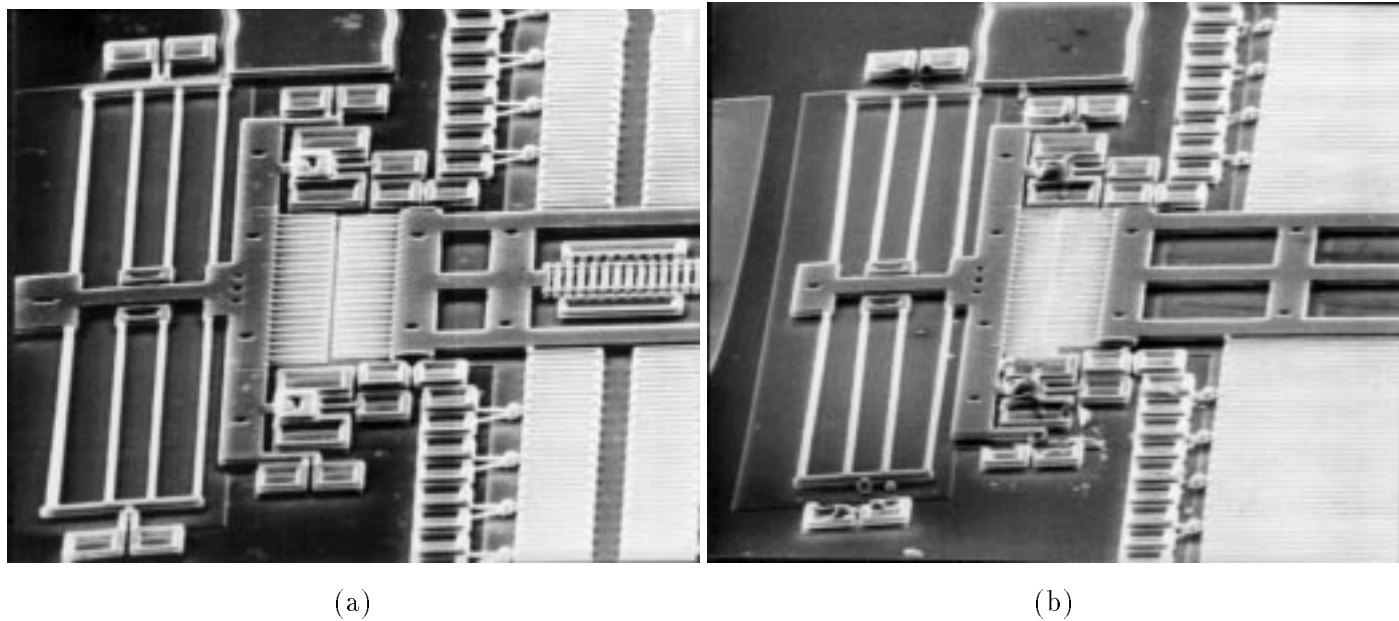


Figure 2.44: Partially assembled microactuator. (a) Before assembly. (b) After assembly.

drives are located on both sides of the shuttle mass. Two welding structures are attached to each stator comb drive. By moving the two sets of stator comb fingers, instead of moving the shuttle mass, a symmetric resonator drive is formed [51].

Thermal assembly of the microactuator consists of three steps: 1) cutting of fuses to release the folded flexure that holds up the stator, 2) welding of the stator to engage the narrow-gap comb fingers and permanently anchor the stator, and 3) cutting of fuses to release the serpentine springs. The assembled microactuator is shown in Figure 2.44(b). We have had limited success in engaging the stator comb drives, because most of the welding structures on this device had cracks between the aluminum microbridge and the polysilicon structure. Also, the mechanical coupling of the two welding structures may affect proper operation. When not mechanically coupled, welding structures of an identical design work reliably. A modified layout, using only one welding structure on the stator, should produce a working microactuator.

The comb drives in Figure 2.44 have 20 fingers and a  $1 \mu\text{m}$  gap. An electrostatic force of 44 nN, obtained from finite-element analysis [52], is calculated for 10 V applied between the fingers. The four serpentine springs each have a spring constant of 1 mN/m, obtained from finite-element analysis using simple beam theory [53]. These springs allow the shuttle to move  $11 \mu\text{m}$  with 10 V across the comb drive.

After the fuses were cut to release the springs, the shuttle mass moved laterally and the springs crashed into the fuse anchor pads. The voltage on the pads was over 30 V, large enough to electrostatically pull in the springs. To reduce the electrostatic force, a shield can be placed around the fusible support, as shown in Figure 2.45. Field lines from the charged fuse pads terminate on the shield. The ultra-compliant springs are atypical for resonators; stiffer springs do not require shielding around the fuses.

## 2.7 Trimmable Microresonators

Microresonator applications include oscillators, strain and force sensors, and signal filters. A large tolerance in the resonant frequency of polysilicon resonators exists because of variations in beam width, and film thickness and stress. In precision applications, a procedure is needed to trim the frequency after completion of the fabrication process. One implementation of frequency trimming uses fuses to change the spring constant of the resonator suspension. A second implementation uses weld structures to tension the suspension,

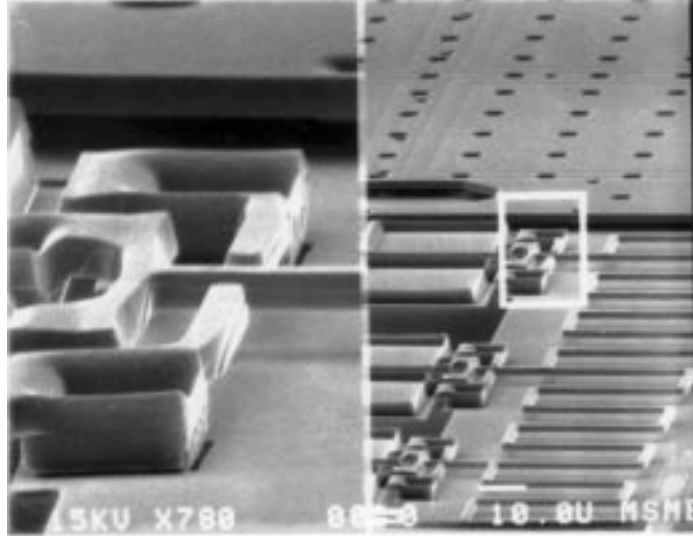


Figure 2.45: Fuse with a grounded shield to reduce electrostatic force.

thereby adjusting the spring constant.

### 2.7.1 Frequency Trimming With Fuses

A folded-flexure microresonator that incorporates fuses for trimming frequency is shown in Figure 2.46. Comb drives are located on both sides of the resonator. The folded flexures are anchored with V-bridge fuses at two points along each inner beam. A permanent anchor point is located at the end of each inner beam. Polysilicon interconnect is included to route current to each fuse. Unfortunately, the interconnect series resistance is large, requiring several hundred volts across the contact pads to cut a fuse. Instead, current is directed to a fuse through micromanipulator probes placed on the fuse's 15  $\mu\text{m}$ -square anchor pads. A magnified view of the anchor points on the inner beams is shown in Figure 2.47. Any of the three anchor points on each beam can be selected by cutting the appropriate fuse or fuses, providing nine combinations of beam lengths per side. Assuming the suspension is kept symmetrical about the vibrational axis, the spring constant can be set to nine values. Placement of the anchor points is designed to provide nine, approximately equal, frequency changes. Resonant frequency of the folded-flexure resonator is calculated using the formula derived by Tang [54].

$$f_r = \sqrt{\frac{k}{M_s + M_t/4 + (12/35)M_b}} \quad (2.37)$$

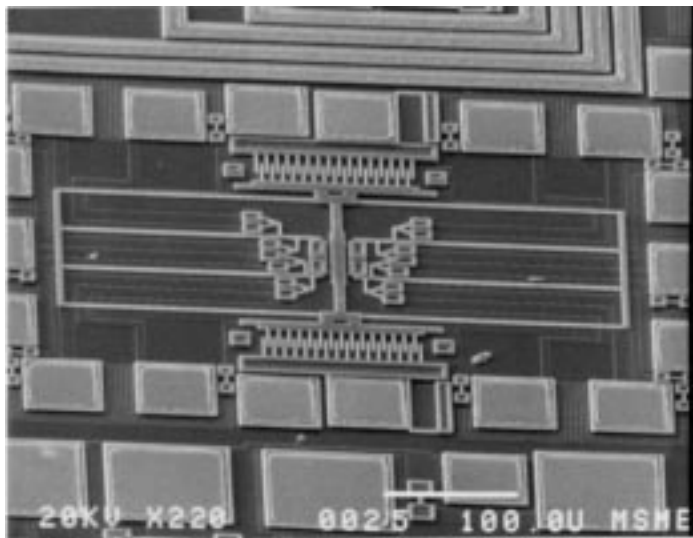


Figure 2.46: Folded-flexure trimmable resonator. Fuses are used to adjust the folded-flexure's beam length.

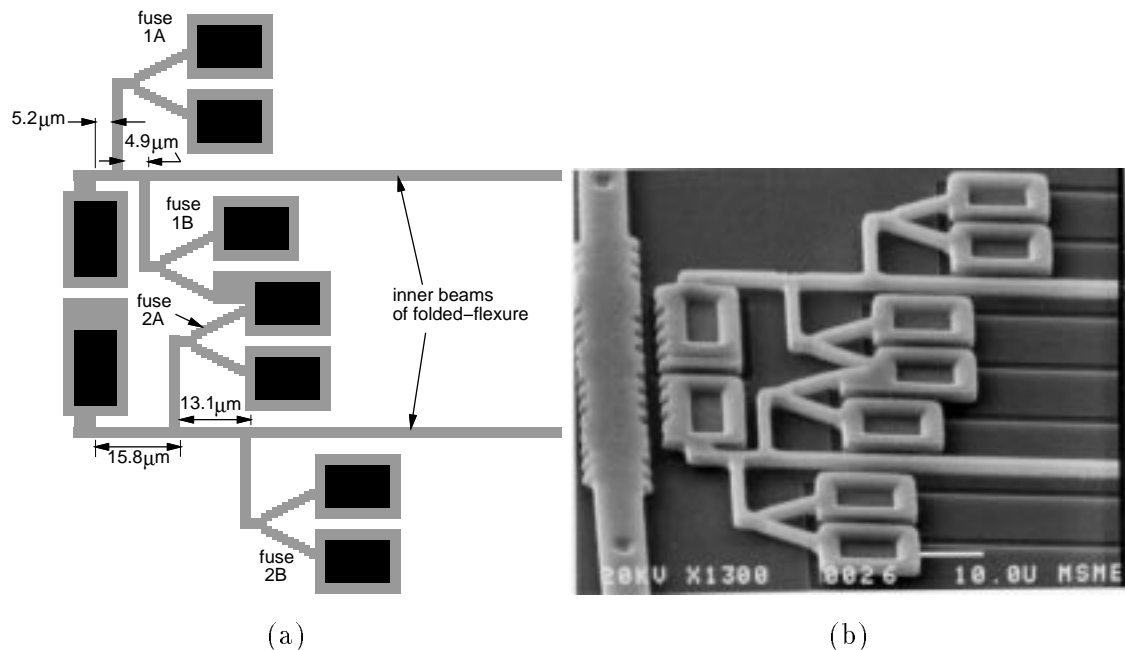


Figure 2.47: Magnified view of the fuse array for adjusting beam length. (a) Schematic of the fuse array, giving dimensions. (b) SEM of the fuse array. A displacement vernier can be seen at the far left.

#	fuse cut? [Y/N]				$k$ [N/m]	$f_r$ [Hz]	$\Delta f/f_5$ [%]
	1B	1A	2B	2A			
1	N	N	N	N	0.766	23358	+3.7
2	Y	N	N	N	0.756	23192	+2.9
3	Y	Y	N	N	0.746	23025	+2.2
4	N	N	Y	N	0.727	22720	+0.9
5	Y	N	Y	N	0.715	22527	0.0
6	Y	Y	Y	N	0.703	22333	-0.9
7	N	N	Y	Y	0.687	22057	-2.1
8	Y	N	Y	Y	0.673	21833	-3.1
9	Y	Y	Y	Y	0.660	21606	-4.1

Table 2.4: Values of spring constant and resonant frequency for the fuse-trimmable resonator

where  $k$  is the spring constant,  $M_s$  is the shuttle mass,  $M_t$  is the truss mass, and  $M_b$  is the mass of the beams. We derive the equation for the folded-flexure spring constant in section 3.4.4.5. Values for the resonator mass are:  $M_s=29$  ng,  $M_t=6.8$  ng, and  $M_b\approx 1.8$  ng. Table 2.4 gives detailed trim values for the resonator design in Figure 2.46. Only two measurements were taken of the resonator frequency, because probing of the fuse pads was difficult. The measured resonant frequency was 21625 Hz with no fuses cut (case #1), and 21375 Hz with fuse 2B cut (case #4). The measured frequency shift of 250 Hz represents a 1.2 % decrease, smaller than the theoretical decrease of 2.7 %. The fuse connection is not an infinitely stiff anchor point; the connecting beam from the fuse to the folded flexure is 15  $\mu$ m long. Our theoretical values assume rigid anchor points, partly explaining the smaller measured frequency shift.

Another trimmable resonator design, dubbed the “centipede” because of its many inner-beam “legs”, is shown in Figure 2.48. Each cut fuse makes the flexure more compliant. However, several factors make this resonator unattractive. The frequency shift is not linear with the number of cut fuses; the more fuses that are cut, the greater the effect on the spring constant. When few fuses are cut, the inner beams form a stiff structure. The resonator then behaves like a fixed-fixed structure, with a highly nonlinear spring constant. Finally, when fuses are cut, the inner beam is left free to vibrate, creating higher resonant modes.

An anchor arrangement similar to the one shown in Figure 2.47 can be used for laser trimming. The key concept is the same whether the trim method is fuse cutting or laser cutting: modification of the suspension’s anchor points to adjust the spring con-

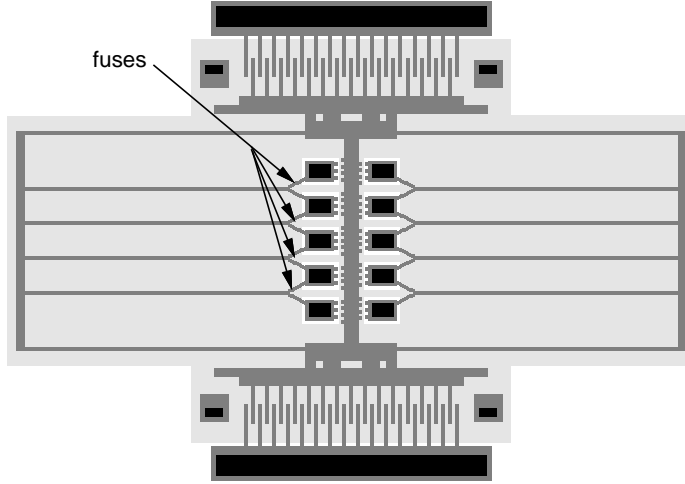


Figure 2.48: “Centipede” trimmable resonator.

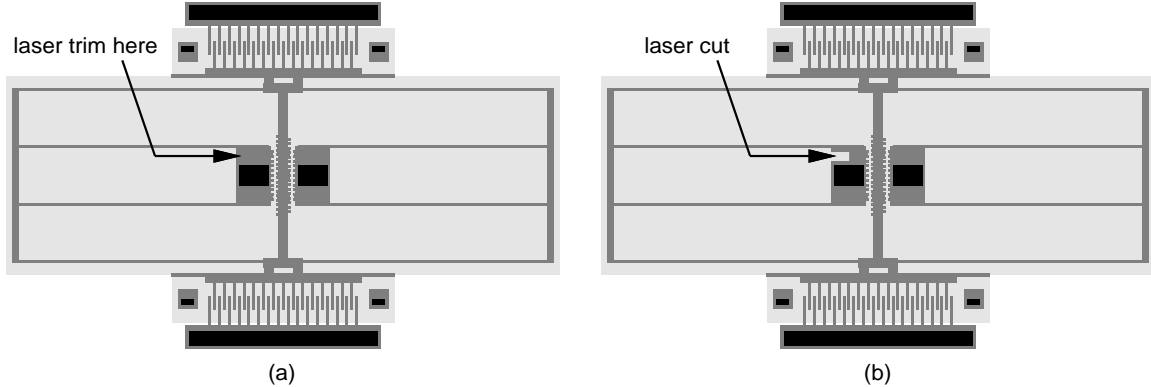


Figure 2.49: Laser-trimmable resonator. (a) Before laser cutting. (b) After laser cutting.

stant. Figure 2.49 illustrates laser trimming for a resonator. One advantage of the laser trim method is that the frequency can be monitored while cutting. A continuous range of frequency can be trimmed, allowing precision adjustment. Anchors can be designed for different sensitivity of frequency shift to cutting depth. Although laser trimming is attractive, fuse cutting offers a unique feature: the ability to perform on-site trimming by the end-user of a device.

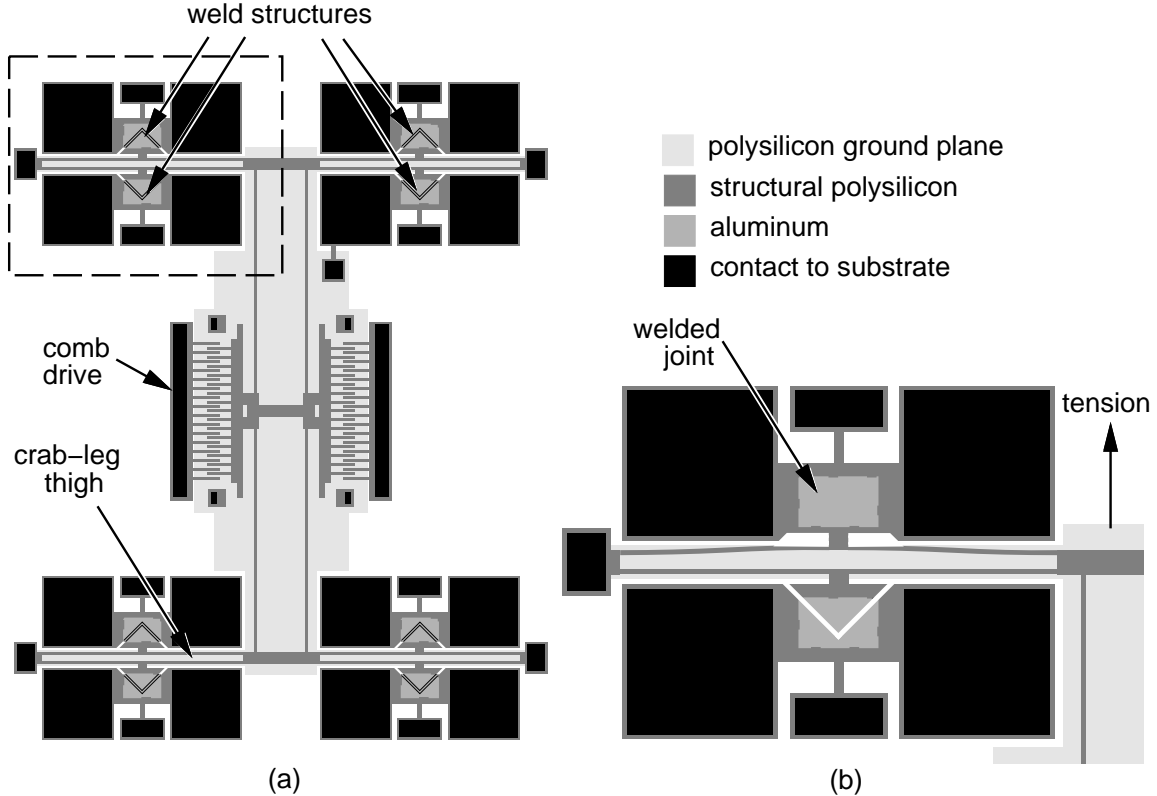


Figure 2.50: Schematic of a modified fixed-fixed resonator with weld structures used to trim frequency. (a) Resonator layout. (b) Enlarged view of the dashed box in (a), showing the beam bending caused by welding.

### 2.7.2 Frequency Trimming With Weld Structures

Another method for trimming resonant frequency employs weld structures that introduce tension into a microresonator's suspension. We have implemented this trimming method on a modified fixed-fixed resonator, shown schematically in Figure 2.50. Instead of being rigidly anchored, the long beams attached to the shuttle mass are connected to a truss at their fixed end. The truss is held up by a fixed-fixed suspension that has aluminum–silicon weld structures located along the sides. As the weld structure melts, lateral surface tension forces pull on the flexure, adjusting tension in the long beams that hold up the shuttle mass (Figure 2.50(b)). The weld structures are a larger-size variation of those described in section 2.5.2. The long V-shaped weld seam is believed to produce more lateral force, to align the weld, and to deliver an adjustable displacement by incrementally pulsing the welding current. By welding on either side of the truss flexure, the shuttle mass suspension

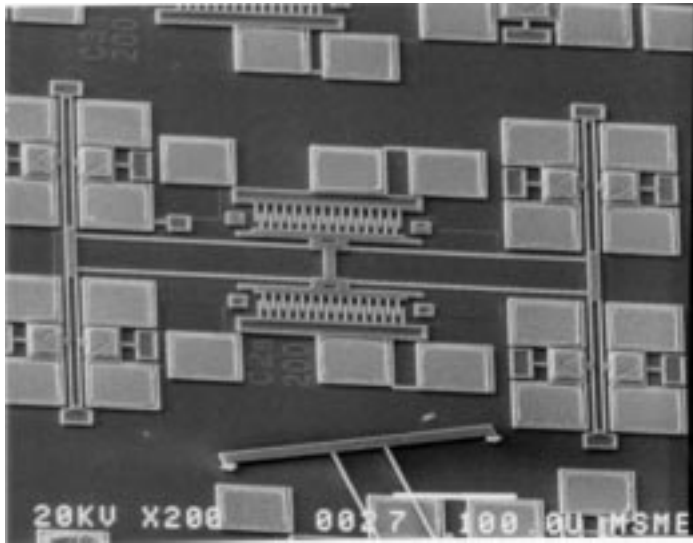


Figure 2.51: Trimmable fixed-fixed resonator. Weld structures are used to adjust tension in the suspension.

can be placed in tension or compression.

An SEM of the fabricated resonator is shown in Figure 2.51. and an enlarged view of the weld structure is shown in Figure 2.51. Unfortunately, fabrication problems (see section 2.5.2.4) produced cracks between the aluminum and structural polysilicon, yielding inoperable weld structures.

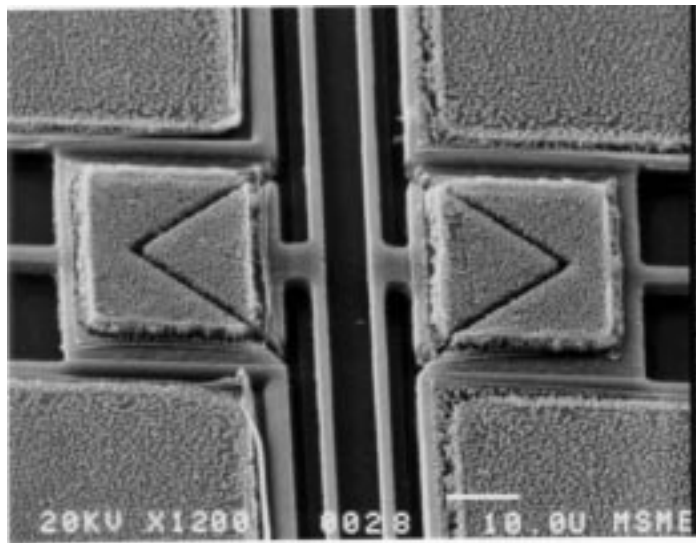


Figure 2.52: Magnified view of weld structures used for tensioning the suspension.

## Chapter 3

# Lumped-Parameter Modeling

### 3.1 Introduction

In this chapter, we will present an overview of a select group of lumped-parameter models for surface microsystems. We will discuss micromechanical equations of motion, squeeze-film damping, spring constants, electrostatic actuation, and capacitive position sensing. Our analyses are focused on application to the micromechanical testbed, which is the topic of following chapters.

### 3.2 Mechanical Equations of Motion

Micromechanical structures can be divided into discrete elements that are modeled using rigid-body dynamics. Finite-element analysis is used to determine the mechanical modes that are within the bandwidth of the feedback and external forces. Some structural elements can be modeled simply as rigid body mass, while other models may include the effects of bending, torsion, axial, and shear stress.

A mechanical system with  $n$  degrees of freedom can be described in terms of  $n$  generalized coordinates,  $q_1, q_2, \dots, q_n$ , and time,  $t$ . A general method of determining the equations of motion involves use of Lagrange's equation [55].

$$\frac{d}{dt} \left( \frac{\partial L}{\partial \dot{q}_i} \right) - \frac{\partial L}{\partial q_i} = Q_{nc,i} \quad ; i = 1, \dots, n \quad (3.1)$$

where  $L = T - V$  is the Lagrangian operator,  $T$  is the total kinetic energy of the system, and  $V$  is the potential energy of the system, arising from conservative forces. Non-conservative

forces, such as dissipative forces, are lumped in the terms  $Q_{nc,i}$ . If only viscous damping terms (damping proportional to velocity) are present, then Lagrange's equation can be written as

$$\frac{d}{dt} \left( \frac{\partial L}{\partial \dot{q}_i} \right) - \frac{\partial L}{\partial q_i} + \frac{\partial F}{\partial q_i} = Q_{ext,i} \quad ; i = 1, \dots, n \quad (3.2)$$

where  $F$  is the Rayleigh dissipation function, and  $Q_{ext,i}$  is an external generalized force associated with the coordinate  $q_i$ . In general, the kinetic energy, potential energy, and dissipation function have the forms

$$T = \frac{1}{2} \sum_{i=1}^n \sum_{j=1}^n m_{ij} \dot{q}_i \dot{q}_j \quad (3.3)$$

$$V = \frac{1}{2} \sum_{i=1}^n \sum_{j=1}^n k_{ij} q_i q_j \quad (3.4)$$

$$F = \frac{1}{2} \sum_{i=1}^n \sum_{j=1}^n B_{ij} \dot{q}_i \dot{q}_j \quad (3.5)$$

where  $m_{ij}$  are inertia coefficients,  $k_{ij}$  are stiffness coefficients, and  $B_{ij}$  are damping coefficients.

We will apply Lagrange's equation to the example, shown in Figure 3.1, of a rigid rectangular plate suspended by four springs located at the plate's corners<sup>1</sup>. Generalized coordinates are chosen to be the three Cartesian directions<sup>2</sup>,  $x$ ,  $y$ , and  $z$ , and the three angles of rotation,  $\theta$ ,  $\phi$ , and  $\psi$ . Potential energy stored in the springs is determined by summing the contributions of each spring. Making small angle approximations, we find

$$V = 2 \left( k_x x^2 + k_y y^2 + k_z z^2 + k_z L_{ky}^2 \theta^2 + k_z L_{kx}^2 \phi^2 + k_y L_{kx}^2 \psi^2 \right) \quad (3.6)$$

where  $k_x$ ,  $k_y$ , and  $k_z$  are spring constants in the  $x$ ,  $y$ , and  $z$  directions, respectively. The dimensions  $L_{kx}$  and  $L_{ky}$  are the distances along the  $x$  and  $y$  axis from the centroid of the plate to the springs<sup>3</sup>. We assume that the spring force varies linearly with displacement; however, nonlinear spring forces can be modeled by substituting stiffness coefficients that are functions of position into Equation (3.6). If we assume massless springs, then the kinetic energy is

$$T = \frac{1}{2} \left( m \dot{x}^2 + m \dot{y}^2 + m \dot{z}^2 + I_\theta \dot{\theta}^2 + I_\phi \dot{\phi}^2 + I_\psi \dot{\psi}^2 \right) \quad (3.7)$$

---

<sup>1</sup>The micromechanical testbed, discussed in chapters 4–6, has this kind of suspension.

<sup>2</sup>In this general discussion, we choose the origin of the axes to be at the center of the plate. However, when we analyze specific micromechanical elements, we will choose the  $z$ -axis origin to be at the substrate. The variable  $\Delta z$  will then be used to describe vertical displacement of a plate from its rest (zero mechanical potential) position.

<sup>3</sup>In the example illustrated in Figure 3.1, the springs are located at  $L_{kx} = L_x/2$  and  $L_{ky} = L_y/2$ .

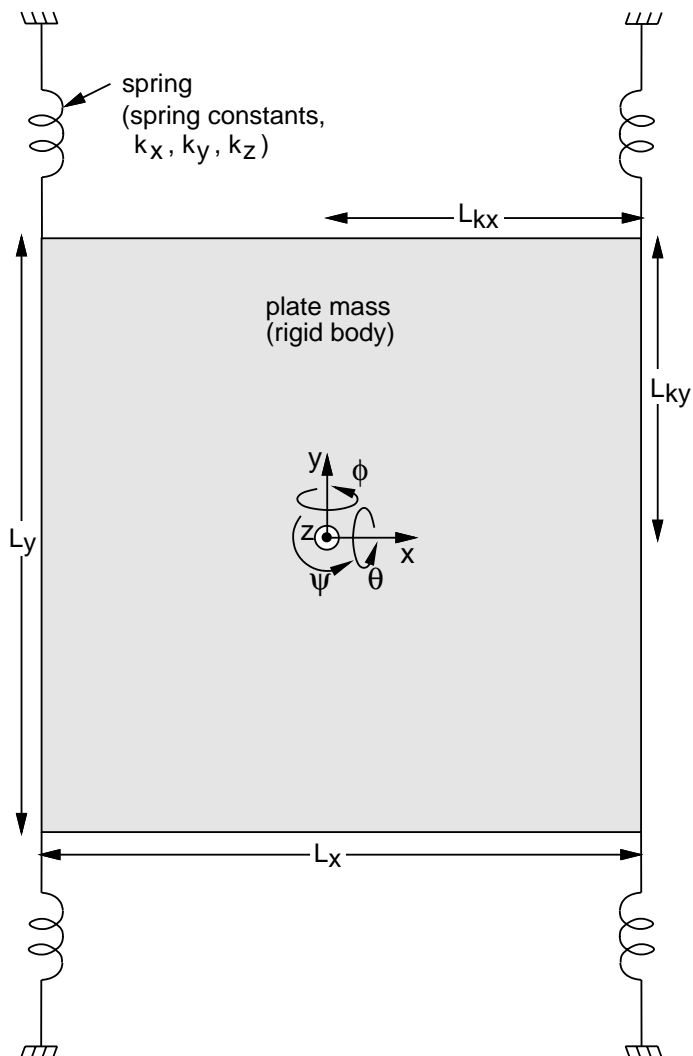


Figure 3.1: Schematic of a rigid rectangular plate, with dimensions  $L_x \times L_y$ . Springs are attached at distances  $L_{kx}$  and  $L_{ky}$  along the  $x$ -axis and  $y$ -axis, respectively, from the centroid of the plate.

where  $m$  is the plate mass and the mass moments of inertia of the plate are given by

$$I_\theta = \frac{m}{12} L_y^2 \quad (3.8)$$

$$I_\phi = \frac{m}{12} L_x^2 \quad (3.9)$$

$$I_\psi = \frac{m}{12} (L_x^2 + L_y^2) \quad (3.10)$$

We will assume viscous damping of the plate can be expressed by the dissipation function,

$$F = \frac{1}{2} (B_x \dot{x}^2 + B_y \dot{y}^2 + B_z \dot{z}^2 + B_\theta \dot{\theta}^2 + B_\phi \dot{\phi}^2 + B_\psi \dot{\psi}^2) \quad (3.11)$$

where  $B_x, B_y, B_z, B_\theta, B_\phi, B_\psi$ , are the damping coefficients of the six modes. The expressions for kinetic energy, potential energy, and dissipation function of the mass-spring-damper system are substituted into Equation (3.2) and then solved for each of the six coordinates, resulting in the following equations of motion:

$$F_x = m\ddot{x} + B_x\dot{x} + k_x x \quad (3.12)$$

$$F_y = m\ddot{y} + B_y\dot{y} + k_y y \quad (3.13)$$

$$F_z = m\ddot{z} + B_z\dot{z} + k_z z \quad (3.14)$$

$$\tau_\theta = I_\theta \ddot{\theta} + B_\theta \dot{\theta} + k_z L_{ky}^2 \theta \quad (3.15)$$

$$\tau_\phi = I_\phi \ddot{\phi} + B_\phi \dot{\phi} + k_z L_{kx}^2 \phi \quad (3.16)$$

$$\tau_\psi = I_\psi \ddot{\psi} + B_\psi \dot{\psi} + k_y L_{kx}^2 \psi \quad (3.17)$$

where  $F_x, F_y, F_z, \tau_\theta, \tau_\phi$ , and  $\tau_\psi$  are external forces and torques that act on the plate. Values for the stiffness and damping coefficients can be determined numerically using finite-element analysis or approximated by analytic formulas, as discussed in the following two sections.

Most of the simulation and modeling described in this thesis involves vertical motion of a suspended plate. Therefore, we will often refer to the vertical equations of motion, Equations (3.14)–(3.16), which can be expressed in the alternative form

$$F_z = m (\ddot{z} + 2\zeta_z \omega_z \dot{z} + \omega_z^2 z) \quad (3.18)$$

$$\tau_\theta = I_\theta (\ddot{\theta} + 2\zeta_\theta \omega_\theta \dot{\theta} + \omega_\theta^2 \theta) \quad (3.19)$$

$$\tau_\phi = I_\phi (\ddot{\phi} + 2\zeta_\phi \omega_\phi \dot{\phi} + \omega_\phi^2 \phi) \quad (3.20)$$

where  $\omega_z, \omega_\theta$ , and  $\omega_\phi$  are resonant frequencies and  $\zeta_z, \zeta_\theta$ , and  $\zeta_\phi$  are dimensionless damping factors of the  $z, \theta$ , and  $\phi$  modes, respectively. In general, the resonant frequency,  $\omega_i$ , and

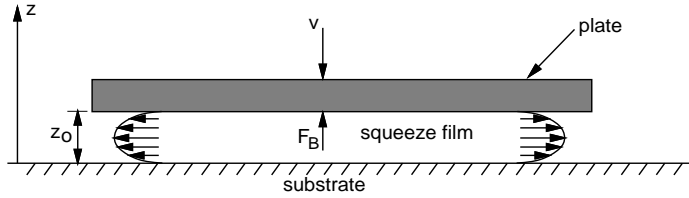


Figure 3.2: Cross-section schematic of a plate with an air gap,  $z_o$ , above the substrate, illustrating the squeeze-film damping arising from vertical motion of the plate with velocity,  $v$ . Pressure in the squeeze film produces a force,  $F_B$ , which is proportional to the velocity.

damping factor,  $\zeta_i$ , of mode  $i$  are given by

$$\omega_i = \sqrt{\frac{k_i}{m_i}} \quad (3.21)$$

$$\zeta_i = \frac{B_i}{2\sqrt{k_i m_i}} \quad (3.22)$$

where  $k_i$  is the stiffness coefficient and  $m_i$  is the inertia coefficient (mass for translational modes or moment of inertia for rotational modes) of mode  $i$ . Effects of spring mass can be included by introducing effective inertia coefficients to adjust the resonant frequency.

### 3.3 Squeeze-Film Damping

Viscous air damping is the dominant dissipation mechanism for microstructures that operate at atmospheric pressure. Squeeze-film damping, illustrated in Figure 3.2, arises from vertical motion which creates a pressure in the thin film of air between the plate and substrate. Detailed reports on general squeeze-film damping are given in [56–58]<sup>4</sup>; a review of squeeze-film damping in micromechanical accelerometers is given by Starr [62]. We will provide a brief review of squeeze-film damping, and apply the results to vertical motion of a 400  $\mu\text{m} \times 400 \mu\text{m}$  plate with a 2  $\mu\text{m}$  air gap.

#### 3.3.1 Simplifying Assumptions for Viscous Flow

Continuum fluid mechanics can be used to analyze squeeze-film damping if the air gap is much larger than the mean-free-path,  $\lambda$ , of the air molecules. Mean-free-path of a

---

<sup>4</sup>Laterally moving microstructures experience a different form of air damping, Couette damping, in the gap under the structure. Several papers report on analytic models of Couette damping for microstructures [59–61].

gas is expressed as

$$\lambda = \frac{1}{\sqrt{2} \pi d_o^2 n} \quad (3.23)$$

where  $\pi d_o^2$  is the collision cross-section of the gas molecules, and  $n$  is the molecular density, which, for an ideal gas, is given by

$$n = \frac{P}{k_B T} \quad (3.24)$$

where  $P$  is pressure of the squeeze film,  $k_B$  is Boltzmann's constant, and  $T$  is absolute temperature. For air at atmospheric pressure and  $T=300^\circ\text{K}$ , the mean-free-path is 65 nm. The 2  $\mu\text{m}$  air gap dimension is about  $31\times$  larger than the mean-free-path, so the air can be modeled approximately as a viscous fluid. At pressures below about 25 T, the mean-free-path is greater than 2  $\mu\text{m}$  and the gas film dynamics must be treated as an ensemble of molecules, not as a viscous fluid. In this molecular-flow regime, the air damping will decrease dramatically with decreasing pressure, and structural damping will eventually dominate the losses.

We describe the viscous-flow regime with the Navier-Stokes equation, which, when several assumptions are made, can be reduced to [62]

$$\frac{\partial^2 P}{\partial x^2} + \frac{\partial^2 P}{\partial y^2} = \frac{12\mu}{z_o^3} \frac{\partial(\Delta z)}{\partial t} \quad (3.25)$$

where  $P$  is pressure of the squeeze film,  $\mu$  is the viscosity of air<sup>5</sup>,  $z_o$  is the air-gap height, and  $\Delta z$  is the plate displacement. Equation (3.25) is valid if the squeeze film is isothermal and has small pressure variations, and if the plate undergoes small displacements with small velocities.

Large relative displacements with respect to the air gap will increase the damping. A plate displacement of  $z_o/4$  results in a 10 % increase in damping relative to the value calculated using the small-displacement assumption [62]. Air velocity in the gap can be considered small if the Reynolds number,  $Re$ , is much less than 1, where

$$Re = \frac{\rho v z_o}{\mu} \quad (3.26)$$

and  $\rho$  is the density of air<sup>6</sup>, and  $v$  is the air velocity. With a 2  $\mu\text{m}$  air gap, and a plate oscillation frequency of 1 kHz and oscillation amplitude of 1  $\mu\text{m}$ , the Reynolds number is very small ( $Re=0.0009$ ). To first order, both the Reynolds number and squeeze number are independent of pressure, since the air viscosity and density vary linearly with pressure.

---

<sup>5</sup>The viscosity of air is  $1.79 \times 10^{-5}$  Pa-s at atmospheric pressure and  $T=288^\circ\text{K}$  [46].

<sup>6</sup>The density of air is 1.22 kg/m<sup>3</sup> at atmospheric pressure and  $T=288^\circ\text{K}$  [46].

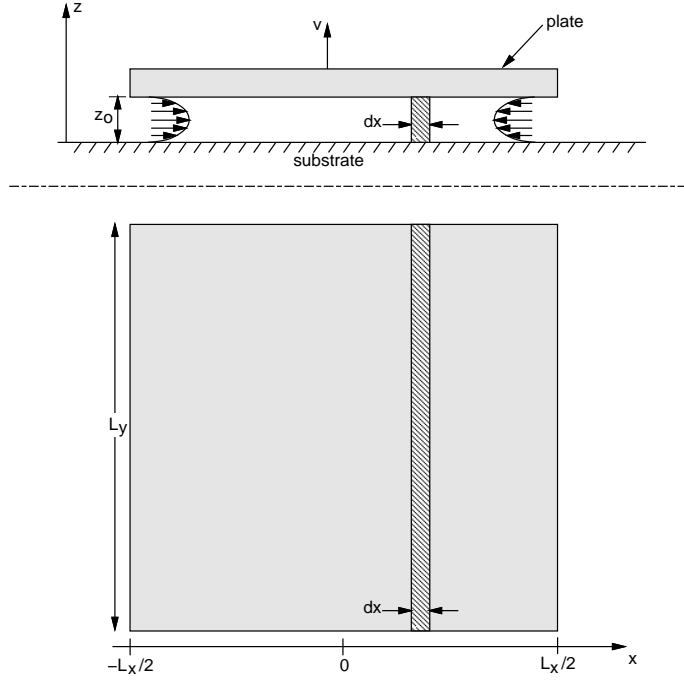


Figure 3.3: Schematic of a plate for one-dimensional analysis of squeeze-film damping. The drawing is not to scale, since we assume  $L_y \gg L_x$ .

### 3.3.2 One-Dimensional Analysis

We will analyze squeeze-film damping of the plate shown in Figure 3.3, where the plate length,  $L_y$ , in the  $y$ -direction is much larger than the length,  $L_x$  in the  $x$ -direction. The squeeze film is modeled with a one-dimensional version of Equation (3.25):

$$\frac{\partial^2 P}{\partial x^2} = \frac{12 \mu v}{z_o^3} \quad (3.27)$$

Double integration of Equation (3.27) and application of the pressure boundary conditions at the edges of the plate gives

$$\Delta P = \frac{6 \mu v}{z_o^3} \left( x^2 - \frac{L_x^2}{4} \right) \quad (3.28)$$

where  $\Delta P$  is the pressure difference from ambient pressure. The average pressure difference across the plate is  $\mu L_x^2 v / z_o^3$ , and the total force from damping exerted on the plate is

$$F_B = - \left( \frac{\mu L_y L_x^3}{z_o^3} \right) v \quad (3.29)$$

The squeeze-film damping coefficient for a rectangular plate is

$$B_z = K_{Bz}(L_x/L_y) \frac{\mu L_y L_x^3}{z_o^3} \quad (3.30)$$

where  $K_{Bz}(L_x/L_y)$  is a form factor that is introduced to account for the finite plate length,  $L_y$ . For a very long plate ( $L_y \gg L_x$ ), we can deduce from Equation (3.29) that  $K_{Bz}=1$ . The two-dimensional flow problem can be solved for other geometries;  $K_{Bz}$  is approximately 0.42 for a square plate ( $L_x = L_y$ ). For the 400  $\mu\text{m} \times 400 \mu\text{m}$  square plate, the damping coefficient is  $B_z = 0.024 \text{ Pa}\cdot\text{s}$ .

Surface-micromachined plates are often perforated with holes to reduce the time to undercut the sacrificial oxide during the release etch. Another effect of the holes is to reduce the squeeze-film damping significantly. McNeil [63] has modeled damping in a perforated plate as an ensemble of  $N$  smaller plates acting independently of each other. We incorporate the effect of perforations in the form factor,  $K_{Bz}$ .

### 3.3.3 Damping of Rotational Modes

The one-dimensional analysis of the preceding section can be repeated for the rotational mode of the plate shown in Figure 3.4, where  $L_y \gg L_x$ . Now, velocity is a function of the distance,  $x$ , from the plate's centroid. Substituting for the velocity, we rewrite Equation (3.27) as

$$\frac{\partial P}{\partial x^2} = -\frac{12 \mu \dot{\phi} x}{z_o^3} \quad (3.31)$$

where small angular displacements are assumed. We integrate Equation (3.27) twice to obtain the differential pressure:

$$P = \frac{2 \mu \dot{\phi}}{z_o^3} \left( \frac{L_x^2}{4} - x^2 \right) x \quad (3.32)$$

The total moment from damping is

$$M_B = -L_y \int_{-L_x/2}^{L_x/2} P x dx = -\frac{\mu L_y L_x^5}{60 z_o^3} \dot{\phi} \quad (3.33)$$

We can define the rotational-mode squeeze-film damping coefficient,  $B_\phi$ , in an analogous manner to the vertical-mode damping coefficient. Thus, for a rectangular plate,

$$\begin{aligned} B_\phi &= K_{B\phi}(L_x/L_y) \frac{\mu L_y L_x^5}{z_o^3} \\ &= K_{B\phi}(L_x/L_y) B_z L_x^2 \end{aligned} \quad (3.34)$$

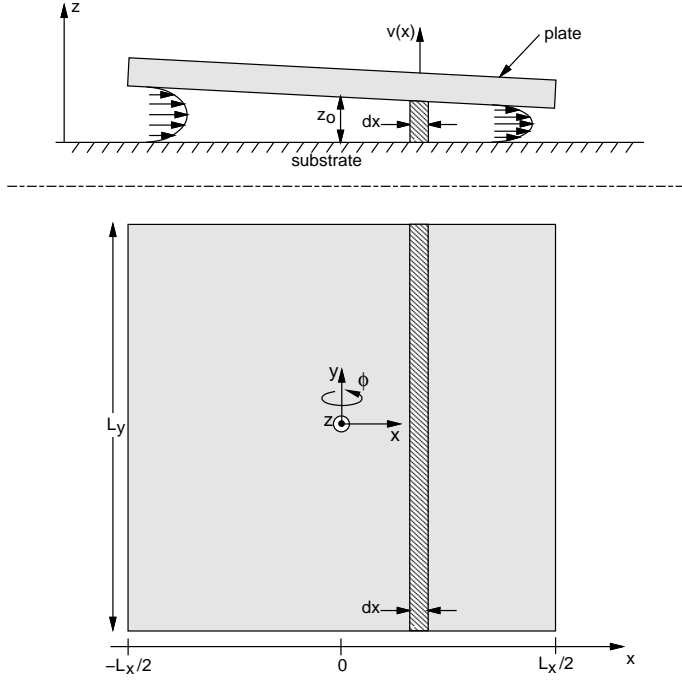


Figure 3.4: Schematic of a plate for one-dimensional analysis of squeeze-film damping of the  $\phi$  rotational mode about the  $y$ -axis.

where  $K_{B\phi}(L_x/L_y)$  is the two-dimensional form factor. For  $L_y \gg L_x$ ,  $K_{B\phi}=0.017$ . An analogous damping coefficient,  $B_\theta$ , can be defined for the rotational mode about the  $x$ -axis, where

$$B_\theta = K_{B\theta}(L_x/L_y) B_z L_y^2 \quad (3.35)$$

The corresponding damping factors for the rotational modes are

$$\zeta_\theta = \frac{B_\theta}{2\sqrt{I_\theta k_z L_{ky}^2}} = \sqrt{12} K_{B\theta} \left( \frac{L_y}{L_{ky}} \right) \zeta_z \quad (3.36)$$

$$\zeta_\phi = \frac{B_\phi}{2\sqrt{I_\phi k_z L_{kx}^2}} = \sqrt{12} K_{B\phi} \left( \frac{L_x}{L_{kx}} \right) \zeta_z \quad (3.37)$$

where the springs are assumed to be connected at the plate's corners. For a solid plate with springs attached at the plate's corners, the rotational-mode damping is around  $17\times$  smaller than the vertical-mode damping; if a square perforated plate with many holes is substituted, the rotational-mode damping is only around  $2\times$  smaller than the vertical-mode damping<sup>7</sup>.

---

<sup>7</sup>If we model the square perforated plate as an ensemble of many small plates, then  $\zeta_\theta = \zeta_\phi = 0.58\zeta_z$ .

## 3.4 Polysilicon Flexure Design

In this section, an overview of polycrystalline silicon (polysilicon) micromechanical flexures is presented. Polysilicon micromechanical flexures are used in accelerometers [64], gripping devices [65], tuning forks [66], resonant sensors [17] and micromotors [20]. In most cases, it is desirable to have a very compliant flexure in one direction while being very stiff in the orthogonal directions. For example, the proof mass for most micromachined accelerometers is designed to move easily in the direction normal to the substrate. Motion in the other directions increases sensitivity to cross-acceleration. Lateral resonant structures require flexures that are compliant in only one tangential direction.

Most polysilicon micromechanical flexures constrain motion to a rectilinear direction, and are created from straight beams. Spiral springs and other torsional flexures have been made, however [20,67]. The following discussion will emphasize design issues for rectilinear-displacement flexures. First, results of small displacement beam theory for simple beams are presented. A comparison is then made with exact theory for large displacements and finite-element simulation results for extensional stress. Practical limitations of polysilicon beam dimensions are discussed, along with possible areas for development. In the bulk of this section, we derive static spring constants for the fixed-fixed flexure, the crab-leg flexure, the folded flexure, and the serpentine flexure. The derivation method is general and can be used to find spring constants of other flexure geometries.

### 3.4.1 Spring Constants for Simple Beams

Cantilever, guided-end, and fixed-fixed beams are shown in Figure 3.5. A concentrated force,  $F$ , is applied to the free end of the cantilever beam (a), to the free end of the guided-end beam (b), and to the center of the fixed-fixed beam (c). A uniform distributed load,  $f$ , is applied to the surface of each beam in Figure 3.5(d-f). Axial displacement is found directly from Hooke's Law: stress =  $E \times$  strain, where  $E$  is Young's modulus of elasticity. Lateral displacement equations are summarized in Table 3.1, assuming a beam with small angles of rotation, no axial loading, and no shear deformation [2]. A rectangular beam cross-section, with width  $w$  and thickness  $h$ , is assumed, however displacement equations for other cross-sectional geometries can be derived.

For cases where concentrated loads are applied to the beam, linear spring constants

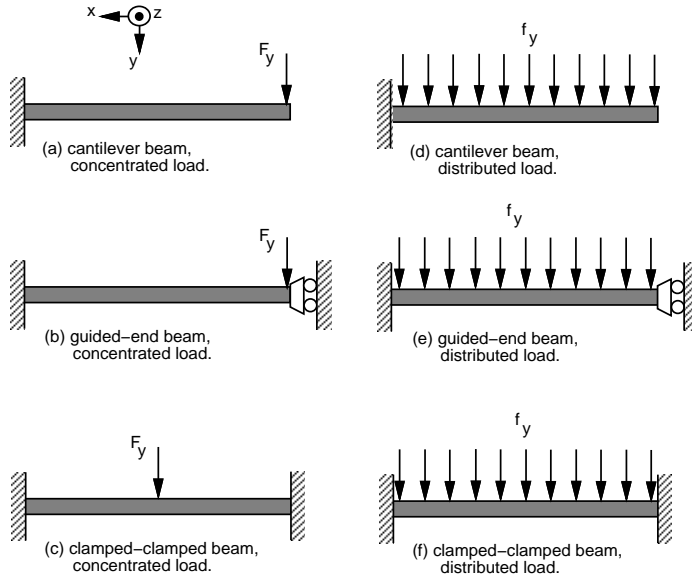


Figure 3.5: Various beams with concentrated load,  $F$ , or distributed load,  $f$ . Only the  $y$ -components of force are shown.

cantilever	guided-end	fixed-fixed
$x = \frac{F_x L}{E h w}$	$x = \frac{F_x L}{E h w}$	$x = \frac{F_x L}{4 E h w}$
$y = 4 \frac{F_y L^3}{E h w^3}$	$y = \frac{F_y L^3}{E h w^3}$	$y = \frac{1}{16} \frac{F_y L^3}{E h w^3}$
$z = 4 \frac{F_z L^3}{E w h^3}$	$z = \frac{F_z L^3}{E w h^3}$	$z = \frac{1}{16} \frac{F_z L^3}{E w h^3}$

(a) Concentrated load.

cantilever	guided-end	fixed-fixed
$x = \frac{f_x L}{E}$	$x = \frac{f_x L}{E}$	$x = \frac{f_x L}{4E}$
$y = \frac{3}{2} \frac{f_y L^4}{E h w^3}$	$y = \frac{1}{2} \frac{f_y L^4}{E h w^3}$	$y = \frac{1}{32} \frac{f_y L^4}{E h w^3}$
$z = \frac{3}{2} \frac{f_z L^4}{E w h^3}$	$z = \frac{1}{2} \frac{f_z L^4}{E w h^3}$	$z = \frac{1}{32} \frac{f_z L^4}{E w h^3}$

(b) Distributed load.

Table 3.1: Displacement equations derived from small displacement theory [2].

are defined as a measure of the beam's stiffness.

$$k_x = F_x/x ; \quad k_y = F_y/y ; \quad k_z = F_z/z$$

The cantilever beam is most compliant and the fixed-fixed beam is stiffest, if the beam dimensions are equal for both cases. The stiffness ratio of the axial to lateral in-plane motion,  $k_x/k_y$ , is proportional to  $(L/w)^2$ . For a cantilever with  $L/w = 100$ , the stiffness ratio is 40000. The stiffness ratio of the vertical to lateral in-plane motion,  $k_z/k_y$ , is equal to  $(h/w)^2$ . If restricted vertical motion is desired, the beam thickness must be much larger than the width. Many polysilicon surface-micromachining processes can produce 1  $\mu\text{m}$ -wide by 3  $\mu\text{m}$ -thick beams, corresponding to  $k_z/k_y = 9$ .

### 3.4.2 Nonlinear Effects

The deflection equations listed in Table 3.1 are derived from differential equations assuming small deflections and angle of rotation. The exact deflection for a cantilever beam is compared with values using the small deflection theory in Figure 3.6 [1]. The small deflection theory is more than 10% in error for deflections greater than 30% of the beam length.

Shear deformation, which is neglected in Table 3.1, is small if [1]

$$w \ll \sqrt{\frac{4}{3(1+\nu)}} L \approx L \quad (3.38)$$

where  $\nu$  is Poisson's ratio and is assumed to be 0.3 for polysilicon. Most micromechanical flexures are long and narrow, thereby satisfying Equation (3.38).

Axial tensile stress is present in laterally deflected fixed-fixed beams. A nonlinear force-displacement relation results from the axial stress, where the effective spring constant increases with increasing load. A finite-element simulation program, ABAQUS [53], is used to obtain values of center deflection vs. load of a fixed-fixed beam<sup>8</sup>. Figure 3.7 compares the simulation results for two 2  $\mu\text{m}$ -wide by 2  $\mu\text{m}$ -thick fixed-fixed beams with theoretical results that assume small deflection. For deflections greater than approximately 1  $\mu\text{m}$ , the effects of tension in the beam become significant. The small deflection theory can only be used to accurately predict deflections smaller than 0.2% of the beam length, for a 600  $\mu\text{m}$ -long beam.

---

<sup>8</sup>The nonlinear finite-element analysis uses two-dimensional, three-node, quadratic beam elements.

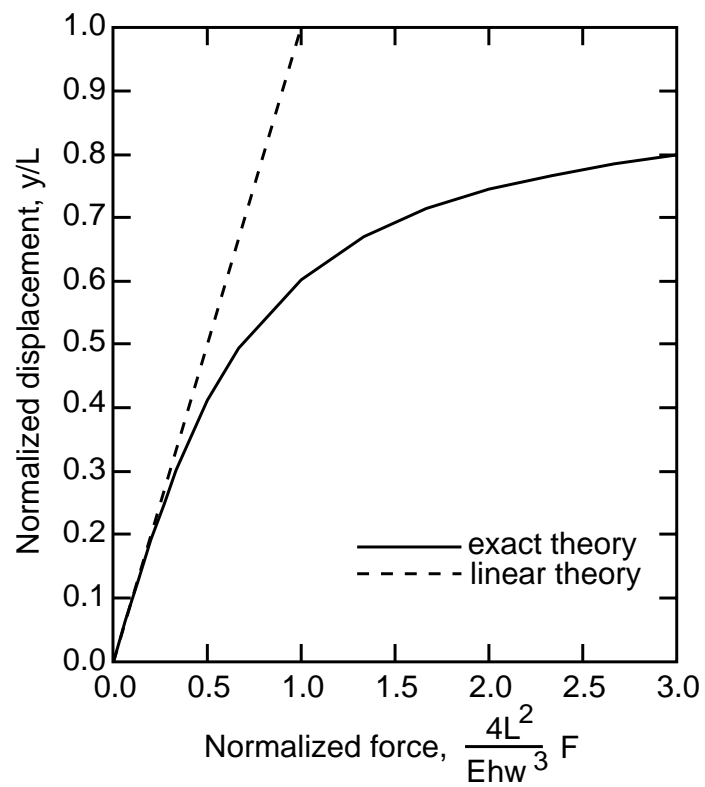


Figure 3.6: Comparison of small deflection theory (linear theory) with exact theory for cantilever beams [1].

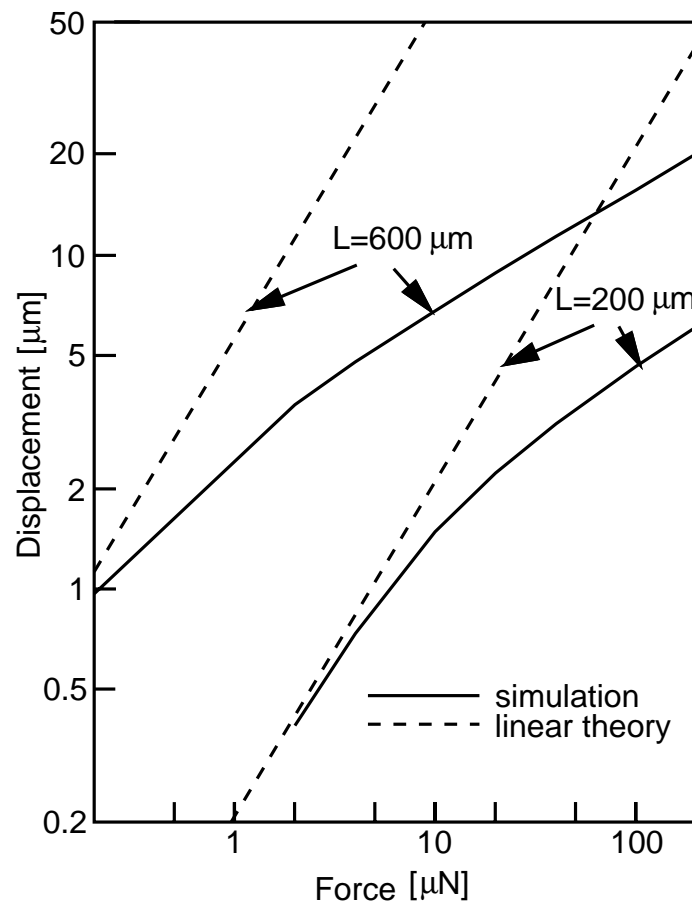


Figure 3.7: Displacement versus force for two fixed-fixed beams. The solid lines are calculated from finite-element simulation. The dotted lines are calculated from small deflection theory (linear theory).

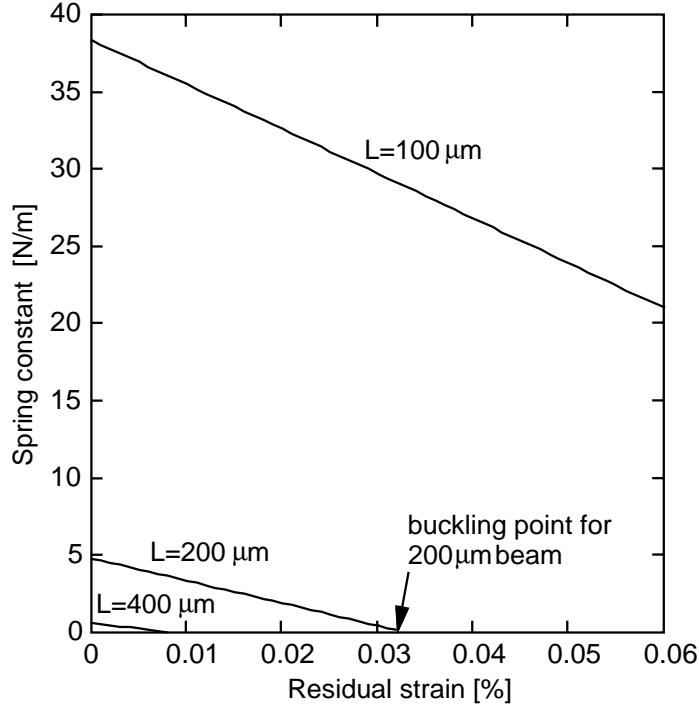


Figure 3.8: Spring constant versus residual strain of three fixed-fixed beams ( $2 \mu\text{m}$ -wide by  $2 \mu\text{m}$ -thick). As indicated, the  $200 \mu\text{m}$ -long beam buckles for residual strain over  $0.033 \%$ .

Residual stress greatly affects the lateral spring constants of fixed-fixed beams. Neglecting end-effects, a fixed-fixed beam buckles when its length exceeds a critical length,  $L_{\text{cr}}$  [15].

$$L_{\text{cr}} = \frac{\pi}{\sqrt{3|\epsilon_r|}} \min(h, w) \quad (3.39)$$

where the residual strain in the film,  $\epsilon_r$ , is linearly related to residual stress,  $\sigma_r$ , by Hooke's Law. For a fixed-fixed beam in compression, the displacement relation at the center of the beam varies nonlinearly with the axial stress [2].

$$y = \frac{FL'_{\text{cr}}}{2\pi Ehw|\epsilon_r|} \left[ \tan\left(\frac{\pi L}{2L'_{\text{cr}}}\right) - \frac{\pi L}{2L'_{\text{cr}}} \right] \quad (3.40)$$

where  $L'_{\text{cr}} = \pi w / \sqrt{3|\epsilon_r|}$ . As seen in Figure 3.8, the spring constant decreases linearly as the compressive strain increases.

### 3.4.3 Design Limitations

In microstructures where lateral motion in one direction is desired, long, thick, and narrow beams are required. Surface-micromachined structures cannot be made with

arbitrary beam dimensions, however. The fabrication process and external forces impose limitations on polysilicon beam dimensions.

### 3.4.3.1 Limitations on Beam Length

Distributed forces, arising from weight of the beam, voltage between the beam and substrate, and fixed charge in the substrate, impose limitations on beam length. As the beam length is increased, these forces eventually cause the beam to touch the substrate. For example, assume a cantilever beam is 2  $\mu\text{m}$ -wide, 2  $\mu\text{m}$ -thick, and has a spacing,  $z_o$ , from the substrate of 1  $\mu\text{m}$ . Using 2.33 gm/cm<sup>3</sup> for the value of polysilicon density, and  $E = 150$  GPa, a maximum length of 3.6 mm can be fabricated without the beam touching the substrate from its own weight.

If a voltage difference,  $V$ , exists between the beam and substrate, a distributed electrostatic force acts on the beam,  $f_V(x)$ .

$$\begin{aligned} f_V &= \frac{1}{2} \frac{V^2}{\Delta x} \frac{\partial C}{\partial z} \\ &= \frac{\eta \epsilon_o w V^2}{2(z_o - \Delta z(x))^2} \end{aligned} \quad (3.41)$$

where  $\Delta x$  is a differential element along the length of the beam, and  $\Delta z$  is the vertical displacement of the beam. Capacitance,  $C$ , has been modeled as a parallel-plate with a multiplicative factor,  $\eta$ , which compensates for field lines from the sides of the beam.  $\eta \approx 2.7$  for a 2  $\mu\text{m}$ -wide beam with  $s = 1 \mu\text{m}$  [52]. The electrostatic force is not constant along the beam length, resulting in a nonlinear differential equation for beam deflection. An overestimate of the maximum allowable beam length is found by assuming a uniform spacing,  $z_o - \Delta z(x) \approx z_o = 1 \mu\text{m}$ . For  $V = 1 \text{ V}$ , the maximum cantilever beam length is approximately 509  $\mu\text{m}$ . The maximum beam length is proportional to  $V^{-1/2}$ , therefore voltages must be kept small. Plates connected to the beam produce concentrated loads, causing a decrease in the maximum beam length.

Fixed charge can exist in insulating thin film layers, such as Si<sub>3</sub>N<sub>4</sub>, below the beam. A nominal value for fixed charge density in MOS gate oxide is 10<sup>10</sup> cm<sup>-2</sup> [68]. To evaluate the significance of fixed charge, this value of charge density is assumed to be in an insulating film above a conducting substrate. An electrostatic field solver, Maxwell [52], is used to obtain a value for force acting on the beam of 2.2  $\mu\text{N}/\text{m}$ , providing a maximum beam length of 780  $\mu\text{m}$ .

Long beams are difficult to release after wet etching of the sacrificial PSG in hydrofluoric acid. During final drying under a heat lamp, the beams pull down to the substrate because of surface tension from liquid trapped under the beams. A supercritical CO<sub>2</sub> drying method has been developed by Mulhern [23] to eliminate surface tension forces. Cantilever beams up to 1.3 mm long (2  $\mu\text{m}$ -wide by 2  $\mu\text{m}$ -thick) have been released with this method without sticking to the substrate. Bushings are sometimes used to limit surface area which can contact the substrate and reduce stiction. In many cases, however, the bushing remains stuck to the substrate if it comes in contact during the drying step. Alternatively, tee bridges are used to support beams during the PSG etch as discussed in Chapter 2. The supports are severed by application of a current pulse, thereby releasing the structure.

### 3.4.3.2 Limitations on Beam Width and Thickness

A fabrication tradeoff exists when simultaneously decreasing polysilicon beam width and increasing thickness in a design. Polysilicon to photoresist selectivity is about 2:1 for CCl<sub>4</sub>/O<sub>2</sub> plasma etching. A thicker photoresist is used, however, to ensure adequate step coverage over anchor cuts in the underlying phosphosilicate glass (PSG). Therefore, 2–3  $\mu\text{m}$ -thick resist is used to etch 2  $\mu\text{m}$  of polysilicon. Thicker polysilicon films would require even thicker resist. Sloping sidewalls on the photoresist cause the mask to shrink in size during the polysilicon etch, thereby limiting the minimum feature size to about 1  $\mu\text{m}$ .

A PSG mask provides much better selectivity to the polysilicon etch (6:1) than a photoresist mask. A thin conformal mask with steep sidewalls is created by defining the PSG with a CHF<sub>3</sub>/CF<sub>4</sub> plasma etch. Thicker polysilicon films are able to be etched using the PSG mask. The CHF<sub>3</sub>/CF<sub>4</sub> plasma etch deposits polymers on sidewall surfaces. As the etch progresses, the surface roughness increases and polymers start depositing on the surface. Anisotropic polysilicon plasma etching is limited to about 5  $\mu\text{m}$ -thick films because of the polymer formation. Trenches up to 100  $\mu\text{m}$  deep have been plasma etched in polysilicon by periodically using an isotropic SF<sub>6</sub> plasma to decrease surface roughness [69], at the expense of linewidth resolution and sidewall integrity.

Polysilicon film thickness is also limited by deposition time. Heavily doped polysilicon is required for electrical sensors and actuators. The undoped polysilicon deposition rate is approximately 1  $\mu\text{m}/\text{hr}$ ; *in situ* heavily doped polysilicon is deposited about three times slower. Structures are often fabricated from undoped polysilicon to decrease total

deposition time. Then, a high-temperature diffusion is used to drive in phosphorus from the surrounding PSG films. Stress gradients are created in thick ( $> 2 \mu\text{m}$ ) polysilicon films, causing the structures to bend toward or away from the substrate. The high-temperature diffusion recrystallizes the polysilicon and reduces stress gradients.

Compressive residual stress in the polysilicon film can cause buckling of fixed-fixed structures, limiting beam length to  $L_{\text{cr}}$ . Residual strain is sensitive to both deposition and annealing conditions. Values of residual strain of 0.1–0.3% in undoped and doped polysilicon have been reported [15, 54]. High temperature annealing at temperatures over 1000 °C will lower the residual strain to around 0.015–0.03% [15, 54], corresponding to  $210 \mu\text{m} < L_{\text{cr}} < 300 \mu\text{m}$  for  $2 \mu\text{m} \times 2 \mu\text{m}$  beams. Undoped films with very low residual strain (0.0053%) have been reported with no high temperature annealing [32]. A comprehensive investigation of stress in undoped polysilicon has reported both compressive and tensile films, depending on deposition conditions [33]. Tensile stress has been created after annealing undoped polysilicon at 835 °C for 1 hour [16]. Rapid thermal annealing (RTA) is effective as an alternative to furnace annealing; some RTA results are presented in section mics-process.

Other process technologies presently under development provide sub-micron polysilicon beam widths. Narrow cantilever beams ( $0.3 \mu\text{m}$ -wide by  $2 \mu\text{m}$ -thick) have been fabricated by maskless, anisotropic etching of polysilicon covering nearly vertical steps of PSG [31]. Stress gradients exist in these beams, however, resulting in out-of-plane deflection. Direct write e-beam patterning can provide  $0.2 \mu\text{m}$  beam widths with  $2 \mu\text{m}$ -thick polysilicon but this technology has not yet been used to fabricate micromechanical flexures.

### 3.4.4 Flexure Spring Constants

In this section, we present static linear spring-constant analysis of four flexures that are commonly used in micromechanical designs: the fixed-fixed flexure, the crab-leg flexure, the folded flexure, and the serpentine flexure.

#### 3.4.4.1 Overview of Flexures

The fixed-fixed flexure, shown in Figure 3.9(a), has a very stiff nonlinear spring constant, because of extensional axial stress in the beams. Approximate analytic expressions for nonlinear fixed-fixed spring constants have been derived by Pisano [70]. Residual stress

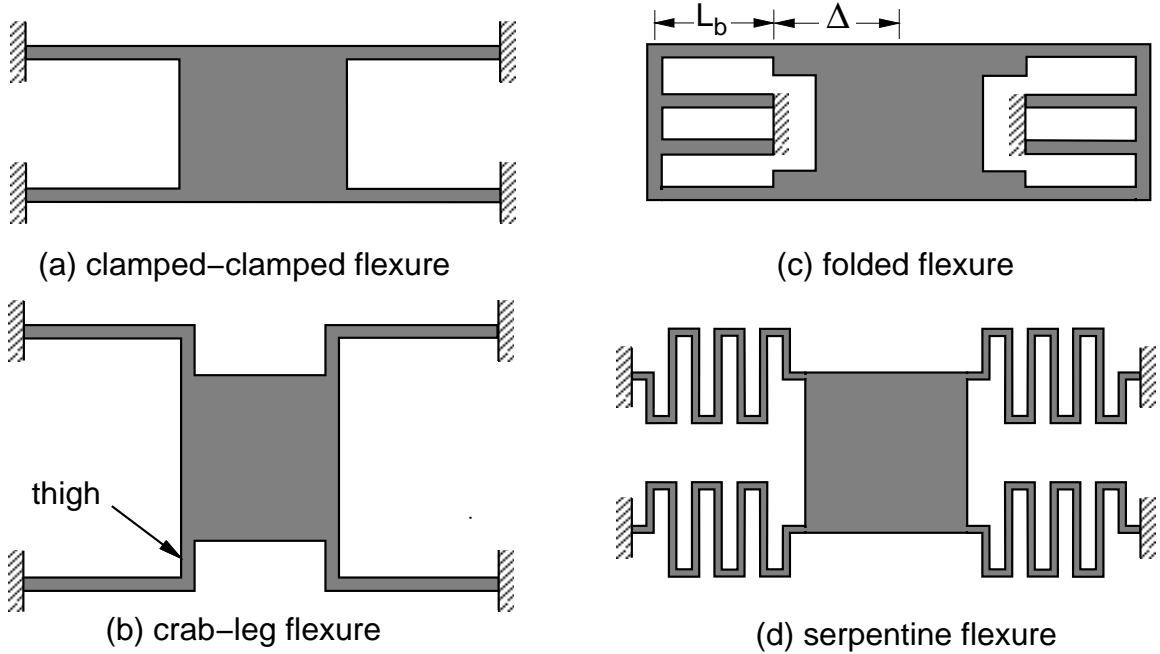


Figure 3.9: Various flexure designs. (a) fixed-fixed flexure. (b) folded flexure. (c) crab-leg flexure. (d) serpentine spring.

in the polysilicon film increases the stiffness. Compressive residual stress can cause buckling of the structure.

A variation of the fixed-fixed flexure, the crab-leg flexure, is shown in Figure 3.9(c) [71]. The “thigh” section, added to create the crab-leg, is designed to minimize peak stress in the flexure at the cost of reducing stiffness in the undesired direction. Deflection of the thigh can also reduce extensional axial stress in the flexure [70].

The folded flexure, shown in Figure 3.9(b), also reduces axial stress components in the beams [20,54]. Each end of the flexure is free to expand or contract in all directions. The original residual stress in a small section of the flexure ( $\Delta$  in Figure 3.9(b)) is averaged over the entire beam length, giving a reduced effective residual stress,  $\sigma_{r,\text{eff}}$ .

$$\sigma_{r,\text{eff}} = \frac{\Delta}{L_b} \sigma_r \quad (3.42)$$

where  $L_b$  is the flexure beam length. The beams in the flexure will alternate in the sign of the stress. A review of several variations of the folded flexure along with a discussion of nonlinear static analysis and modal analysis are found in Judy’s Ph.D. thesis [51].

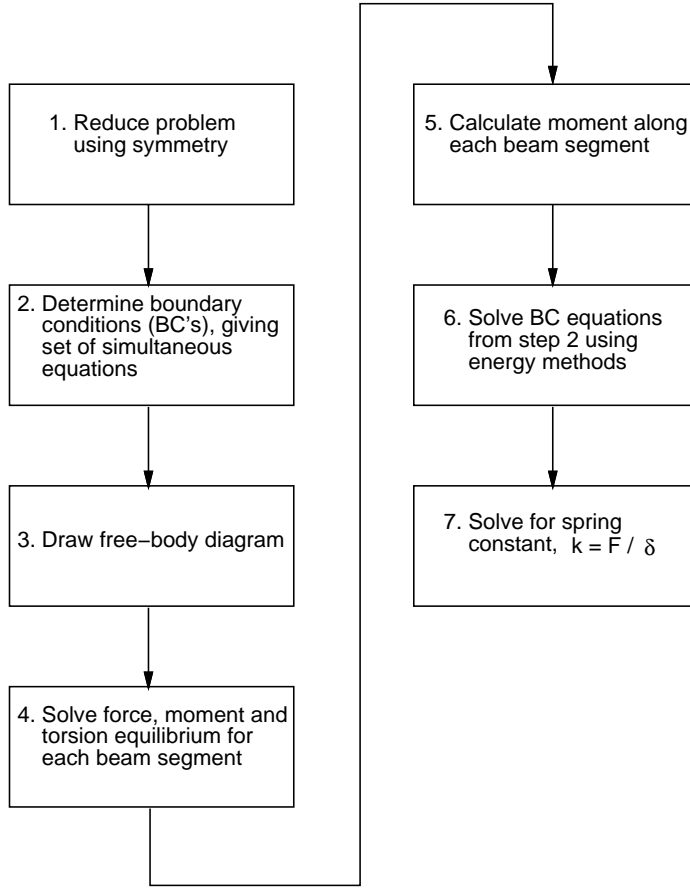


Figure 3.10: Flow-chart for spring constant analysis using energy methods.

A serpentine flexure is shown in Figure 3.9(d). Several micromechanical suspension designs use serpentine flexures [20, 54]. Compliant serpentine flexures can be designed with compact springs. The width of the meanders is adjusted to give the desired stiffness ratio. Residual stress and extensional axial stress are relieved through bending of the meanders.

#### 3.4.4.2 Linear Spring-Constant Analytic Method

In the following analysis of micromechanical flexures, we use energy methods [1] to derive analytic formulas for linear spring constants. The goal is to find the displacement,  $\delta$ , resulting from a force,  $F$ , applied in the appropriate direction. The spring constant is defined as  $k = F/\delta$ . Only displacement from bending and torsion is considered in the analysis. Deformation from shear, beam elongation, and beam shortening is neglected.

A flow-chart for obtaining analytic spring-constant equations is given in Fig-

ure 3.10. First, we simplify the problem by taking advantage of geometric symmetry of the flexure. For example, each of the flexures in Figure 3.9 is made from four springs and has two-fold symmetry. We only need to analyze one spring; the resulting spring constant is one-quarter of the flexure spring constant. Second, we identify boundary conditions at the ends of the spring. Flexure symmetry is important in determining the boundary conditions. For translation of the mass, the flexures in Figure 3.9 impose a guided-end boundary condition. Displacement and rotation of the spring end are constrained to be zero, except in the direction of the applied force. Third, we separate the spring into beam segments and draw a free-body diagram. Fourth, we determine the boundary conditions at the ends of each beam segment by solving  $\sum F = 0$ ,  $\sum M = 0$ , and  $\sum T = 0$ . These boundary conditions are expressed in terms of the reaction forces, moments, and torsion at the end of the spring. Fifth, we calculate the moment and torsion of each beam segment as a function of position along the beam,  $x$ . Sixth, using energy methods, we solve the set of simultaneous equations that describe the boundary conditions and obtain the reaction forces, moments, torsion, and displacement at the end of the spring. Castiglano's second theorem states that the partial derivative of the strain energy of a linear structure,  $U$ , with respect to a given load,  $P_i$ , is equal to the displacement at the point of application of the load,  $\delta_i$ .

$$\delta_i = \frac{\partial U}{\partial P_i} \quad (3.43)$$

This theorem extends to applied moments,  $M_i$ , and their corresponding angular displacements,  $\theta_i$ .

$$\theta_i = \frac{\partial U}{\partial M_i} \quad (3.44)$$

Our last step is to calculate the spring constant, equal to the applied force divided by the displacement.

In the following four sections, we derive spring constant equations for the fixed-fixed flexure, the folded flexure, the crab-leg flexure, and the serpentine flexure. In all cases, we assume small deflection theory. A guided-end condition is used in finding spring constants; this condition is valid for translation of the suspended plates in Figure 3.9.

#### 3.4.4.3 Spring Constants for the Fixed-Fixed Flexure

The fixed-fixed flexure in Figure 3.11(a) is modeled as four guided-end beams. Residual stress and extensional stress are neglected in the following analysis. Although the

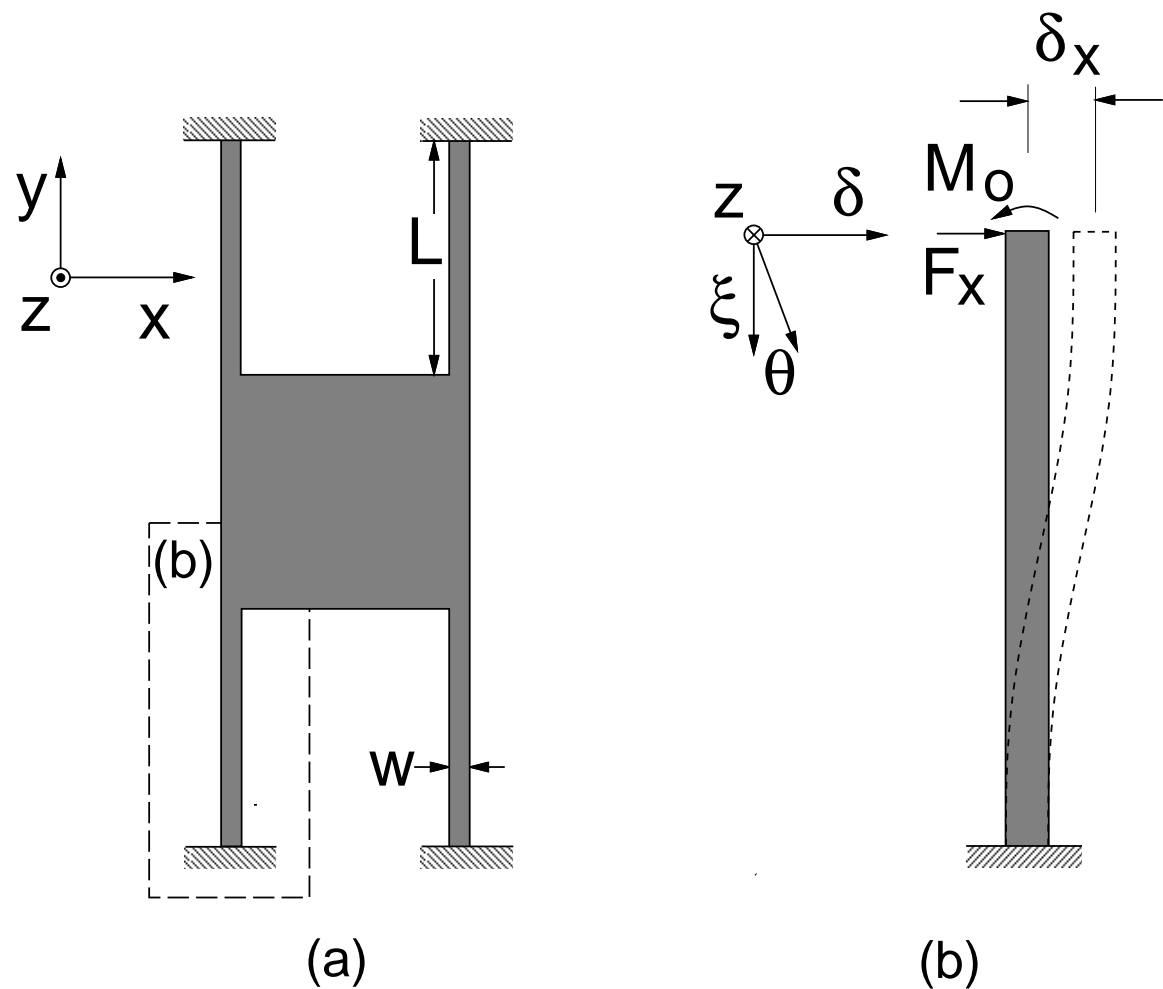


Figure 3.11: (a) Fixed-fixed flexure. (b) Guided-end beam with length  $L$ , width  $w$ , and thickness  $t$ . The dotted outline is the beam displaced by  $\delta_x$ .

linear analysis is usually not valid for fixed-fixed flexures, it illustrates a simple application of Castigliano's theorem. For the other flexures, linear analysis provides a good approximation of spring constants.

Figure 3.11(b) is a schematic of one guided-end beam having length  $L$ , width  $w$ , and thickness  $t$ . A lateral force,  $F_x$ , is applied at the end of the beam, resulting in a displacement,  $\delta_x$ . We choose the  $x$ -coordinate to point in the direction of the most compliant lateral spring constant. This convention makes it easier to compare spring constants of different flexures. The guided-end beam has a separate  $\delta$ - $\xi$  coordinate system where the  $\xi$ -coordinate points along the beam's axis. The angle at the end of the beam,  $\theta_o$ , is fixed at zero by symmetry of the flexure. An external bending moment,  $M_o$ , constrains the angle in the analysis. The beam bending moment is  $M = M_o - F_x \xi$ , where  $\xi$  is the distance from the guided-end. The strain energy of the beam is found by integrating the strain energy density along the beam.

$$U = \int_0^L \frac{M^2}{2EI_z} d\xi \quad (3.45)$$

where  $E$  is Young's modulus of elasticity and  $I_z$  is the bending moment of inertia about the  $z$ -axis. The moment of inertia of the rectangular beam cross-section is given by

$$I_z = \int_{-t/2}^{t/2} \int_{-w/2}^{w/2} x^2 dx dz = \frac{tw^3}{12} \quad (3.46)$$

The product  $EI_z$  is called the flexural rigidity of the beam.

A first invocation of Castigliano's second theorem, combined with the constraint  $\theta_o = 0$ , gives a relation between the external moment and the load.

$$\theta_o = \frac{\partial U}{\partial M_o} = \int_0^L \frac{M}{EI_z} \frac{\partial M}{\partial M_o} d\xi = \frac{1}{EI_z} \int_0^L (M_o - F_x \xi) d\xi = 0 \quad (3.47)$$

Solving for the bending moment gives  $M_o = F_x L/2$  and  $M = F_x(L/2 - \xi)$ . The calculation is simplified by bringing the partial derivative inside the integral in Equation (3.47). The partial derivative in the integrand ( $\partial M / \partial M_o$  in Equation (3.47)) is the moment resulting from a unit load ( $M_o$ ) applied to the beam. Hence, this modification of Castigliano's second theorem is called the unit-load method; it is used throughout the analysis in this section.

The unit-load method is employed a second time to determine the deflection at the end of the beam.

$$\delta_x = \frac{\partial U}{\partial F_x} = \int_0^L \frac{M}{EI_z} \frac{\partial M}{\partial F_x} d\xi = \frac{F_x}{EI_z} \int_0^L \left( \frac{L}{2} - \xi \right)^2 d\xi = \frac{F_x L^3}{12EI_z} \quad (3.48)$$

The guided-end cantilever beam spring constant is

$$k_{x,\text{beam}} = \frac{F_x}{\delta_x} = \frac{12EI_z}{L^3} \quad (3.49)$$

The spring constant of the flexure is four times the beam's spring constant.

$$k_x = \frac{48EI_z}{L^3} = \frac{4Et w^3}{L^3} \quad (3.50)$$

Except for the substitution of  $I_x$  for  $I_z$ , an identical derivation provides the spring constant in the  $z$ -direction,

$$k_z = \frac{48EI_x}{L^3} = \frac{4Et w t^3}{L^3} \quad (3.51)$$

The spring constant in the axial direction is found directly from Hooke's law.

$$k_y = \frac{Et w}{L} \quad (3.52)$$

The flexure is very stiff in the  $y$ -direction because there is no beam bending.

#### 3.4.4.4 Spring Constants for the Crab-Leg Flexure

**Spring Constant in the  $x$ -direction,  $k_x$ :** Figure 3.12 shows the free-body diagram of the crab-leg beam for lateral displacements. Each beam segment has its own coordinate system. The thigh segment has length  $L_a$  and width  $w_a$ , the shin segment has length  $L_b$  and width  $w_b$ . Bending moments of the thigh ( $M_a$ ) and shin ( $M_b$ ) are

$$M_a = M_o - F_y \xi \quad (3.53)$$

$$M_b = M_o - F_y L_1 - F_x \xi \quad (3.54)$$

where  $\xi$  is in the direction along the length of each beam. The unit-load method is used with the guided-end condition, providing a solution for the bending moment in terms of the applied forces.

$$\theta_o = \frac{\partial U}{\partial M_o} = \int_0^{L_a} \frac{M_a}{EI_{z,a}} \frac{\partial M_a}{\partial M_o} d\xi + \int_0^{L_b} \frac{M_b}{EI_{z,b}} \frac{\partial M_b}{\partial M_o} d\xi = 0 \quad (3.55)$$

where  $I_{z,a}$  and  $I_{z,b}$  are the moments of inertia for the thigh and shin, respectively. Solving Equation (3.55) gives

$$M_o = \frac{L_b^2 F_x + 2L_a L_b F_y + \alpha L_a^2 F_y}{2(L_b + \alpha L_a)} \quad (3.56)$$

where  $\alpha \equiv I_b/I_a = (w_b/w_a)^3$ .

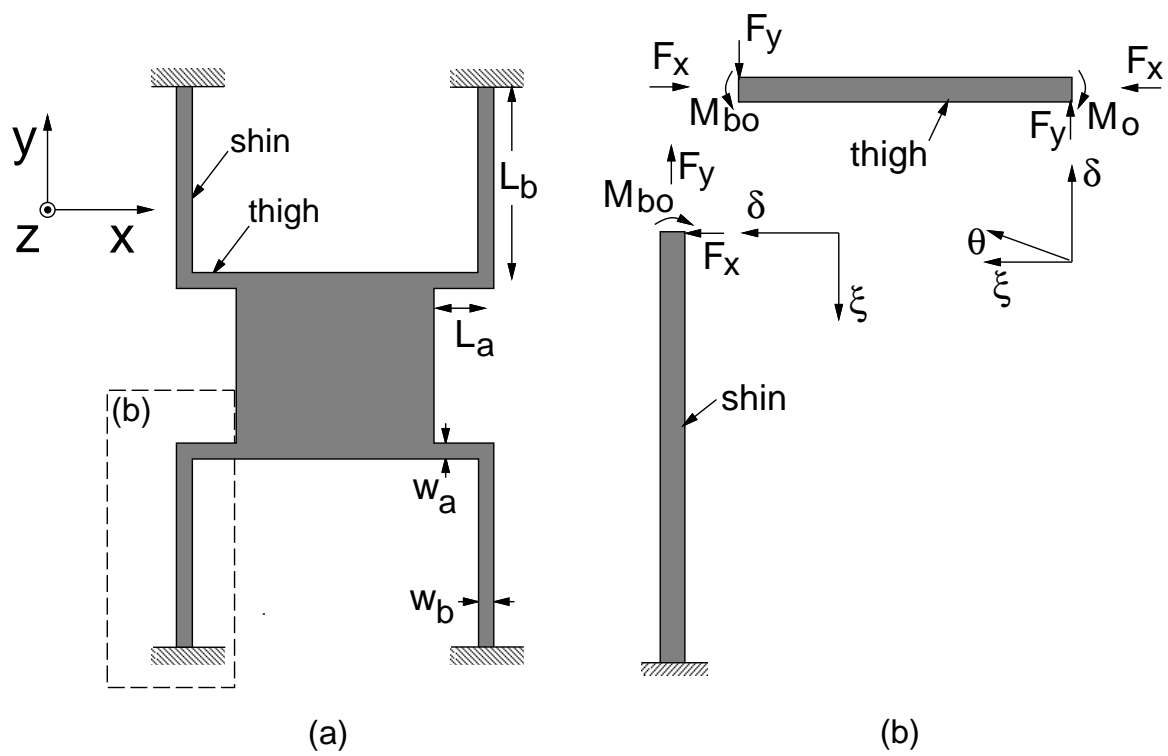


Figure 3.12: (a) Crab-leg flexure. (b) Free-body diagram of a crab-leg beam.

We find the spring constant  $k_x$  by applying a force  $F_x$  in the  $x$ -direction. Because of flexure symmetry, the reaction force  $F_y$  keeps the beam end from moving in the  $y$ -direction. The constraint on the beam end is  $y = 0$ , when solving for  $k_x$ .

$$\delta_y = \frac{\partial U}{\partial F_y} = \int_0^{L_a} \frac{M_a}{EI_{z,a}} \frac{\partial M_a}{\partial F_y} d\xi + \int_0^{L_b} \frac{M_b}{EI_{z,b}} \frac{\partial M_b}{\partial F_y} d\xi = 0 \quad (3.57)$$

Solving Equation (3.57) for the reaction force gives

$$F_y = -\frac{3L_b^2 F_x}{L_a(4L_b + \alpha L_a)} \quad (3.58)$$

A final application of unit-load method gives the  $x$  displacement.

$$\begin{aligned} \delta_x = \frac{\partial U}{\partial F_x} &= \int_0^{L_a} \frac{M_a}{EI_{z,a}} \frac{\partial M_a}{\partial F_x} d\xi + \int_0^{L_b} \frac{M_b}{EI_{z,b}} \frac{\partial M_b}{\partial F_x} d\xi \\ &= \frac{L_b^3(L_b + \alpha L_a)F_x}{3EI_{z,b}(4L_b + \alpha L_a)} \end{aligned} \quad (3.59)$$

The flexure spring constant in the  $x$ -direction (all four crab-legs) is

$$k_x = \frac{4F_x}{\delta_x} = \frac{Et w_b^3 (4L_b + \alpha L_a)}{L_b^3 (L_b + \alpha L_a)} \quad (3.60)$$

**Spring Constant in the  $y$ -direction,  $k_y$ :** The  $y$ -direction spring constant is found in an analogous manner. Now the beam is kept from moving in the  $x$ -direction ( $x = 0$ ) by the reaction force  $F_x$ .

$$\delta_x = \frac{\partial U}{\partial F_x} = \int_0^{L_a} \frac{M_a}{EI_{z,a}} \frac{\partial M_a}{\partial F_x} d\xi + \int_0^{L_b} \frac{M_b}{EI_{z,b}} \frac{\partial M_b}{\partial F_x} d\xi = 0 \quad (3.61)$$

We obtain the reaction force by solving Equation (3.61).

$$F_x = -\frac{3\alpha L_a^2 F_y}{L_b(L_b + 4\alpha L_a)} \quad (3.62)$$

Next, the  $y$ -displacement is found.

$$\begin{aligned} \delta_y = \frac{\partial U}{\partial F_y} &= \int_0^{L_a} \frac{M_a}{EI_{z,a}} \frac{\partial M_a}{\partial F_y} d\xi + \int_0^{L_b} \frac{M_b}{EI_{z,b}} \frac{\partial M_b}{\partial F_y} d\xi \\ &= \frac{L_a^3(L_b + \alpha L_a)F_y}{3EI_{z,a}(L_b + 4\alpha L_a)} \end{aligned} \quad (3.63)$$

The flexure spring constant (all four crab-legs) is

$$k_y = \frac{4F_y}{\delta_y} = \frac{Et w_a^3 (L_b + 4\alpha L_a)}{L_a^3 (L_b + \alpha L_a)} \quad (3.64)$$

The ratio of spring constants is found by dividing Equation (3.64) by Equation (3.60).

$$\frac{k_y}{k_x} = \frac{w_a^3 L_b^3}{w_b^3 L_a^3} \frac{L_b + 4\alpha L_a}{4L_b + \alpha L_a} \quad (3.65)$$

Equations (3.64) and (3.60) match analytic equations presented by Cho [71] when  $w_a \ll L_a$  and  $w_b \ll L_b$ . Cho's equations are derived from the finite-element method and include beam-shearing effects. We will present further finite-element verification of the spring constant expressions after deriving the  $z$ -directed spring constant.

**Spring Constant in the  $z$ -direction,  $k_z$ :** A free-body diagram of a crab-leg with an applied force in the  $z$  direction,  $F_z$ , is shown Figure 3.13. Strain energy from torsion must be included in the  $z$  spring constant calculation.

$$U = \int_0^L \left( \frac{M^2}{2EI_x} + \frac{T^2}{2GJ} \right) d\xi \quad (3.66)$$

where  $T$  is the torsion,  $G$  is the torsion (or shear) modulus of elasticity, and  $J$  is the torsion constant. The torsion modulus is related to Young's modulus and Poisson's ratio,  $\nu$ , by

$$G = \frac{E}{2(1+\nu)} \quad (3.67)$$

The torsion constant for a beam of rectangular cross-section is given by [72]

$$J = \frac{1}{3}t^3 w \left( 1 - \frac{192}{\pi^5} \frac{t}{w} \sum_{i=1, i \text{ odd}}^{\infty} \frac{1}{i^5} \tanh \left( \frac{i\pi w}{2t} \right) \right) \quad (3.68)$$

where  $t < w$ . If  $t > w$ , then the roles of  $t$  and  $w$  are switched in Equation (3.68). In Figure 3.14, the ratio of the torsion constant to the polar moment of inertia ( $I_p = I_x + I_z$ ) is plotted versus the aspect ratio of the rectangular cross-section. The aspect ratio is the maximum of  $w/t$  and  $t/w$ . For beams with a square cross-section,  $J/I_p = 0.843$ ; the value drops rapidly for higher aspect ratios.

The moment and torsion in each beam segment is ascertained from the free-body diagram.

$$M_a = M_o - F_z \xi \quad (3.69)$$

$$T_a = T_o \quad (3.70)$$

$$M_b = T_o - F_z \xi \quad (3.71)$$

$$T_b = M_o - F_z L_a \quad (3.72)$$

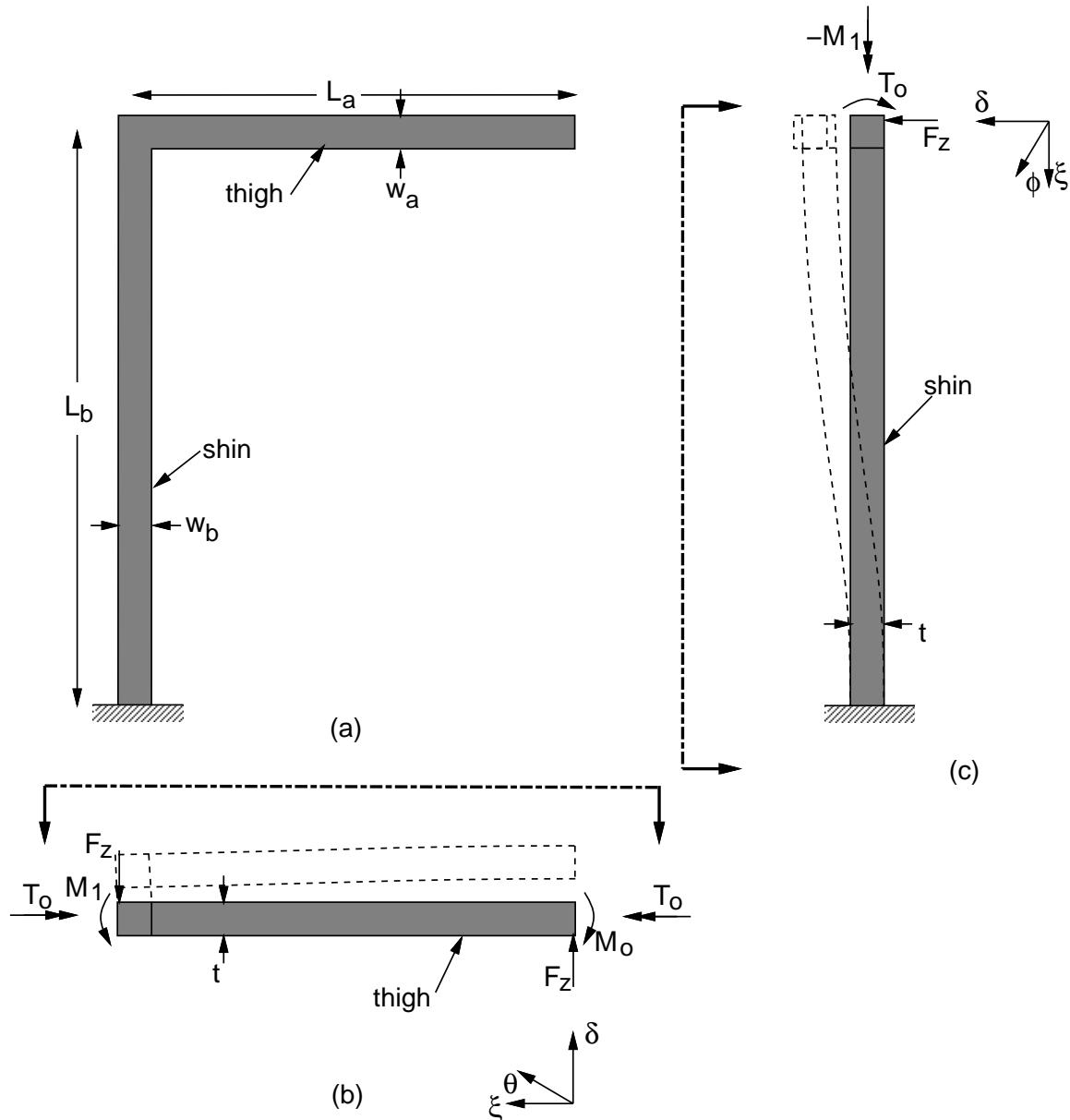


Figure 3.13: Free-body diagram of a crab-leg beam with an applied force in the  $z$  direction. Dashed outline is the displaced beam shape. (a) Plan view. (b) Side view along shin axis. (c) Side view along thigh axis.

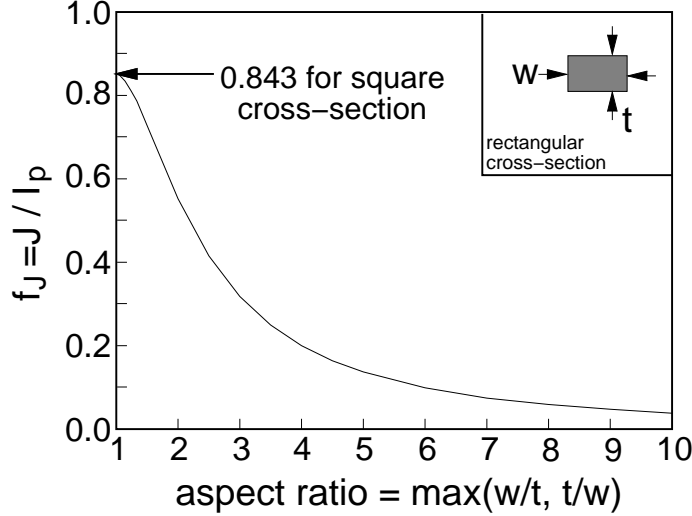


Figure 3.14: Plot of  $J/I_p$  versus the aspect ratio of the rectangular beam cross-section. A schematic of the rectangular cross-section is shown in the inset.

The guided-end constrains tilt,  $\theta_o$ , and rotation,  $\phi_o$ , at the end of the thigh.

$$\theta_o = \int_0^{L_a} \left( \frac{M_a}{EI_{x,a}} \frac{\partial M_a}{\partial M_o} + \frac{T_a}{GJ_a} \frac{\partial T_a}{\partial M_o} \right) d\xi + \int_0^{L_b} \left( \frac{M_b}{EI_{x,b}} \frac{\partial M_b}{\partial M_o} + \frac{T_b}{GJ_b} \frac{\partial T_b}{\partial M_o} \right) d\xi = 0 \quad (3.73)$$

$$\phi_o = \int_0^{L_a} \left( \frac{M_a}{EI_{x,a}} \frac{\partial M_a}{\partial T_o} + \frac{T_a}{GJ_a} \frac{\partial T_a}{\partial T_o} \right) d\xi + \int_0^{L_b} \left( \frac{M_b}{EI_{x,b}} \frac{\partial M_b}{\partial T_o} + \frac{T_b}{GJ_b} \frac{\partial T_b}{\partial T_o} \right) d\xi = 0 \quad (3.74)$$

After solving Equations (3.73) and (3.74), we substitute for  $M_o$  and  $T_o$  in Equations (3.69)–(3.72) and apply Castigliano's theorem to obtain the vertical displacement.

$$\delta_z = \int_0^{L_a} \left( \frac{M_a}{EI_{x,a}} \frac{\partial M_a}{\partial F_z} + \frac{T_a}{GJ_a} \frac{\partial T_a}{\partial F_z} \right) d\xi + \int_0^{L_b} \left( \frac{M_b}{EI_{x,b}} \frac{\partial M_b}{\partial F_z} + \frac{T_b}{GJ_b} \frac{\partial T_b}{\partial F_z} \right) d\xi \quad (3.75)$$

The  $z$ -direction spring constant for the flexure is

$$\begin{aligned} k_z &= \frac{4F_z}{\delta_z} \\ &= \frac{48S_{ea}S_{eb}(S_{gb}L_a + S_{ea}L_b)(S_{eb}L_a + S_{ga}L_b)}{\left( S_{eb}^2S_{gb}L_a^5 + 4S_{ea}S_{eb}^2L_a^4L_b + S_{eb}S_{ga}S_{gb}L_a^4L_b + 4S_{ea}S_{eb}S_{ga}L_a^3L_b^2 + \right.} \\ &\quad \left. 4S_{ea}S_{eb}S_{gb}L_a^2L_b^3 + 4S_{ea}^2S_{eb}L_aL_b^4 + S_{ea}S_{ga}S_{gb}L_aL_b^4 + S_{ea}^2S_{ga}L_b^5 \right) \end{aligned} \quad (3.76)$$

where  $S_{ea} \equiv EI_{x,a}$ ,  $S_{eb} \equiv EI_{x,b}$ ,  $S_{ga} \equiv GJ_a$ , and  $S_{gb} \equiv GJ_b$ . Although Equation (3.76) is lengthy, it is useful for numeric calculations in place of finite-element analysis.

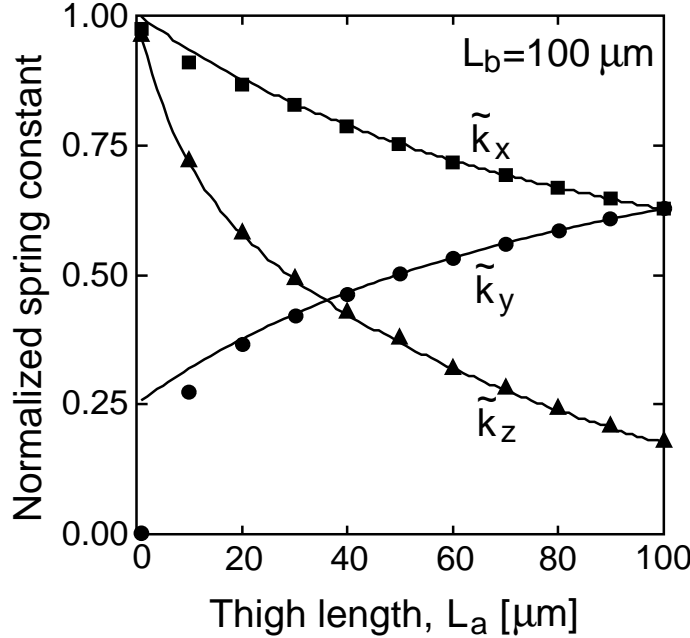


Figure 3.15: Comparison of analytic crab-leg spring constants (solid lines) with finite-element analysis (points). Spring constants are normalized (see text for normalization factor).

**Comparison with Finite Element Analysis:** Values calculated from the crab-leg spring-constant expressions are compared with finite-element calculations in Figure 3.15. The fixed parameters are:  $E = 165 \text{ GPa}$ ,  $\nu = 0.3$ ,  $w_a = w_b = t = 2\mu\text{m}$ , and  $L_b = 100 \mu\text{m}$ . Normalized spring constants in the  $x$  and  $z$  directions, ( $\tilde{k}_x$  and  $\tilde{k}_z$ ), are chosen such that the normalized values equal 1 when the thigh length is zero. The normalized spring constant in the  $y$  direction ( $\tilde{k}_y$ ) is chosen such that the normalized value equals 1 when the shin length is zero.

$$\tilde{k}_x = \frac{L_b^3}{48EI_{z,b}} k_x \quad (3.77)$$

$$\tilde{k}_y = \frac{L_a^3}{48EI_{z,a}} k_y \quad (3.78)$$

$$\tilde{k}_z = \frac{L_b^3}{48EI_{x,b}} k_z \quad (3.79)$$

Finite element calculations are performed using commercial finite-element program, ABAQUS [53]. We use a linear finite-element analysis with three-node quadratic beam elements. Ten elements are used to model the shin, ten more elements are used to

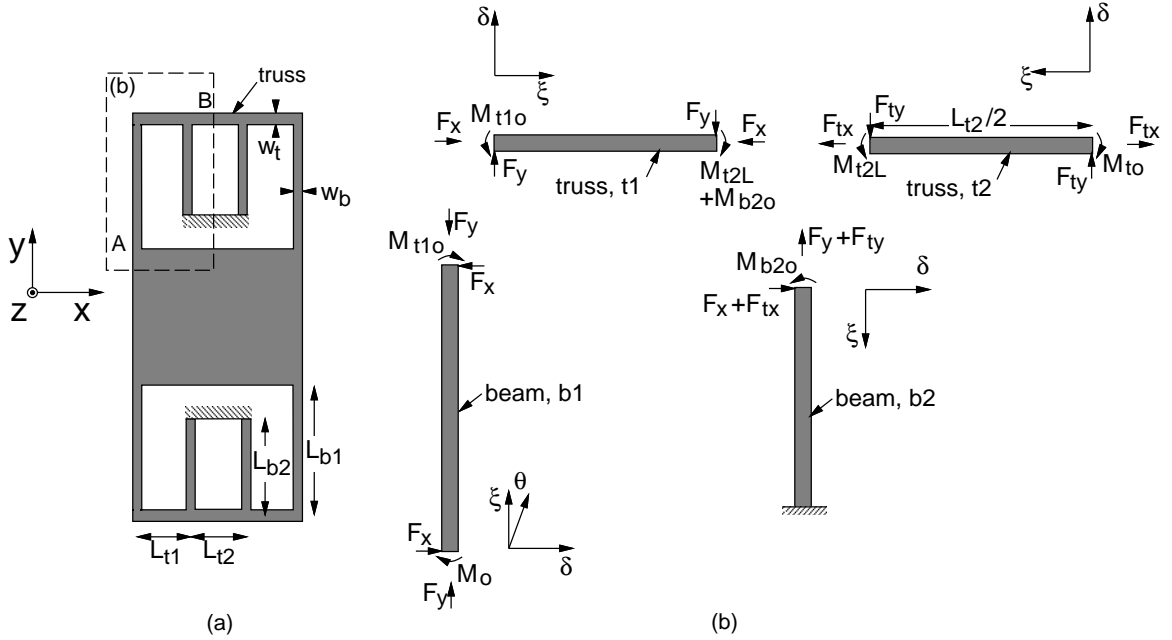


Figure 3.16: (a) Folded-flexure schematic. (b) Free-body diagram.

model the thigh. The finite-element and analytic calculations match to better than 3 % for all cases except for  $k_y$  when  $L_a < 20 \mu\text{m}$ . The effect of extensional or compressional axial stress in the shin is not included in the analytic expression for  $k_y$ . This effect becomes important for thigh lengths below  $20 \mu\text{m}$ , and explains why the finite-element calculation is smaller than the analytic calculation.

All of the spring constants decrease with increasing thigh length; the plot of  $\tilde{k}_y$  versus  $L_a$  increases because the cubic dependence on thigh length is absorbed in the normalization factor. Interpretations of Figure 3.15 are restricted to the flexure geometry used in the calculation, but are loosely applicable to flexures of similar size. The vertical spring constant is more sensitive than  $k_x$  to thigh length because torsion in the thigh has a greater affect on  $k_z$  than bending in the thigh has on  $k_x$ .

### 3.4.4.5 Spring Constants for the Folded Flexure

A schematic of the folded flexure is shown in Figure 3.16(a), and the free-body diagram is shown in (b). Only one-quarter of the flexure is necessary to include in the analysis because of the two-fold symmetry. The truss is broken into an outer section with length  $L_{t1}$  and an inner section with length,  $L_{t2}$ . We find the beam moments by applying

force and moment balance to each beam segment.

$$M_{b1} = M_o - F_x \xi \quad (3.80)$$

$$M_{b2} = -M_o + F_x L_{b1} - F_y L_{t1} - M_{to} + F_{ty} \frac{L_{t2}}{2} - (F_x + F_{tx}) \xi \quad (3.81)$$

$$M_{t1} = -M_o + F_x L_{b1} - F_y \xi \quad (3.82)$$

$$M_{t2} = M_{to} - F_{ty} \xi \quad (3.83)$$

Orientation of the integration coordinates for each beam segment is arbitrary. We select each coordinate origin such that the beam moment results in the simplest expression.

**Spring Constant in the  $x$ -direction,  $k_x$ :** Boundary conditions are found for one-quarter of the folded flexure by using symmetry. Referring to Figure 3.16, point A of the flexure has a guided-end condition. The angle  $\theta_o$  and the  $y$ -directed motion are constrained to zero.

$$\delta_y = \frac{\partial U}{\partial F_y} = 0 \quad (3.84)$$

$$\theta_o = \frac{\partial U}{\partial M_o} = 0 \quad (3.85)$$

$$\delta_x = \frac{\partial U}{\partial F_x} \quad (3.86)$$

Point B of the flexure has a rolling-pin condition, where the moment and  $x$ -directed force are zero and the  $y$ -directed motion is constrained to zero.

$$M_{to} = 0 \quad (3.87)$$

$$F_{tx} = 0 \quad (3.88)$$

$$\delta_{ty} = \frac{\partial U}{\partial F_{ty}} = 0 \quad (3.89)$$

We obtain the spring constant for the flexure by solving Equations (3.85)–(3.89).

$$\begin{aligned} k_x &= \frac{4F_x}{\delta_x} \\ &= \frac{24EI_{z,t}}{L_{b1}^3} \left( \frac{12\alpha^2(2\tilde{L}_{t1} + \tilde{L}_{t2})\tilde{L}_{b2} + 6\alpha\tilde{L}_{b2}\tilde{L}_{t1}^2 + 4\alpha\tilde{L}_{t1}\tilde{L}_{t2}(1 + \tilde{L}_{b2}) + \tilde{L}_{t1}^2\tilde{L}_{t2}}{6\alpha^2\tilde{L}_{b2}(2\tilde{L}_{t1} + \tilde{L}_{t2})(1 + \tilde{L}_{b2}^3) + \alpha(3\tilde{L}_{b2}\tilde{L}_{t1}^2(4 + \tilde{L}_{b2}^3) + 2\tilde{L}_{t1}\tilde{L}_{t2}(\tilde{L}_{b2}^4 + 4\tilde{L}_{b2}^3 + 3\tilde{L}_{b2}^2 + 4\tilde{L}_{b2} + 1)) + 2\tilde{L}_{t1}^2\tilde{L}_{t2}(1 + \tilde{L}_{b2}^3)} \right) \end{aligned} \quad (3.90)$$

where  $\alpha = I_{z,t}/I_{z,b}$ ,  $\tilde{L}_{b2} = L_{b2}/L_{b1}$ ,  $\tilde{L}_{t1} = L_{t1}/L_{b1}$ , and  $\tilde{L}_{t2} = L_{t2}/L_{b1}$ .

When the beam lengths and truss segment lengths are equal ( $L_b = L_{b1} = L_{b2}$  and  $L_t = L_{t1} = L_{t2}$ ), Equation (3.90) reduces to

$$k_x = \frac{24EI_{z,b}}{L_b^3} \frac{\tilde{L}_t^2 + 14\tilde{L}_t\alpha + 36\alpha^2}{4\tilde{L}_t^2 + 41\tilde{L}_t\alpha + 36\alpha^2}. \quad (3.91)$$

where  $\tilde{L}_t = L_t/L_b$ . In the limit of a very stiff truss ( $I_{z,t} \gg I_{z,b}$ ), Equation (3.91) reduces to the spring constant equation used by Tang [54]:  $k_x = 24EI_{z,b}/L_b^3$ .

**Spring Constant in the  $y$ -direction,  $k_y$ :** We use Figure 3.16 to identify the boundary conditions from symmetry. Point A of the flexure has a guided-end condition, but now the angle  $\theta_o$  and the  $x$ -directed motion are constrained to zero.

$$\delta_x = \frac{\partial U}{\partial F_x} = 0 \quad (3.92)$$

$$\theta_o = \frac{\partial U}{\partial M_o} = 0 \quad (3.93)$$

$$\delta_y = \frac{\partial U}{\partial F_y} \quad (3.94)$$

Point B of the flexure also has a guided-end condition, where the  $y$ -directed force is zero and the  $x$ -directed motion and angle  $\theta_{to}$  are constrained to zero.

$$F_{ty} = 0 \quad (3.95)$$

$$\delta_{tx} = \frac{\partial U}{\partial F_{tx}} = 0 \quad (3.96)$$

$$\theta_{to} = \frac{\partial U}{\partial M_{to}} = 0 \quad (3.97)$$

The resulting  $y$ -directed spring constant for the entire folded-flexure is

$$k_y = \frac{24EI_{z,t}\tilde{L}_{t1}}{L_{t1}^3} \frac{\alpha^2\tilde{L}_{b2} + 2\alpha(\tilde{L}_{t2} + \tilde{L}_{b2}(2\tilde{L}_{t1} + \tilde{L}_{t2})) + 8\tilde{L}_{t1}\tilde{L}_{t2}}{\alpha^2\tilde{L}_{b2}(2\tilde{L}_{t1} + 3\tilde{L}_{t2}) + 2\alpha\tilde{L}_{t1}(2\tilde{L}_{t2}(1 + \tilde{L}_{b2}) + \tilde{L}_{t1}\tilde{L}_{b2}) + 4\tilde{L}_{t1}^2\tilde{L}_{t2}} \quad (3.98)$$

When  $L_b = L_{b1} = L_{b2}$  and  $L_t = L_{t1} = L_{t2}$ , Equation (3.98) reduces to

$$k_y = \frac{24EI_{z,t}}{L_t^3} \frac{8\tilde{L}_t^2 + 8\tilde{L}_t\alpha + \alpha^2}{4\tilde{L}_t^2 + 10\tilde{L}_t\alpha + 5\alpha^2}. \quad (3.99)$$

In the limit of a very stiff beams ( $I_{z,b} \gg I_{z,t}$ ), Equation (3.99) reduces to that of the fixed-fixed flexure (given by Equation (3.50)):  $k_y = 48EI_{z,t}/L_t^3$ . When the truss is much stiffer than the beams ( $I_{z,t} \gg I_{z,b}$ ), the spring constant becomes  $k_y = 4.8EI_{z,t}/L_t^3$ . The  $y$ -directed

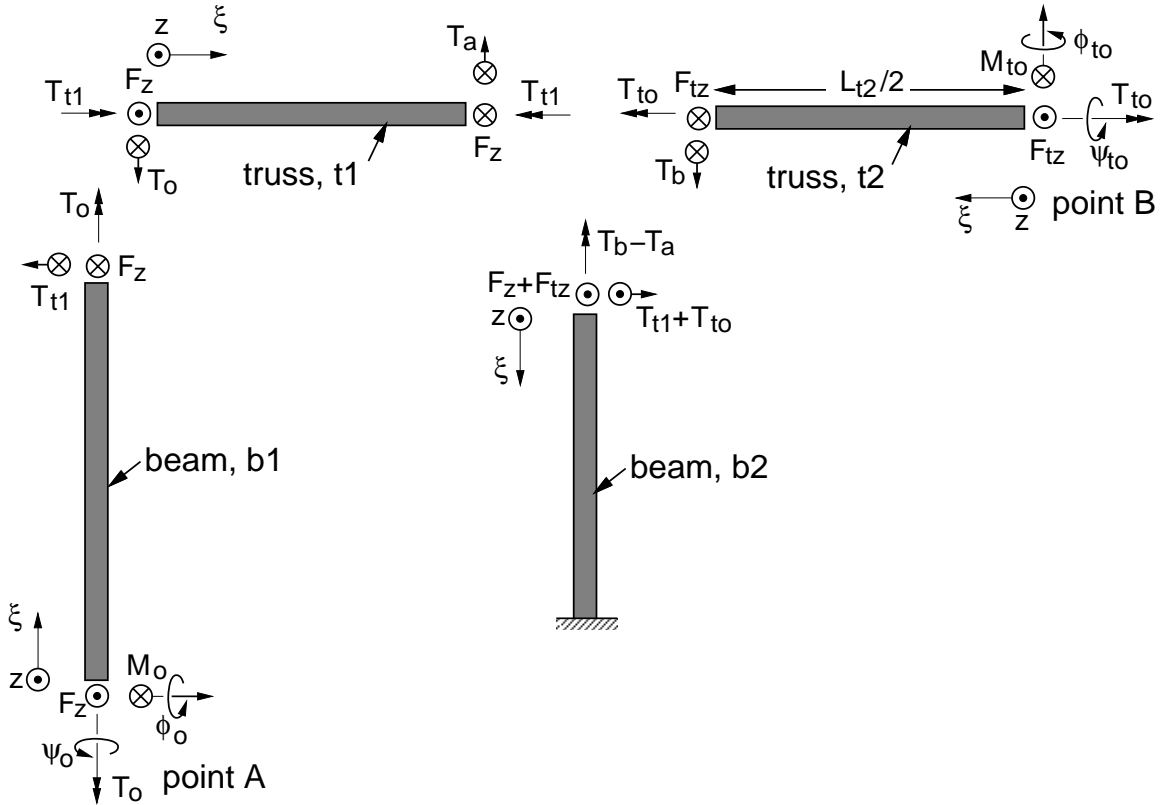


Figure 3.17: Folded-flexure free-body diagram for calculation of the  $z$ -directed spring constant.

spring constant is ten times more compliant than the value in the fixed-fixed flexure case. An accurate calculation of  $k_y$  for flexures with very stiff trusses must include axial extension and compression in the beams in addition to bending of the truss. Additionally, for very stiff trusses,  $k_y$  will decrease with increasing displacement in the  $x$  direction; this dependence of  $k_y$  on  $x$  must be included in an accurate model.

**Spring Constant in the  $z$ -direction,  $k_z$ :** A free-body diagram for calculation of the  $z$ -directed spring constant is given in Figure 3.17. A special notation is used for moments twisting out of the  $x$ - $y$  plane. The arrows in the symbols  $\odot$  and  $\oslash$  represent the moment's axis of rotation using the right-hand rule. Force, moment, and torque balance are applied to each beam segment. The resulting moment and torque expressions are:

$$M_{b1} = M_o - F_z \xi \quad (3.100)$$

$$T_{b1} = T_o \quad (3.101)$$

$$M_{b2} = M_o - F_z L_{b1} + T_{to} + (F_z + F_{tz})\xi \quad (3.102)$$

$$T_{b2} = M_{to} - F_{tz} \frac{L_{t2}}{2} - T_o + F_z L_{t1} \quad (3.103)$$

$$M_{t1} = T_o - F_z \xi \quad (3.104)$$

$$T_{t1} = M_o - F_z L_{b1} \quad (3.105)$$

$$M_{t2} = M_{to} - F_{zt} \xi \quad (3.106)$$

$$T_{t2} = T_{to} \quad (3.107)$$

Boundary conditions are found from flexure symmetry. The rotation angles,  $\phi_o$  and  $\psi_o$ , are constrained to zero at the guided-end of the flexure (point A in Figure 3.17). One of the rotation angles,  $\phi_{to}$ , is constrained to zero at point B.

$$\phi_o = \frac{\partial U}{\partial M_o} = 0 \quad (3.108)$$

$$\psi_o = \frac{\partial U}{\partial T_o} = 0 \quad (3.109)$$

$$\phi_{to} = \frac{\partial U}{\partial M_{to}} = 0 \quad (3.110)$$

$$T_{to} = 0 \quad (3.111)$$

$$F_{tz} = 0 \quad (3.112)$$

$$\delta_z = \frac{\partial U}{\partial F_x} \quad (3.113)$$

We now solve the boundary condition equations and determine the spring constant.

$$k_z = \frac{\frac{48S_{eb}}{L_b^3} \left\{ S_{et} (S_{gt} + S_{gt}\tilde{L}_{b2} + S_{eb}\tilde{L}_{t1}) \times \right.}{\left. (2S_{et}^2\tilde{L}_{b2} + 2S_{et}S_{gb}\tilde{L}_{b2}\tilde{L}_{t1} + S_{et}S_{gb}\tilde{L}_{t2} + S_{et}S_{gb}\tilde{L}_{b2}\tilde{L}_{t2} + S_{gb}^2\tilde{L}_{t1}\tilde{L}_{t2}) \right\}}{\left\{ 2S_{et}^3S_{gt}\tilde{L}_{b2} + 8S_{et}^3S_{gt}\tilde{L}_{b2}^2 - 12S_{et}^3S_{gt}\tilde{L}_{b2}^3 + 8S_{et}^3S_{gt}\tilde{L}_{b2}^4 + 2S_{et}^3S_{gt}\tilde{L}_{b2}^5 + \right.} \\ \left. 8S_{eb}S_{et}^3\tilde{L}_{b2}\tilde{L}_{t1} + 2S_{et}^2S_{gb}S_{gt}\tilde{L}_{b2}\tilde{L}_{t1} + 8S_{et}^2S_{gb}S_{gt}\tilde{L}_{b2}^2\tilde{L}_{t1} - 12S_{et}^2S_{gb}S_{gt}\tilde{L}_{b2}^3\tilde{L}_{t1} + \right. \\ \left. 8S_{eb}S_{et}^3\tilde{L}_{b2}^4\tilde{L}_{t1} + 8S_{et}^2S_{gb}S_{gt}\tilde{L}_{b2}^4\tilde{L}_{t1} + 2S_{et}^2S_{gb}S_{gt}\tilde{L}_{b2}^5\tilde{L}_{t1} + 8S_{eb}S_{et}^2S_{gb}\tilde{L}_{b2}\tilde{L}_{t1}^2 + \right. \\ \left. 8S_{eb}S_{et}^2S_{gb}\tilde{L}_{b2}^4\tilde{L}_{t1}^2 + 8S_{eb}S_{et}^2S_{gt}\tilde{L}_{b2}\tilde{L}_{t1}^3 + 8S_{eb}S_{et}^2S_{gt}\tilde{L}_{b2}^2\tilde{L}_{t1}^3 + 8S_{eb}^2S_{et}^2\tilde{L}_{b2}\tilde{L}_{t1}^4 + \right. \\ \left. 2S_{eb}S_{et}S_{gb}S_{gt}\tilde{L}_{b2}\tilde{L}_{t1}^4 + 2S_{eb}S_{et}S_{gb}S_{gt}\tilde{L}_{b2}^2\tilde{L}_{t1}^4 + 2S_{eb}^2S_{et}S_{gb}\tilde{L}_{b2}\tilde{L}_{t1}^5 + \right. \\ \left. S_{et}^2S_{gb}S_{gt}\tilde{L}_{b2}\tilde{L}_{t2} + 5S_{et}^2S_{gb}S_{gt}\tilde{L}_{b2}\tilde{L}_{t2} - 2S_{et}^2S_{gb}S_{gt}\tilde{L}_{b2}^2\tilde{L}_{t2} - 2S_{et}^2S_{gb}S_{gt}\tilde{L}_{b2}^3\tilde{L}_{t2} + \right. \\ \left. 5S_{et}^2S_{gb}S_{gt}\tilde{L}_{b2}^4\tilde{L}_{t2} + S_{et}^2S_{gb}S_{gt}\tilde{L}_{b2}^5\tilde{L}_{t2} + 4S_{eb}S_{et}^2S_{gb}\tilde{L}_{t1}\tilde{L}_{t2} + \right. \\ \left. S_{et}S_{gb}^2S_{gt}\tilde{L}_{t1}\tilde{L}_{t2} + 4S_{eb}S_{et}^2S_{gb}\tilde{L}_{b2}\tilde{L}_{t1}\tilde{L}_{t2} + 4S_{et}S_{gb}^2S_{gt}\tilde{L}_{b2}\tilde{L}_{t1}\tilde{L}_{t2} - \right. \\ \left. 6S_{et}S_{gb}^2S_{gt}\tilde{L}_{b2}^2\tilde{L}_{t1}\tilde{L}_{t2} + 4S_{eb}S_{et}^2S_{gb}\tilde{L}_{b2}^3\tilde{L}_{t1}\tilde{L}_{t2} + 4S_{et}S_{gb}^2S_{gt}\tilde{L}_{b2}^3\tilde{L}_{t1}\tilde{L}_{t2} + \right. \\ \left. 4S_{eb}S_{et}^2S_{gb}\tilde{L}_{b2}^4\tilde{L}_{t1}\tilde{L}_{t2} + S_{et}S_{gb}^2S_{gt}\tilde{L}_{b2}^4\tilde{L}_{t1}\tilde{L}_{t2} + 4S_{eb}S_{et}S_{gb}^2\tilde{L}_{t1}^2\tilde{L}_{t2} + \right. \\ \left. 12S_{eb}S_{et}^2S_{gt}\tilde{L}_{b2}\tilde{L}_{t1}^2\tilde{L}_{t2} + 12S_{eb}S_{et}^2S_{gt}\tilde{L}_{b2}^2\tilde{L}_{t1}^2\tilde{L}_{t2} + 4S_{eb}S_{et}S_{gb}^2\tilde{L}_{b2}^3\tilde{L}_{t1}^2\tilde{L}_{t2} + \right. \\ \left. 4S_{eb}S_{et}S_{gb}S_{gt}\tilde{L}_{t1}^3\tilde{L}_{t2} + 12S_{eb}S_{et}^2\tilde{L}_{b2}\tilde{L}_{t1}^3\tilde{L}_{t2} + 8S_{eb}S_{et}S_{gb}S_{gt}\tilde{L}_{b2}\tilde{L}_{t1}^3\tilde{L}_{t2} + \right. \\ \left. 4S_{eb}S_{et}S_{gb}S_{gt}\tilde{L}_{b2}^2\tilde{L}_{t1}^3\tilde{L}_{t2} + 4S_{eb}^2S_{et}S_{gb}\tilde{L}_{t1}^4\tilde{L}_{t2} + S_{eb}S_{gb}^2S_{gt}\tilde{L}_{t1}^4\tilde{L}_{t2} + \right. \\ \left. 4S_{eb}^2S_{et}S_{gb}\tilde{L}_{b2}\tilde{L}_{t1}^4\tilde{L}_{t2} + S_{eb}S_{gb}^2S_{gt}\tilde{L}_{b2}\tilde{L}_{t1}^4\tilde{L}_{t2} + S_{eb}^2S_{gb}^2\tilde{L}_{t1}^5\tilde{L}_{t2} \right\} \quad (3.114)$$

where  $S_{eb} \equiv EI_{x,b}$ ,  $S_{et} \equiv EI_{x,t}$ ,  $S_{gb} \equiv GJ_b$ , and  $S_{gt} \equiv GJ_t$ .

When the beam lengths and truss segment lengths are equal ( $L_b = L_{b1} = L_{b2}$  and  $L_t = L_{t1} = L_{t2}$ ), Equation (3.114) reduces to

$$k_z = \frac{48S_{eb}}{L_b^3} \frac{S_{et} (2S_{gt} + S_{eb}\tilde{L}_t) (2S_{et}^2 + 4S_{et}S_{gb}\tilde{L}_t + S_{gb}^2\tilde{L}_t^2)}{\left\{ \begin{array}{l} 8S_{et}^3S_{gt} + 16S_{et}^2(S_{eb}S_{et} + S_{gb}S_{gt})\tilde{L}_t + 4S_{et}S_{gb}(8S_{eb}S_{et} + S_{gb}S_{gt})\tilde{L}_t^2 + \\ 8S_{eb}S_{et}(S_{gb}^2 + 5S_{et}S_{gt})\tilde{L}_t^3 + 20S_{eb}S_{et}(S_{eb}S_{et} + S_{gb}S_{gt})\tilde{L}_t^4 + \\ 2S_{eb}S_{gb}(5S_{eb}S_{et} + S_{gb}S_{gt})\tilde{L}_t^5 + S_{eb}^2S_{gb}^2\tilde{L}_t^6 \end{array} \right\}} \quad (3.115)$$

In the limit of a very stiff truss ( $I_{x,t} \gg I_{x,b}$ ) Equation (3.115) reduces to  $k_z = 24EI_{x,b}/L_b^3$ .

**Comparison with Finite Element Analysis:** Values calculated from the folded-flexure spring-constant expressions are compared with finite-element calculations in Figure 3.18. The fixed parameters are:  $E = 165$  GPa,  $\nu = 0.3$ ,  $w_b = t = 2\mu\text{ m}$ ,  $L_t = 40\text{ }\mu\text{m}$ , and  $L_b = 100\text{ }\mu\text{m}$ . Normalized spring constants in the  $x$  and  $z$  directions, ( $\tilde{k}_x$  and  $\tilde{k}_z$ ), are

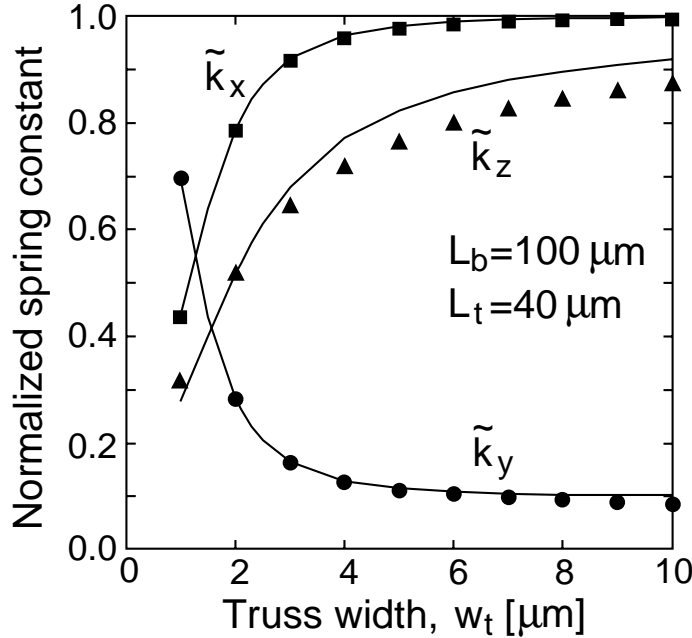


Figure 3.18: Comparison of analytic folded-flexure spring constants (solid lines) with finite-element analysis (points). Spring constants are normalized (see text for normalization factors).

chosen such that their values approach 1 when the truss is much stiffer than the beams. The normalized spring constant in the  $y$  direction ( $\tilde{k}_y$ ) is chosen such that its value approaches 1 when the beams are much stiffer than the truss.

$$\tilde{k}_x = \frac{L_b^3}{24EI_{z,b}} k_x \quad (3.116)$$

$$\tilde{k}_y = \frac{L_t^3}{48EI_{z,t}} k_y \quad (3.117)$$

$$\tilde{k}_z = \frac{L_b^3}{24EI_{x,b}} k_z \quad (3.118)$$

Finite element calculations are performed using commercial finite-element program, ABAQUS [53]. We use a linear finite-element analysis with three-node quadratic beam elements. Four elements are used to model each of the beam and truss segments. The finite-element and analytic calculations match to better than 0.5 % for  $k_x$ , 1 % for  $k_y$  when  $w_t < 6 \mu\text{m}$ , and 0.5 % for  $k_z$  when  $t = w_t$ . The effect of stress from extension or compression in the shin is not included in the analytic expression for  $k_y$ . The effect of stress from beam extension or compression becomes important for truss widths above 6  $\mu\text{m}$ , and

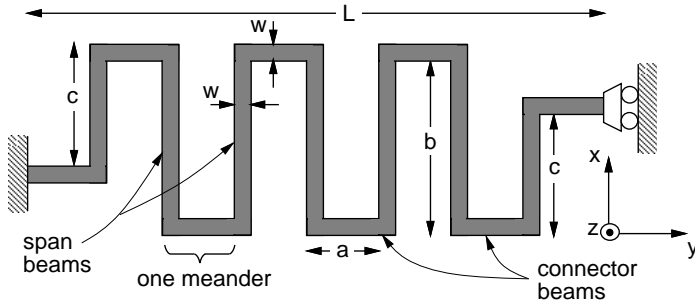


Figure 3.19: Serpentine spring schematic.

explains why the finite-element calculation of  $k_y$  is smaller than the analytic calculation. For larger truss widths, the analytic  $k_z$  calculation is greater than the finite-element values by about 7 %. However, the analytic equation for  $k_z$  is very accurate for trusses with square cross-sections, even trusses that are much stiffer than the beams.

All of the spring constants increase with increasing truss width; the plot of  $\tilde{k}_y$  versus  $w_t$  decreases because the cubic dependence on truss width is absorbed in the normalization factor. As we noted earlier when deriving  $k_y$ , the normalized spring constant approaches 0.1 for very stiff trusses, however the axial stress in the beams must be included in this regime.

### 3.4.4.6 Spring Constants for the Serpentine Flexure

The serpentine flexure in Figure 3.9(d) is made of four serpentine springs. A schematic of a spring is shown in Figure 3.19. Serpentine springs get their name from the meandering snake-like pattern of the beam segments. Each meander is of length  $a$ , and width  $b$ , except for the first and last meanders, which are of width  $c$ . The beam segments that span the meander width are called span beams, or spans. The beam segments that connect the spans are called connector beams, or connectors. In some spring designs, the width of the first and last meanders is half that of the other meanders ( $c = b/2$ ) [73]. An optical microshutter uses serpentine meanders made of two beams across the width and connected by a rigid truss [74]. In the following spring-constant analysis, we assume that all spans are equal ( $c = b$ ). This kind of serpentine spring is used in the integrated testbed, described in chapter 4. Because of the flexure symmetry, the end of the spring has a guided-end boundary condition, where only motion in the preferred direction is allowed.

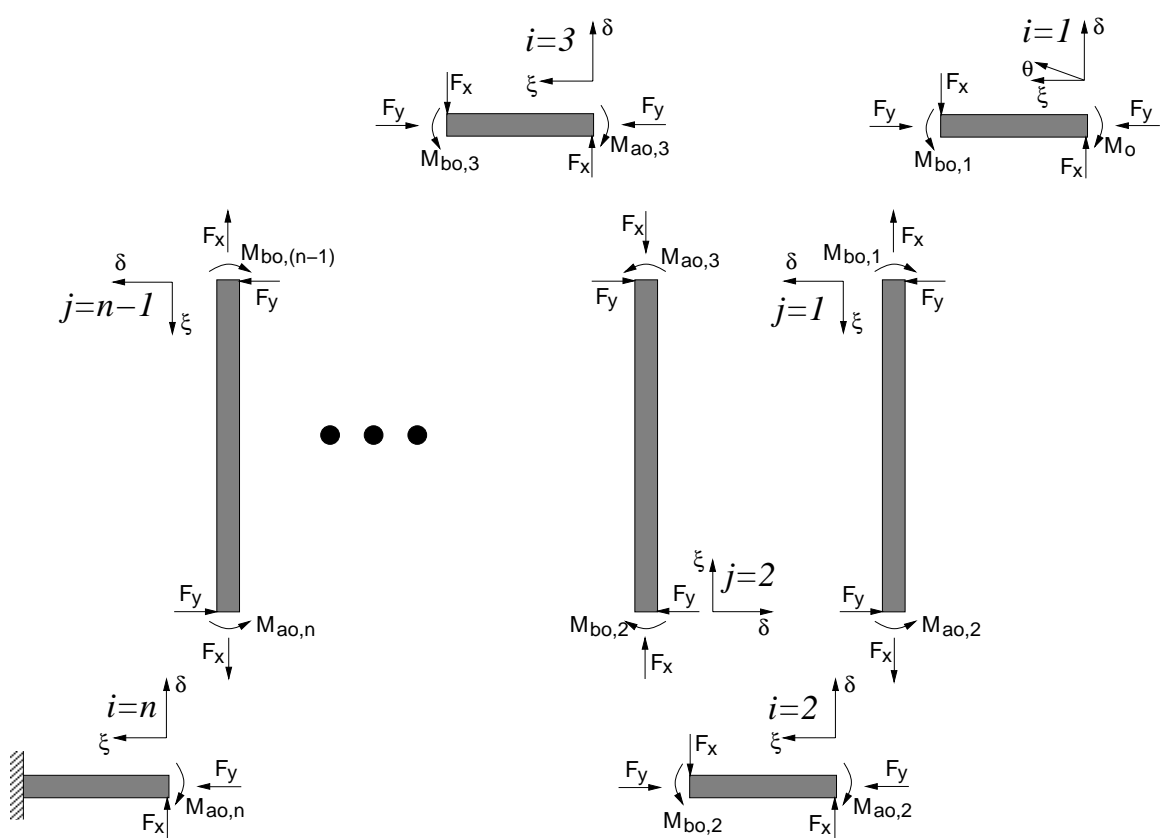


Figure 3.20: Free-body diagram of a serpentine spring.

A free body diagram of a serpentine spring with  $n$  meanders is shown in Figure 3.20. The connector beams are indexed from  $i = 1$  to  $n$  and the span beams are indexed from  $j = 1$  to  $n-1$ .

The moment of each beam segment is deduced from the free body diagram.

$$\begin{aligned} M_{a,i} &= M_o - F_x [\xi + (i-1)a] - \left(\frac{1+(-1)^i}{2}\right) F_y b \quad ; i = 1 \text{ to } n \\ M_{b,j} &= M_o - jF_x a + F_y \left[(-1)^j \xi - \left(\frac{1+(-1)^j}{2}\right) b\right] \quad ; j = 1 \text{ to } n-1 \end{aligned} \quad (3.119)$$

$M_{a,i}$  is the moment of the  $i$ th connector, where  $i = 1$  at the guided-end of the spring.  $M_{b,j}$  is the moment of the  $j$ th span, where  $j = 1$  at the guided-end of the spring. The total energy in the serpentine spring is

$$U = \sum_{i=1}^n \int_0^a \frac{M_{a,i}^2}{2EI_{z,a}} d\xi + \sum_{j=1}^{n-1} \int_0^b \frac{M_{b,j}^2}{2EI_{z,b}} d\xi \quad (3.120)$$

An alternative moment,  $M'_{b,j}$ , is used in place of  $M_{b,j}$  to provide a simpler calculation of the second integral in Equation 3.119.

$$\int_0^b \frac{M_{b,j}^2}{2EI_{z,b}} d\xi = \int_0^b \frac{(M'_{b,j})^2}{2EI_{z,b}} d\xi \quad (3.121)$$

where  $M'_{b,j} = M_o - F_x ja - F_y \xi$ .

When determining the  $x$ -directed spring constant, displacement of the spring end in the  $y$ -direction ( $\delta_y$ ) and rotation of the spring end ( $\theta_o$ ) are constrained to be zero. Application of Castigliano's second theorem produces three equations in three unknown variables ( $F_x$ ,  $M_o$ , and  $\delta_x$ ).

$$\delta_y = \frac{\partial U}{\partial F_y} = 0 \quad (3.122)$$

$$\theta_o = \frac{\partial U}{\partial M_o} = 0 \quad (3.123)$$

$$\delta_x = \frac{\partial U}{\partial F_x} \quad (3.124)$$

The partial derivative is brought inside the integrals of Equation (3.120) to simplify the calculations, as done in previous sections. The flexure spring constant (four springs) is  $k_x = 4F_x/\delta_x$ . A similar procedure yields the  $y$ -directed spring constant, but now displacement of the spring end in the  $x$ -direction is constrained to zero.

For even  $n$ ,

$$k_x = \frac{48EI_{z,b}[(3\tilde{a} + b)n - b]}{a^2n[(3\tilde{a}^2 + 4\tilde{a}b + b^2)n^3 - 2b(5\tilde{a} + 2b)n^2 + (5b^2 + 6\tilde{a}b - 9\tilde{a}^2)n - 2b^2]} \quad (3.125)$$

$$k_y = \frac{48EI_{z,b}[(\tilde{a}+b)n^2 - 3bn + 2b]}{b^2[(3\tilde{a}^2 + 4\tilde{a}b + b^2)n^3 - 2b(5\tilde{a} + 2b)n^2 + (5b^2 + 6\tilde{a}b - 9\tilde{a}^2)n - 2b^2]} \quad (3.126)$$

where  $\tilde{a} \equiv I_{z,b}a/I_{z,a}$ .

For odd  $n$ ,

$$k_x = \frac{48EI_{z,b}}{a^2n[(\tilde{a}+b)n^2 - 3bn + 2b]} \quad (3.127)$$

$$k_y = \frac{48EI_{z,b}[(\tilde{a}+b)n - b]}{b^2(n-1)[(3\tilde{a}^2 + 4\tilde{a}b + b^2)n + 3\tilde{a}^2 - b^2]} \quad (3.128)$$

Simpler spring constant equations for large  $n$ , defined as  $n \gg 3b/(\tilde{a} + b)$ , are

$$k_x \approx \frac{48EI_{z,b}}{a^2(\tilde{a}+b)n^3} \quad (3.129)$$

$$k_y \approx \frac{48EI_{z,b}}{b^2(3\tilde{a}+b)n} \quad (3.130)$$

The ratio of the lateral spring constants, for large  $n$ , is proportional to  $n^2$ .

$$\frac{k_y}{k_x} = \frac{\tilde{a}+b}{3\tilde{a}+b} \left( \frac{an}{b} \right)^2 \quad (3.131)$$

Values for the spring constant ratio can be approximated by the square of the ratio of projected spring length divided by spring width,  $(an/b)^2$ , for  $b \gg 3\tilde{a}$ .

Calculation of the  $z$ -directed spring constant requires a different free-body diagram, shown in Figure 3.21. The rotation angles,  $\phi_o$  and  $\psi_o$ , are constrained by the guided-end condition. Torsion and moment of each beam segment are

$$\begin{aligned} M_{a,i} &= M_o - F_z[\xi + (i-1)a] & ; i = 1 \text{ to } n \\ T_{a,i} &= T_o + \left( \frac{1+(-1)^i}{2} \right) F_z b & ; i = 1 \text{ to } n \\ M_{b,j} &= (-1)^j T_o - F_z \xi + \left( \frac{1+(-1)^j}{2} \right) F_z b & ; j = 1 \text{ to } n-1 \\ T_{b,j} &= (-1)^j (iF_z a - M_o) & ; j = 1 \text{ to } n-1 \end{aligned} \quad (3.132)$$

where  $T_{a,i}$  is the torsion of the  $i$ th connector and  $T_{b,j}$  is the torsion of the  $j$ th span. Alternative expressions for moment and torsion, used in place of  $M_{b,j}$  and  $T_{b,j}$ , give equivalent results in the energy integral and simplify the calculations.

$$M'_{b,j} = T_o + F_z \xi \quad (3.133)$$

$$T'_{b,j} = M_o - jF_z a \quad (3.134)$$

The total energy in the serpentine spring is

$$U = \sum_{i=1}^n \int_0^a \left( \frac{M_{a,i}^2}{2EI_{x,a}} + \frac{T_{a,i}^2}{2GJ_a} \right) d\xi + \sum_{j=1}^{n-1} \int_0^b \left( \frac{M_{b,j}^2}{2EI_{x,b}} + \frac{T_{b,j}^2}{2GJ_b} \right) d\xi \quad (3.135)$$

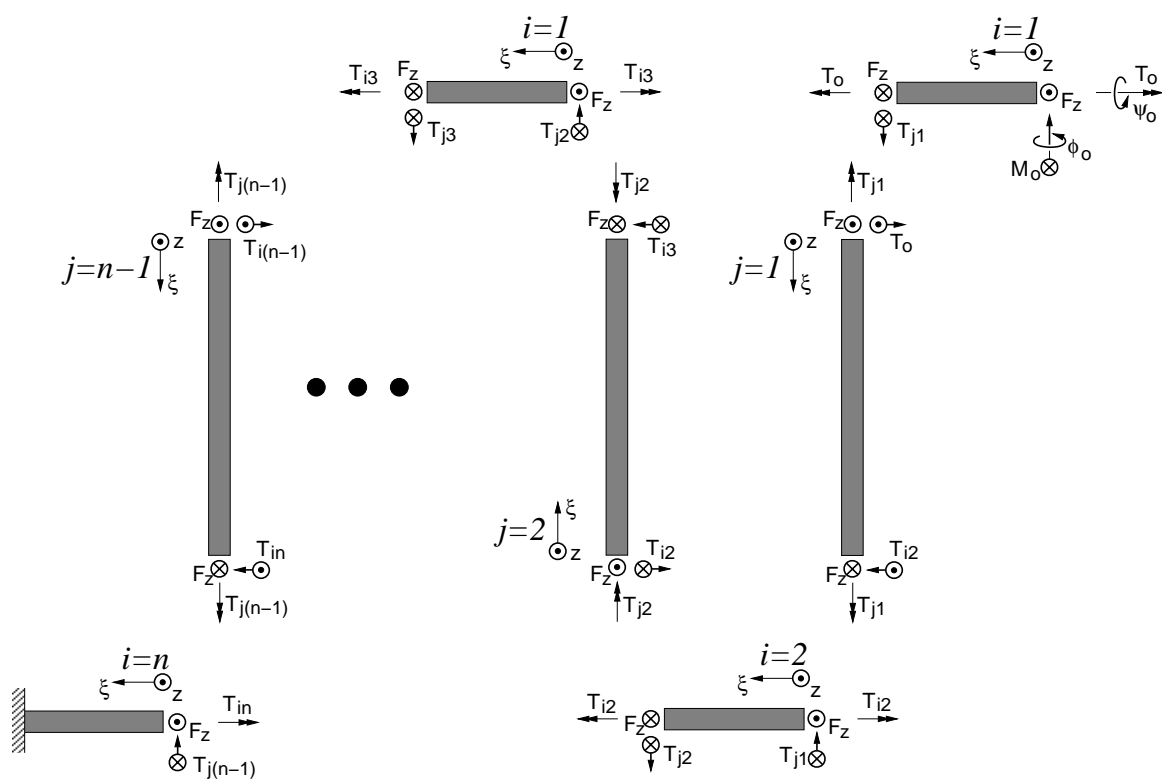


Figure 3.21: Free-body diagram of a serpentine spring with an applied force in the  $z$  direction.

We find  $\delta_z$  by solving the three simultaneous equations:

$$\phi_0 = \frac{\partial U}{\partial M_o} = 0 \quad (3.136)$$

$$\psi_o = \frac{\partial U}{\partial T_o} = 0 \quad (3.137)$$

$$\delta_z = \frac{\partial U}{\partial F_z} \quad (3.138)$$

The  $z$ -direction spring constant for the flexure is  $k_z = 4F_z/\delta_z$ . For  $n$  even,

$$k_z = \frac{48S_{ea}S_{eb}S_{ga}S_{gb}}{\left\{ S_{eb}S_{ga}a^2(S_{gb}a + S_{ea}b)n^3 - 3S_{ea}S_{eb}S_{ga}a^2bn^2 + S_{ea}b(2S_{eb}S_{ga}a^2 + 3S_{eb}S_{gb}ab + S_{ga}S_{gb}b^2)n - S_{ea}S_{ga}S_{gb}b^3 \right\}} \quad (3.139)$$

where  $S_{ea} \equiv EI_{x,a}$ ,  $S_{eb} \equiv EI_{x,b}$ ,  $S_{ga} \equiv GJ_a$ , and  $S_{gb} \equiv GJ_b$ . For  $n$  odd,

$$k_z = \frac{48S_{ea}S_{eb}S_{ga}S_{gb}(S_{ga}b(n-1) + S_{eb}an)}{\left\{ S_{eb}S_{ga}a^2(S_{eb}S_{gb}a^2 + (S_{ea}S_{eb} + S_{ga}S_{gb})ab + S_{ea}S_{ga}b^2)n^4 - S_{eb}S_{ga}a^2b((3S_{ea}S_{eb} + S_{ga}S_{gb})a + 4S_{ea}S_{ga}b)n^3 + S_{ea}b(2S_{eb}^2S_{ga}a^3 + (5S_{eb}S_{ga}^2 + 3S_{eb}^2S_{gb})a^2b + 4S_{eb}S_{ga}S_{gb}ab^2 + S_{ga}^2S_{gb}b^3)n^2 - 2S_{ea}S_{ga}b^2(S_{eb}S_{ga}a^2 + 2S_{eb}S_{gb}ab + S_{ga}S_{gb}b^2)n + S_{ea}S_{gb}b^2(S_{ga}^2b^2 - 3S_{eb}^2a^2) \right\}} \quad (3.140)$$

The spring constant equation is simplified for  $n \gg 3b/((GJ_b/EI_{x,a})a + b)$ .

$$k_z \approx \frac{48GJ_b}{a^2((GJ_b/EI_{x,a})a + b)n^3} \quad (3.141)$$

For large  $n$ , the spring constant ratio is

$$\frac{k_z}{k_x} = \frac{GJ_b((I_{z,b}/I_{z,a})a + b)}{EI_{z,b}((GJ_b/EI_{x,a})a + b)} \quad (3.142)$$

For  $a \gg b$ , the ratio approaches the value for a cantilever beam:  $k_z/k_x = I_{x,a}/I_{z,a}$ . If  $b \gg a$ , the ratio is  $k_z/k_x = f_{J,b}(I_{x,b}/I_{z,b} + 1)/2/(1 + \nu)$ , where  $f_{J,b}$  is the torsion form factor for the span beams. The ratio must lie between these two limits. The only effective way to adjust  $k_z/k_x$  is by changing the vertical to lateral stiffness ratio of the dominant beams. The stiffness ratio is insensitive to changes in the span or connector beam lengths.

**Comparison with Finite Element Analysis:** Values calculated from the serpentine spring-constant expressions are compared with finite-element calculations in Figure 3.22. The fixed parameters are:  $E = 165$  GPa,  $\nu = 0.3$ ,  $w_a = w_b = t = 2\mu$  m,  $n = 6$ , and

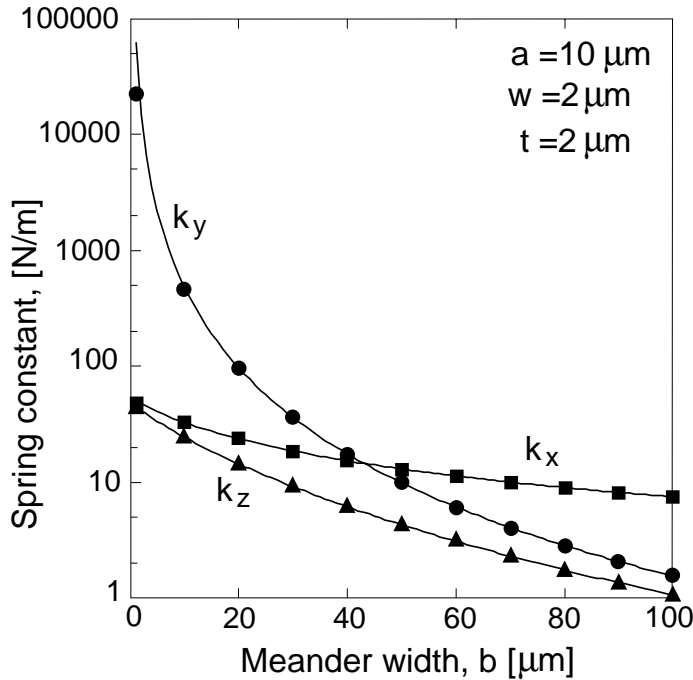


Figure 3.22: Comparison of analytic serpentine spring constants (solid lines) with finite-element analysis (points).

$$a = 10 \mu\text{m}.$$

Finite element calculations are performed using commercial finite-element program, ABAQUS [53]. We use a linear<sup>9</sup> finite-element analysis with three-node quadratic beam elements. Four elements are used to model each beam segment. The finite-element and analytic calculations match to better than 1 % for all but two limiting cases. In the first case, the analytic calculation of  $k_y$  for span lengths below 20  $\mu\text{m}$  has a large error because axial stress is neglected. In the second case, the analytic calculation of  $k_x$  for very small span lengths ( $b < 2 \mu\text{m}$ ) and even  $n$  has an error of around 5 % because axial stress is neglected.

Since the cross-section of the beams is square,  $k_y$  approaches  $k_z$  as the span length is increased. Also,  $k_x$  approaches  $k_z$  as the span length is decreased and the flexure acts like a fixed-fixed suspension.

---

<sup>9</sup>Spring-constant values obtained from nonlinear finite-element analysis are within 1.6 % of the linear values, since we restrict the simulation to deflections of 0.1  $\mu\text{m}$ .

label	$n$	$a$ [ $\mu\text{m}$ ]	$b$ [ $\mu\text{m}$ ]	$L$ [ $\mu\text{m}$ ]	$L_{total}$ [ $\mu\text{m}$ ]	$k_x$ [N/m]	$k_y/k_x$
A	10	63	81	630	1360	0.0146	28
B	10	65	64	650	1230	0.0150	45
C	10	37	47	370	793	0.0727	29
D	10	38	37	380	713	0.0757	46
E	20	27	63	540	1740	0.0148	42
F	20	29	50	580	1530	0.0145	72
G	20	16	37	320	1020	0.0715	43
H	20	17	29	340	891	0.0722	73
I	10	22	28	220	472	0.345	29
L	20	10	17	200	523	0.356	74

Table 3.2: Geometrical parameters of serpentine microresonators.

**Comparison with Measured Results:** Ten polysilicon microresonators, each with a different serpentine flexure, are used to measure lateral spring constants. The polysilicon surface-micromachining process, described in Chapter 2, is used to fabricate the resonators. Layout of the resonators, labeled A through L, is shown in Figure 3.23. The rigid central shuttle, suspended by the four springs, is identical for each resonator, and has a mass of approximately  $2.5 \times 10^{-11}$  kg. Comb drives, located on two sides of the shuttle, have a theoretical lateral force coefficient of approximately 0.14 nN/V<sup>2</sup>, calculated from a two-dimensional finite-element analysis<sup>10</sup>. Small square anchors are placed inside the shuttle frame to act as lateral displacement limit stops. Table 3.2 gives the spring parameters of each design. Analytic spring constant values are calculated from Equations (3.125) and (3.126) using a beam thickness of 1.78  $\mu\text{m}$ , beam width of 1.81  $\mu\text{m}$ , and  $E = 165$  GPa. The projected spring length is  $L = na$  and the total length of the beams in the spring is  $L_{total} = na + (n - 1)b$ .

Spring constants are determined by applying a known force to the spring and measuring the displacement. No displacement verniers are included on the designs, so measurement accuracy is about  $\pm 0.3$   $\mu\text{m}$ . To make the measurements, the comb-drive voltage,  $V_c$ , is increased until the comb fingers are unengaged, corresponding to a 5  $\mu\text{m}$

<sup>10</sup>The comb-drive force is

$$F = \alpha \frac{\epsilon N t V_c^2}{g} = \left(0.14 \frac{\text{nN}}{\text{V}^2}\right) V_c^2 \quad (3.143)$$

where  $V_c$  is the comb-drive voltage,  $\alpha$  is a fringe-field correction factor and the finger thickness is  $t = 1.78$   $\mu\text{m}$ . Each side of the comb drive has  $N = 16$  fingers and a gap of  $g \approx 2.2$   $\mu\text{m}$ .

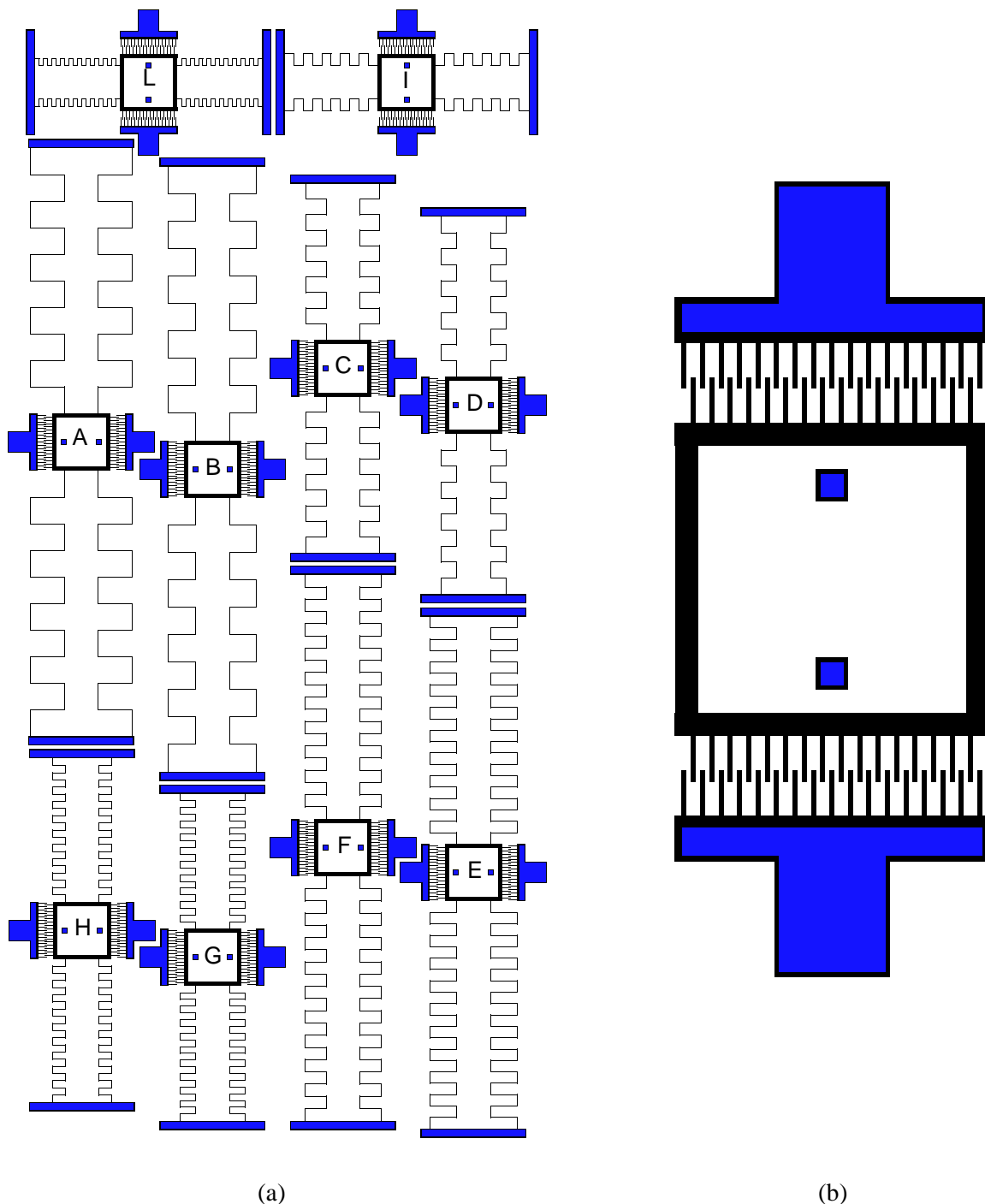


Figure 3.23: (a) Layout of ten microresonators, each with a different serpentine flexure. (b) Close-up view of the central shuttle and comb drive.

label	lateral position [ $\mu\text{m}$ ]	comb-drive voltage, $V_c$					measured $k_x$ [N/m]	$\Delta k_x$ [%]
		left [V]	cntr [V]	bttm [V]	avg [V]	std dev [V]		
A	$5 \pm 0.3$	22	19	22	21	1.7	$0.013 \pm 0.002$	-11.0 %
B	$5 \pm 0.3$	22	24	23	23	1	$0.015 \pm 0.002$	-0.3 %
C	$5 \pm 0.3$	54	46	46	48.7	4.6	$0.067 \pm 0.001$	-7.8 %
D	$5 \pm 0.3$	54	50	53	52.3	2.1	$0.078 \pm 0.008$	+3.1 %
E	$5 \pm 0.3$	24	22	24	23.3	1.2	$0.015 \pm 0.002$	+1.4 %
F	$5 \pm 0.3$	24	22	23	23	1	$0.015 \pm 0.002$	+3.7 %
G	$5 \pm 0.3$	52	46	51	49.7	3.2	$0.070 \pm 0.010$	-2.1 %
H	$5 \pm 0.3$	52	46	50	49.3	3.1	$0.069 \pm 0.010$	-4.5 %
I	$2.5 \pm 0.3$	80	80	80	80	0	$0.36 \pm 0.04$	+4.3 %
L	$2.5 \pm 0.3$	80	80	80	80	0	$0.36 \pm 0.04$	+1.2 %

Table 3.3: Measured comb-drive voltage and lateral position of serpentine microresonators. Measurements were taken on dice located at the left, center, and bottom of the wafer. The last column,  $\Delta k_x$ , gives the percent difference between the measured spring constant values and values from Table 3.2.

displacement. Voltage data shown in Table 3.3 is recorded for three locations on the wafer, and average and sample standard deviation is calculated. The comb drives could not be fully disengaged for the two stiffest resonators (I and L) because the voltage limit of the power supply was reached. The measured spring constant is calculated by dividing the comb-drive force by the displacement. Differences between measured and analytic spring constant values are within experimental error, and are attributed to inaccuracies in measurement of displacement and variations in beam width across the wafer.

Measured lateral resonant frequency values are given in Table 3.4. Finite-element resonant frequency values are within  $\pm 13$  % of the average measured values for all resonators except for the A resonator. An estimation of resonant frequency, tabulated in the last column of Table 3.4, is calculated using

$$f_r = \frac{1}{2\pi} \sqrt{\frac{k_x}{m}} \quad (3.144)$$

where  $m$  is the shuttle mass and  $k_x$  is taken from Table 3.2. These analytic resonant frequency values are 10–30% larger than the finite-element values because the effect of spring mass on resonant frequency is neglected. More accurate expressions for resonant frequency can be determined by substituting an effective mass for  $m$  in Equation (3.144) to account for inertial effects of the springs. Neglecting the spring mass is a particularly

label	measured $f_r$					finite element $f_r$ [Hz]	analytic $f_r = \sqrt{k_x/m}/2\pi$ [Hz]
	left [Hz]	center [Hz]	bottom [Hz]	avg [Hz]	std dev [Hz]		
A	2810	2485	2795	2697	183	3032	3866
B	3230	3165	3120	3172	55	3137	3920
C	7870	7180	7595	7548	347	7376	8614
D	8430	7760	8210	8133	342	7635	8791
E	4260	2770	3015	3348	799	2899	3887
F	3095	2780	2980	2952	159	2947	3843
G	7520	6800	7320	7213	372	7053	8546
H	7625	6905	7445	7325	375	7243	8589
I	18395	16910	18305	17870	833	17029	18780
L	18290	16935	18055	17760	724	17130	19058

Table 3.4: Measured lateral resonant frequency of serpentine microresonators.

bad approximation for resonators A, B, E, and F, where the total spring length is greater than 0.5 mm. Residual stress in the film has less than 1 % effect on the spring constants or resonant frequency of these structures, based on finite-element simulations. Accurate measurement of spring constants can be done using a static force versus displacement test, or using a resonant frequency test with models that include the effects of spring mass.

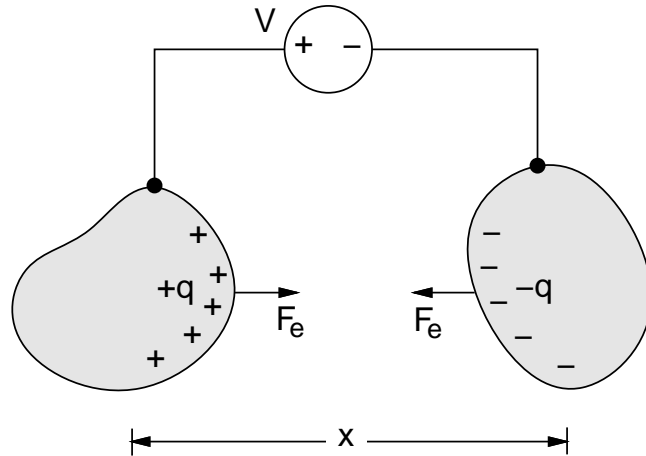


Figure 3.24: Schematic of two charged conductors, where  $V$  is the voltage between the conductors,  $q$  is the amount of differential charge on each conductor,  $x$  is the relative displacement, and  $F_e$  is the electrostatic force acting on the conductors.

## 3.5 Electrostatic Actuators

### 3.5.1 Electrostatic Force

Electrostatic force between two charged conductors, shown in Figure 3.24, can be determined from conservation of power of the system [75]:

$$\underbrace{\frac{d}{dt}W_e(q, x)}_{\substack{\text{rate of change of} \\ \text{stored energy}}} = \underbrace{V \frac{dq}{dt}}_{\substack{\text{electric} \\ \text{power}}} - \underbrace{F_e \frac{dx}{dt}}_{\substack{\text{mechanical} \\ \text{work}}} \quad (3.145)$$

where  $W_e(q, x)$  is the stored electrical energy,  $V$  is the voltage between the conductors,  $q$  is the amount of differential charge on each conductor,  $x$  is the relative displacement, and  $F_e$  is the electrostatic force acting on the conductors. Multiplying Equation (3.145) by  $dt$  gives the differential energy-balance relation<sup>11</sup>,

$$dW_e = V dq - F_e dx \quad (3.147)$$

---

<sup>11</sup>For a general system of  $n + 1$  conductors (one of the conductors is the ground reference) and  $p$  forces, the differential energy balance is

$$dW_e = \sum_{i=1}^n V_i dq_i - \sum_{j=1}^p F_{e,j} dx_j \quad (3.146)$$

where  $V_i$  and  $q_i$  are the respective voltages and charges associated with the  $i$ th conductor, and  $F_{e,j}$ , and  $x_j$  are the respective generalized forces and relative displacements associated with the  $j$ th conductor.

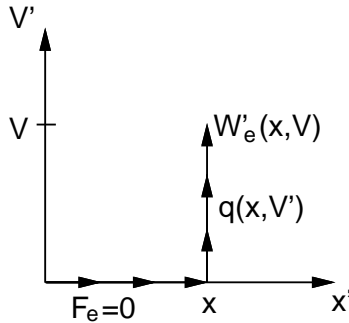


Figure 3.25: Path of integration in the  $x$ - $V$  variable space used to calculate coenergy.

Balance of energy can be alternatively expressed in terms of  $V$  and  $x$  as the independent variables, by

$$dW'_e = q dV + F_e dx \quad (3.148)$$

where the coenergy,  $W'_e(V, x)$ , is defined as

$$W'_e = q V - W_e \quad (3.149)$$

We can integrate Equation (3.148) along an arbitrary path in the variable space  $x$ - $V$ ; we choose the path shown in Figure 3.25 to find the coenergy,

$$\begin{aligned} W'_e &= \underbrace{\int_0^x F_e(x', V = 0) dx'}_{= 0} + \int_0^V q(x, V') dV' \\ &= \int_0^V C(x) V' dV' = \frac{1}{2} C(x) V^2 \end{aligned} \quad (3.150)$$

where  $C(x)$  is the capacitance between the conductors<sup>12</sup>. Our choice of integrating over  $x$  with  $V$  fixed at zero has simplified the evaluation by eliminating the first term in Equation (3.150).

The electrostatic force is found by taking the partial derivative with respect to  $x$  in Equation (3.148). After rearranging terms, we find

$$F_e = \frac{\partial W'_e}{\partial x} - \underbrace{q \frac{\partial V}{\partial x}}_{= 0} \quad (3.151)$$

---

<sup>12</sup>The charge-voltage relationship is linear for a pair of conductors in air. Therefore,  $q = C V$ , where  $C$  is the capacitance.

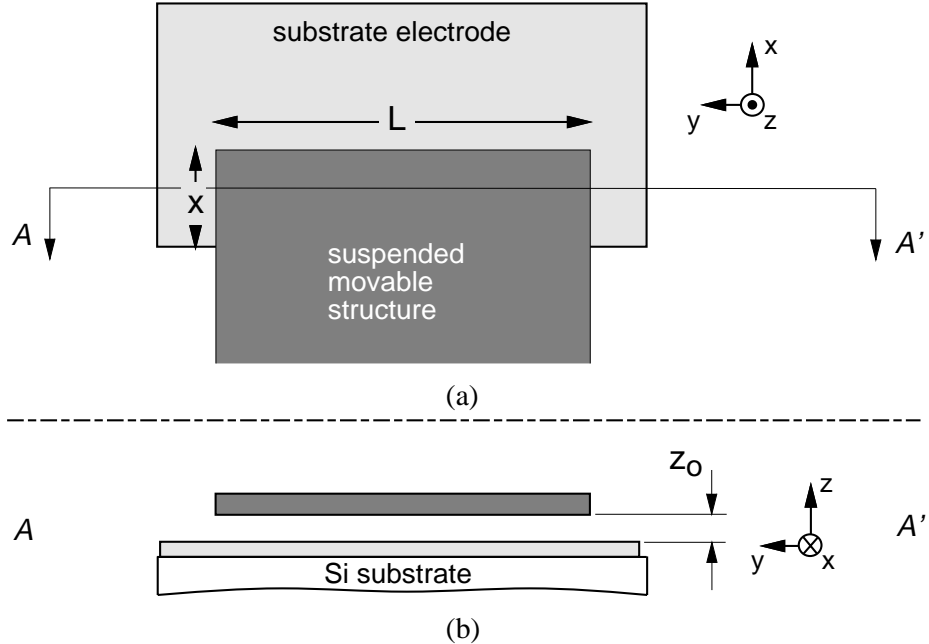


Figure 3.26: Parallel-plate microactuator. (a) Top view. (b) Side view.

where the second term is zero because  $V$  is constant. Substituting Equation (3.150) into (3.151), we obtain

$$F_e = \frac{1}{2} \frac{dC(x)}{dx} V^2 \quad (3.152)$$

Equation (3.152) can be used to calculate the electrostatic force of any two-conductor system, given the capacitance as a function of position. We will revisit the energy-method derivation of electrostatic force for a system with three conductors in section 3.5.3.

### 3.5.2 Parallel-Plate Actuators

The parallel-plate microactuator, shown schematically in Figure 3.26, produces electrostatic force in the  $x$  and  $z$  directions. The parallel-plate area has a fixed dimension,  $L$ , and a variable dimension,  $x$ . Neglecting fringing fields, the parallel-plate capacitance is

$$C = \frac{\epsilon_0 L x}{z} \quad (3.153)$$

where  $\epsilon_o$  is the permittivity of air<sup>13</sup>, and  $z$  is the vertical air-gap spacing. Application of Equation (3.152) gives the forces that act on the movable plate.

$$F_{e,x} = \frac{\epsilon_o L}{2 z} V^2 \quad (3.154)$$

$$F_{e,z} = -\frac{\epsilon_o L x}{2 z^2} V^2 \quad (3.155)$$

A second-order correction to Equation (3.155) includes the effect of fringing capacitance from the edge of the movable plate to the lower electrode, and has been used to model electrostatically deformed beams and diaphragms [76]. Analytic approximations to parallel-plate edge-fringe capacitance can be found in texts on microstrip transmission lines [77–79]. Plates that are perforated with holes will have a smaller capacitance than that of a solid plate. The edge-fringe and hole-fringe capacitances change with vertical position, and, therefore, affect the value of electrostatic force.

We have used two-dimensional finite-element analysis to model specific parallel-plate-capacitor geometries. In system-level simulations, we use the following approximate relation for vertical parallel-plate electrostatic force:

$$F_{e,z} \simeq -\frac{\gamma}{1 - (\Delta z/z_o)^2} V^2 \quad (3.156)$$

where  $\gamma$  is a form factor that includes the fringe-field effects, and  $\Delta z$  is a vertical displacement about the nominal air gap,  $z_o$ .

### 3.5.3 Comb-Finger Actuators

The comb-finger microactuator (comb-drive), shown schematically in Figure 3.27, was first used by Tang [20] in a laterally driven polysilicon resonator. Two sets of engaged comb fingers, one movable set (rotor) and one stationary set (stator), are patterned from a single polysilicon film. A ground plane is located under the comb fingers, and is normally electrically connected to the rotor to eliminate electrostatic pull-down force to the substrate. We will use the subscripts  $s$ ,  $r$ , and  $p$  to denote variables relating to the stator fingers, rotor fingers, and underlying plane, respectively.

#### 3.5.3.1 Comb-Drive Lateral Force

In Figure 3.28, a comb-finger cross section illustrates the partitioning of capacitance per unit length into the stator-to-rotor capacitance,  $C_{rs}$ , the rotor-to-plane capac-

---

<sup>13</sup>The permittivity of air is approximately equal to that of a vacuum,  $8.854 \times 10^{-12}$  F/m.

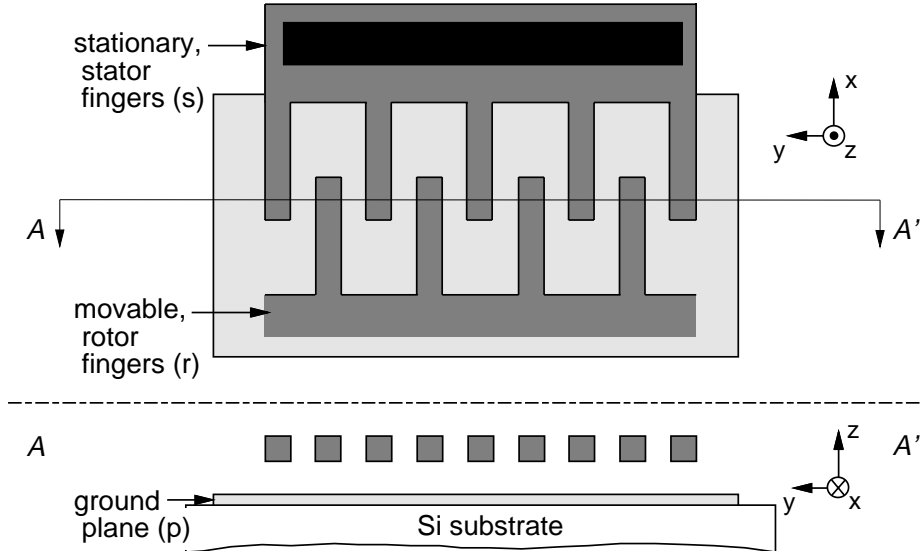


Figure 3.27: Electrostatic comb drive (a) Top view. (b) Side view.

itance,  $\mathcal{C}_{rp}$ , and the stator-to-plane capacitance,  $\mathcal{C}_{sp}$ <sup>14</sup>. Extension of the analysis of section 3.5.1 to three conductors yields the differential coenergy of the comb-drive,

$$dW'_e = q_s dV_s + q_r dV_r + f_{e,x} dx \quad (3.157)$$

where  $f_{e,x}$  is the  $x$ -directed force per unit length. We integrate Equation (3.157) along the path shown in Figure 3.29 and obtain

$$W'_e = \underbrace{\int_0^x f_e(x', V_s = 0, V_r = 0) dx'}_{= 0} + \quad (3.158)$$

$$\begin{aligned} & \int_0^{V_s} q_s(x, V'_s, V_r = 0) dV'_s + \int_0^{V_r} q_r(x, V_s, V'_r) dV'_r \\ &= \frac{1}{2} \mathcal{C}_{sp}(x) V_s^2 + \frac{1}{2} \mathcal{C}_{rp}(x) V_r^2 + \frac{1}{2} \mathcal{C}_{rs}(x) (V_s - V_r)^2 \end{aligned} \quad (3.159)$$

where charges per unit length associated with the stator and rotor fingers are

$$q_s = (\mathcal{C}_{sp} + \mathcal{C}_{rs}) V_s - \mathcal{C}_{rs} V_r \quad (3.160)$$

$$q_r = -\mathcal{C}_{rs} V_s + (\mathcal{C}_{rp} + \mathcal{C}_{rs}) V_r \quad (3.161)$$

We apply Equation (3.151) to get the comb-drive electrostatic force,

<sup>14</sup>In the two-dimensional analysis, the coenergy, charge, and capacitance are expressed per unit length of the comb finger. We use the symbol  $\mathcal{C}$  for capacitance per unit length, and  $f_e$  for force per unit length. We retain the symbols for charge ( $q$ ) and coenergy ( $W_e$ ) when discussing per-unit-length quantities; which definition is used will be apparent in the context.

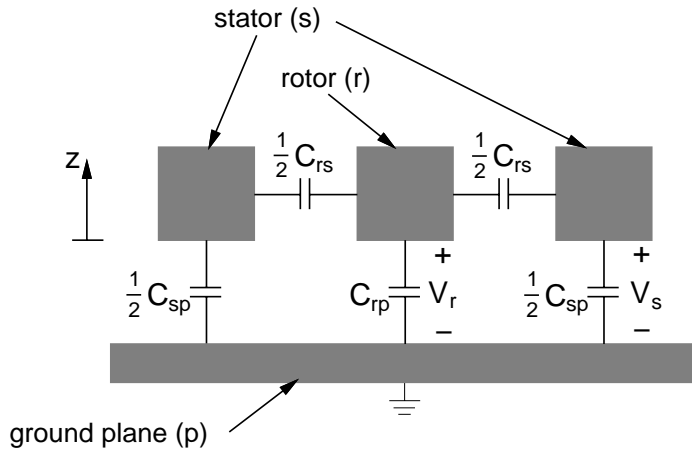


Figure 3.28: Cross-section of one rotor finger between two stator fingers, showing the partitioning of capacitance for comb-drive force evaluation.

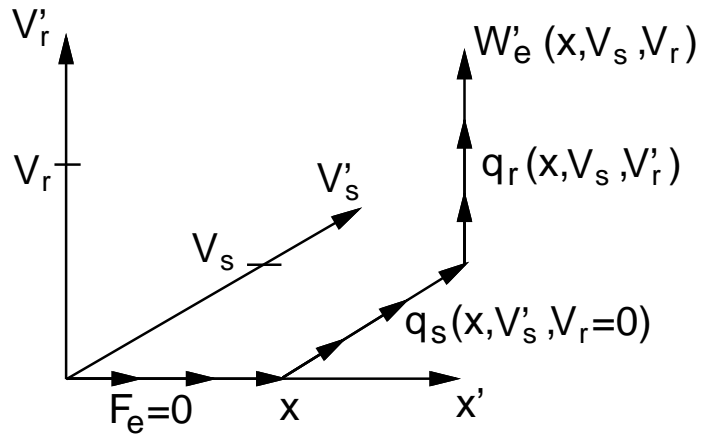


Figure 3.29: Path of integration in the  $x$ - $V_s$ - $V_r$  variable space used to calculate the comb-drive coenergy.

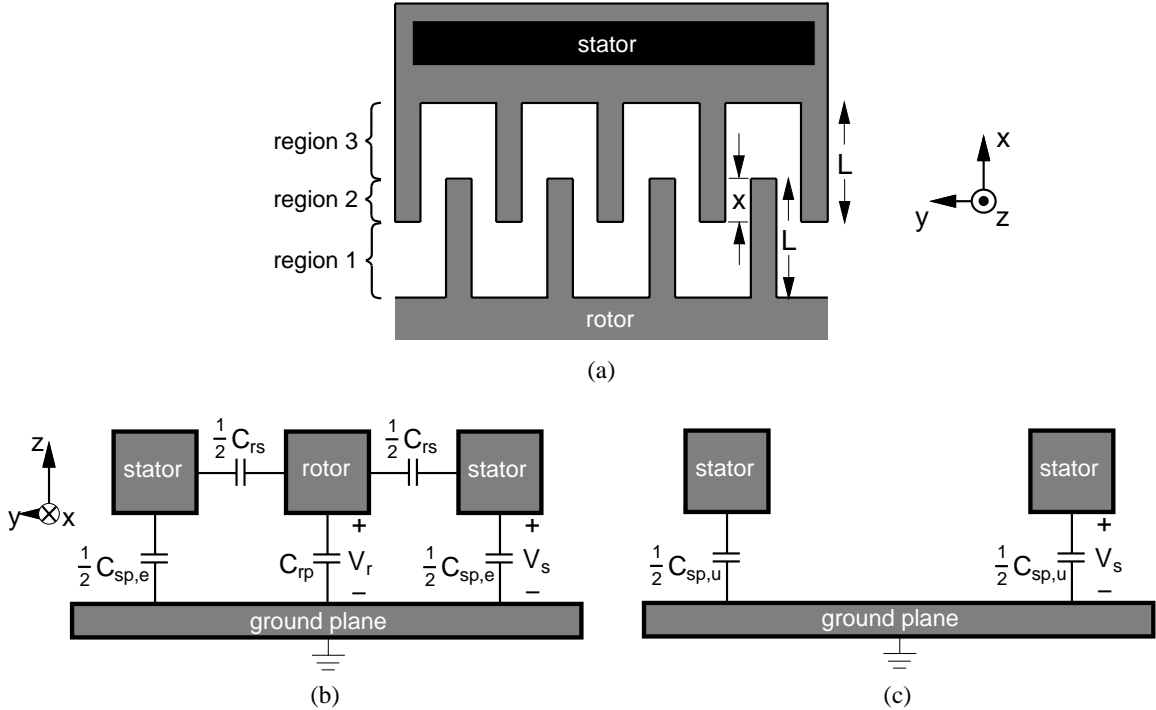


Figure 3.30: Comb-drive schematics for evaluation of lateral force. (a) Comb-drive layout, showing the three comb-finger regions: 1. unengaged rotor fingers, 2. engaged fingers, and 3. unengaged stator fingers. (b) Cross section of engaged comb fingers. (c) Cross section of unengaged stator fingers.

$$F_{e,x} = \frac{1}{2} \frac{dC_{sp}}{dx} V_s^2 + \frac{1}{2} \frac{dC_{rp}}{dx} V_r^2 + \frac{1}{2} \frac{dC_{rs}}{dx} (V_s - V_r)^2 \quad (3.162)$$

where we have switched from per-unit-length capacitances to total capacitances. When the ground plane is electrically connected to the rotor ( $V_r = 0$ ), Equation (3.162) reduces to

$$F_{e,x} = \frac{1}{2} \frac{d}{dx} (C_{sp} + C_{rs}) V_s^2 \quad (3.163)$$

To find the total change in comb-finger capacitances with  $x$ , we can evaluate comb-drive cross sections where the fingers are engaged and unengaged, as shown in Figure 3.30. Since we assume that  $V_r = 0$ , there is no energy storage in region 1 (unengaged rotor fingers in Figure 3.30(a)) and we can ignore its capacitance contribution. Region 2 (engaged fingers) and region 3 (unengaged stator fingers) correspond to the cross sections in Figures 3.30(b) and (c), respectively. Then, the total rotor-to-stator and stator-to-plane capacitances are

$$C_{rs} = N C_{rs} x \quad (3.164)$$

$$C_{sp} = N [C_{sp,e} x + C_{sp,u}(L - x)] \quad (3.165)$$

where  $N$  is the number of rotor comb fingers<sup>15</sup>,  $L$  is the comb-finger length,  $x$  is the finger overlap, and  $\mathcal{C}_{sp,e}$  and  $\mathcal{C}_{sp,u}$  are the capacitances per unit length of the engaged and unengaged fingers, respectively. Using Equation (3.163), we find the lateral comb-finger force,

$$F_{e,x} = \frac{N}{2} (\mathcal{C}_{rs} + \mathcal{C}_{sp,e} - \mathcal{C}_{sp,u}) V_s^2 \quad (3.166)$$

The lateral force is independent of the  $x$  position, if three-dimensional fringe fields are neglected. In system-level simulations, we express the lateral comb-drive force in terms of the parallel-plate, rotor-to-stator finger capacitance ( $= 2\epsilon_0 N t/g$ ), giving

$$F_{e,x} = \alpha \frac{\epsilon_0 N t}{g} V^2 \quad (3.167)$$

where  $t$  is the comb finger thickness,  $g$  is the gap between the comb fingers, and  $\alpha$  is a form factor that includes the fringe-field effects.

Plots of the capacitances and lateral force versus vertical displacement of the rotor comb fingers are given in Figure 3.31(b), for the comb-drive geometry in Figure 3.31(a). Values are generated with the Maxwell™ electrostatic finite-element software [52]. For  $\Delta z = 0$ , the lateral force is 10.1 pN/V<sup>2</sup>/finger, corresponding to a form factor ( $\alpha$  in Equation (3.167)) of 1.14. The force varies with the rotor's vertical displacement, having a maximum value at around  $\Delta z = +1 \mu\text{m}$ . The stator-to-plane capacitance terms in Equation (3.166) ( $\mathcal{C}_{sp,e}$  and  $\mathcal{C}_{sp,u}$ ) were not included in an initial analysis of the comb drive [54]. Neglecting these terms results in a 20–45 % overestimate<sup>16</sup> of the lateral force since  $\mathcal{C}_{sp,u} > \mathcal{C}_{sp,e}$ .

### 3.5.3.2 Comb-Drive Levitation Force

The relation for comb-drive levitation ( $z$ -directed) force is analogous to Equation (3.162) for lateral force, and given by

$$F_{e,z} = \frac{1}{2} \frac{dC_{sp}}{dz} V_s^2 + \frac{1}{2} \frac{dC_{rp}}{dz} V_r^2 + \frac{1}{2} \frac{dC_{rs}}{dz} (V_s - V_r)^2 \quad (3.168)$$

If we neglect fringing fields and assume  $V_r = 0$ , the vertical force relation reduces to

$$F_{e,z} = \frac{1}{2} N x \frac{d}{dz} (\mathcal{C}_{sp} + \mathcal{C}_{rs}) V_s^2 \quad (3.169)$$

---

<sup>15</sup>We assume that the capacitance at the outside edge of the first and last stator comb fingers does not change with  $x$  and can be ignored.

<sup>16</sup>For  $\Delta z = 0$ , the calculation of lateral force using  $f_{e,x} = 0.5 \mathcal{C}_{rs} V^2$  gives 14.6 pN/V<sup>2</sup>/finger, which is a 44 % overestimate of the actual value.

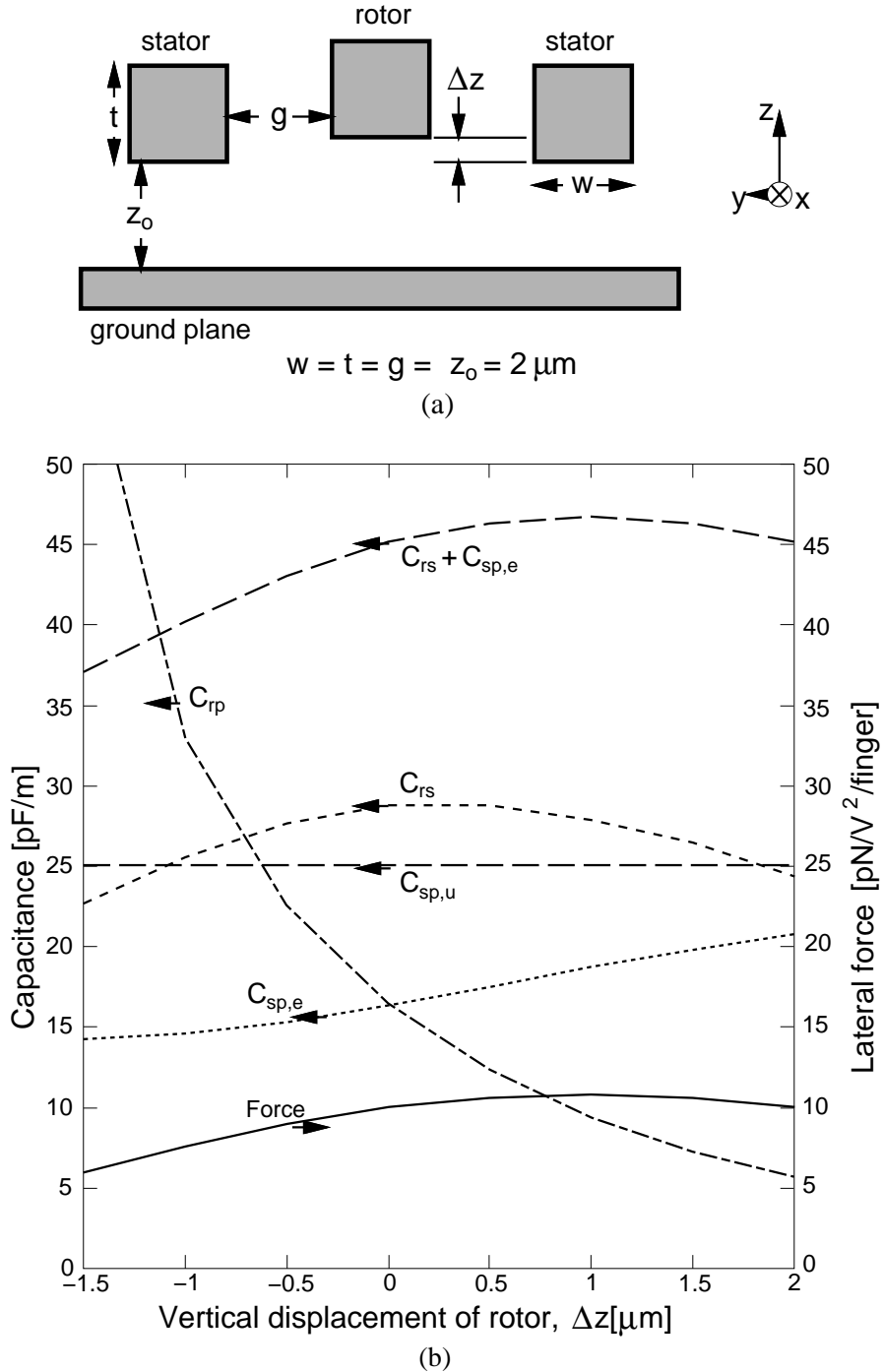


Figure 3.31: Finite-element calculations of capacitance and lateral force for a common comb-drive geometry. (a) Cross section of comb-finger geometry with  $w = t = g = z_o = 2 \mu\text{m}$ . ( $w$  is the finger width, and  $z_o$  is the stator finger spacing above the substrate.) (b) Plots of capacitance and lateral force versus the rotor's vertical displacement,  $\Delta z$ .

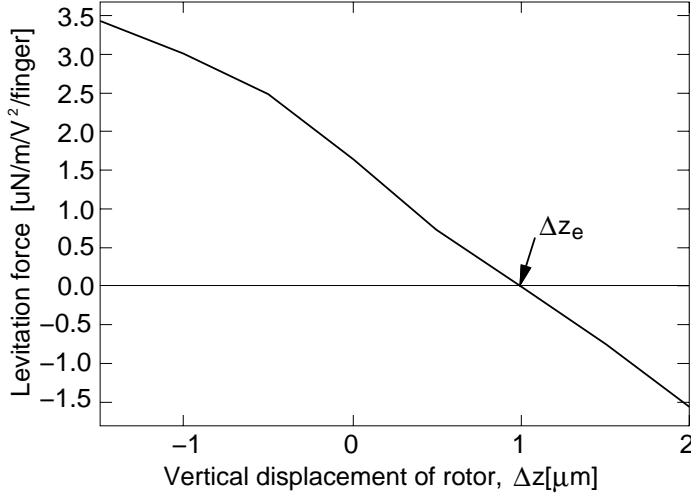


Figure 3.32: Plot of vertical force,  $f_{e,z}$ , versus the rotor's vertical displacement,  $\Delta z$ , for the comb-drive geometry of Figure 3.31(a), where  $w = t = g = z_o = 2 \mu\text{m}$ .

where  $\mathcal{C}_{sp}$  and  $\mathcal{C}_{rs}$  are independent of lateral position.

In Figure 3.32, the levitation force is plotted as a function of the rotor's vertical displacement for the comb-drive geometry of Figure 3.31(a). Again, values are calculated using the Maxwell finite-element analysis software. The force is proportional to the slope of the  $\mathcal{C}_{sp} + \mathcal{C}_{rs}$  curve in Figure 3.31(b) and is positive for displacements less than  $\Delta z = \Delta z_e \approx 1 \mu\text{m}$ . Since the force is approximately linear with displacement, it can be modeled with an electrical spring constant,  $k_e$ , by the relation [80]

$$F_{e,z} = k_e (\Delta z_e - \Delta z) \quad (3.170)$$

For the comb-drive geometry in Figure 3.31(a),  $k_e$  corresponds to about  $1.7 \text{ N}/\text{m}^2/\text{V}^2$  per comb finger. If the rotor suspension has spring constant  $k_z$ , then the equilibrium displacement is

$$\Delta z = \frac{k_e}{k_z + k_e} \Delta z_e \quad (3.171)$$

At this displacement, the electrostatic levitation force equals the spring's restoring force.

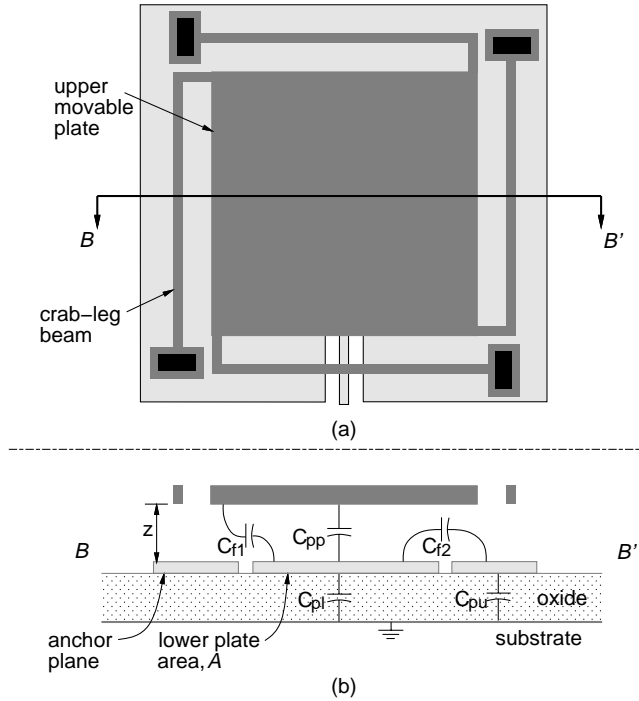


Figure 3.33: Schematic views of a micromechanical parallel-plate capacitor. (a) Top view. (b) Side view.

### 3.6 Capacitive Position Sensing

Sensing the position of a micromechanical structure is a key part of many microsystems. For polysilicon surface Microsystems, capacitive sensing is a robust method of determining position, having low sensitivity to temperature and stress. A limitless number of capacitor geometries can be formed with surface-micromachined structures, however, we will concentrate on the parallel-plate arrangement commonly used to detect vertical displacement of a movable plate. Most of the concepts outlined here are applicable to other micromechanical capacitors.

A movable air-gap capacitor is shown schematically in Figure 3.33. Four crab-leg beams suspend the movable plate above a lower electrode by a distance,  $z$ . The sensor capacitance has a parallel-plate component and fringing components given by

$$C_s = \frac{\epsilon_0 A}{z} + C_{f1} + C_{f2} \quad (3.172)$$

where  $A$  is the lower electrode area. Contributions to the fringing capacitance come from electric fields between the upper and lower plates ( $C_{f1}$ ) and from fields between the lower

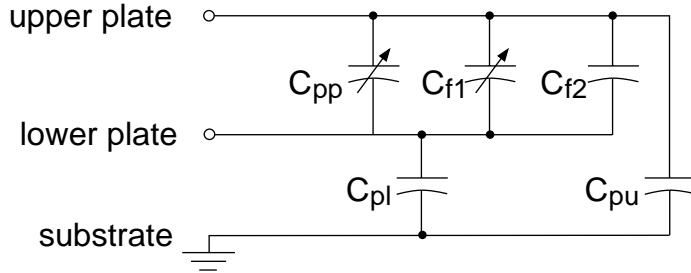


Figure 3.34: Equivalent circuit of the micromechanical capacitor.

plate and anchor plane ( $C_{f2}$ ). The sensor capacitance varies nonlinearly with position, and the sensitivity,  $dC/dz$ , varies as  $-1/z^2$ , approximately. Nonlinearity is a drawback for position control, but does not affect closed-loop sensors where the position is nulled<sup>17</sup>.

Other, parasitic capacitance exists between each plate to the substrate, which is assumed to be an ac ground. Both the lower plate parasitic capacitance,  $C_{pl}$ , and the upper-plate parasitic capacitance,  $C_{pu}$ , can be much larger than the sensor capacitance, because the oxide dielectric constant is higher than air and the oxide thickness is typically smaller than the air gap. If a depletion capacitance to the substrate is present, then  $C_{pl}$  is a function of the lower plate voltage.

The equivalent circuit for the capacitive element is given in Figure 3.34. Capacitance associated with the air gap is variable, but the fringe capacitance to the anchor plane is approximated as constant.

We will discuss two approaches to measurement of the sensor capacitance (and, hence, vertical position): voltage sensing using a unity-gain buffer and current sensing using a transresistance amplifier. Another important capacitance sensing method using charge-redistribution sense techniques has been developed in a pressure sensor [81,82].

### 3.6.1 Capacitive Position Sensing Using a Unity-Gain Buffer

One way to measure capacitance involves driving voltage on one node of the capacitor and sensing voltage on the other node. We will first describe a sensor made from a single micromechanical capacitor, then improve the circuit by connecting another capacitor to form a voltage divider. Then, we analyze the unity-gain buffer circuit used in our sensors.

---

<sup>17</sup>However, capacitive sensing produces a nonlinear vertical force that can affect sensor stability. Effects of feedback-force nonlinearity are discussed in section 5.5.4.

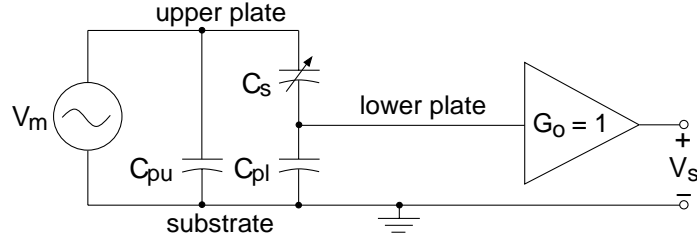


Figure 3.35: Capacitive divider circuit using a single micromechanical capacitor.

Last, experimental results for the buffer are presented.

### 3.6.1.1 Single-Capacitor Sensor

The micromechanical sense capacitor in Figure 3.33 forms an ac voltage divider when one plate is driven by an ac voltage source. In the circuit of Figure 3.35, the upper plate is connected to the ac modulation source,  $V_m$ , and the lower plate becomes the high-impedance divider output node. A unity-gain buffer senses the voltage on the lower plate, providing a low-impedance output,  $V_s$ , where

$$V_s = G_o V_m \left( \frac{C_s}{C_s + C_{pl}} \right) \quad (3.173)$$

where the buffer gain,  $G_o$ , is 1 nominally. Since the upper plate is a low-impedance node, the upper-plate parasitic capacitance to ground has no effect on the circuit. The roles of the plates can be switched, with the lower plate driven; such upper-plate sensing has been used in a surface-micromachined accelerometer [64]. Then, the upper-plate capacitance to ground replaces  $C_{pl}$  in the denominator of Equation (3.173). The dc bias for the high-impedance node can be set with a large resistor or a back-biased diode that leaks charge to ground.

For small-signal calculations, it is convenient to separate the sense capacitance into a fixed part,  $C_{sf}$ , and a variable part,  $C_{sv}$ , instead of using a parallel-plate and fringe decomposition.

$$C_s = C_{sf} + C_{sv} = C_{sf} + \frac{C_{svo}}{1 + \Delta z / z_o} \quad (3.174)$$

where a small displacement around an operating point is defined such that  $z = z_o + \Delta z$ . For simplicity, we assume that all of the fringing capacitance is fixed, so  $C_{svo} = \epsilon_0 A / z_o$ . Substitution of Equation (3.174) into Equation (3.173) leads to the linearized relation between

displacement and sensor output voltage.

$$V_s = G_o V_m \frac{C_{so}}{C_{so} + C_p} \left[ 1 + \left( \frac{C_{sf}}{C_{so}} - \frac{C_{sf} + C_p}{C_{so} + C_p} \right) \frac{\Delta z}{z_o} \right] \quad (3.175)$$

where  $C_{so} = C_s|_{\Delta z=0} = C_{sf} + C_{svo}$ , and  $C_p$  is the parasitic capacitance from the high-impedance node to ground ( $C_p=C_{pl}$ , for the present configuration). The sensor gauge factor,  $\partial V_s / \partial \Delta z$ , approaches zero in the limit of very small or very large parasitic capacitance, and is maximized when  $C_p=C_{svo}$ .

There are two objections to using this single air-gap capacitor as a position sensor. First, the parasitic capacitance can be relatively large, yielding unacceptably low sensitivity. If the lower electrode is the high-impedance node, the parasitic capacitance is typically around 16 times the sensor capacitance, assuming a 2  $\mu\text{m}$  air-gap and 5000 Å of oxide under the lower plate. Thicker oxide films can be used, but this solution may cause processing problems. If the upper plate is used as the high-impedance node, the anchors represent a large parasitic capacitance ( $C_{pu}$  in Figure 3.33). Interconnect from the capacitor to the buffer also adds to the parasitic capacitance. The second objection to single air-gap capacitive sensors is the large, common-mode component of the sensor gain. In order to amplify the displacement signal, the common-mode component must first be subtracted from the overall output.

### 3.6.1.2 Balanced Capacitive Divider With Driven Shield

Parasitic capacitance to ground can be greatly reduced by incorporating an extra shield electrode around the high-impedance node, as shown in the cross-section of Figure 3.36<sup>18</sup>. An extra layer of polysilicon is located under the lower sensor plate, shielding electric field lines from the substrate. If the buffer drives the shield at the same potential as the high-impedance node, then the effective parasitic capacitance is reduced to nearly zero.

An improved position detector circuit, including the shield, is shown in Figure 3.37. The lower plates of two air-gap capacitors are connected to form a voltage divider. One of the capacitors has a clamped upper plate and serves as a reference, with a fixed air-gap. In some applications [64], fully-differential capacitive bridges can be made; however, we will restrict our discussion to the divider circuit with a fixed reference capacitor. The two ac

---

<sup>18</sup>For simplicity, we schematically represent the variable ( $C_{sv}$ ) and fixed ( $C_{sf}$ ) components of the sensor capacitance as lumped elements in Figure 3.36.

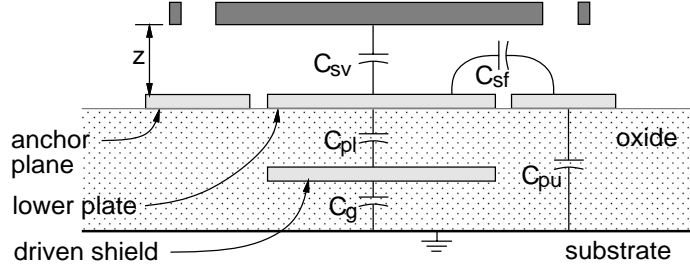


Figure 3.36: Schematic cross-section of a micromechanical parallel-plate sense capacitor with a driven shield. The sense capacitor is connected in series with an identically sized reference capacitor (not shown) to form a capacitive voltage divider.

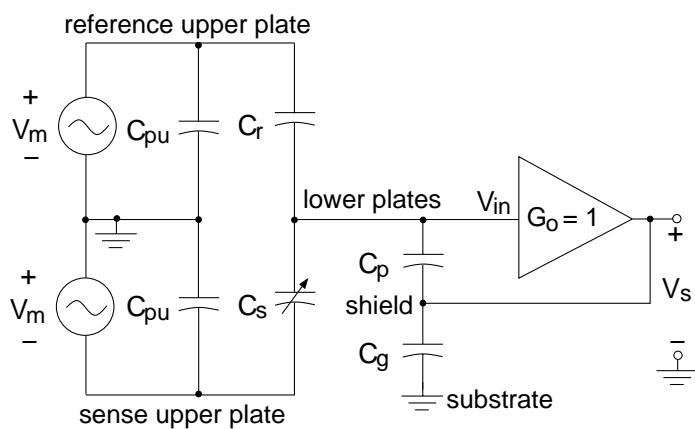


Figure 3.37: Balanced capacitive divider circuit.

modulation voltages that drive the upper plates are generated by sine-wave or square-wave sources that are 180° out of phase with each other.

Parasitic capacitance directly to ground is eliminated, because the shield terminates electric fields from the lower plates. The buffer circuit drives the voltage across  $C_p$  to nearly zero, with the resulting effective capacitance to ground<sup>19</sup> given by

$$C'_p = (1 - G_o)C_p \quad (3.176)$$

and the sensor output voltage is

$$V_s = G_o V_m \left( \frac{C_r - C_s}{C_r + C_s + C'_p} \right) \quad (3.177)$$

By substituting Equation (3.174) into Equation (3.177), the relation between sensor output and displacement is derived.

$$V_s = G_o V_m \left( \frac{C_r - C_{so}}{C_r + C_{so} + C'_p} \right) \left[ \frac{1 + \left( \frac{C_r - C_{sf}}{C_r - C_{so}} \right) \frac{\Delta z}{z_o}}{1 + \left( \frac{C_r + C_{sf} + C'_p}{C_r + C_{so} + C'_p} \right) \frac{\Delta z}{z_o}} \right] \quad (3.178)$$

If the sense and reference capacitors are matched ( $C_r = C_{so}$ ), Equation (3.178) reduces to

$$V_s = G_o V_m \left( \frac{C_{svo}}{C_r + C_{so} + C'_p} \right) \left[ \frac{\Delta z / z_o}{1 + \left( \frac{C_r + C_{sf} + C'_p}{C_r + C_{so} + C'_p} \right) \frac{\Delta z}{z_o}} \right] \equiv G_o V_m \left( \frac{C_{svo}}{C_r + C_{so} + C'_p} \right) \frac{\Delta z}{z_o} \quad (3.179)$$

Notice that the drawbacks associated with the single-capacitor sensor are remedied with the shielded, matched-capacitor divider. The sensitivity is not impacted by the parasitic capacitance, as long as  $C'_p \ll C_{so}$ . The fixed term of Equation (3.175) has no counterpart in Equation (3.179); the balanced modulation combined with the matched divider cancels out the common-mode components.

### 3.6.1.3 Unity-Gain Buffer

#### Buffer Description

---

<sup>19</sup>Any parasitic capacitance that cannot be shielded, such as buffer input capacitance, is added directly to  $C'_p$  to give the total effective parasitic capacitance to ground.

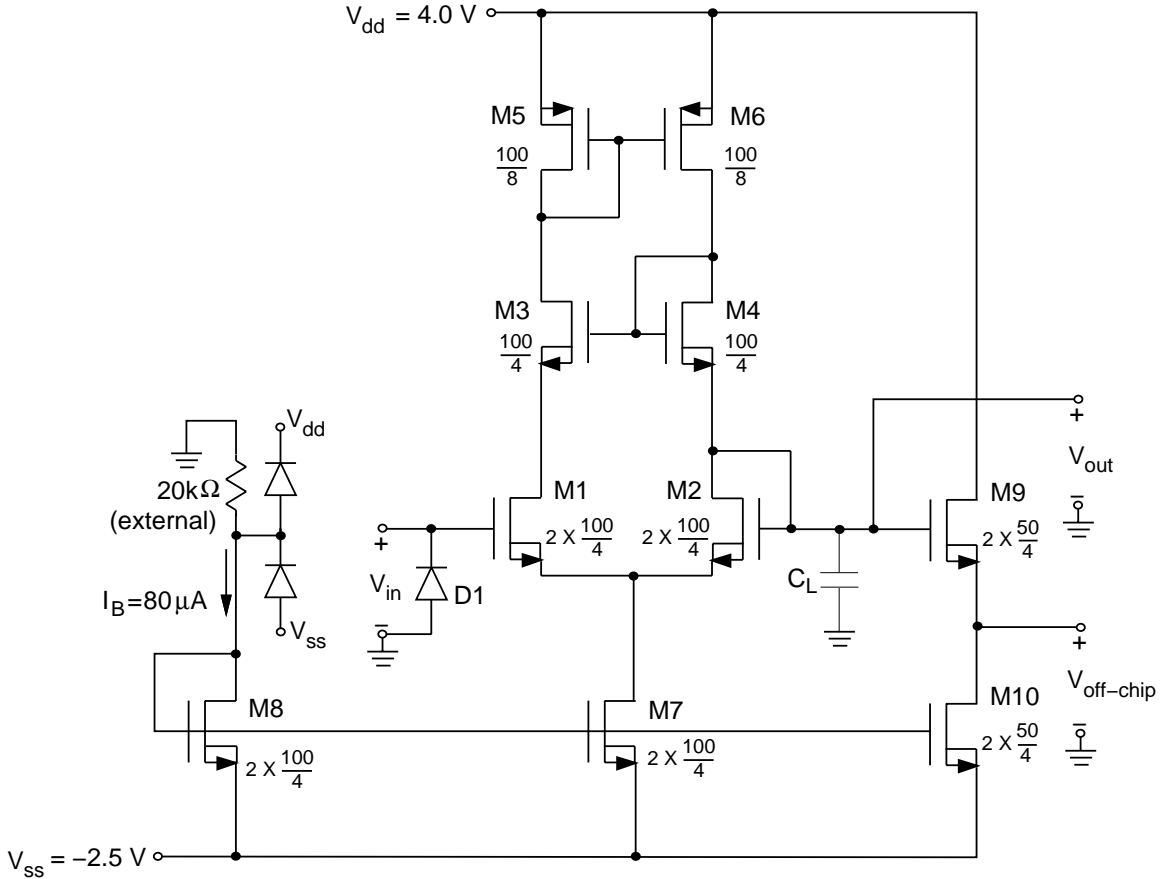


Figure 3.38: CMOS unity-gain buffer circuit.

The capacitive sense circuits described above require a buffer with gain close to unity for effective shielding of the parasitic capacitance to ground. We use the CMOS unity-gain buffer circuit, shown in Figure 3.38, which is an improved version of a previous design [83, 64]. Gate width to length ratios ( $W/L$ ) are given next to each transistor, with paralleled ( $2\times$ ) transistors noted. The single-stage design has a moderate open-loop voltage gain, but is stable even when driving large capacitive loads. Unity-gain feedback is achieved by connecting the output node (M2 drain) to the negative input node (M2 gate) of the differential pair. The diode,  $D1$ , sets the input dc bias to ground, and a  $20\text{k}\Omega$  external resistor supplies bias current for the circuit. Load current in each branch is matched with the p-channel current mirror (M5–M6). The differential stage drives a substantial on-chip load capacitance,  $C_L$ , which comes from the interconnect and shield, while a source follower (M9–M10) drives the even larger, off-chip capacitance.

For micromechanical capacitive sensing applications, a key design issue is minimization of buffer input capacitance, which adds directly to parasitic capacitance on the high-impedance node and decreases the output sensitivity. The requirement of a reasonable open-loop gain value dictates that the input transistor size cannot be made arbitrarily small. There are three contributors to capacitance at the gate of M1: gate-to-source capacitance ( $C_{gs}$ ), gate-to-drain capacitance ( $C_{gd}$ ), and gate-to-body capacitance ( $C_{gb}$ ). Buffer input capacitance can be reduced by forcing the source, drain, and body voltages to track the gate voltage. The small-signal gate-to-source voltage of M1 is approximately inversely proportional to the open-loop voltage gain of the differential stage, providing the desired reduction in the  $C_{gs}$  component of input capacitance. Since a p-well CMOS process is used, we can connect the input transistor well and source together, thereby reducing the effect of  $C_{gb}$  on input capacitance. Transistors M3 and M4 are included to mirror the output voltage to the drain of M1. Thus, because the drain and gate voltage track, the effect of  $C_{gd}$  on input capacitance is reduced. In our analysis, both  $C_{gb}$  and  $C_{gd}$  can be added to the capacitance to ground,  $C_p$ ; however, the addition should not be necessary, since interconnect capacitance will be the dominant component of the parasitic capacitance.

### Buffer Circuit Analysis

Using the low-frequency, small-signal equivalent circuit shown in Figure 3.39, we can determine the buffer performance specifications: gain transfer function ( $G(s)$ ), input impedance ( $Z_i(s)$ ), output resistance ( $R_o$ ), and bandwidth ( $f_o$ ). The resulting equations are

$$G(s) = \left( 1 + \frac{1}{g_{m,M1} r_{o,M6}} + \frac{sC_L}{g_{m,M1}} \right)^{-1} \quad (3.180)$$

$$Z_i(s) = \left[ \frac{sC_{gs,M1}}{2g_{m,M1}} \left( \frac{1}{r_{o,M7}} + \frac{1}{r_{o,M6}} + sC_L \right) \right]^{-1} \quad (3.181)$$

$$R_o = \frac{1}{g_{m,M1}} \quad (3.182)$$

$$f_o = \frac{g_{m,M1}}{2\pi C_L} \quad (3.183)$$

where  $g_m$  is the transconductance and  $r_o$  is the output resistance of a transistor. Only first-order effects are included, where the gain of each transistor is assumed to be much greater than one. We have also assumed that  $C_{gs}$  is much larger than  $C_{gd}$  and  $C_{gb}$ . The input impedance is capacitive at lower frequencies, and has a resistive component that becomes

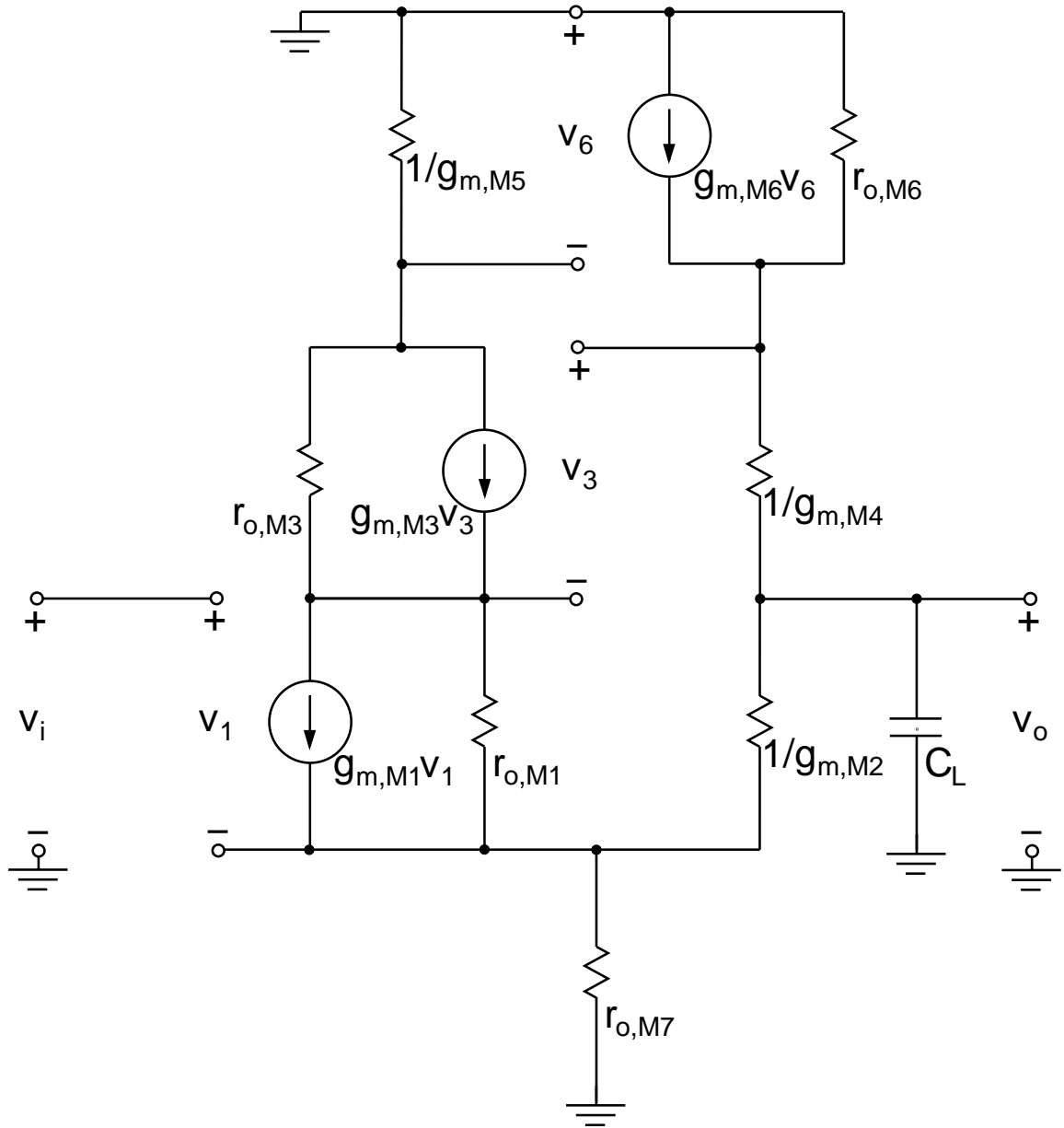


Figure 3.39: Low-frequency, small-signal model of buffer circuit.

dominant above 230 kHz. Compared to the previous buffer design (which omitted M5 and tied the drain of M3 to  $V_{dd}$ ), the dc gain error is reduced by a factor of 4, and the input capacitance is reduced by a factor of 2.

Further improvement of the gain can be made by using a cascode p-channel current mirror in place of the M5–M6 mirror. Notice that the output resistance of the n-channel mirror, M7–M8, does not affect the gain. Input capacitance can be reduced by increasing the output resistance of both n- and p-channel current mirrors. The resistive input impedance can be reduced by minimizing load capacitance. The input gate length should be of minimum size, since input capacitance ( $C_i$ ) scales as<sup>20</sup>  $L^{3/2}W^{1/2}$ .

### Values for Buffer Specifications

To obtain values for the buffer specifications, we must first define the MOS field-effect-transistor (FET) parameters, then calculate values of transconductance and output resistance for the buffer-circuit transistors. MOSFET drain current, transconductance, output resistance, and gate-to-source capacitance in the saturation region are given by [84]

$$I_d = \frac{k' W}{2 L} (V_{gs} - V_t)^2 (1 + \lambda V_{ds}) \quad (3.184)$$

$$g_m = \sqrt{2k' I_d (W/L)} \quad (3.185)$$

$$r_o = \frac{1}{\lambda I_d} \quad (3.186)$$

$$C_{gs} = \frac{2}{3} C_{ox} WL \quad (3.187)$$

where  $V_t$  is the threshold voltage,  $C_{ox}$  is the gate oxide capacitance per unit area,  $k'$  is the intrinsic transconductance factor<sup>21</sup> and  $\lambda$  is the channel length modulation factor. These are all treated as constant parameters, dependent on the fabrication process. The body and source are connected for all transistors in the circuit, so there is no body effect on the threshold voltage. Parameters for our 3-μm p-well CMOS technology are, for n-channel devices:

$$k'_n = 33 \mu\text{A/V}^2$$

$$\lambda_n = 0.043 \text{ V}^{-1}$$

$$V_{tn} = 0.56 \text{ V}$$

---

<sup>20</sup>The input capacitance,  $C_i$ , is proportional to  $C_{gs}/(g_m r_o)$ , where  $g_m$ ,  $r_o$ , and  $C_{gs}$  are given by Equations (3.185) through (3.187). Therefore,  $C_i \propto C_{ox} \lambda I_d L \sqrt{2k'_n I_d W L}$ .

<sup>21</sup>In theory,  $k' = \mu C_{ox}$ , where  $\mu$  is the carrier mobility. In practice,  $k'$  is determined experimentally from transistor I–V measurements.

$$C_{ox} = 0.69 \text{ fF}/\mu\text{m}^2$$

$$L_d = 0.22 \text{ } \mu\text{m}$$

and for p-channel devices:

$$k'_p = 17 \mu\text{A}/\text{V}^2$$

$$\lambda_p = 0.023 \text{ V}^{-1} (\text{L} = 8 \text{ } \mu\text{m})$$

$$V_{tp} = -0.56 \text{ V}$$

$$C_{ox} = 0.69 \text{ fF}/\mu\text{m}^2$$

$$L_d = 0.16 \text{ } \mu\text{m}$$

where  $L_d$  is the source/drain lateral diffusion distance. These process parameters are used in Equations (3.185)–(3.187) to obtain values for selected device parameters.

$$g_{m,\text{M1}} = 0.385 \text{ mS}$$

$$r_{o,\text{M6}} = 1.09 \text{ M}\Omega$$

$$r_{o,\text{M7}} = 291 \text{ k}\Omega$$

$$C_{gs,\text{M1}} = 552 \text{ fF}$$

$$C_{go,\text{M1}} = 150 \text{ fF}$$

The last parameter is the total overlap capacitance,  $C_{go}$ , between the gate to the source, drain, and substrate, which is specified as a process parameter. We add the overlap capacitance directly to  $C_{gs}$  when calculating the input capacitance of the buffer. The buffer specifications are calculated from Equations (3.180)–(3.183). We assume a load capacitance of 3 pF, reflecting the size of the shield-to-ground capacitance in our experimental test structures. Table 3.5 lists the analytical values of buffer specifications alongside values determined using the HSPICE [3] simulation program. The HSPICE simulations use the

specification	symbol	analytic	HSPICE
dc gain	$G_o$	$0.991 \mu\text{A}/\text{V}$	$0.9965 \mu\text{A}/\text{V}$
input capacitance	$C_i$	3.97 fF	4.32 fF
output resistance	$R_o$	2.60 k $\Omega$	2.80 k $\Omega$
bandwidth	$f_o$	20.4 MHz	20.2 MHz

Table 3.5: Values of buffer performance specifications, calculated from analytic analysis and HSPICE [3] simulation.

input deck in appendix B.1. Source/drain junction and overlap capacitance are included in the transistor models. Analytic and simulated results are in reasonable agreement.

### Diode Capacitance

The input diode has junction capacitance to ground that must be included in the total input capacitance. Assuming a step junction, capacitance per unit area of the p-n diode is given by [68]

$$C_j = \left[ \frac{q\epsilon_s}{2 \left( \frac{1}{N_a} + \frac{1}{N_d} \right) (\phi_i - V_a)} \right]^{-1} \quad (3.188)$$

where the terms in the equation are

electronic charge:  $q = 1.602 \times 10^{-19}$  C

permittivity of silicon:  $\epsilon_s = 1.04 \times 10^{-10}$  F/m

acceptor (p-type) dopant concentration:  $N_a = 2 \times 10^{16}$  cm<sup>-3</sup>

donor (n-type) dopant concentration:  $N_d = 2 \times 10^{18}$  cm<sup>-3</sup>

built-in junction voltage:  $\phi_i = 0.6$  V

forward bias voltage across diode:  $V_a = 0$  V

Diode D1 has an n+ diffusion area of  $135 \mu\text{m}^2$ . Plugging numbers into Equation (3.188), we arrive at a diode capacitance value of 71 fF, much larger than the buffer input capacitance value of 3 fF.

When the diode is exposed to light, minority carriers are generated, producing a reverse current. This photocurrent is balanced in steady-state by a forward bias across the junction. Equation (3.188) is only valid for forward-bias voltages up to about 0.3 V. For greater forward-bias voltages up to about 0.6 V, the junction capacitance increases to about 2–3× its zero-bias value, but remains finite [85]. Future designs should consider other means of dc biasing the buffer, since the diode junction capacitance dominates the effective parasitic capacitance to ground. An undoped polysilicon resistor or a long-channel transistor may provide a high-resistance dc path to ground with lower capacitance than the diode.

### Buffer Noise

MOS transistor noise is modeled by an equivalent, input-referred voltage source with thermal noise and flicker noise ( $1/f$  noise) components [84].

$$\overline{v_{\text{eq}}^2} = 4k_B T \left( \frac{2}{3g_m} \right) \Delta f + \frac{K_f}{C_{ox}WL} \Delta f \quad (3.189)$$

where  $k_B$  is Boltzmann's constant,  $T$  is temperature,  $K_f$  is the flicker noise coefficient, and  $\Delta f$  is a small bandwidth.  $\overline{v_{\text{eq}}^2}$  denotes the mean-square of the equivalent noise distribution.

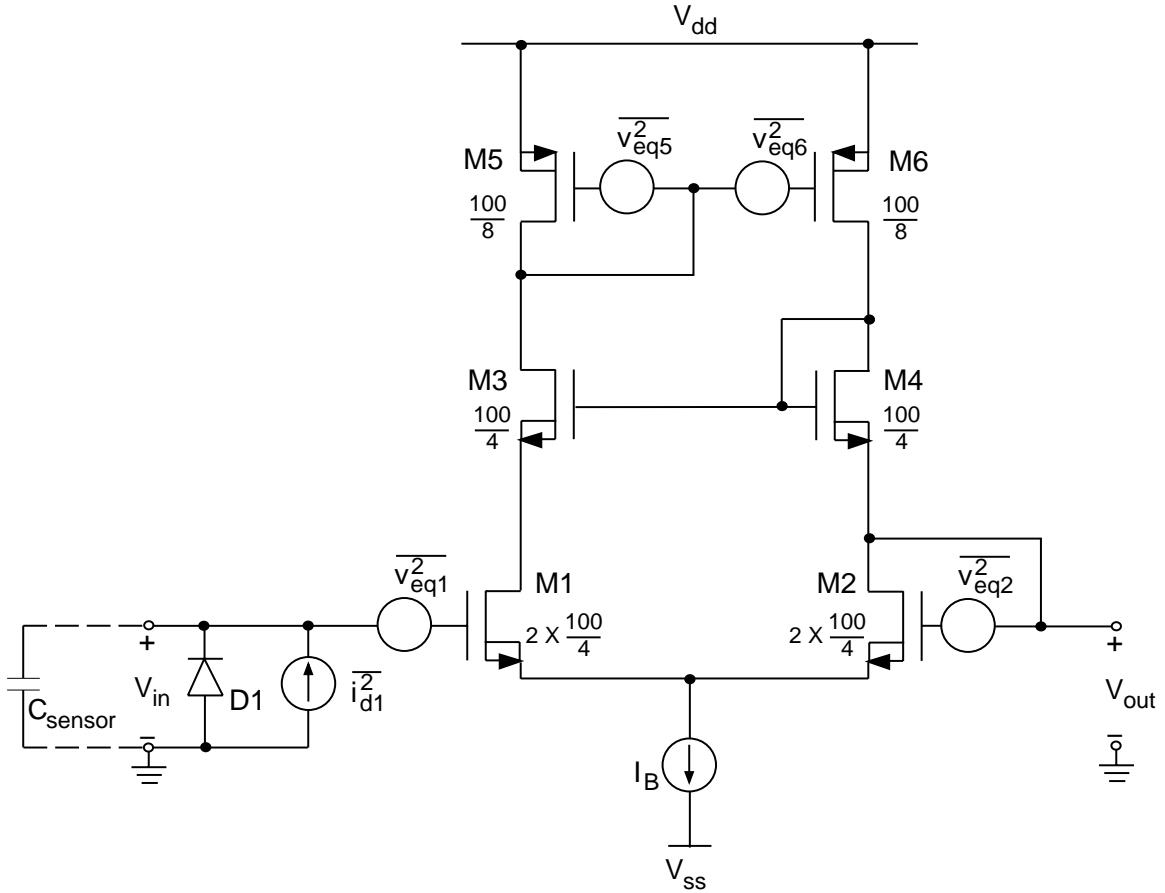


Figure 3.40: Noise model of buffer circuit.

Shot noise and flicker noise are present in p-n diodes, which are modeled by an equivalent current source,  $\overline{i_d^2}$ .

$$\overline{i_d^2} = 2qI_d\Delta f + K_d \frac{I_d}{f}\Delta f \quad (3.190)$$

where  $q$  is the electronic charge,  $I_d$  is the diode current, and  $K_d$  is the flicker noise coefficient for the diode.

Buffer input-referred noise is determined using the equivalent circuit shown in Figure 3.40. Noise contributions come from transistors M1, M2, M5, and M6, and diode D1. The bias-current transistors (M7 and M8) only affect the common-mode current, and transistors M3 and M4 are cascoded, so none of these devices add to the output noise. Noise from the source-follower stage will be ignored, but extra thermal noise is contributed from transistors M8, M9, and M10. Interconnect thermal noise will be ignored for now, but

will be reconsidered when calculating the minimum detectable displacement of the position sensor, in section 3.6.3. The total equivalent input-referred noise voltage,  $\overline{v_b^2}$ , is given by

$$\overline{v_b^2} = \overline{v_{\text{eq1}}^2} + \overline{v_{\text{eq2}}^2} + \left( \frac{g_{m,\text{M6}}}{g_{m,\text{M1}}} \right)^2 \left( \overline{v_{\text{eq5}}^2} + \overline{v_{\text{eq6}}^2} \right) + \overline{v_{\text{eq,d1}}^2} \quad (3.191)$$

where  $\overline{v_{\text{eq,d1}}^2}$  is the equivalent noise voltage of the diode, discussed next.

In steady-state and assuming the circuit is in darkness, the dc diode current is zero; however, an ac current of amplitude  $2\pi f C_j V_{\text{in}}$  flows across the diode junction. The noise current can be expressed as an equivalent noise voltage,  $\overline{v_{\text{eq,d1}}^2}$ , assuming the buffer is connected to the capacitive divider sensing circuit. This gives

$$\overline{v_{\text{eq,d1}}^2} = \left( 2q + \frac{K_d}{f} \right) \frac{C_j}{2\pi f(C_j + C_i + C_{\text{sensor}})^2} \sqrt{\overline{V_{\text{in}}^2}} \Delta f \quad (3.192)$$

where  $C_{\text{sensor}}$  is the total effective sensor capacitance<sup>22</sup>, and  $\sqrt{\overline{V_{\text{in}}^2}}$  is the root-mean-square (rms) buffer input voltage. Notice that the diode shot noise current produces a  $1/f$  dependence in the input-referred noise voltage.

Substituting Equation (3.189) and (3.192) into Equation (3.191), we arrive at

$$\begin{aligned} \overline{v_b^2} = & 4k_B T \left( \frac{4}{3g_{m,\text{M1}}} \right) \left( 1 + \sqrt{\frac{k'_p(W/L)_{\text{M6}}}{k'_n(W/L)_{\text{M1}}}} \right) \Delta f + \frac{2K_p}{C_{ox}(WL)_{\text{M1}} f} \left( 1 + \frac{K_p k'_p L_{\text{M1}}^2}{K_n k'_n L_{\text{M6}}^2} \right) \Delta f + \\ & \frac{C_j}{2\pi f(C_j + C_i + C_{\text{sensor}})^2} \left( 2q + \frac{K_d}{f} \right) \sqrt{\overline{V_{\text{in}}^2}} \Delta f \end{aligned} \quad (3.194)$$

where  $K_n$  and  $K_p$  are the flicker coefficients for the n-channel and p-channel transistors, respectively. The first term in Equation (3.194) is from transistor thermal noise, the remaining terms are from flicker and shot noise. We now plug the transistor parameter values into Equation (3.194) and obtain

$$\frac{\overline{v_b^2}}{\Delta f} = 7.7 \times 10^{-17} \text{V}^2 + \frac{1.3 \times 10^{-7} \text{V/s}}{f} \sqrt{\overline{V_{\text{in}}^2}} + \frac{1.3 \times 10^{-4} \text{V/s}^2}{f^2} \sqrt{\overline{V_{\text{in}}^2}} \quad (3.195)$$

where we have used typical values for the flicker coefficients,  $K_n = K_p = 3 \times 10^{-24} \text{V}^2 \cdot \text{F}$  and  $K_d = 3 \times 10^{-16} \text{A}$ , and the total sensor capacitance is assumed to be 90 fF. A plot of the input-referred noise voltage spectral density is shown in Figure 3.41 for a 0.1 mV-rms input signal. For this level of input signal, the input-referred transistor flicker noise and diode shot noise

---

<sup>22</sup>For the balanced capacitive divider,

$$C_{\text{sensor}} = C_s + C_r + C'_p \quad (3.193)$$

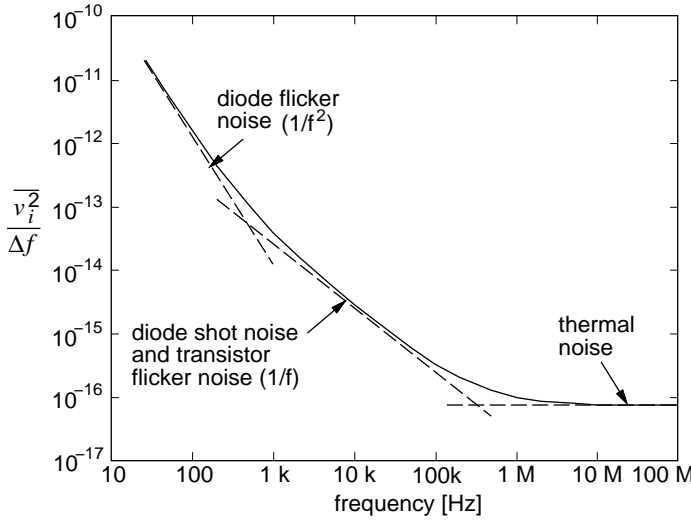


Figure 3.41: Typical buffer noise voltage spectral density.

are approximately equal and are the dominant contributors to noise voltage between 470 Hz and 350 kHz. Larger input signals, or the presence of diode photocurrent, will make the shot noise dominate over the transistor noise. Below 470 Hz, the diode flicker noise voltage becomes the largest noise component, while thermal noise dominates above 350 kHz.

In position-sensing applications, the buffer signal of interest may only span a limited bandwidth. Noise at frequencies outside of the signal band can then be filtered, thus reducing the total noise voltage. As an example, we can calculate the equivalent noise voltage of the position-sensor circuit in Figure 3.37, using the CMOS unity-gain buffer. The balanced modulation driving the capacitor divider produces an amplitude-modulated output signal. If we assume a modulation frequency of 100 kHz, a filter bandwidth of 50 kHz, and an input signal level of 0.1 mV rms, the total noise is 4.6  $\mu$ V rms. The total noise rises to 81  $\mu$ V rms when the input signal is increased to 100 mV rms. The diode noise is a large portion of the total noise, providing more motivation (in addition to parasitic capacitance reduction) to eliminate the diode from the buffer circuit.

#### 3.6.1.4 Buffer Test Circuit

In order to test the balanced capacitive sensor and the unity-gain buffer design, we fabricated the test circuit shown schematically in Figure 3.42. The divider is made of eight identical capacitors which can be disconnected from the circuit by cutting microbridge fuses.

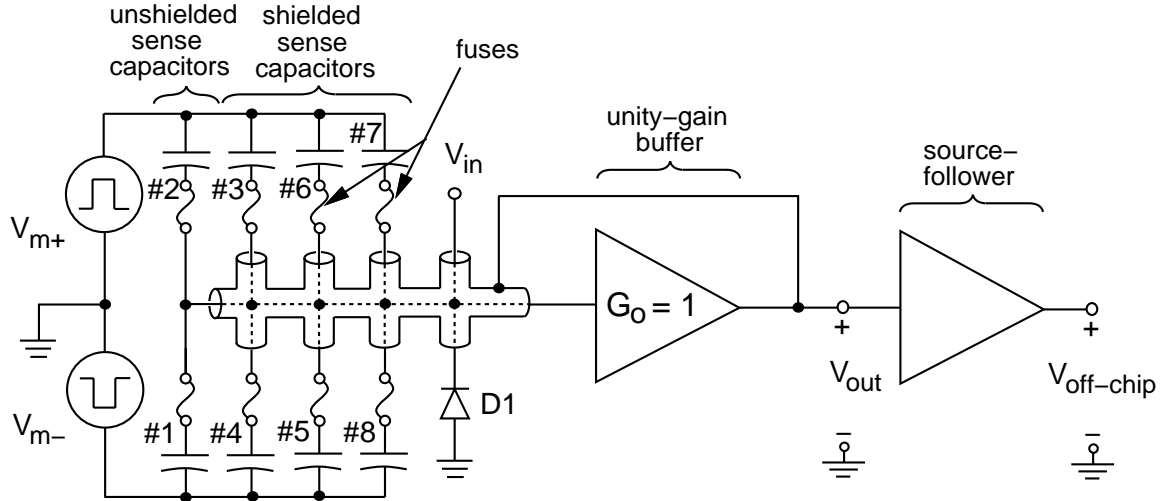


Figure 3.42: Schematic of the capacitive position-sense test circuit with a unity-gain buffer.

Six capacitors have driven shields to reduce parasitic capacitance; the other two capacitors do not have shields so we can experimentally compare sensing with and without shielding.

The completed test circuit is shown in Figure 3.43. The eight square, parallel-plate capacitors, located above the circuitry in the micrograph, are  $100 \mu\text{m}$  on a side with a  $2 \mu\text{m}$  air gap, giving a capacitance value of  $44 \text{ fF}$ . The two unshielded capacitors have some extra fringing capacitance, which increases their capacitance value to  $47 \text{ fF}$ . Each capacitor is suspended by eight, 3-meander serpentine springs, which provide a stiff support. The springs are included to relieve any residual stress that might cause the upper plates to buckle, and to allow verification that the plates are released by pushing them with a probe tip. Tungsten interconnect from the capacitors to the buffer is shielded using the underlying gate-polysilicon layer. A shielded test pad is included to access the buffer input. Other bondpads are labeled for power, ground, bias current, modulation voltages, and outputs. The pad labeled “OUT-” is the on-chip buffer output, and the “OUT+” pad is the off-chip output. We had room on the chip to provide a large output driver, so the source-follower transistors were increased in size to  $W/L=500/4$ .

A plot of the buffer output voltages ( $V_{\text{out}}$  and  $V_{\text{off-chip}}$ ) versus input voltage is shown in Figure 3.44. Originally, we planned to use symmetric  $\pm 2.5 \text{ V}$  power supplies, but the output saturated for input voltages above  $0 \text{ V}$  (dashed line). Instead, a larger  $V_{dd}$  value of  $4 \text{ V}$  allows at least  $\pm 0.5 \text{ V}$  of input swing without degrading the output. The dc gain is 0.983, and the offset voltage is  $3.9 \text{ mV}$ . The source-follower dc gain is 0.994, and the off-chip

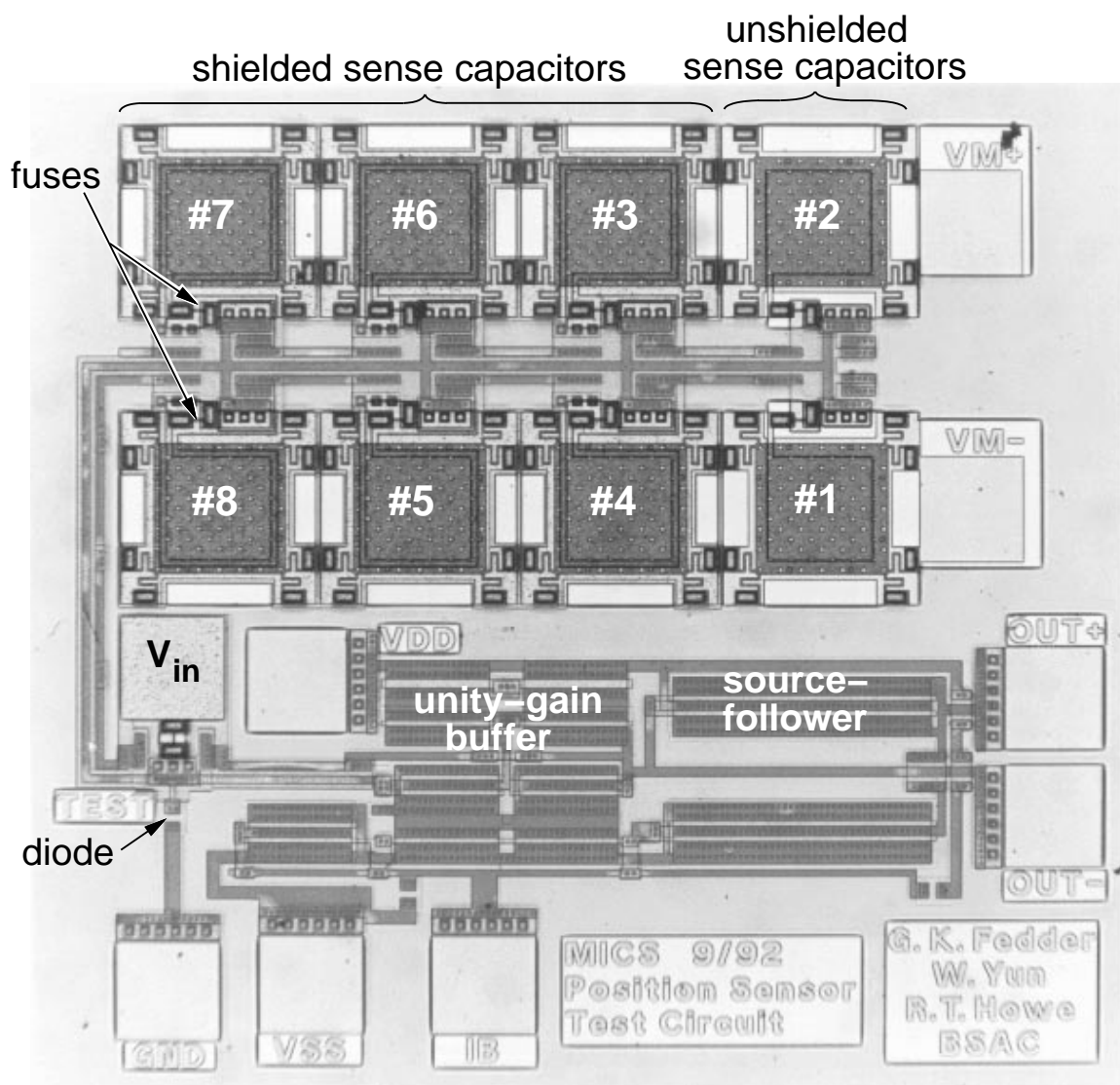


Figure 3.43: SEM of the capacitive position-sense test circuit with a unity-gain buffer.

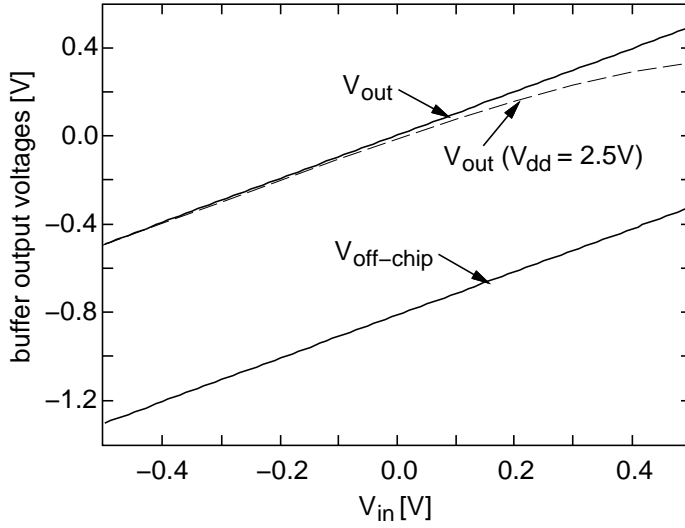


Figure 3.44: Plot of unity-gain buffer output voltages versus input voltage.

#	configuration description	$V_{pp}$ [mV]
#0	no fuses cut	+0.6
#1	#1 fuse cut	+41.2
#2	#1,#2 fuses cut	+0.3
#3	#1,#2,#3 fuses cut	-65.6
#4	#1,#2,#3,#4 fuses cut	-0.3
#5	#1,#2,#3,#4,#5 fuses cut	+85.3
#6	#1,#2,#3,#4,#5,#6 fuses cut	-0.6

Table 3.6: Description of each capacitive divider configuration and corresponding measured peak-to-peak output voltage,  $V_{pp}$ , for the waveforms in Figure 3.45.

signal has a dc offset of  $-0.81$  V.

To verify operation of the sensor, we measured the buffer output response to balanced square-wave modulation across the divider. The modulation-voltage sources<sup>23</sup>,  $V_{m+}$  and  $V_{m-}$ , have a peak-to-peak amplitude of  $0.606$  V, as shown in Figure 3.45(a). Output voltage waveforms are presented in Figure 3.45(b) for seven configurations of the capacitor divider. A description of the divider configurations and the corresponding measured peak-to-peak output voltages are given in Table 3.6. The fuse numbering (and corresponding capacitor numbering) is defined in Figure 3.42. Fuses were cut in succession, starting with

<sup>23</sup>A circuit schematic of the modulation-voltage sources is given in appendix A.2.1.

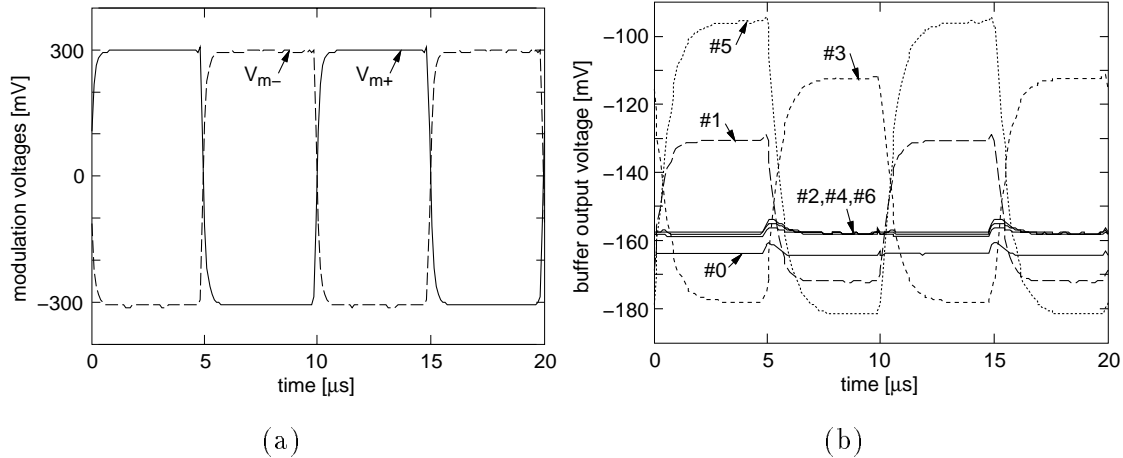


Figure 3.45: Measured voltage waveforms from the position-sense test-circuit. (a) Modulation voltages. (b) Buffer output voltage for seven different capacitor divider configurations.

fuse #1 and ending with fuse #6, and measurements were made after each cut. When the divider is balanced (configurations #0, #2, #4, and #6), the peak-to-peak output is nearly zero, reflecting the good matching of capacitance in the layout. There is more capacitance in series with  $V_{m+}$  than  $V_{m-}$  for configurations #1 and #5, so the output voltage is in phase with  $V_{m+}$ . In configuration #3, the divider weighting is reversed and the output voltage is in phase with  $V_{m-}$ . For the unbalanced cases, the peak-to-peak voltage increases as fewer capacitors are left in the circuit, because the capacitance difference becomes a larger percentage of the total divider capacitance.

The output waveforms have a dc offset between  $-140$  mV and  $-164$  mV, arising from ambient light generating a forward-bias across the diode. A darker ambient (room lights off) results in dc offsets between  $0$  V and  $-27$  mV, which is in the range of the buffer offset. The asymmetric current-voltage diode characteristic is responsible for the positive output dc-bias shift with increasing signal amplitude. The measured buffer bandwidth is about 2.8 MHz, corresponding to a 22 pF load that includes wiring to an external buffer amplifier. This external buffer amplifier drives several feet of coaxial cable and is responsible for the slower signal risetime of  $1.3$  μs.

An expression for the effective parasitic capacitance in terms of known parameters is obtained by inverting Equation (3.177).

$$C'_p = \frac{G_o |V_m|(C_r - C_s)}{|V_s|} - C_r - C_s \quad (3.196)$$

where  $|V_m|$  is the modulation amplitude,  $|V_s|$  is the output amplitude,  $C_r$  is the capac-

itance in series with  $V_{m+}$ , and  $C_s$  is the capacitance in series with  $V_{m-}$ . The parasitic capacitance is separated into three components: effective parasitic capacitance associated with a shielded capacitor,  $C'_p(\text{shielded})$ , parasitic capacitance associated with an unshielded capacitor,  $C_p(\text{unshielded})$ , and other parasitic capacitance associated with the diode and interconnect,  $C_p(\text{other})$ . Using Equation (3.196) and the measured data in Table 3.6, we extract the following values:

$$C'_p(\text{shielded}) = 3 \text{ fF} \pm 1 \text{ fF}$$

$$C_p(\text{unshielded}) = 197 \text{ fF} \pm 1 \text{ fF}$$

$$C_p(\text{other}) = 172 \text{ fF} \pm 1 \text{ fF}$$

Note the large reduction in effective parasitic capacitance due to the shield under the capacitors. The measured capacitance reduction corresponds to an approximate buffer gain<sup>24</sup> of 0.985, which is close to the measured buffer gain (0.983). The substantial parasitic capacitance associated with the diode and interconnect is mostly attributed to the diode junction capacitance, since the interconnect is shielded. This capacitance falls within the predicted range of values, and is about 2.5 times larger than the zero-bias junction capacitance value of 71 fF.

### 3.6.2 Capacitive Position Sensing Using a Transresistance Amplifier

#### 3.6.2.1 Balanced Capacitive Divider

An alternate way to measure capacitance involves driving voltage across the capacitor and sensing the resulting displacement current. The same capacitive divider shown in Figure 3.37 can be used with a transresistance amplifier to sense the differential displacement current in the divider; the resulting schematic is shown in Figure 3.46. We have swapped the connections of the sense and reference capacitors to reverse the sign of the sensor output. The lower plates of the capacitive divider are forced to ground potential by the operational amplifier. A driven shield to reduce parasitic capacitance is unnecessary, since the underlying substrate is an incremental ground.

---

<sup>24</sup>The buffer gain is estimated from the shielded and unshielded parasitic capacitances by inverting Equation (3.176)), giving  $G_o = 1 - C'_p/C_p$ . However, because of differences in the divider layout, the unshielded plate's parasitic capacitance to ground is somewhat smaller than the shielded plate's capacitance to the shield. Considering the uncertainty in our measurement of the  $C'_p(\text{shielded})$ , we can only make a rough check against the measured buffer gain.

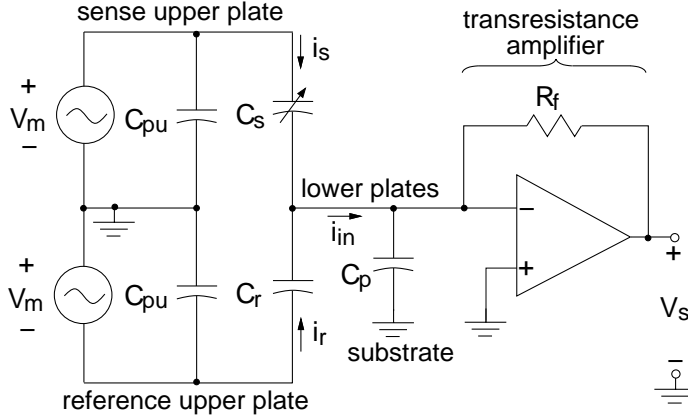


Figure 3.46: Balanced capacitive divider circuit with displacement current-sense using a transresistance amplifier.

The displacement current,  $i_s$ , through the sense capacitor is given by

$$i_s = \frac{d}{dt}(C_s V_m) \approx (C_{svo} + C_{sf}) \frac{dV_m}{dt} + C_{svo} \left( \frac{\Delta z}{z_o} \right) \frac{dV_m}{dt} + \left( \frac{C_{svo} V_m}{z_o} \right) \frac{d\Delta z}{dt} \quad (3.197)$$

where we assume small displacements in the linear approximation. The first term in Equation (3.197) is equal to the displacement current,  $i_r$ , in the reference capacitor, with the difference between the currents given by

$$i_{in} \approx C_{svo} \left( \frac{\Delta z}{z_o} \right) \frac{dV_m}{dt} + \left( \frac{C_{svo} V_m}{z_o} \right) \frac{d\Delta z}{dt} \quad (3.198)$$

This input current flows through the feedback resistor,  $R_f$ , and is converted to the output voltage, where

$$V_s = -R_f i_{in} \quad (3.199)$$

assuming an ideal operational amplifier.

The balanced sinusoidal modulation voltage is

$$V_m = |V_m| \sin(2\pi f_m t) \quad (3.200)$$

where  $|V_m|$  and  $f_m$  are the modulation amplitude and frequency, respectively. In contrast to the voltage-sense method, a square-wave modulation source cannot be used, because displacement current would only flow during the switching transient. The modulation frequency must be at least twice the bandwidth of the displacement signal, to avoid aliasing at the sensor output; however,  $f_m$  is usually chosen to be much larger to ease the demodulation

filter requirements. In our analysis, we will assume that the modulation frequency is much larger than the displacement signal bandwidth, so the second term in Equation (3.198) can be neglected. Then,

$$i_{in} \approx C_{svo} \left( \frac{\Delta z}{z_o} \right) \frac{dV_m}{dt} \quad (3.201)$$

A Laplace transform for the input current can be defined where the  $s$  parameter is a function of the modulation frequency. Taking the transform of Equation (3.201), we obtain

$$I_{in}(s) \simeq s|V_m|C_{svo} \left( \frac{\Delta z}{z_o} \right) \quad (3.202)$$

where  $s=j2\pi f_m$ .

The limited gain and bandwidth of the transresistance amplifier produces a non-ideal output response, which we will now explore. The output voltage Laplace transform is given by

$$V_s(s) = sR_f(C_s - C_r)|V_m| \left[ 1 + \frac{1}{A_v(s)} + \frac{sR_f(C_r + C_s + C_p)}{A_v(s)} \right]^{-1} \quad (3.203)$$

where  $A_v(s)$  is the transform of the operational-amplifier's open-loop gain. For large open-loop gain, the small-signal output voltage transform is

$$V_s(s) \simeq sR_fC_{svo}|V_m| \left( \frac{\Delta z}{z_o} \right) \quad (3.204)$$

We can increase feedback resistance or the modulation frequency and voltage to increase the sensor gain. However, modulation voltage should be as small as possible to reduce the effects of electrostatic force on the structure, modulation frequency is limited by the bandwidth of the operational amplifier, and feedback resistance is limited by available die area. A reasonable set of values are  $|V_m|=0.3$  V,  $f_m=1$  MHz,  $R_f=200$  k $\Omega$ ,  $C_{svo}=44$  fF, and  $z_o=2$   $\mu$ m, giving a sensitivity of 8.2 mV/ $\mu$ m.

### 3.6.2.2 Transresistance Amplifier

#### Circuit Description

We have implemented the transresistance amplifier using a conventional two-stage CMOS operational amplifier. A circuit schematic of the transresistance amplifier is shown in Figure 3.47. The differential input stage is followed by a common-source second stage. A complementary source-follower output stage is used to drive the signal off-chip.

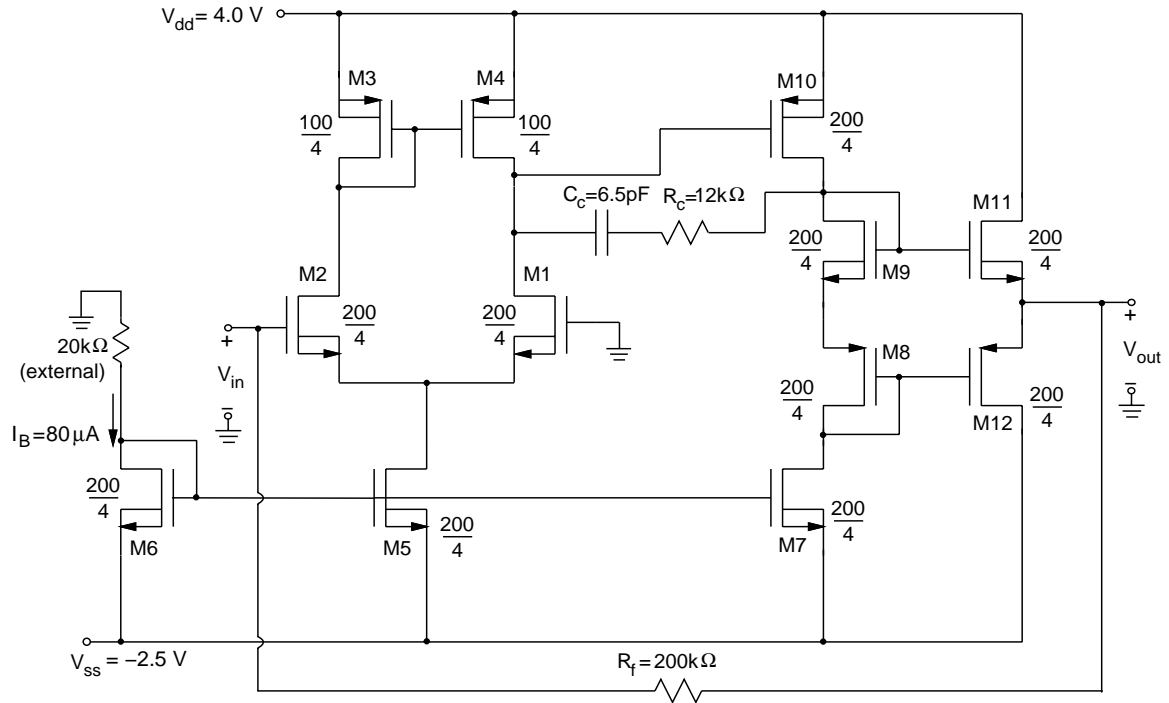
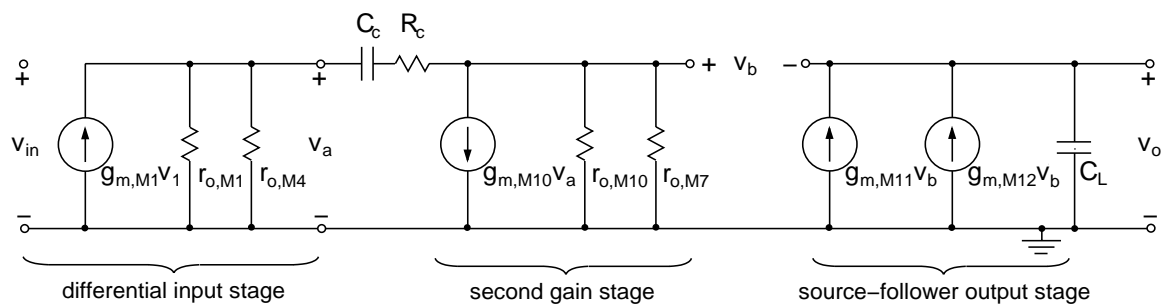


Figure 3.47: Transresistance amplifier circuit schematic.

Figure 3.48: Low-frequency, small-signal equivalent circuit of the two-stage CMOS operational amplifier, where  $C_c$  sets the dominant pole.

### Transresistance Amplifier Gain and Bandwidth

A low-frequency, small-signal equivalent circuit is shown in Figure 3.48. The operational-amplifier open-loop gain is modeled with a two-pole transfer function given by

$$A_v(s) = \frac{A_{vo}}{(1 + s/p_1)(1 + s/p_2)} \quad (3.205)$$

where the low-frequency open-loop gain,  $A_{vo}$ , is

$$A_{vo} = \left( \frac{g_{m,M1}}{g_{o,M1} + g_{o,M4}} \right) \left( \frac{g_{m,M10}}{g_{o,M7} + g_{o,M10}} \right) \quad (3.206)$$

The transistor output conductance  $g_o \equiv 1/r_o$ . The dominant pole,  $p_1$ , in the gain transfer function is set by the compensation capacitor,  $C_c$ , and is approximately equal to

$$p_1 = 2\pi f_1 = \frac{(g_{o,M1} + g_{o,M4})(g_{o,M7} + g_{o,M10})}{g_{m,M10}C_c} \quad (3.207)$$

Neglecting the non-dominant pole,  $p_2$ , the gain-bandwidth product, GBW, is

$$\text{GBW} = A_{vo}f_1 = \frac{g_{m,M1}}{2\pi C_c} \quad (3.208)$$

Values for the amplifier dc gain and gain-bandwidth product are determined using the transistor parameter values from section 3.6.1.3, yielding  $A_{vo}=5800$ , and  $\text{GBW}=9.4$  MHz.

For a large capacitive load,  $C_L$ , at the output, the non-dominant pole is approximately given by

$$p_2 = \frac{g_{m,M11} + g_{m,M12}}{C_L} \quad (3.209)$$

where we have neglected the body effect in the p-channel transistor, M12. Thus, an approximate stability criterion for the amplifier is

$$C_L \leq \left( \frac{g_{m,M11} + g_{m,M12}}{g_{m,M1}} \right) C_c \quad (3.210)$$

Substituting Equation (3.205) into (3.203) and neglecting  $p_2$ , we find the position-sensor output voltage transform to be

$$V_s(s) = \frac{sR_fC_{svo}|V_m|}{(1 + s/p_+)(1 + s/p_-)} \left( \frac{\Delta z}{z_o} \right) \quad (3.211)$$

where the poles,  $p_+$  and  $p_-$ , are located at

$$p_{\pm} = \frac{p_1 + p_f}{2} \left[ 1 \pm \sqrt{1 - 4(A_{vo} + 1) \frac{p_1 p_f}{(p_1 + p_f)^2}} \right] \quad (3.212)$$

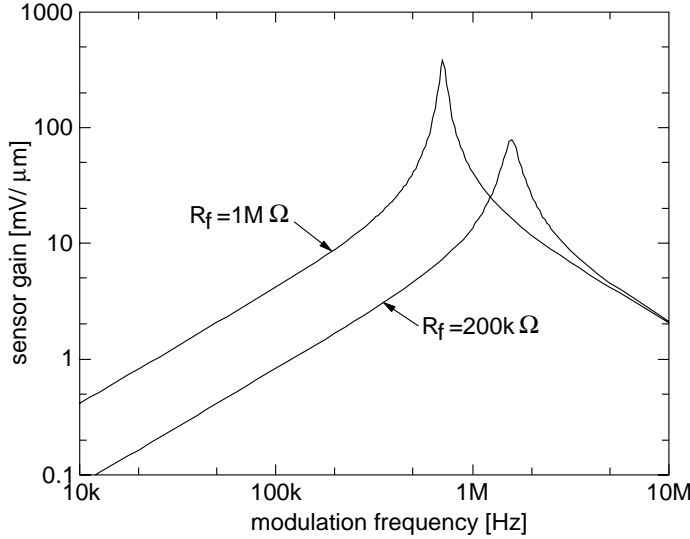


Figure 3.49: Plot of position-sensor gain versus modulation frequency for two values of feedback resistance,  $R_f=200\text{ k}\Omega$  and  $1\text{ M}\Omega$ .

and where  $p_f \equiv [R_f(C_r + C_s + C_p)]^{-1}$ . If we assume that the poles are complex pairs, which will be the case using typical parameter values, then Equation (3.212) simplifies to

$$p_{\pm} = \frac{p_1 + p_f}{2} \pm j\sqrt{\text{GBW } p_f} \quad (3.213)$$

Using  $R_f=200\text{ k}\Omega$  and  $C_p=3\text{ pF}$ , the poles are located at  $p_{\pm}=130\text{ kHz} \pm j1.6\text{ MHz}$ .

Position-sensor gain,  $V_s/\Delta z$ , is plotted as a function of the modulation frequency in Figure 3.49 for two values of feedback resistance,  $200\text{ k}\Omega$  and  $1\text{ M}\Omega$ . The complex-pole pair causes the gain to peak around a modulation frequency of  $1.6\text{ MHz}$ . Higher values of modulation frequency produce a roll-off in the gain. The usable range of modulation frequency values can be extended by increasing the gain-bandwidth product of the operational amplifier, or by reducing the parasitic capacitance to ground. Increasing the feedback resistor value increases the low-frequency sensor gain, reduces the complex-pole frequency, and increases the peak value of the gain. Eventually, when the complex-poles are located below the modulation frequency, increasing the feedback resistance will cause a decrease in sensor gain.

### Transresistance Amplifier Noise

Noise models for the transresistance amplifier are shown in Figure 3.50. Transistors M1 through M4 in the differential input stage contribute to the equivalent noise voltage of

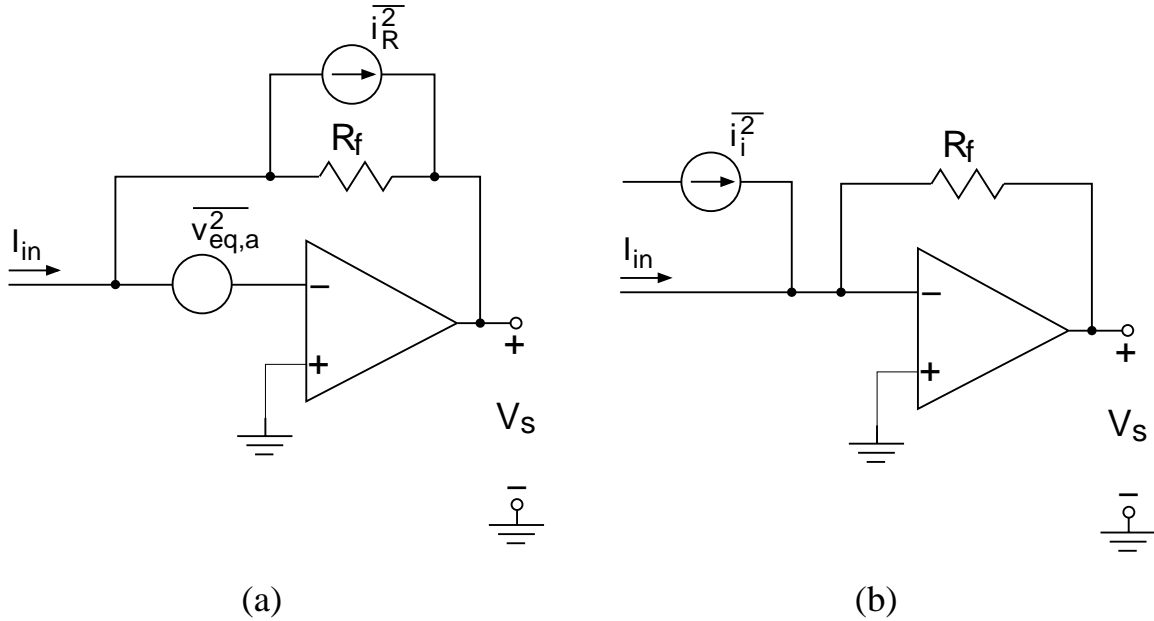


Figure 3.50: Noise models of the transresistance amplifier. (a) Model including equivalent noise voltage of the transresistance amplifier. (b) Equivalent input-referred noise current model.

the operational amplifier,  $\overline{v_{eq,a}^2}$ .

$$\overline{v_{eq,a}^2} = \overline{v_{eq1}^2} + \overline{v_{eq2}^2} + \left( \frac{g_{m,M4}}{g_{m,M1}} \right)^2 \left( \overline{v_{eq3}^2} + \overline{v_{eq4}^2} \right) \quad (3.214)$$

where  $\overline{v_{eq}^2}$  for individual transistors is given by Equation (3.189). Transistor noise voltage from the other stages are neglected, since the input-referred noise is reduced by the first-stage gain. As in the buffer noise analysis, interconnect thermal noise is ignored, but will be considered in section 3.6.3, when we calculate the sensor noise position.

The equivalent input-referred noise current,  $\overline{i_i^2}$ , shown in Figure 3.50(b), has components from  $\overline{v_{eq,a}^2}$  and from the feedback resistor.

$$\overline{i_i^2} = 4k_B T \left( \frac{1}{R_f} \right) \Delta f + \left( \frac{\overline{v_{eq,a}^2}}{R_f^2} \right) \Delta f \quad (3.215)$$

Most of the input-referred noise current is generated by the feedback resistor, assuming  $g_m R_f \gg 1$  (where  $g_m$  represents any of the transistor transconductance values). For the circuit in Figure 3.47,

$$\frac{\overline{i_i^2}}{\Delta f} = 8.5 \times 10^{-26} \text{A}^2 + \frac{4.5 \times 10^{-22} \text{A}^2/\text{s}}{f} \quad (3.216)$$

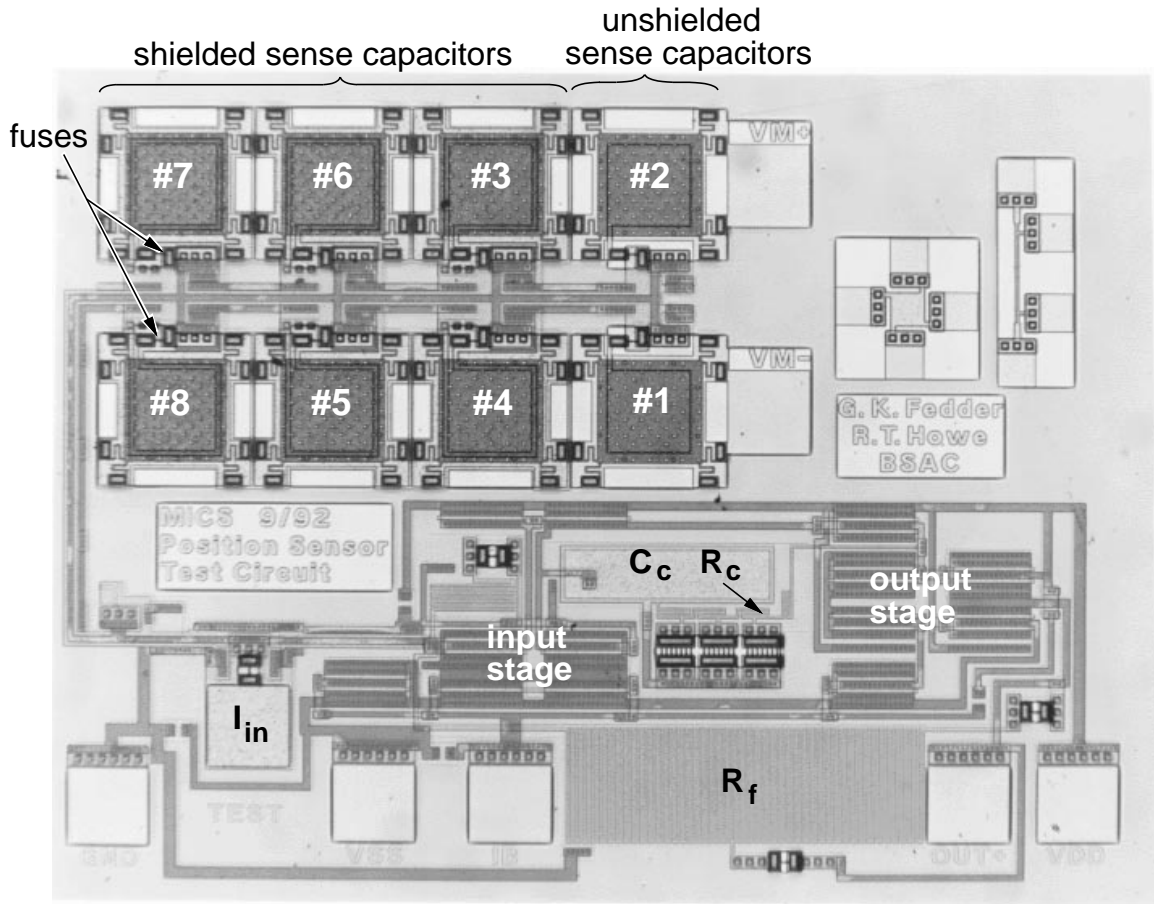


Figure 3.51: SEM of the capacitive position-sense test circuit with a transresistance amplifier.

where the feedback resistor contributes 97 % of the thermal input-referred noise current. Thermal noise dominates flicker noise at frequencies above about 5.3 kHz.

### 3.6.2.3 Transresistance Amplifier Test Circuit

We used the capacitive divider design in Figure 3.42 in conjunction with the transresistance amplifier to test the displacement-current sensing method. The fabricated test circuit is shown in Figure 3.51.

When the transresistance amplifier output node is connected to a coaxial cable, the output voltage oscillates with a frequency of around 1 MHz. The load capacitance due to the cabling is much larger than the 6.5 pF compensation capacitor, making the circuit unstable. After lowering the load capacitance, the output stabilizes; however, we do not see a sensor

signal when we apply the modulation voltages to the capacitive divider. Unfortunately, the sensor gain is much smaller than anticipated because the measured feedback resistor value of  $34\text{ k}\Omega$  is much lower than the design value of  $200\text{ k}\Omega$ . We designed the resistor using the sheet resistance value of the sensor “ground-plane” polysilicon layer,  $197\text{ }\Omega/\square$ ; however, the resistor is formed from the gate polysilicon layer, which has a lower sheet resistance of  $12.5\text{ }\Omega/\square$ . The two polysilicon films are deposited using the same recipe, but in different reactors, giving an order of magnitude difference in sheet resistance. We made sheet resistance measurements on several runs showing a consistent difference between the two films. No further testing was done on the transresistance amplifier test circuit.

### 3.6.3 Sensor Noise and Minimum Detectable Signal

We will derive the minimum detectable displacement for both the voltage-sensing and current-sensing methods by referring noise to the position input. Thermal noise from the sensor interconnect can contribute a significant fraction of the total sensor noise and, thus, will be added to the analysis. Noise performance of the two detection methods can be compared by calculating the ratio of the voltage-sensing-method input-referred noise position,  $\overline{z_v^2}$ , to the current-sensing-method input-referred noise position,  $\overline{z_i^2}$ . We then compare the electronic noise with Brownian (thermal) noise position of the micromechanical sensor mass and discuss how the position-sensitivity limit can be increased.

#### 3.6.3.1 Interconnect Noise

Interconnect to the capacitive divider is commonly formed from resistive polysilicon layers. An especially large resistance often exists in series with the micromechanical upper plate, since electrical connection must be made through the slender beams of the polysilicon suspension. This resistance,  $R_m$ , is illustrated in the equivalent circuit models of Figure 3.52, where we have lumped the resistance on one side of the divider. Also, a substantial resistance  $R_p$  may exist between the high-impedance node of the divider and input of the buffer or transresistance amplifier. For the voltage-sensing case, the equivalent interconnect noise voltage, referred to the buffer input, is

$$\overline{v_R^2} = 4k_B T \left( \frac{C_{so}}{C_r + C_{so} + C'_p} \right)^2 R_m \Delta f + 4k_B T R_p \Delta f \quad (3.217)$$

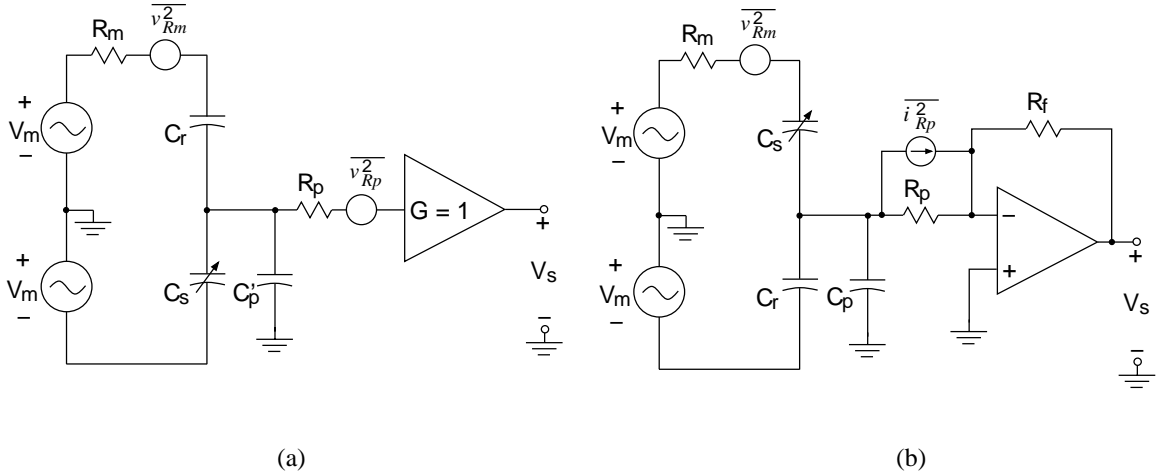


Figure 3.52: Equivalent circuit models, illustrating interconnect noise sources. (a) Unity-gain-buffer sensor. (b) Transresistance-amplifier sensor.

Both  $R_m$  and  $R_p$  directly contribute to the input-referred noise voltage and should be included when determining the total sensor noise. For the current-sensing case, the equivalent interconnect noise current, referred to the transresistance-amplifier input, is

$$\overline{i_R^2} = \frac{4k_B T}{R_m} \left( \frac{(\omega R_m C_{so})^2}{(\omega R_m C_{so})^2 + 1} \right) \Delta f + \frac{4k_B T}{R_p} \left( \frac{[\omega R_p (C_r + C_{so} + C_p)]^2}{[\omega R_p (C_r + C_{so} + C_p)]^2 + 1} \right) \Delta f \quad (3.218)$$

where  $\omega = 2\pi f$ . The input-referred noise current is pushed to high frequencies, becoming constant above the  $1/RC$  pole locations. Even though  $R_m$  and  $C_p$  can be large, the time constants  $R_p C_p$  and  $R_m C_{so}$  are usually below 10 ns and the interconnect noise can be neglected. However, some care should be taken to keep  $R_p$  small.

### 3.6.3.2 Electronic Sensor Noise

Relations between the displacement and sensor output voltage are needed to determine the input-referred noise position. The voltage-sensing-method position-sensor gain is found by rearranging Equation (3.179) to give

$$\frac{|V_s|}{\Delta z} \equiv \frac{G_o |V_m|}{z_o} \left( \frac{C_{svo}}{C_r + C_{so} + C'_p} \right) \quad (3.219)$$

where  $|V_s|$  is the output amplitude. By scaling the buffer noise voltage by the gain<sup>25</sup>, we find the input-referred noise position,

$$\overline{z_v^2} \equiv \left( \frac{z_o}{|V_m|} \right)^2 \left( \frac{C_r + C_{so} + C'_p}{C_{svo}} \right)^2 \left( \overline{v_b^2} + \overline{v_R^2} \right) \quad (3.220)$$

where  $\overline{v_b^2}$  is the buffer noise voltage, given by Equation (3.194). Additionally, if we assume that the frequencies of interest are sufficiently large such that  $1/f$  noise can be neglected, then

$$\begin{aligned} \overline{z_v^2} \equiv & 4k_B T \left( \frac{z_o}{|V_m|} \right)^2 \left( \frac{C_r + C_{so} + C'_p}{C_{svo}} \right)^2 \left( \frac{4}{3g_{m,M1}} \left( 1 + \frac{g_{m,M6}}{g_{m,M1}} \right) + R_p \right) \Delta f + \\ & 4k_B T \left( \frac{z_o}{|V_m|} \right)^2 R_m \Delta f \end{aligned} \quad (3.221)$$

For the voltage-sense method, the minimum detectable displacement can be improved by decreasing the air gap or parasitic capacitance, or by increasing the modulation amplitude or the transconductance of the buffer input transistors. The input-referred noise position is  $0.0045 \text{ \AA}/\sqrt{\text{Hz}}$  for the capacitive divider and buffer in section 3.6.1, where  $C_r = C_{so} = C_{svo} = 44 \text{ fF}$ ,  $C'_p = 100 \text{ fF}$ ,  $z_o = 2 \mu\text{m}$ ,  $|V_m| = 0.3 \text{ V}$ ,  $R_m = R_p = 10 \text{ k}\Omega$ , and  $\sqrt{\overline{v_b^2}} = 8.8 \text{ nV}/\sqrt{\text{Hz}}$ . The interconnect thermal noise represents 45% of the total value.

The sensor application dictates the noise bandwidth of the system. In accelerometer applications, the signal bandwidth of interest is usually very low — around dc to 1 kHz — but in position-control applications, a high signal bandwidth is desirable. The noise position value given above corresponds to a minimum detectable signal of  $0.14 \text{ \AA}$  in a 1 kHz bandwidth, which is equivalent to a change in the sense capacitance of  $0.3 \text{ aF}$  ( $1 \text{ aF} \equiv 10^{-18} \text{ F}$ ), or about a 0.6-electron average difference on the plates (out of about 82000 electrons).

Similarly, the current-sensing-method position-sensor gain is found directly from Equation (3.203) and restated as

$$\frac{|V_s|}{\Delta z} \simeq \frac{2\pi f_m R_f C_{svo} |V_m|}{z_o} \quad (3.222)$$

where we have neglected the effects of gain peaking. For our noise calculations, we will assume the optimum modulation frequency to achieve the maximum sensor gain. From

---

<sup>25</sup>The buffer noise voltage is already referred to the buffer input, so the factor of  $G_o$  is not included when referring back to the position input.

Equation (3.213), this maximum modulation frequency,  $f_{mm}$ , is approximately

$$f_{mm} \approx \sqrt{\frac{\text{GBW}}{2\pi R_f(C_r + C_{so} + C_p)}} \quad (3.223)$$

We find the relation between the transresistance-amplifier input current,  $i_{in}$ , and displacement by substituting Equation (3.223) into (3.222) and using  $i_{in} \simeq V_s/R_f$ .

$$\frac{|i_{in}|}{\Delta z} \simeq \frac{C_{svo}|V_m|}{z_o} \sqrt{\frac{2\pi \text{ GBW}}{R_f(C_r + C_{so} + C_p)}} \quad (3.224)$$

Input-referred noise position is

$$\overline{z_i^2} = \left( \frac{\Delta z}{|i_{in}|} \right)^2 (\overline{i_i^2} + \overline{i_R^2}) \simeq \left( \frac{z_o}{C_{svo}|V_m|} \right)^2 \frac{R_f(C_r + C_{so} + C_p)}{2\pi \text{ GBW}} (\overline{i_i^2} + \overline{i_R^2}) \quad (3.225)$$

where  $\overline{i_i^2}$  is the transresistance-amplifier noise current, given by Equation (3.215). If we assume the feedback resistor's thermal noise is dominant, the input-referred noise position becomes

$$\overline{z_i^2} \simeq \left( \frac{z_o}{C_{svo}|V_m|} \right)^2 \frac{4k_B T (C_r + C_{so} + C_p)}{2\pi \text{ GBW}} \Delta f \quad (3.226)$$

The minimum detectable displacement can be improved by decreasing the air gap or parasitic capacitance, or by increasing the amplifier bandwidth or modulation amplitude. Changing the feedback resistance does not affect the minimum detectable displacement, however, the modulation frequency must then compensate for the change in transresistance-amplifier gain. For the capacitive divider and transresistance amplifier in section 3.6.2, the input-referred noise position is  $0.045 \text{ \AA}/\sqrt{\text{Hz}}$ , where  $C_r = C_{so} = C_{svo} = 44 \text{ fF}$ ,  $C_p = 3 \text{ pF}$ ,  $z_o = 2 \mu\text{m}$ ,  $|V_m| = 0.3 \text{ V}$ , and  $\text{GBW} = 9.4 \text{ MHz}$ . Addition of the interconnect noise, using resistance values  $R_m = R_p = 10 \text{ k}\Omega$ , increases the input-referred noise position to  $0.064 \text{ \AA}/\sqrt{\text{Hz}}$  at the modulation frequency of 1.5 MHz. In this case, the minimum detectable signal in a 1 kHz bandwidth is about  $2 \text{ \AA}$ .

The ratio of input-referred noise position for the two sensing methods is found by dividing Equation (3.221) by (3.226), yielding

$$\frac{\overline{z_v^2}}{\overline{z_i^2}} \approx \left[ \frac{2\pi \text{ GBW} (C_r + C_{so} + C'_p)^2}{(C_r + C_{so} + C_p)} \right] \left( \frac{4}{3g_{m,\text{M1}}} \right) \left( 1 + \frac{g_{m,\text{M6}}}{g_{m,\text{M1}}} \right) \quad (3.227)$$

For simplicity, we have ignored the interconnect noise. Using values from the two sensor designs, we find that the voltage-sensing method is about 18 times more sensitive than the current-sensing method.

### 3.6.3.3 Brownian Noise

Air molecules impinging on the micromechanical plate gives rise to a Brownian noise force,  $\overline{f_n^2}$ , which is related to the damping associated with the plate by [86]

$$\overline{f_n^2} = 4k_B T B \Delta f \quad (3.228)$$

where  $B$  is the damping coefficient. For a micromechanical mass-spring-damper system, like the sensor plate, the external force is given by Equation (3.14), and has a velocity-proportional damping force equal to

$$F_B = B \frac{dx}{dt} \quad (3.229)$$

The damping coefficient can be expressed in terms of the damping factor,  $\zeta_z$ , by matching velocity terms in Equations (3.14) and (3.229), giving

$$B = 2\zeta_z m \omega_z \quad (3.230)$$

or, for underdamped systems, it can be expressed in terms of quality factor,  $Q$ , by

$$B \simeq \frac{m \omega_z}{Q} \quad (3.231)$$

Substituting Equation (3.230) into (3.228), we arrive at

$$\overline{f_z^2} = 4k_B T (2\zeta_z m \omega_z) \Delta f \quad (3.232)$$

The Brownian noise force can be referred to the plate position; for open-loop systems,

$$\overline{z_{eq}^2} = 4k_B T \left( \frac{2\zeta_z}{m \omega_z^3} \right) \frac{1}{(1 - \omega^2/\omega_z^2)^2 + (2\zeta_z \omega/\omega_z)^2} \Delta f \quad (3.233)$$

where the noise spectral density has the same frequency response as the mechanical mass-spring-damper. A resonance peak will occur in the equivalent noise position of underdamped systems. In force-feedback systems, the Brownian noise force can be detected and nulled at frequencies below the electrical bandwidth of the system. Therefore, equivalent Brownian noise position is much lower in closed-loop systems.

In our open-loop position-sensor test circuits, the extremely stiff plate suspension of the capacitors produces a large resonant frequency, a large Brownian noise force, and a very small equivalent Brownian noise position. Mechanical parameter values for these capacitors are  $m=47$  ng,  $\zeta_z=0.15$ , and  $\omega_n=1.1$  MHz; the resulting value for low-frequency

equivalent Brownian noise position is  $5 \times 10^{-6} \text{ \AA}/\sqrt{\text{Hz}}$ . Thus, for our position-sensor test circuits, the minimum detectable signal is limited by the electronic noise. Compliant microstructures will have a much larger equivalent Brownian noise position in open-loop operation.

For accelerometers, Brownian noise is usually referred to an external acceleration input instead of position. Brownian noise acceleration is given by

$$\overline{a_{\text{eq},z}^2} = 4k_B T \left( \frac{2\zeta\omega_z}{m} \right) \Delta f \quad (3.234)$$

Unlike the noise position, the noise acceleration has a constant spectral density. By reducing the damping or increasing the proof mass<sup>26</sup>, minimum detectable acceleration can be pushed lower. A large micromechanical plate is usually overdamped in air. Quality factor can be increased by reducing the ambient pressure. Micromechanical quality factors up to 80000 have been reported [87], which translates into greater than a 300-fold decrease in Brownian noise.

A high-performance accelerometer would have a larger mass and a lower resonant frequency than our position-sense test structures. Mechanical parameter values for a high-Q accelerometer design are  $m=500 \text{ ng}$ ,  $Q=80000$ , and  $\omega_n=1 \text{ kHz}$ , corresponding to an equivalent Brownian noise acceleration of  $1.6 \mu\text{G}/\sqrt{\text{Hz}}$ . ( $1 \text{ G} \equiv 9.8 \text{ m/s}^2$ ). In comparison, the unity-gain-buffer equivalent noise contribution<sup>27</sup> of  $18 \mu\text{G}/\sqrt{\text{Hz}}$  is about 125 times larger (in noise power) than the Brownian noise. Therefore, electronic noise from the unity-gain buffer limits the minimum detectable acceleration to  $560 \mu\text{G}$  in a 1 kHz signal bandwidth. Further improvements in acceleration sensitivity require noise reduction in the buffer electronics. Eventually, Brownian noise will limit the minimum detectable acceleration to  $51 \mu\text{G}$  in a 1 kHz bandwidth.

If the current-sense method is used, the mean-square transresistance-amplifier noise contribution is about 25000 times larger (in noise power) than the Brownian noise. Thus, the transresistance amplifier is a poor choice for position sensing of high-Q accelerometers.

---

<sup>26</sup>A larger proof mass gives a larger Brownian noise force, but also increases the external force signal. The net result is a decrease in equivalent noise acceleration

<sup>27</sup>Equivalent noise acceleration of the unity-gain buffer is

$$\sqrt{\overline{a_{\text{eq},v}^2}} = \omega_z^2 \sqrt{\overline{z_v^2}} = 4\pi^2 (1 \text{ kHz})^2 (0.0045 \text{ \AA}/\sqrt{\text{Hz}}) = 18 \mu\text{G}/\sqrt{\text{Hz}}$$

## Chapter 4

# Integrated Micromechanical Testbed

### 4.1 Introduction

Digital closed-loop control of MEMS involves the design and simulation of mixed analog-digital, electro-mechanical systems. Prior work has focussed exclusively on the sigma-delta ( $\Sigma$ - $\Delta$ ) stabilization of single-mode microaccelerometers [88, 64, 89]. MEMS applications such as vibratory rate gyroscopes, multi-axis accelerometers and actively positioned mirrors require digital control of multiple degrees of freedom. In this chapter, we present an integrated testbed that enables the experimental verification of models and simulations of general control strategies for a suspended plate with three degrees of freedom.

The testbed project closely followed work at U. C. Berkeley on a force-balanced  $\Sigma$ - $\Delta$  accelerometer by Yun [64]. In particular, the fabrication process, capacitive position sensor, and two-bit<sup>1</sup> feedback concepts are borrowed from his accelerometer design. Based on this previous work, we have made improvements in all three of these areas, with the details described in sections 4.4, 3.6.1, and 5.5.

In this chapter, we will first discuss the  $\Sigma$ - $\Delta$  architecture. Then, the testbed design will be presented, followed by a description of the fabrication process. Modeling, simulation, and experimental results are presented in the following chapters.

---

<sup>1</sup>That is, in the digital sense.

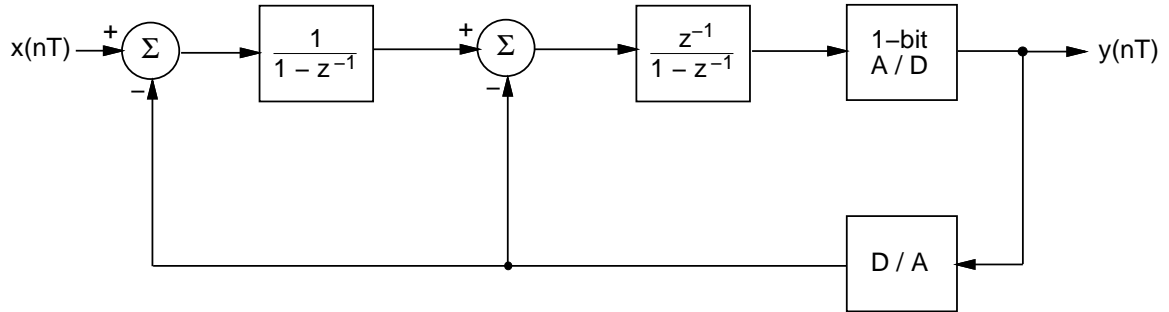


Figure 4.1: Block diagram of a conventional  $\Sigma$ - $\Delta$  modulator.

## 4.2 Sigma-Delta Architecture

An understanding of micromechanical  $\Sigma$ - $\Delta$  control requires an introduction to the conventional second-order  $\Sigma$ - $\Delta$  modulator [90], shown in Figure 4.1. The input data,  $x(nT)$ , is sampled with period,  $T$ , and passed through a closed-loop system that has two discrete integrators and a one-bit analog-to-digital (A/D) converter in the forward path. The A/D output,  $y(nT)$ , is converted to an analog signal (D/A conversion) and fed back to the summing nodes in front of the integrators. If the sampling rate is much higher than the input signal bandwidth, the digital output will be a pulse-density-modulated version of the input signal. Subsequent digital low-pass filtering of the output bitstream provides a precision A/D conversion of the input signal.

Advantages of the  $\Sigma$ - $\Delta$  architecture over other A/D-converter designs include superior linearity, large dynamic range, and simple electronics. The input-to-output relationship is inherently linear, because the D/A feedback signal has only two states. The integrators attenuate the high-frequency switching component of the feedback, reducing the switching effects on the low-frequency output signal. Because the feedback is quantized into two states, unwanted noise from these high-frequency switching components is called quantization noise. Output precision is dependent on timing precision, not on the analog precision of the components in the loop. Essentially, crude two-state precision in the feedback is compensated by having excellent temporal resolution. Thus, the  $\Sigma$ - $\Delta$  loop can be implemented with fast, accurate digital timing circuitry that is easy to construct.

Sigma-delta feedback was first applied to micromechanical elements in a bulk-micromachined accelerometer by Henrion [88]. In that paper, the basic concepts of the micromechanical  $\Sigma$ - $\Delta$  loop were introduced. The testbed  $\Sigma$ - $\Delta$  loop, shown in Figure 4.2, is

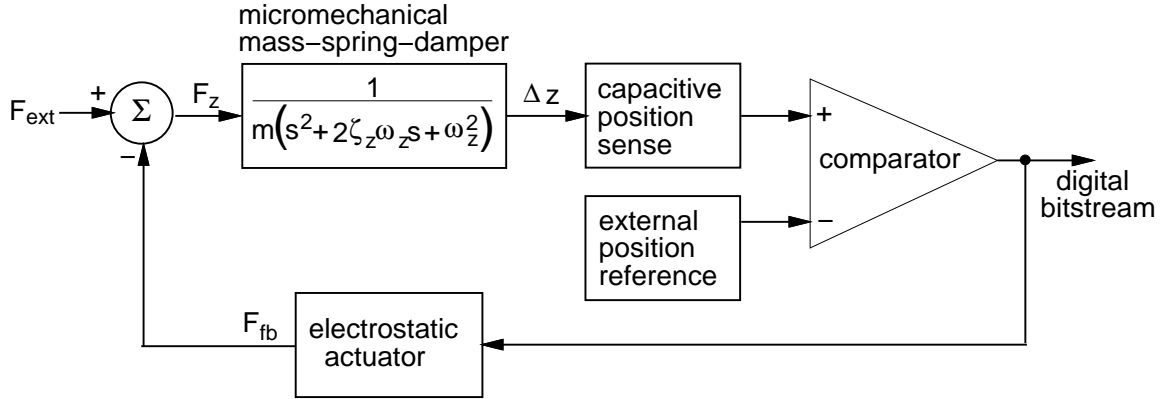


Figure 4.2: Block diagram of a micromechanical  $\Sigma$ - $\Delta$  loop.

based on a high-frequency one-bit comparison between the output of a position sensor and an external reference, which generates a serial bitstream. An electrostatic actuator converts the bitstream into two force-feedback levels that act on the structure. The benefits of  $\Sigma$ - $\Delta$  control extend to the micromechanical system, providing inherently linear, precision sensing of the external force input, without the need for precision position sensing. The micromechanical mass-spring-damper replaces the two discrete-time integrators in the conventional  $\Sigma$ - $\Delta$  modulator. Frequency components of the feedback above mechanical resonance are attenuated by the mechanical double integration. With proper attention to stability of the digital control loop, the mass is forced to the average position corresponding to the reference input. The critical circuit design issues are the position-sensor sensitivity, (not precision) and speed to reduce the quantization position noise. An analysis of quantization noise will be presented later, in section 5.6.2.

Unlike the conventional  $\Sigma$ - $\Delta$  modulator, the micromechanical version has no inner-feedback loop. In mechanically underdamped operation, direct feedback from the  $\Sigma$ - $\Delta$  comparator provides a force which is  $180^\circ$  out of phase with the displacement, resulting in uncontrolled oscillation at the resonant frequency. Thus, some other form of compensation is necessary to implement velocity-proportional feedback that would stabilize an underdamped micromechanical mass-spring-damper. With compensation, the displacement stabilizes to a bounded limit-cycle oscillation. Limit cycles in conventional  $\Sigma$ - $\Delta$  modulators have been studied previously to determine the structure of quantization noise [91].

Details of the digital compensation and an analysis of limit cycles are presented in

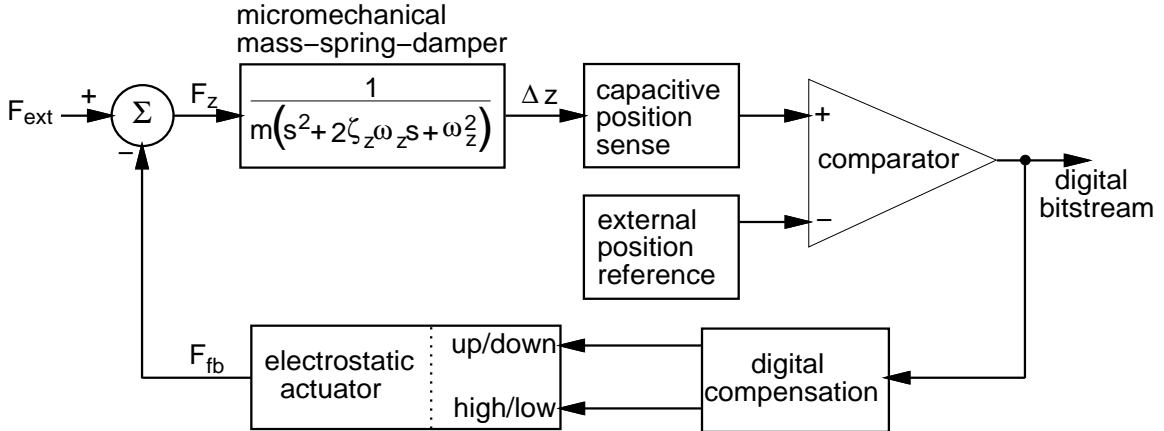


Figure 4.3: Block diagram of a micromechanical  $\Sigma$ - $\Delta$  loop with digital compensation in the feedback path.

section 5.5; we will only provide a brief description of the compensation here. Previously, analog lead-lag compensation was used in the Henrion accelerometer, to permit operation in a vacuum. Two-bit digital compensation of a high- $Q$  micromechanical  $\Sigma$ - $\Delta$  loop was first proposed by Yun [64]. A similar digital feedback scheme is implemented in the testbed, but, instead of a fixed two-bit gain, an adjustable gain can be set to minimize the limit-cycle amplitude. A digital compensation circuit in the feedback path drives a differential electrostatic actuator, as shown in Figure 4.3. The extra high-force levels are introduced to implement digital velocity-proportional feedback. Sensor linearity is not affected, because the high-force pulses average to zero. Previous compensation schemes were presented without experimental verification. We have successfully operated the testbed at low pressures, with the results reported in section 6.9.

### 4.3 Testbed Description

A rendering of one quarter of the testbed is shown in Figure 4.4. A polysilicon plate, which measures  $360 \mu\text{m} \times 380 \mu\text{m} \times 1.6 \mu\text{m}$  in thickness, is suspended  $2.2 \mu\text{m}$  above the substrate by four serpentine springs. The springs passively constrain lateral motion of the plate. Spring compliances can be configured in seven different ways<sup>2</sup> by

<sup>2</sup>The serpentine spring layout is shown in Figure A.3 followed by a tabulation of spring constants and resonant frequencies in Table A.2.

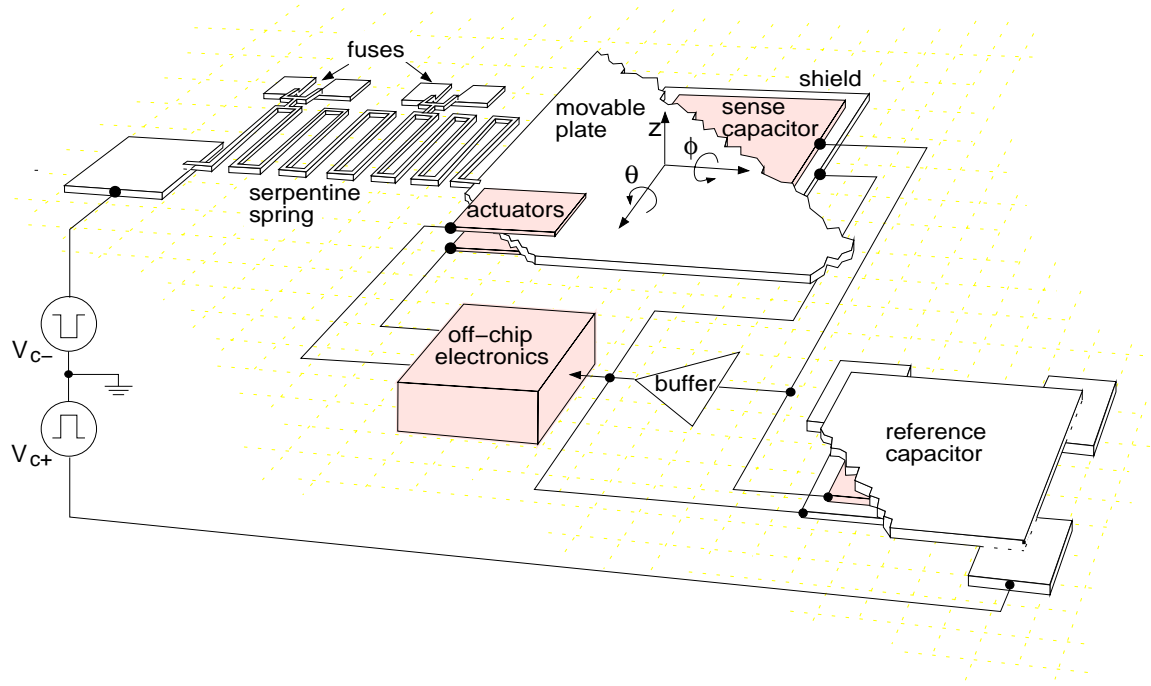


Figure 4.4: Schematic drawing of one quarter of the integrated testbed.

selectively cutting fuses<sup>3</sup> that anchor the springs in several locations. Physical dimensions and other parameters of the testbed are listed in appendix A.1. The plate is overdamped at room-ambient pressure; damping can be reduced to nearly zero by reducing the pressure. Vertical position,  $z$ , and angular rotation about the lateral axes,  $\theta$  and  $\phi$ , are controlled by four digital feedback loops. A parallel-plate vertical-position sense capacitor is located under each quadrant of the plate, forming a bridge with a fixed reference capacitor. Use of a driven shield electrode together with an integrated CMOS buffer amplifier, are required to detect the voltage change on the high-impedance node of the capacitive bridge. Integration of the buffer amplifiers eliminates most of the interconnect parasitic capacitance that would cause signal degradation. Off-chip  $\Sigma\Delta$  electronics supply digital feedback to electrostatic actuators at each corner of the plate.

The testbed is part of the multi-project chip shown in Figure 4.5. Microsystem designs from several other micromechanical research projects at U. C. Berkeley share area on the  $1 \text{ cm} \times 1 \text{ cm}$  die, including an accelerometer (designed by Crist Lu and Weijie Yun), gyroscopes (Per Ljung), microresonator oscillators (Clark Nguyen), microposition

<sup>3</sup>A close-up of one of the fuses is shown in Figure 2.45.

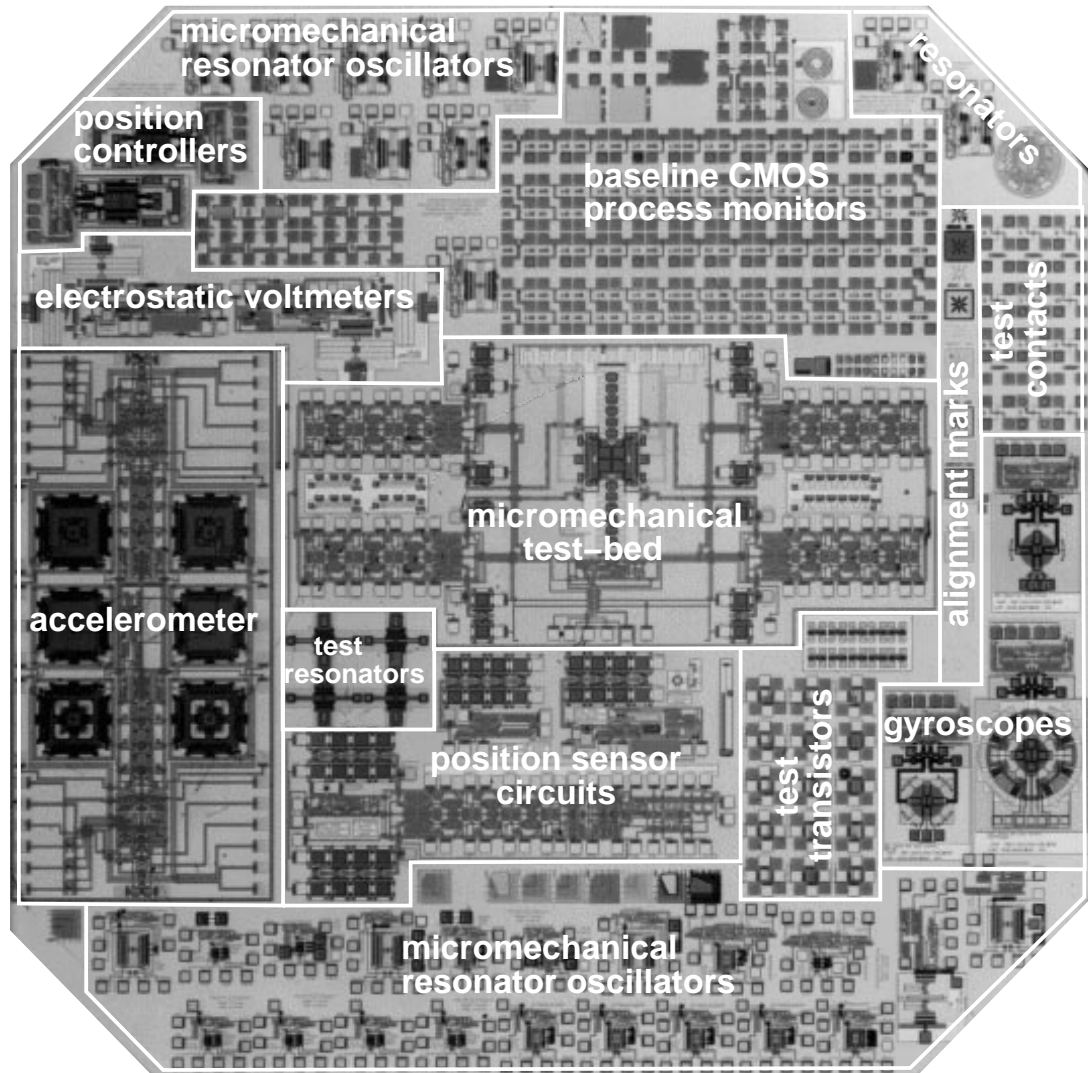


Figure 4.5: Optical photograph of the multi-project MICS chip.

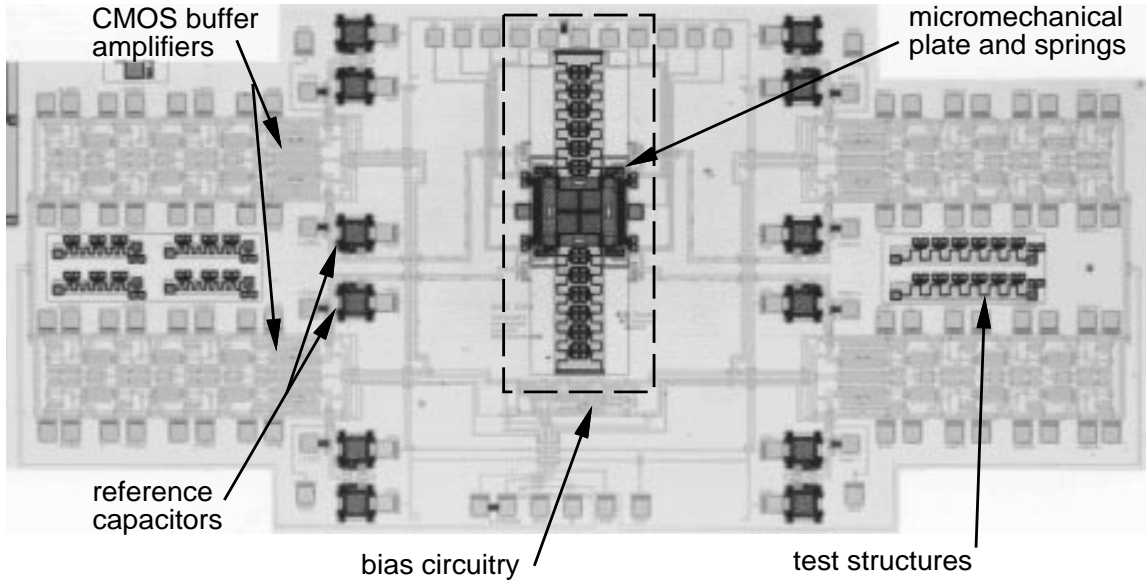


Figure 4.6: Die photograph of the integrated testbed. The dashed rectangle delimits the area shown in Figure 4.7.

controllers (Patrick Cheung), and electrostatic voltmeters (Kai Chen and David Loconto). The remaining real-estate is used for process monitors and test structures.

Figure 4.6 is an optical micrograph of the testbed, showing the micromechanical elements integrated with CMOS circuitry. Reference capacitors are made from rigidly supported micromechanical structures which match the sense capacitor layout. Variable gain differential amplifiers, included in the layout, suffer from a design error and are not used in the system. The eight reference capacitors located at the upper and lower corners of the layout are associated with the differential amplifiers, and are also not used. Bias circuitry is shared by the four buffer amplifiers. An expanded view of the polysilicon plate is shown in Figure 4.7. Two comb drives, located on two opposing sides of the plate, provide both a vertical levitation force and a lateral force for displacements up to  $10 \mu\text{m}$ . Each comb has 39,  $2 \mu\text{m}$ -wide,  $10 \mu\text{m}$ -long fingers. The four capacitive position sensors underneath the plate are identified, along with the upper parallel-plate feedback actuators.

A block diagram of one of the four independent feedback channels is shown in Figure 4.8. Each movable sense capacitor,  $C_s$ , forms a voltage divider with a corresponding fixed reference capacitor,  $C_r$ . Balanced square-wave voltage signals,  $V_{m+}$  and  $V_{m-}$ , provide up to 100 kHz,  $\pm 300 \text{ mV}$  modulation across the divider. A minimum-area diode,

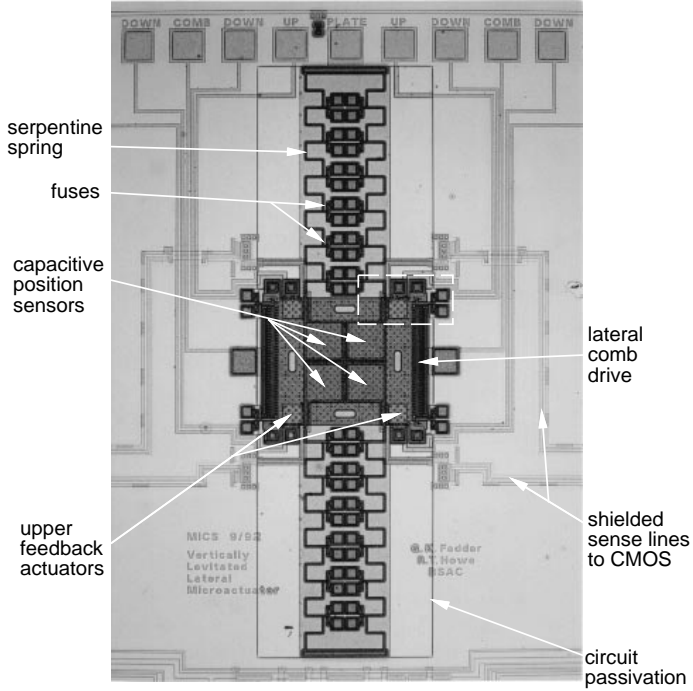


Figure 4.7: Expanded view of the polysilicon plate and serpentine springs. The white dashed rectangle delimits the area shown in Figure 4.10.

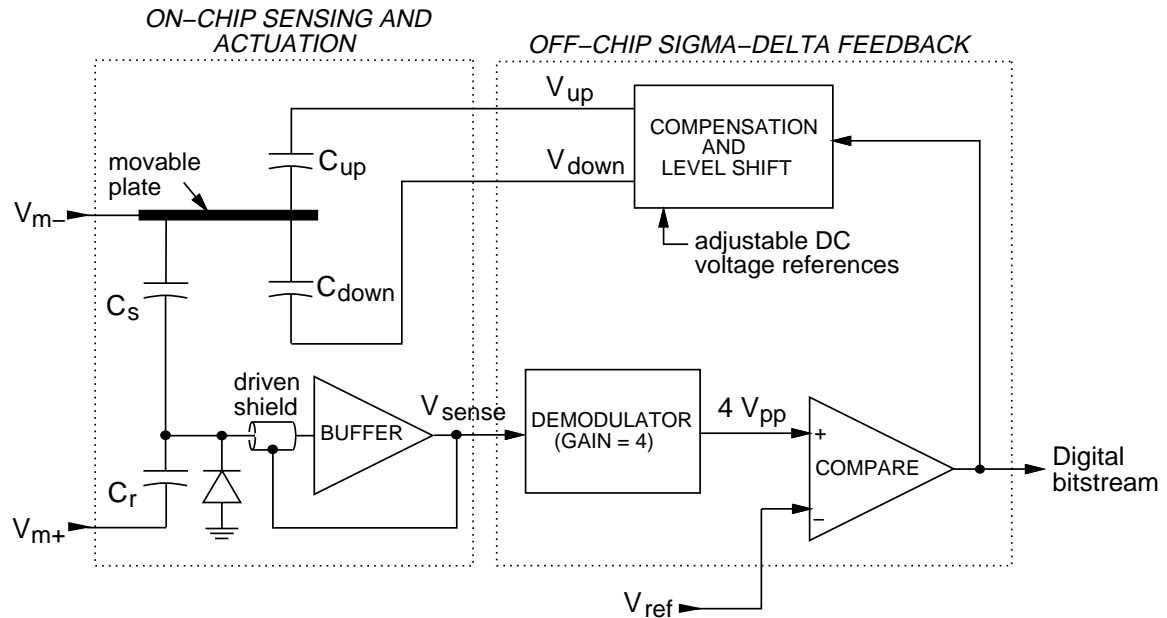


Figure 4.8: Block diagram of one corner of the integrated testbed.

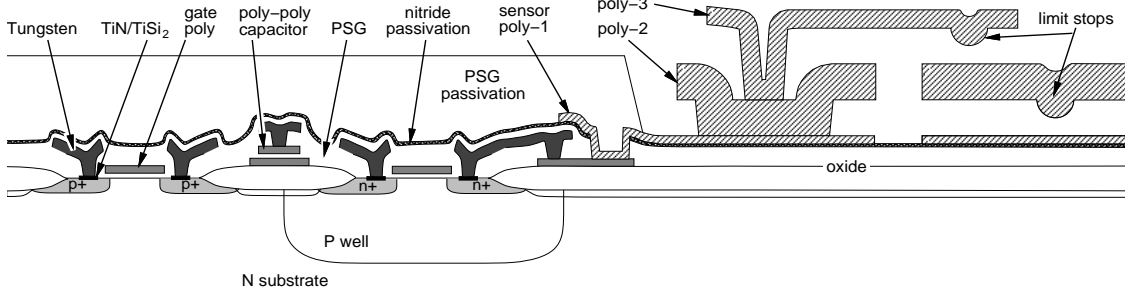


Figure 4.9: MICS process cross-section.

connected to the buffer input, supplies a dc bias to ground. The buffer output,  $V_{\text{sense}}$ , is routed off-chip, demodulated, and amplified to generate a signal proportional to the peak-to-peak buffer output,  $V_{pp}$ . This signal is compared with an external position reference voltage,  $V_{\text{ref}}$ , quantizing the plate position into two states. The external reference enables multi-mode position control, self-test, and offset trim. The comparator output drives a level-shifting network, which generates feedback voltages containing a difference term to stabilize underdamped mechanical systems. Feedback voltage levels are adjustable, allowing experimentation with values of full-scale force and compensation. The feedback voltages are sent on-chip to the parallel-plate actuators,  $C_{\text{up}}$  and  $C_{\text{down}}$ . Digital bitstreams from the comparators are filtered and combined to form multi-mode acceleration sense signals. More detailed schematics and photographs of the external electronics are in appendix A.2.1.

## 4.4 Fabrication

Fabrication of the integrated testbed utilizes the Berkeley MICS process: p-well 3- $\mu\text{m}$  CMOS integrated with polysilicon microstructures [64, 92]. A MICS process cross-section is shown in Figure 4.9. We will highlight some of the processing features and issues in this section. A complete MICS process flow can be referenced in appendix C.

### 4.4.1 Second Structural Polysilicon Layer

We have extended the original MICS process to include a second structural polysilicon layer (sensor poly-3 in Figure 4.9). The upper feedback actuator is made from the

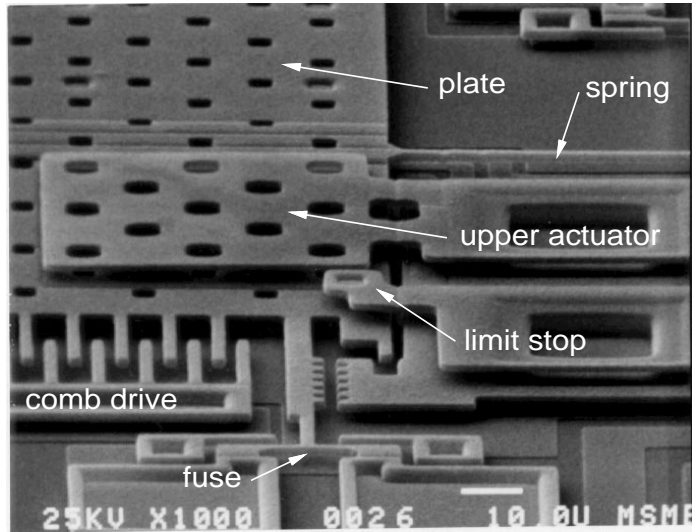


Figure 4.10: SEM of one corner of the movable plate, suspended below the upper actuator cantilever.

second structural layer, and shown in Figure 4.10. Upper limit stops, which prevent shorting of the actuators, are also made from the second structural layer. The spacer PSG acts as passivation for the tungsten metallization, and is only removed around the microstructure areas. Microstructure release in 5:1 BHF is done in darkness to avoid electrochemical etching of the polysilicon bonding pads.

Our original attempts at forming the second structural layer resulted in unwanted polysilicon stringers being deposited in 2  $\mu\text{m}$ -wide gaps between structures in the first structural layer (poly-2). The SEM of a comb-finger cross-section in Figure 4.11 shows the poly-3 stringers lodged between the poly-2 comb fingers. The phosphosilicate glass (PSG) film that acts as a vertical spacer between poly-2 and poly-3 does not conformally coat the region in the gap; instead, a keyhole-shaped void is formed. Subsequent deposition of the poly-3 layer fills this void from the open ends, forming a stringer. Isotropic etching will not remove the stringers, since they are covered with the PSG spacer film. In order to avoid the stringer formation, the sacrificial layer underlying the poly-3 layer is planarized by using a spin-on glass (SOG) film to fill the gaps. Processing the 2.7  $\mu\text{m}$ -thick sacrificial layer involves several steps: a 7000 Å-thick PSG deposition, two coats of spin-on glass (SOG) film and curing up to 425°C, etch-back of the SOG, a 2  $\mu\text{m}$ -thick PSG deposition, and rapid-thermal annealing (RTA) at 900°C for 30 s to densify the PSG. We observe some

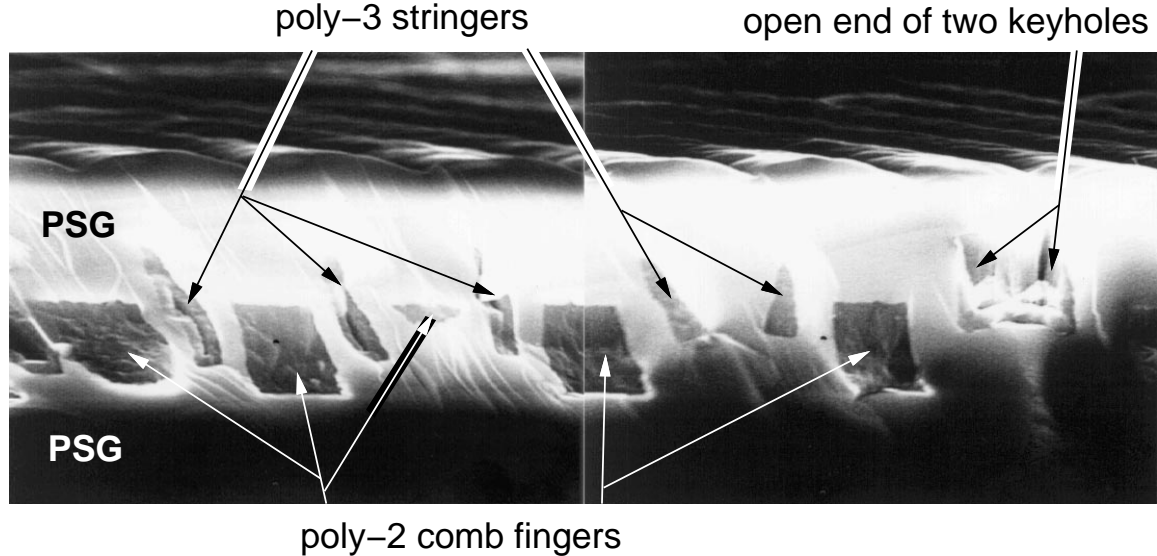


Figure 4.11: Composite of two SEMs of a cross-section of a comb drive, showing the poly-3 stringers between comb fingers. The cleave is made at an angle across the comb drive. At the left, both sets of comb fingers are visible, and at the right, only one side is visible. The voids on the left are not filled completely with polysilicon, because the ends of the void are filled, thereby prohibiting further deposition.

cracking and browning of the SOG film after the RTA. The cracks are of sub- $\mu\text{m}$  width and encased in PSG, therefore, they do not cause problems in subsequent processing steps. After sacrificial release, however, very small ( $< 2000\text{\AA}$ -wide) polymer stringers, shown in Figure 4.12, appear at the former SOG-crack locations, which are possibly formed from residual solvent left in the SOG and baked at  $900^\circ\text{C}$ . We are able to remove the stringers with a 1 hour, 5:1  $\text{H}_2\text{SO}_4:\text{H}_2\text{O}_2$  (pirahna) soak immediately after the BHF release.

#### 4.4.2 Rapid-Thermal Annealing of Residual Stress

As-deposited highly-doped polysilicon films have a large compressive residual stress and a large stress gradient through the film thickness, causing microstructures to buckle and deflect out of plane. Residual stress and stress gradients are greatly reduced by annealing the polysilicon film at temperatures above  $1000^\circ\text{C}$  for 1 hour [20]. The CMOS circuits and contacts under our microstructures cannot survive this long of an annealing step. Instead, we substitute an RTA step in the MICS process to anneal the structural polysilicon layers.

We performed a simple experiment to determine the optimum RTA time and tem-

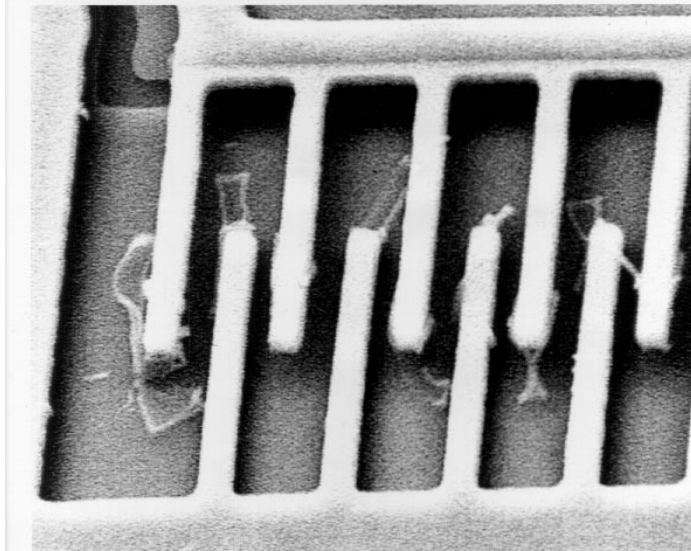


Figure 4.12: Polymer stringers after microstructure release.

perature to achieve minimum film stress. We deposited  $1.87 \mu\text{m}$  of *in situ* doped polysilicon (12 hr deposition at  $610^\circ\text{C}$ , 375 mT, 100 sccm SiH<sub>4</sub>, 1 sccm PH<sub>3</sub>) on top of  $2 \mu\text{m}$  PSG, and then patterned microstructural strain gauges. The wafer was cleaved into 4-die samples, each sample was subjected to a different RTA cycle, and all samples were simultaneously released in 10:1 HF. Our strain gauge design, pictured in Figure 4.13, is similar to the design reported by Lin [93]. Upon microstructure release, the 1 mm-long,  $16 \mu\text{m}$ -wide polysilicon beam in the strain gauge will release its residual stress by expanding, assuming compressive residual stress. The beam exerts a force on the crab-leg pivot, and the resulting angular deflection is magnified  $18\times$  by a cantilevered pointer. Deflection at the end of the pointer is measured optically using a displacement vernier (shown in Figure 4.13(b)) and the results are converted to strain. A summary of experimental results are presented in Table 4.1. Although the measurement uncertainty is large for the  $1050^\circ\text{C}$  anneals, we can draw some conclusions from this data. Values of residual stress are reduced more than  $20\times$  below the as-deposited value of 289 MPa. Microstructure stress gradients are not observable for RTA below  $950^\circ\text{C}$ , except on the sample annealed at 2 min,  $950^\circ\text{C}$ . We chose to anneal our MICS wafers twice at  $900^\circ\text{C}$  for 30 s, which is the same RTA cycle used to densify the PSG films. Therefore, the first structural polysilicon layer is annealed with three RTA cycles at  $900^\circ\text{C}$ . The resulting structural polysilicon is very flat, with no observable buckling, as illustrated

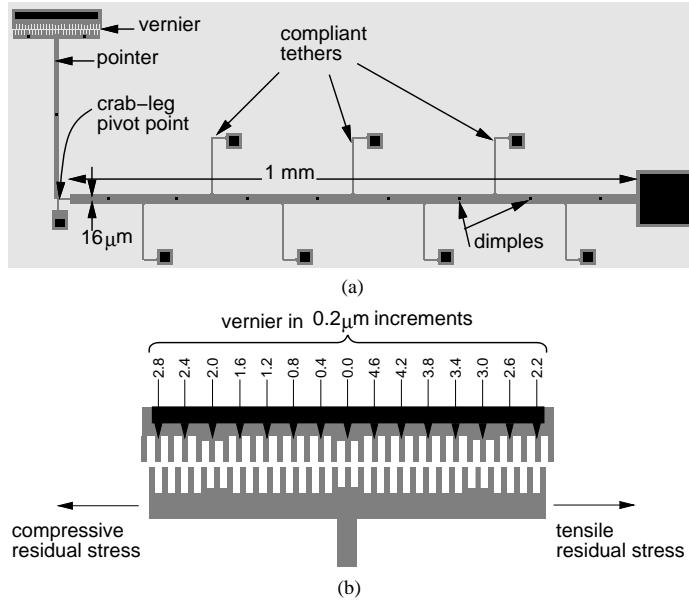


Figure 4.13: Strain-gauge design used to measure residual stress in microstructural polysilicon films. (a) Layout showing the 1 mm-long, 16  $\mu\text{m}$ -wide beam that releases its built-in axial stress. Crab-leg tethers and dimples keep the beam from sticking to the substrate without significantly affecting the strain measurement. (b) Enlargement of the displacement vernier with 0.2  $\mu\text{m}$  resolution.

temperature [°C]	time [min]	strain $\times 10^{-6}$	stress (E=165GPa) [MPa]	curl (see caption)
850	0.5	66±13 <sup>†</sup>	11±2 <sup>†</sup>	0
850	1	73±20 <sup>†</sup>	12±3 <sup>†</sup>	0
850	2	47±16 <sup>†</sup>	8±3 <sup>†</sup>	0
950	0.5	49±36	8±6	0
950	1	73±28	12±5	0
950	1	63±16	10±3	0
950	2	82±42	14±7	+
1050	0.5	33±95	5±16	+
1050	1	53±54	9±9	+
1050	2	70±45	12±7	++
no anneal		1750±16	289±3	++

Table 4.1: Experimental results of *in situ* phosphorous-doped polysilicon stress annealing using RTA. Stress and strain are given with  $\pm 3$ -sigma bounds. Out-of-plane curl of 940  $\mu\text{m}$ -long, 2  $\mu\text{m}$ -wide cantilever beams is qualitatively measured with an optical microscope, where “0” is no observable curl, “+” is up to 1  $\mu\text{m}$  of vertical deflection at the cantilever tip, and “++” is more than 1  $\mu\text{m}$  of deflection at the cantilever tip. <sup>†</sup> Some fixed-fixed beams are buckled on the samples annealed at 850°C, casting doubt on the accuracy of these strain values.

in Figure 4.10.

#### 4.4.3 TiSi<sub>2</sub> Contacts

Tungsten interconnect with TiN/TiSi<sub>2</sub> contacts is necessary to withstand the temperature of subsequent microstructure processing steps. The original MICS process used a 600 Å-thick sputtered Ti layer followed by a 600°C, 30 s RTA in N<sub>2</sub> to form the TiSi<sub>2</sub> regions in the contacts [83]. After the excess Ti is stripped in 3:1 NH<sub>4</sub>OH:H<sub>2</sub>O<sub>2</sub>, another RTA (1000 °C, 30 s, N<sub>2</sub>) is performed which lowers the contact resistance by creating stoichiometric TiSi<sub>2</sub>. Tungsten metallization is then sputtered and patterned. A thin TiN layer formed during the second RTA acts as a diffusion barrier to tungsten during the subsequent 835°C silicon-nitride deposition.

We found that the Ti reaction with Si consumed much of the boron in the p+ regions, producing high-resistance non-ohmic contacts. We modified the process by reducing the Ti thickness to 250 Å, lowering the second RTA temperature to 850°C, and including a 250 Å-thick reactively sputtered TiN layer on top of the TiSi<sub>2</sub>. The thicker diffusion barrier allows deposition of a thick, low-stress silicon-nitride film at 835°C to effectively protect the circuits from HF attack during the microstructure release step. Measured contact resistance is 27 Ω for n+ contacts at currents under 100 μA, and 55 Ω for p+ contacts at currents under 2 mA. For both kinds of contacts, the sample standard deviation is about 5 Ω across the wafer. When larger currents are passed through the contacts, the resistance drops to about half the low-current value.

#### 4.4.4 Testbed Fabrication Results

One wafer, the cmos30-2 wafer<sup>4</sup>, survived the 20-mask MICS process flow and provided working testbed devices. The end-product is not without some flaws, however. There are problems with HF attack of the silicon-nitride passivation over and near tungsten interconnect, resulting in open tungsten-polysilicon contacts in some regions. In particular, the sense and reference capacitors in the testbed position sensors are disconnected from the buffer on many samples. Unfortunately, the connection to the reference capacitors

---

<sup>4</sup>Wafers originating from the Berkeley baseline CMOS process are numbered by run and wafer in the lot. The cmos30-2 wafer is the second wafer out of the 30th baseline run in the microlab. Specific process information on each run is accessible by computer from the Berkeley Microfabrication Laboratory process logs.

has a yield close to zero, so the position sensors resemble the single-capacitor sensor of section 3.6.1.1.

One device was packaged in a 24-pin dual-inline package (DIP) for testing. Pin assignments are supplied in Table A.4. This device has three working position sensors, located at the upper-right, upper-left, and lower-left quadrants. A resistive short between the input sense line and the shield has rendered the lower-right position sensor inoperable. Only the first fuse is cut from the serpentine springs, providing a vertical spring constant of 0.25 N/m and a resonant frequency of 3.7 kHz<sup>5</sup>. We did not have enough samples to study the testbed with more compliant spring configurations.

---

<sup>5</sup>However, the fundamental mode is not in the vertical direction. The  $\theta$ -rotational mode has a resonant frequency of 2.9 kHz.

## Chapter 5

# System Simulation and Analysis

### 5.1 Introduction

Our approach to system simulation of the testbed uses the lumped-parameter components introduced in chapter 3. Groundwork for the simulations requires identification and construction of the component macro-models. We have made macro-models compatible with two simulation tools: SPICE and MATLAB<sup>TM</sup> [12]. Low-level simulation of circuits with microstructures is best done using SPICE, but the simulations are slow, and time-step convergence can be problematic. Tools for numerical computation, such as MATLAB, can be used to provide a faster, high-level simulation, using behavioral macro-models.

In the last sections of this chapter, two topics specific to micromechanical  $\Sigma\text{-}\Delta$  loops, limit cycles and equivalent noise in the acceleration signal, will be analyzed. High-frequency limit cycles arise from the digital feedback force imposed on the testbed, causing chatter in the plate's position. In particular, loop compensation is needed to bound limit cycles under mechanically underdamped conditions. Dynamic range of the output acceleration signal, generated by digitally filtering the  $\Sigma\text{-}\Delta$  bitstreams, is affected by several noise sources, including Brownian noise, quantization noise, electronic noise, and interconnect noise.

### 5.2 System Modeling

The micromechanical elements of the testbed, shown in simplified layout form in Figure 5.1, can be partitioned into several kinds of components: a rigid body (the suspended

plate), electrostatic actuators, and capacitive position sensors. Models of these components are then incorporated into the testbed simulations. We will simulate behavior of the testbed in the vertical direction,  $z$ ,  $\theta$ , and  $\phi$ , but lateral motion will be ignored. Actuator modeling will be restricted to the parallel-plate feedback actuators; the comb drives are turned off in the simulations. In all of our experiments, the testbed suspension is configured with one fuse cut on each spring. Therefore, we will present modeling and simulation results for that configuration, unless otherwise specified. A summary of model parameter definitions and values for the testbed are given in appendix A.1 for reference.

### 5.2.1 Testbed Plate Model

The resonant modes of the testbed plate are determined from a linear finite-element analysis [53], using 3-node quadratic beam elements for the springs and 9-node quadrilateral shell elements for the plate. Figure 5.2 displays the lowest eight modes for the plate, where each spring is configured with one fuse cut<sup>1</sup>. Resonant frequency values of the lowest four modes,  $\theta$ -rotation (rotation about the  $x$  axis),  $z$ -translation,  $\phi$ -rotation (rotation about the  $y$  axis), and  $x$ -translation are between 2.8 kHz and 3.9 kHz. The other two rigid-body modes of the plate,  $y$ -translation and  $\psi$ -rotation (rotation about the  $z$  axis), have slightly larger values of resonant frequency. Plate bending modes and spring-vibration modes have resonant frequency values that are over 24 times higher than the fundamental mode.

There are three controllable mechanical modes of the plate:  $z$ -translation, and the two rotations,  $\theta$  and  $\phi$ , about the lateral axes. These modes are modeled with the rigid-body, mass-spring-damper equations of motion introduced in section sec:eqns-of-motion. Transfer functions for the modes are obtained by taking the Laplace transform of Equations (3.18)–(3.20) yielding

$$H_z(s) = \Delta z(s)/F_z(s) = \frac{1}{m(s^2 + 2\zeta_z\omega_z s + \omega_z^2)} \quad (5.1)$$

$$H_\theta(s) = \theta(s)/\tau_\theta(s) = \frac{1}{I_\theta(s^2 + 2\zeta_\theta\omega_\theta s + \omega_\theta^2)} \quad (5.2)$$

$$H_\phi(s) = \phi(s)/\tau_\phi(s) = \frac{1}{I_\phi(s^2 + 2\zeta_\phi\omega_\phi s + \omega_\phi^2)} \quad (5.3)$$

where the vertical displacement,  $\Delta z$ , is defined relative to the fabricated spacer gap of 2.2  $\mu\text{m}$ .

---

<sup>1</sup>A list of spring constants and resonant modes for each spring configuration is given in Table A.2.

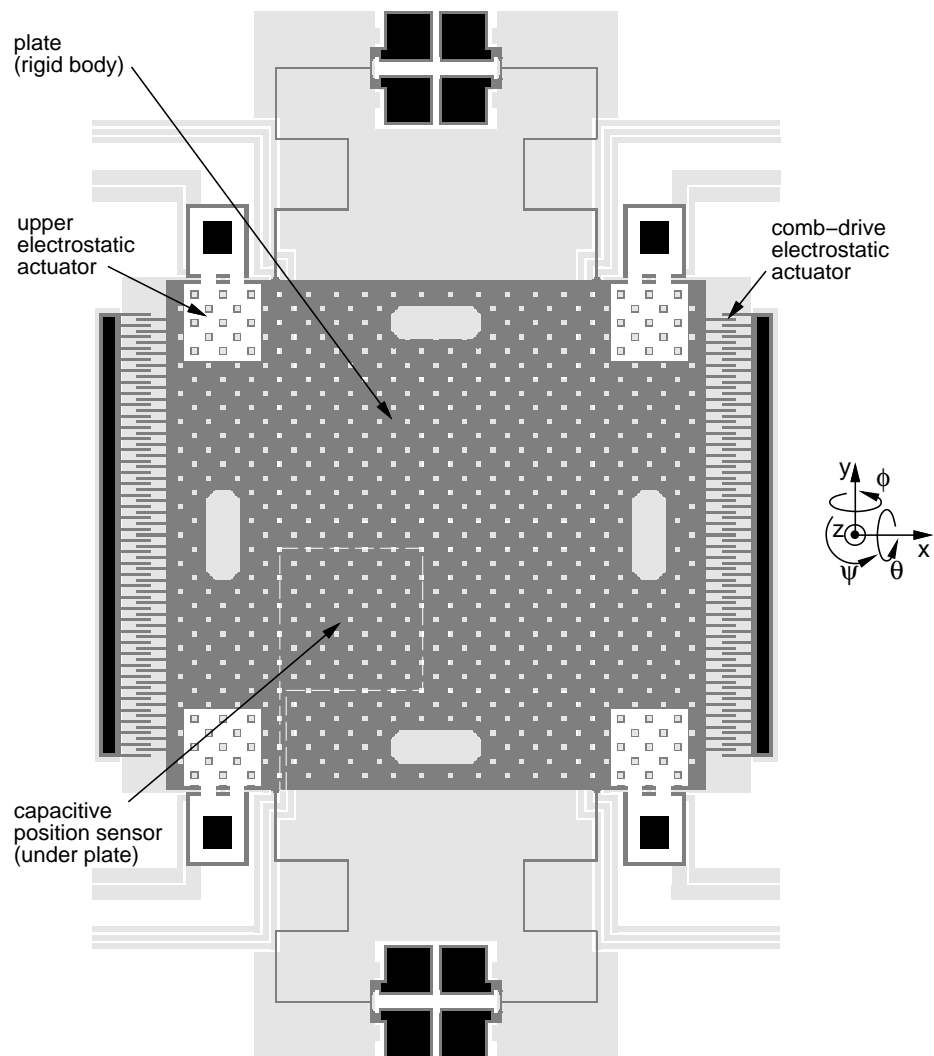


Figure 5.1: Simplified layout of the testbed, where the plate's suspension is configured with one fuse cut on each spring.

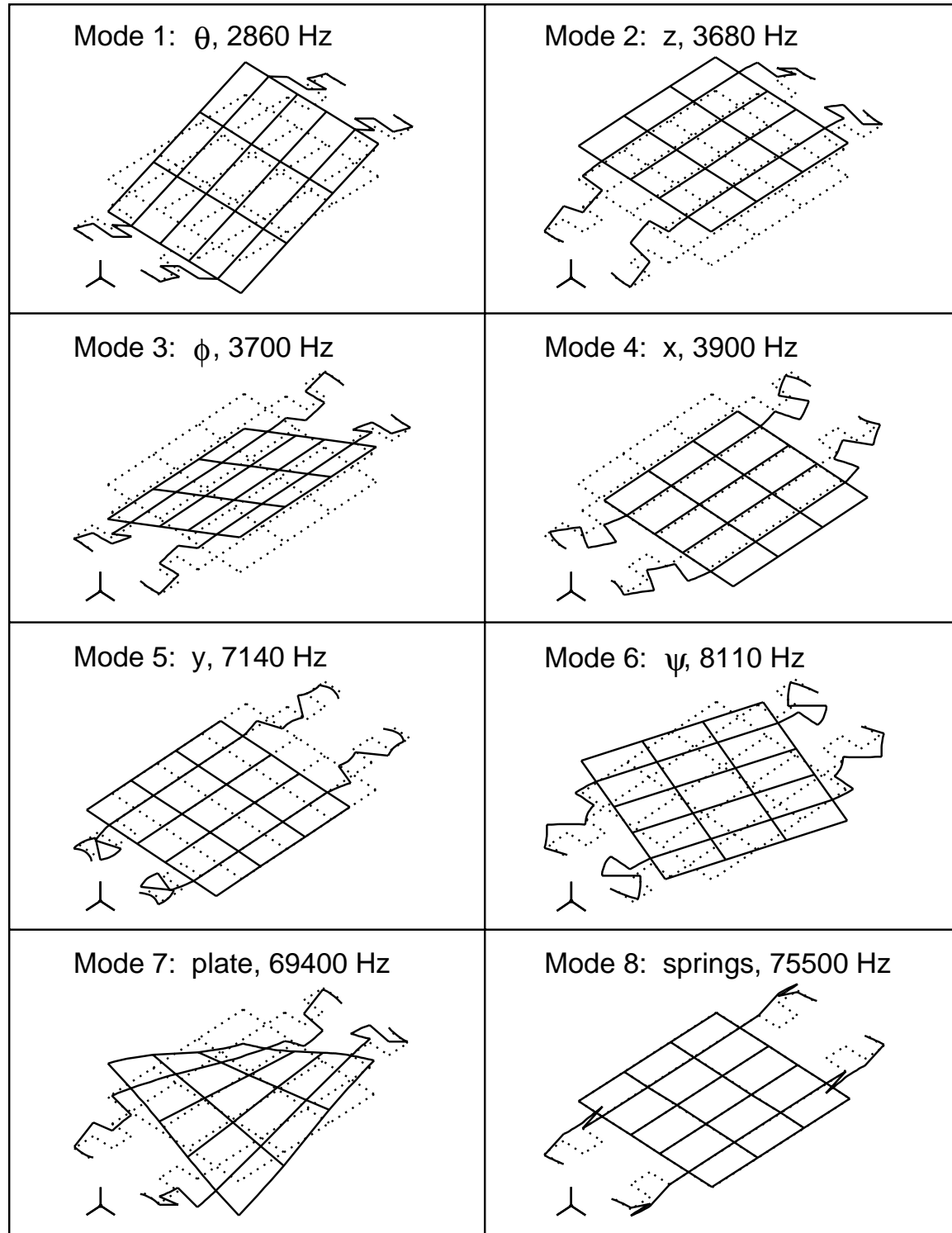


Figure 5.2: Illustration of the eight lowest mechanical modes of the testbed, where each spring is configured with one fuse cut.

The testbed system is analyzed by transforming the four quad-symmetric feedback loops into the three modes. However, since there are four feedback loops and only three controllable modes, the system is over-constrained. Offsets must be precisely adjusted to avoid undesired oscillations or force limiting in one of the loops. If the feedback signal levels were continuous, any position offsets would have resulted in four stable states for the plate position. With the quantized-state feedback, however, the electrostatic actuators will not limit as long as the position offsets are less than the amplitude of the limit cycles inherent in the system.

### 5.2.2 Position-Sensor Model

The testbed can control the plate position with a large range of motion relative to the gap spacing. An accurate model of the position sensor is needed to relate each position reference input to the vertical displacement. A layout of the position sensor electrodes under the plate is shown in Figure 5.3. We will use the quadrant numbering convention in Figure 5.3 throughout our discussion of the testbed. Numbering starts with “1” at the upper-right quadrant and progresses counter-clockwise to “4” at the lower-right quadrant. We will use the symbol  $i$  as the quadrant index in equations. The square plate electrodes have dimensions  $L_{sx,i} = L_{sy,i} = 100 \mu\text{m}$  and are located a distance  $|x_{so,i}| = |y_{so,i}| = 60 \mu\text{m}$  from the centerlines of the plate.

The position sensor model has inputs of plate displacement and rotation, from which the sensor output voltage, force, and torque are calculated. In our first-order model, we assume a constant air gap across the sensor electrode area, and use a small-angle approximation. Because of their modular integration, models that incorporate the second-order effects of plate tilt can be easily substituted into the simulation. The air gap for each sensor is calculated at the center of the electrodes.

$$z_{s,i} = z_o + \Delta z + y_{so,i} \theta - x_{so,i} \phi \quad (5.4)$$

In SPICE, the capacitive divider and unity-gain buffer amplifier, discussed in section 3.6.1.2, can be simulated directly to obtain the sensor output voltage; in MATLAB simulations, the sensor output voltage is calculated from Equation (3.178). A force and torque from the parallel-plate sensor electrodes act on the plate, and are given by

$$F_{sz,i} = -\frac{\alpha_s \epsilon A_{s,i}}{z_{s,i}^2} (V_{m-} - V_{s,i})^2 \quad (5.5)$$

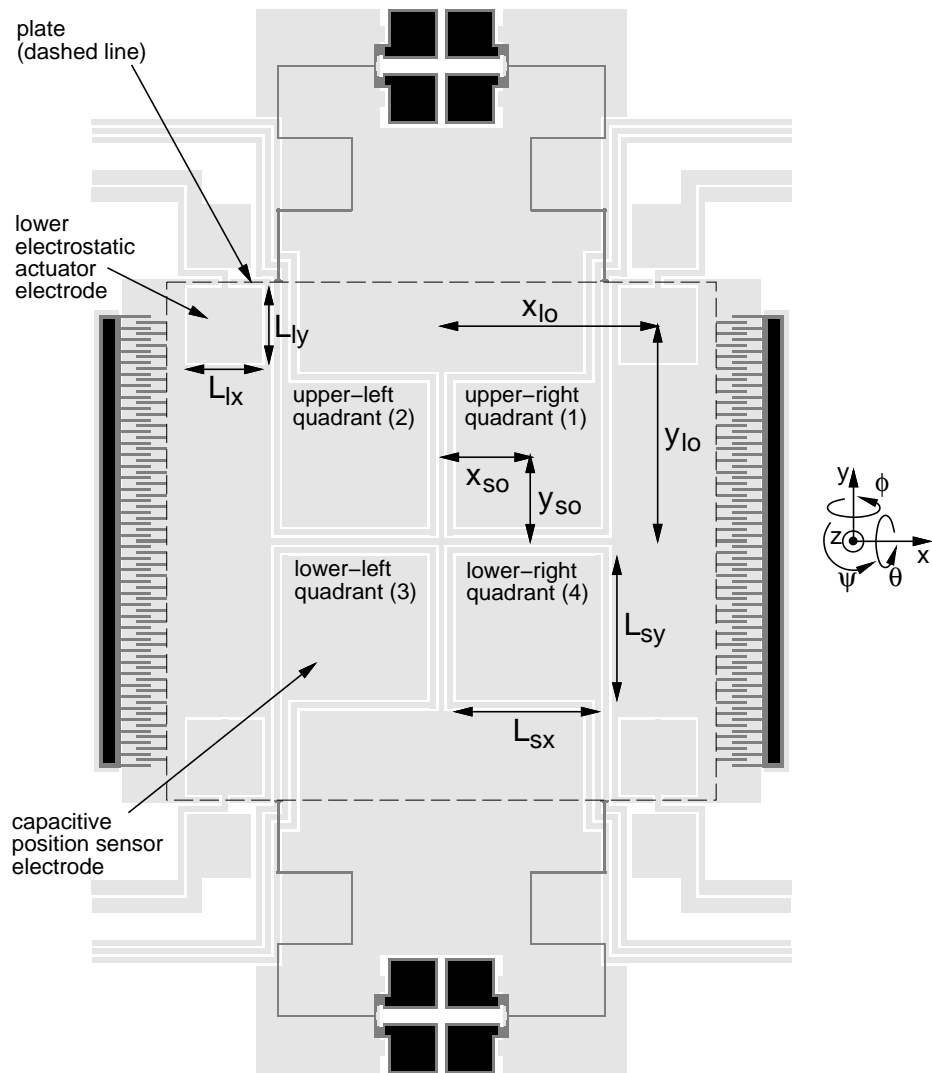


Figure 5.3: Simplified testbed layout, identifying the position-sensor electrodes and lower-actuator electrodes.

$$\tau_{s\theta,i} = y_{so,i} F_{sz,i} \quad (5.6)$$

$$\tau_{s\phi,i} = -x_{so,i} F_{sz,i} \quad (5.7)$$

where  $A_{si} \equiv L_{sx,i} L_{sy,i}$ , and  $\alpha_s$  is a form factor that compensates for fringing around etch holes.

### 5.2.3 Electrostatic Actuator Model

The parallel-plate actuators, located at the plate's corners, have electrodes above and below the plate to provide a differential force. Figure 5.4 shows the size and location of the upper actuators. The square plate electrodes have dimensions  $L_{ux,i} = L_{uy,i} = 54 \mu\text{m}$  and are located a distance  $|x_{uo,i}| = |y_{uo,i}| = 150 \mu\text{m}$  from the centerlines of the plate. The lower-actuator electrodes, identified in Figure 5.3, are located directly below the upper actuators, and are  $2 \mu\text{m}$  smaller on each side. The displacement, force, and torque equations are similar to those for the sense electrodes. For the upper-actuator,

$$z_{u,i} = z_{uo} + \Delta z + y_{uo,i} \theta - x_{uo,i} \phi \quad (5.8)$$

$$F_{uz,i} = \frac{\alpha_u \epsilon A_{u,i}}{z_{u,i}^2} (V_{m-} - V_{up,i})^2 \quad (5.9)$$

$$\tau_{u\theta,i} = y_{uo,i} F_{uz,i} \quad (5.10)$$

$$\tau_{u\phi,i} = -x_{uo,i} F_{uz,i} \quad (5.11)$$

and for the lower-actuator,

$$z_{l,i} = z_o + \Delta z + y_{lo,i} \theta - x_{lo,i} \phi \quad (5.12)$$

$$F_{lz,i} = -\frac{\alpha_l \epsilon A_{l,i}}{z_{l,i}^2} (V_{m-} - V_{down,i})^2 \quad (5.13)$$

$$\tau_{l\theta,i} = y_{lo,i} F_{lz,i} \quad (5.14)$$

$$\tau_{l\phi,i} = -x_{lo,i} F_{lz,i} \quad (5.15)$$

where  $z_{uo}$  is the fabricated air-gap between the plate and the upper actuator. We have again introduced form-factors,  $\alpha_u$  and  $\alpha_l$ , to compensate for the fringe fields from etch holes in the plates.

## 5.3 SPICE Simulation

We perform low-level simulation of microstructures with circuits using a commercial version of SPICE, HSPICE [3]. Each of the models described above is implemented as a

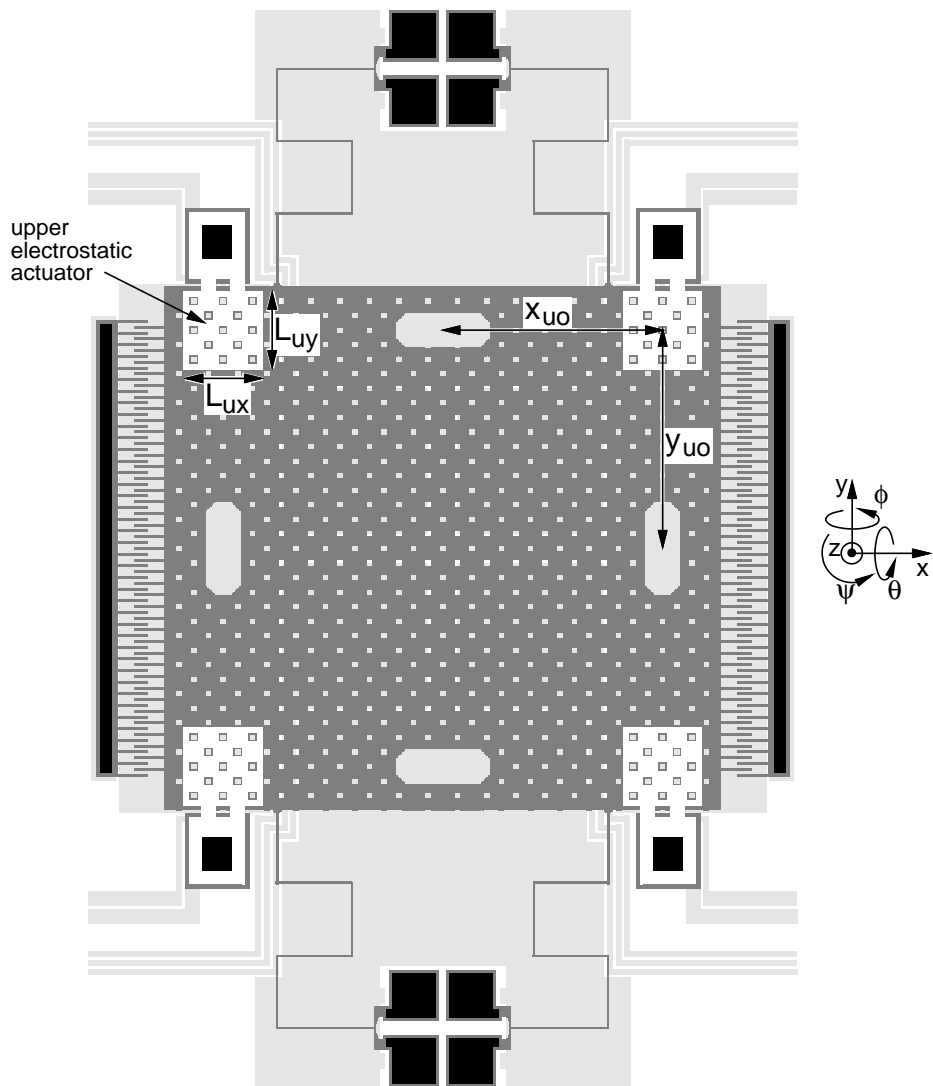


Figure 5.4: Simplified testbed layout, identifying the upper-actuator electrodes.

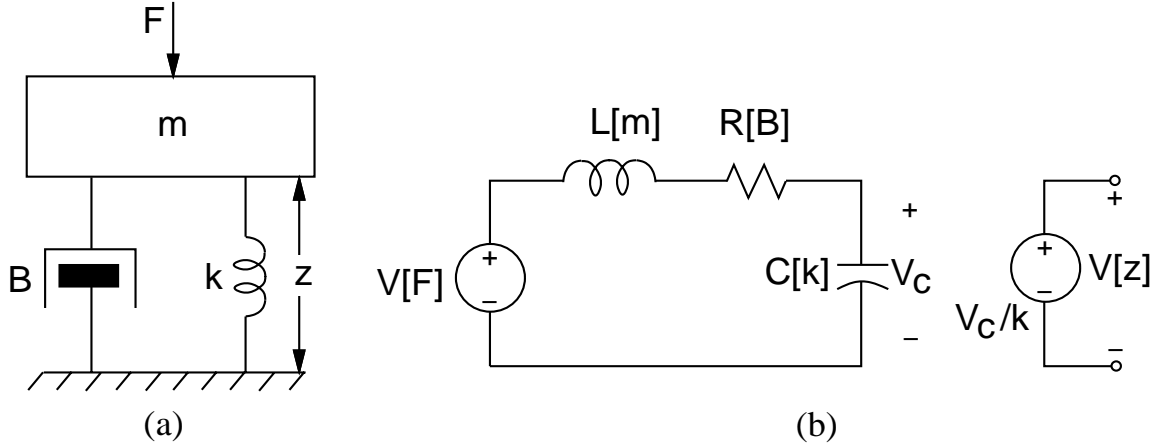


Figure 5.5: Electrical analogy to a second-order mechanical system. (a) Mechanical mass-spring-damper. (b) Equivalent LCR circuit.

subcircuit. Mechanical interactions are communicated through node voltages in SPICE. By maintaining modular subcircuit models, we can improve the models without affecting the overall simulation. HSPICE input files of the testbed simulation and the subcircuit models are listed in appendix B.

### 5.3.1 Equivalent Circuit Model of a Mass-Spring-Damper

A mechanical mass-spring-damper can be modeled in SPICE by making an electrical analogy to an inductor-capacitor-resistor (LCR) circuit. Either the series-connected or parallel-connected LCR circuit can model the second-order mechanical system; we have chosen to use the series-connected LCR circuit shown in Figure 5.5. Each mechanical parameter is represented by an equivalent electrical parameter.

$$L [m] = A m \quad (5.16)$$

$$R [B] = A B \quad (5.17)$$

$$C [k] = \frac{1}{A k} \quad (5.18)$$

$$V [F] = A F \quad (5.19)$$

$$V_c = A k z \quad (5.20)$$

$$V [z] = A z \quad (5.21)$$

The scaling factor,  $A$ , is needed to keep the electrical impedance values of the LCR circuit from being very small, thereby avoiding convergence problems in SPICE. A useful value

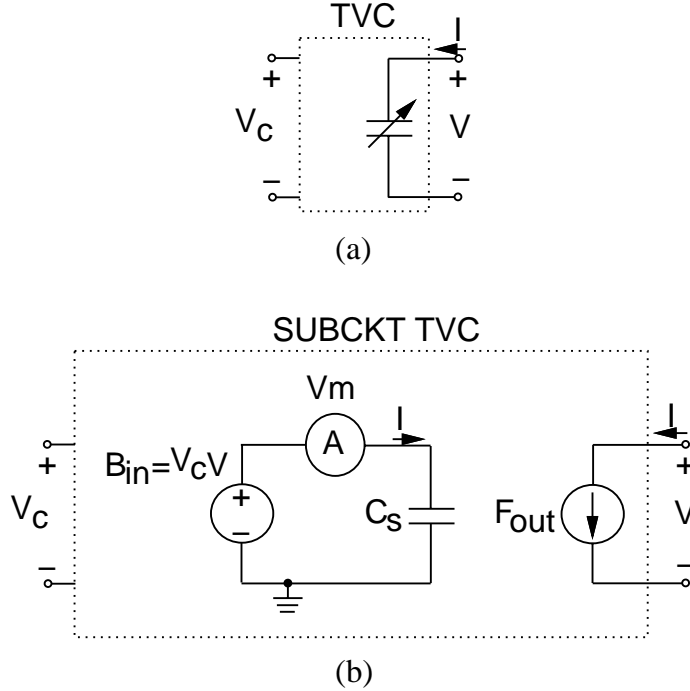


Figure 5.6: Time-varying capacitor (TVC) model in SPICE. (a) Circuit instance. (b) Subcircuit.

for  $A$  is  $10^6$  for micromechanical components, producing the following parameter values, typical in the testbed operation:

Mechanical parameters:

$$m = 4.7 \times 10^{-10} \text{ kg}$$

$$k_z = 0.25 \text{ N/m}$$

$$B_z = 2.6 \times 10^{-4} \text{ N-s/m} \quad \Longleftrightarrow$$

$$F_z = 100 \text{ nN}$$

$$z = 1.0 \mu\text{m}$$

Electrical parameters:

$$L_z [m] = 0.47 \text{ mH}$$

$$C_z [k_z] = 4.0 \mu\text{F}$$

$$R_z [B_z] = 260 \Omega$$

$$V [F_z] = 0.1 \text{ V}$$

$$V [z] = 1 \text{ V}$$

### 5.3.2 Time-Varying Capacitor Model

A time-varying capacitor (TVC) subcircuit model for SPICE is shown in Figure 5.6. The TVC I-V characteristic is given by

$$I = \frac{d}{dt} (C_s V_c V) \quad (5.22)$$

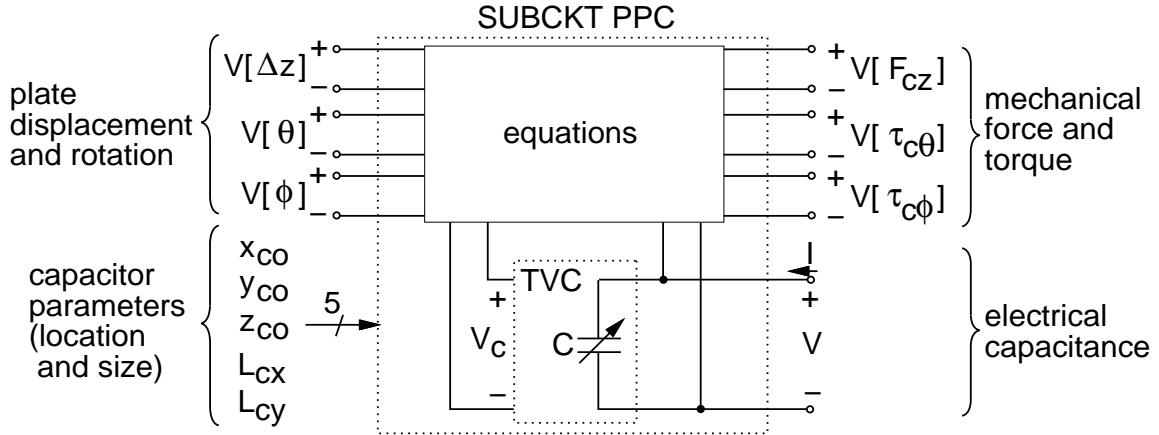


Figure 5.7: Parallel-plate micromechanical capacitor macro-model in SPICE.

where  $C_s$  is a capacitance scaling factor, and  $V_c$  is a voltage that specifies the instantaneous scaled capacitance value<sup>2</sup>. Since micromechanical capacitor values are usually between 1 fF and 1 pF, a good value for the capacitance scaling factor is 1 pF. The TVC subcircuit can be implemented in any version of SPICE that supports nonlinear voltage-controlled voltage sources.

### 5.3.3 Micromechanical Capacitor Model

We model both the actuators and the sensor capacitors with the parallel-plate capacitor (PPC) subcircuit, shown in Figure 5.7. External node voltages supply the plate position to the subcircuit. Other node voltages are used to output the force and torque produced by the capacitor. Static parameters include the location ( $x_{co}$ ,  $y_{co}$ ) and size ( $L_{cx}$ ,  $L_{cy}$ ) of the capacitor, the size of the fabricated air gap,  $z_{co}$ , and the etch-hole form factor,  $\alpha_c$ . Upper and lower actuators are distinguished by the sign of the fabricated air-gap value; capacitors above the plate are supplied with a negative fabricated air-gap value in the simulation. With this sign convention, a positive plate displacement reduces the size of the upper-actuator air gap.

Force, torque, and capacitance are calculated in the subcircuit as

$$F_{cz} = -\text{sgn}(z_{co}) \frac{\alpha_c \epsilon L_{cx} L_{cy}}{(z_{co} + \Delta z + y_{co} \theta - x_{co} \phi)^2} V^2 \quad (5.23)$$

---

<sup>2</sup>The quantity  $C_s V_c$  in Equation (5.22) is in units of farads, because the nonlinear voltage source,  $B_{in}$ , converts the product  $V_c V$  to a voltage.

$$\tau_{l\theta,i} = y_{co} F_{cz} \quad (5.24)$$

$$\tau_{l\phi,i} = -x_{co} F_{cz} \quad (5.25)$$

$$C = \frac{\alpha_c \epsilon L_{cx} L_{cy}}{|z_{co} + \Delta z + y_{co} \theta - x_{co} \phi|} \quad (5.26)$$

### 5.3.4 Testbed Simulation

A block diagram of the testbed SPICE simulation<sup>3</sup> is given in Figure 5.8. On the left side of the diagram, voltage sources that represent electrostatic forces and torques are summed. The total force and torques are connected to the equivalent LCR-circuit model for each respective mode. Plate displacement and rotation are output as voltages from the LCR circuits and supplied as inputs to the parallel-plate capacitor subcircuit instances. The sensor and actuator time-varying-capacitor connections are shown on the right side of Figure 5.8. Both the capacitive divider and the unity-gain buffer circuit for each quadrant are modeled explicitly. The demodulator and comparator are represented by simple behavioral models.

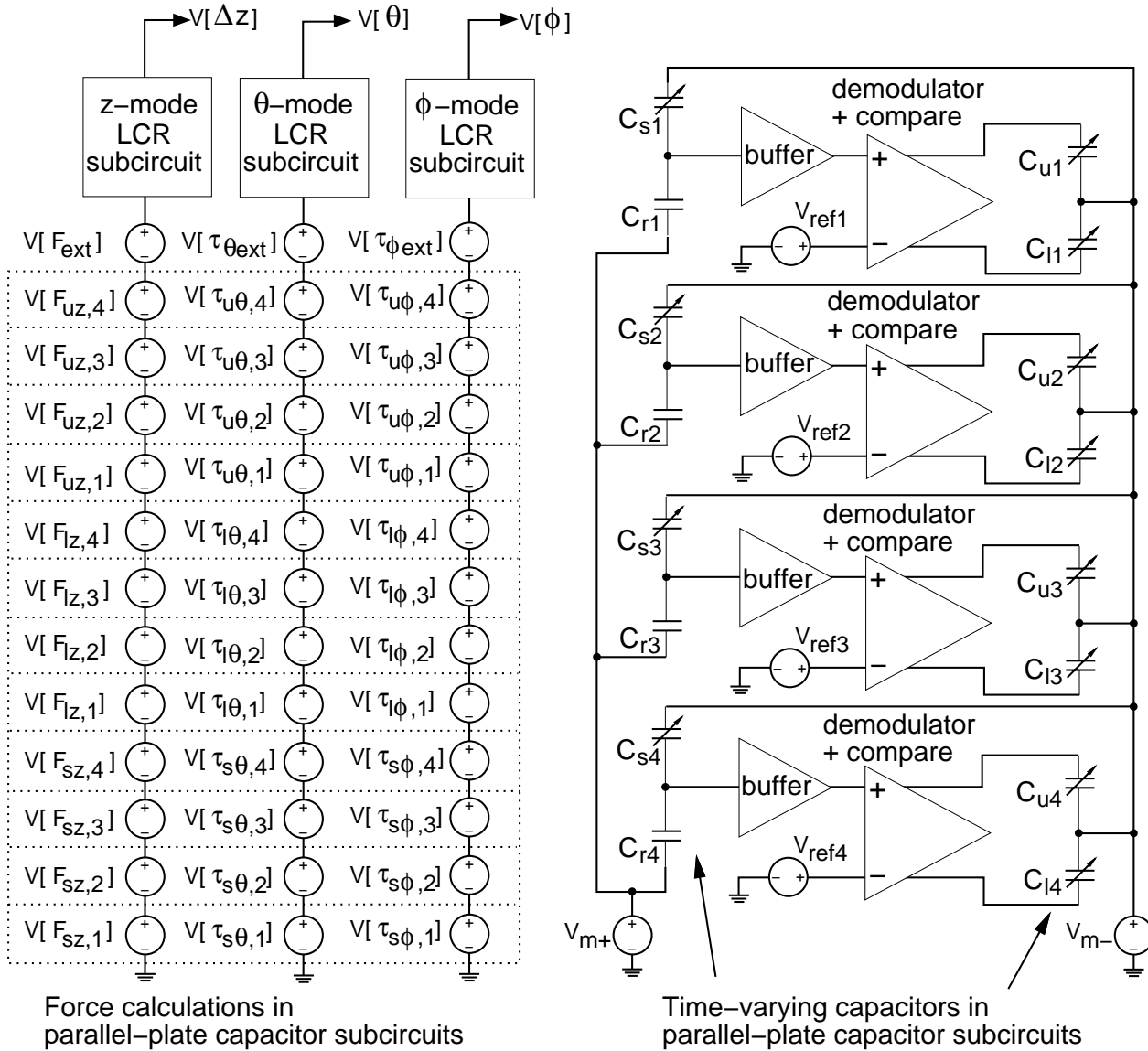
A closed-loop step response of the testbed operating in air at a 50 kHz sampling rate is shown in Figure 5.9. At  $t=200 \mu s$ , the position-reference inputs are stepped from 0 V to 56 mV, corresponding to a vertical plate displacement of about  $0.5 \mu m$ . Since all four position references are set to equal values, only the vertical ( $\Delta z$ ) plate mode is excited. The plate rises to its new steady-state position in about 0.6 ms, with a constant velocity due to the overdamped mechanical system. The steady-state displacement exhibits sawtooth-shaped limit cycles at half the sampling frequency; the  $\Sigma-\Delta$  feedback force generates the limit cycles. One of the capacitive-divider output voltage waveforms is shown in Figure 5.9(c). The buffer's voltage offset does not affect operation of the loop, because the position signal is modulated at 50 kHz. Most of this offset is an artifact of the simulator, which initially places extra charge on the high-impedance node of the capacitive divider. We have ignored the offset, but it may be eliminated in the future by proper setting of initial conditions and simulation parameters. As the displacement increases, the modulation amplitude also increases, but not symmetrically about the dc level. This asymmetry is caused by the nonlinear I-V characteristic of the diode that is connected between the high-impedance node and ground<sup>4</sup>. Demodulation of the sensor output voltage pro-

---

<sup>3</sup>The HSPICE listing is in appendix B.

<sup>4</sup>The diode sets the dc bias of the high-impedance node. See section 3.6 for more information.

Figure 5.8: Block diagram of the testbed, modeled in SPICE.



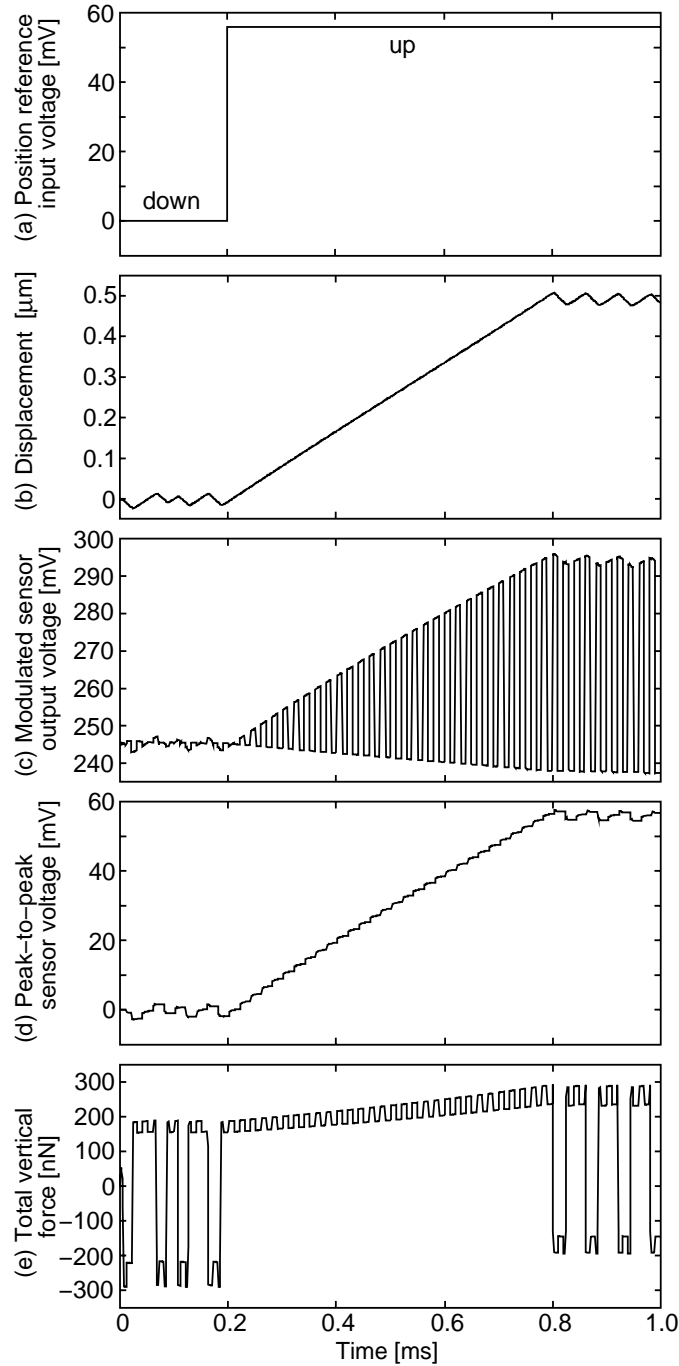


Figure 5.9: SPICE simulation of the testbed closed-loop step response in air. (a) Position reference input voltage,  $V_{\text{ref}}$ . (b) Plate displacement,  $\Delta z$ . (c) Modulated sensor output voltage (output from the upper-right capacitive divider),  $V_{\text{sense}}$ . (d) Peak-to-peak (demodulated) sensor voltage,  $V_{\text{pp}}$ . (e) Total vertical force acting on the plate,  $F_z$ .

duces the peak-to-peak sensor voltage,  $V_{pp}$ , shown in Figure 5.9(d). This voltage tracks the position-reference input voltage. The total force acting on the plate (Figure 5.9(e)) is, to first-order, quantized to two states; however, parallel-plate nonlinearity, force from the sensor electrodes, and the modulation voltage on the plate cause the total force to deviate from ideality. Changes in the actuator force levels arise from the change in parallel-plate air gap as the plate rises. The upper-actuator force level increases, while the lower-actuator force level is reduced. The  $\pm 0.3$  V modulation voltage impressed on the plate produces an actuator force component at the sampling frequency, and also generates a dc force from the sensor electrodes.

Figure 5.10 shows simulation results of the testbed operation under vacuum, with a mechanical Q of 50. The plate oscillations increase to the mechanical limit stops (at  $\pm 2 \mu\text{m}$ ) since there is no loop compensation to stabilize the system. The amplitude-modulated sensor output, and demodulated peak-to-peak sensor voltage are plotted in Figure 5.10(b–c). Large effects from the parallel-plate nonlinearity in the feedback force are evident in Figure 5.10(d).

With the preceding examples, we have demonstrated detailed SPICE simulation of the testbed using modular subcircuit models. Second-order effects in the system, such as the effects of modulation voltage on the force, are predicted by using this simulation approach. Further modeling improvements can be made without affecting the overall simulation.

One important drawback of SPICE is that the time to complete a simulation is usually very long; a 1 ms simulation, corresponding to 50 cycles at a 50 kHz sampling rate, takes about 30 minutes of CPU time on a DecStation 5100 with 32 Megabytes of RAM. Behavioral simulation, discussed next, alleviates the lengthy simulation times and allows a quick turnaround of analyses.

## 5.4 MATLAB Simulation

We have implemented a behavioral simulation of the testbed using the Simulink [94] extension to MATLAB. Simulink provides a convenient graphical user interface (GUI) for system simulation. A block diagram of the testbed simulation, taken from the GUI screen, is shown in Figure 5.11. Mechanical equations of motion and electrostatic actuator forces are modeled by their explicit transfer functions. The position sensor and buffer circuit are bundled together and modeled by Equation (3.178), which is repeated here for

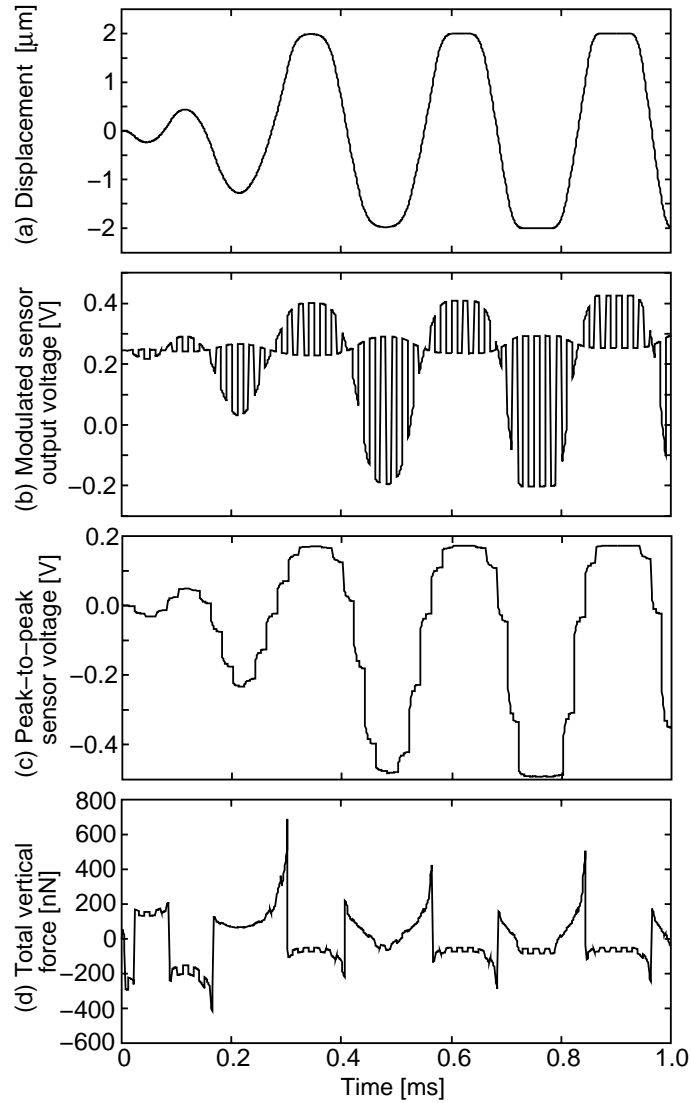


Figure 5.10: SPICE simulation of the testbed under vacuum, with a mechanical Q of 50. (a) Plate displacement,  $\Delta z$ . (b) Modulated sensor output voltage (output from the upper-right capacitive divider),  $V_{\text{sense}}$ . (c) Peak-to-peak (demodulated) sensor voltage,  $V_{\text{pp}}$ . (d) Total vertical force acting on the plate,  $F_z$ .

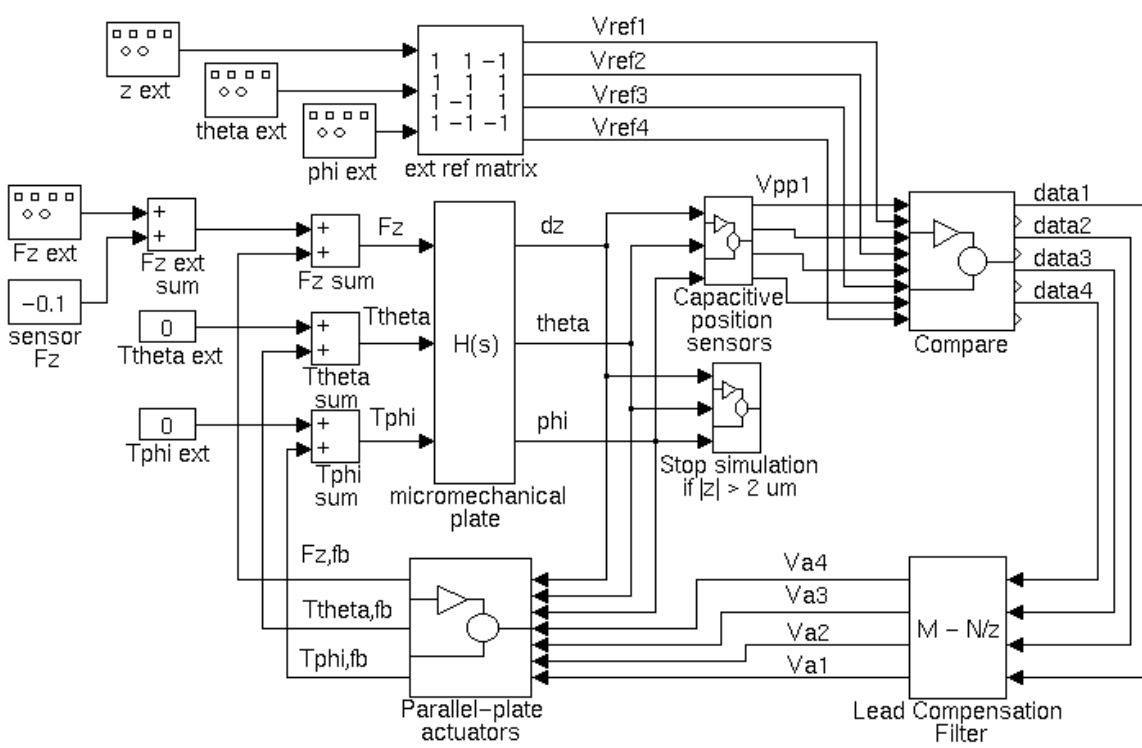


Figure 5.11: Block diagram of the testbed, modeled in MATLAB.

convenience.

$$V_s = G_o V_m \left( \frac{C_r - C_{so}}{C_r + C_{so} + C'_p} \right) \left[ \frac{1 + \left( \frac{C_r - C_{sf}}{C_r - C_{so}} \right) \frac{\Delta z}{z_o}}{1 + \left( \frac{C_r + C_{sf} + C'_p}{C_r + C_{so} + C'_p} \right) \frac{\Delta z}{z_o}} \right]$$

Capacitive circuit models of the sensors and actuators are not included, and any electrical interactions among the components are ignored. SPICE simulation is more appropriate for examining these second-order electrical effects. Simulation examples are deferred to chapter 6, where we present experimental and simulated results for the testbed closed-loop step response in air and underdamped response at low pressure.

## 5.5 Limit-Cycle Analysis

The presence of nonlinear elements in a feedback loop can produce stable bounded oscillations, called limit cycles. In the testbed  $\Sigma$ - $\Delta$  loops, the nonlinearity of the one-bit quantizer gives rise to limit cycles. Describing-function analysis [95] is used to predict the existence of limit cycles, and the amplitude and frequency of the oscillation. A describing function for a nonlinear element is found by determining the fundamental frequency component of the response to a sinusoidal input signal. A low-pass transfer function is assumed to exist in the loop to attenuate higher-order harmonic components. In micromechanical digital-feedback systems, the high-frequency harmonics are attenuated by the two-pole rolloff of the mechanical mass-spring-damper.

In this section, two methods for evaluating limit cycles of the testbed will be discussed. The first method requires the derivation of a describing function for the entire feedback path. The second method requires the describing function of only the quantizer, with digital compensation in the feedback path being modeled separately as a z-transform. Both methods provide equivalent expressions for the loop transfer function. The limit-cycle condition occurs when the loop transfer function equals  $-1$ . Magnitude and frequency of the limit cycle are found from this condition.

Delays in the loop due to discrete-time sampling will vary because the limit-cycle frequency will never exactly equal a multiple of the sampling rate. The delay is also affected by circuit noise. If the noise is smaller than the plate oscillation amplitude, the assumption of a steady-state limit cycle can provide bounds on the oscillation amplitude and frequency. The ensuing analysis assumes that the delay is a fixed parameter and the limit-cycle frequency is constant.

### 5.5.1 Describing Function of the Feedback Path

A simple, single-axis model of the testbed, shown in Figure 5.12, is used to examine limit cycles of the vertical-displacement mode. The mass-spring-damper transfer function for the  $\Delta z$  mode was presented in Equation (5.1), and is repeated here for convenience.

$$H_z(s) = \frac{1}{m(s^2 + 2\zeta_z\omega_z s + \omega_z^2)}$$

The plate displacement is assumed to be sinusoidally varying with time.

$$\Delta z = z_1 \sin(\omega t) \tag{5.27}$$

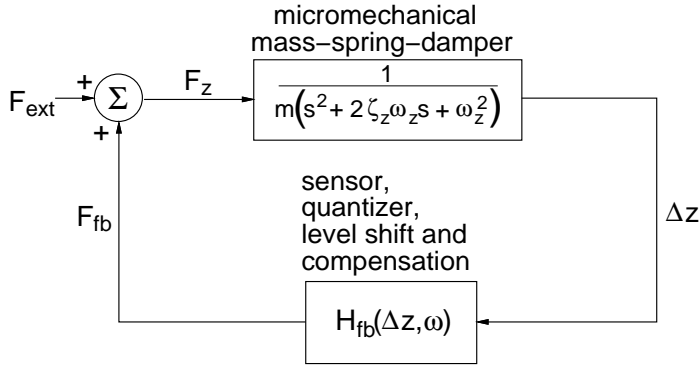


Figure 5.12: Loop model of the  $\Delta z$  mode, modeling the entire feedback path as a describing function.

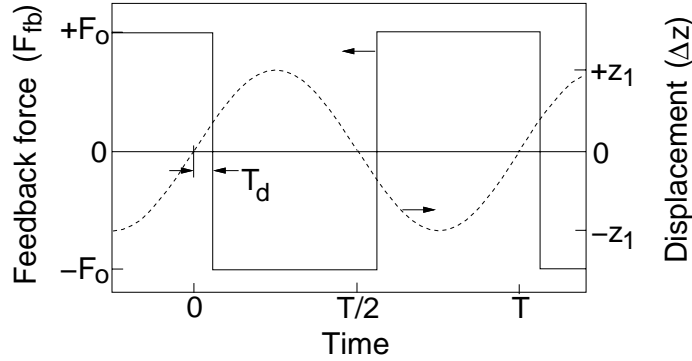


Figure 5.13: Limit-cycle waveforms of linearized feedback force with no compensation (solid line), and vertical plate displacement (dashed line).

where  $z_1$  is the displacement amplitude and  $\omega$  is the frequency of the limit cycle. A single describing function,  $H_{fb}(z_1, \omega)$ , models the entire feedback path, including the position sensor, quantizer, compensation, and level shift.

A description of the feedback force is necessary to determine the describing function. Limit-cycle waveforms of linearized feedback force,  $F_{fb}$ , and plate displacement,  $\Delta z$ , are given in Figure 5.13 for an underdamped mechanical system with no loop compensation. After a reference crossing of the plate is sensed, a restoring force of magnitude  $F_o$  is output to the appropriate actuator. The feedback response must occur at a clock edge, and will be delayed by  $T_d$  from the time of the reference-crossing. A constant magnitude of actuator force,  $F_o$ , will be assumed in the analysis of this section and section 5.5.2. The value  $F_o$  is referred to as the full-scale force, because external forces exceeding this value will pull the device out of closed-loop operation. The full-scale force must be large enough

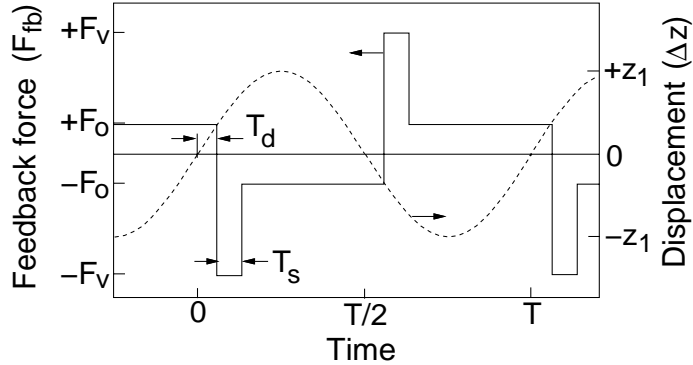


Figure 5.14: Limit-cycle waveforms of linearized feedback force with compensation (solid line), and vertical plate displacement (dashed line).

to balance forces from gravity, acceleration, and electrostatic sources. Nonlinear effects of plate position on the actuator force will be discussed in section 5.5.4.

Compensation is necessary for closed-loop stability when the mechanical system is underdamped. Without compensation and neglecting the extra delay  $T_d$ , the feedback force is exactly  $180^\circ$  out of phase with the displacement. Including the delay, the feedback force is more than  $180^\circ$  out of phase with the displacement, resulting in an unstable system. Introduction of the compensation term,  $1 - z^{-1}$ , in the feedback path, adds phase lead to the loop, and acts to stabilize the system. Limit-cycle waveforms with this type of lead compensation are given in Figure 5.14. After a reference crossing of the plate is sensed, a restoring force pulse of magnitude  $F_v$ , is output to the actuators. The lead pulse lasts one sample period,  $T_s$ , after which a smaller force magnitude,  $F_o$ , is applied until the plate crosses the displacement reference. The phase delay,  $T_d$ , arising from the position sampling in the loop, partly negates the effect of the compensation. The limit-cycle oscillation condition occurs when the phase lead from the compensation balances the phase delay due to the sampling. No compensation is a special case, specified when  $F_v = F_o$ .

The describing function,  $H_{fb}(z_1, \omega)$ , is the ratio of the fundamental frequency component of the feedback force to a sinusoidal plate displacement. The fundamental of the feedback force is found using Fourier analysis. One period of the feedback-force limit

cycle is approximated by a piecewise-linear expression.

$$F_{\text{fb}} = \begin{cases} +F_v & ; -\frac{T}{2} + T_d < t \leq -\frac{T}{2} + T_s + T_d \\ +F_o & ; -\frac{T}{2} + T_s + T_d < t \leq T_d \\ -F_v & ; T_d < t \leq T_s + T_d \\ -F_o & ; T_s + T_d < t \leq \frac{T}{2} + T_d \end{cases} \quad (5.28)$$

where  $T$  is the period of the limit cycle, and the plate displacement is given by Equation (5.27).

The feedback force can be expressed as a sum of complex exponential basis functions.

$$F_{\text{fb}} = \sum_{n=-\infty}^{\infty} A_n e^{jn\omega t} \quad (5.29)$$

where  $\omega = 2\pi/T$  is the limit cycle frequency. The Fourier coefficients,  $A_n$ , are determined by first multiplying Equation (5.28) by  $e^{-jm\omega t}$  and integrating over a period.

$$\int_{-T/2}^{T/2} F_{\text{fb}} e^{-jm\omega t} dt = \sum_{n=0}^{\infty} \int_{-T/2}^{T/2} A_n e^{j(n-m)\omega t} dt \quad (5.30)$$

Since the exponential basis functions are orthogonal, all terms in the summation are zero except when  $n = m$ . Equations (5.28) and (5.30) are combined and solved for the coefficients.

$$A_m = -\frac{1 - (-1)^m}{2jm\pi} e^{-j\omega m T_d} [F_v + F_o - (F_v - F_o)e^{-j\omega m T_s}] \quad (5.31)$$

The fundamental component of feedback force,  $F_{\text{fb}1}$ , is the sum of the  $|m| = 1$  contributions to Equation (5.29).

$$F_{\text{fb}1} = A_1 e^{j\omega t} + A_{-1} e^{-j\omega t} = -\frac{2}{\pi} e^{-j\omega T_d} \{(F_v + F_o) \sin(\omega t) - (F_v - F_o) \sin[\omega(t - T_s)]\} \quad (5.32)$$

A feedback describing function,  $H_{\text{fb}}(z_1, \omega)$ , is determined by finding the ratio of the amplitude and offset in phase of Equations (5.32) and (5.27).

$$H_{\text{fb}}(z_1, \omega) = -\frac{2}{\pi z_1} e^{-j\omega T_d} [F_v + F_o - (F_v - F_o) e^{-j\omega T_s}] \quad (5.33)$$

Feedback nonlinearity with position can be included in the Fourier analysis, and will be introduced in section 5.5.4. Determination of the loop transmission and limit-cycle condition is deferred to the next section.

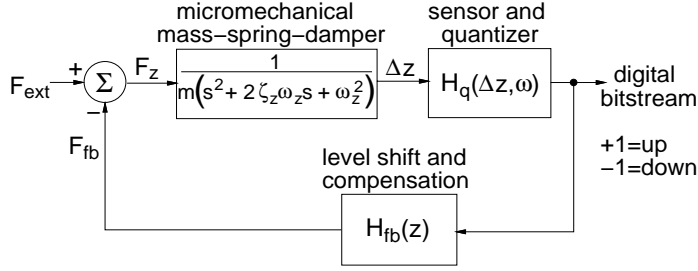


Figure 5.15: Alternative loop model of the  $\Delta z$  mode for limit-cycle analysis.

### 5.5.2 Describing Function of Only the Quantizer

In the preceding section, the describing function for the entire feedback path was derived. As an alternative, the quantizer and digital feedback can be modeled separately, as illustrated in Figure 5.15. The position sensor, demodulator, and comparator are modeled together in the quantizer describing function  $H_q(z_1, \omega)$ . The quantizer has an output value of +1 or -1, corresponding to the plate being above or below the position reference.

The quantizer describing function can be found using the Fourier analysis method of the preceding section. In Figure 5.13, we recognize that the limit cycle output from the quantizer is a square wave delayed by  $T_d$  from the displacement. The first-harmonic amplitude of the square wave is  $4/\pi$ , which is divided by the sinusoidal displacement amplitude to determine the describing-function gain.

$$H_q(z_1, \omega) = \frac{4}{\pi z_1} e^{-j\omega T_d} \quad (5.34)$$

Digital compensation and level shift are expressed as a z-transform,  $H_{fb}(z)$ .

$$H_{fb}(z) = -F_o \left[ 1 + G_v \frac{(1 - z^{-1})}{2} \right] \quad (5.35)$$

where  $G_v = F_v/F_o - 1$  is the adjustable lead-compensation gain. Since a unit delay is the sampling period,  $T_s$ , we can substitute  $z = e^{j\omega T_s}$  in Equation (5.35) and form the continuous-time transfer function,  $H_{fb}(e^{j\omega T_s})$ . The product  $H_q(z_1, \omega)H_{fb}(e^{j\omega T_s})$  is equivalent to the feedback describing function derived in the preceding section, given by Equation (5.33).

The system loop gain,  $L(z_1, \omega)$ , is the product of Equations (5.1), (5.35), and (5.34).

$$L(z_1, \omega) = -H_z(j\omega)H_q(z_1, \omega)H_{fb}(e^{j\omega T_s}) = \frac{4F_o e^{-j\omega T_d} [1 + G_v(1 - e^{-j\omega T_s})/2]}{\pi z_1 m (-\omega^2 + j2\zeta_z\omega_r\omega + \omega_r^2)} \quad (5.36)$$

The amplitude,  $z_1$ , and frequency,  $\omega$ , of the limit cycle are found by setting the loop gain equal to  $-1$ . The two transcendental equations,  $\Re\{L(z_1, \omega)\} = -1$  and  $\Im\{L(z_1, \omega)\} = 0$ , can be solved iteratively for  $z_1$  and  $\omega$ .

$$\Re\{L(z_1, \omega)\} = \frac{4F_o \left( \begin{array}{l} (\omega_z^2 - \omega^2) \{(1 + G_v/2) \cos(\omega T_d) - (G_v/2) \cos[\omega(T_s + T_d)]\} - \\ 2\zeta_z \omega_z \omega \{(1 + G_v/2) \sin(\omega T_d) - (G_v/2) \sin[\omega(T_s + T_d)]\} \end{array} \right)}{\pi z_1 m [(\omega_z^2 - \omega^2)^2 + (2\zeta_z \omega_z \omega)^2]} \quad (5.37)$$

$$\Im\{L(z_1, \omega)\} = \frac{4F_o \left( \begin{array}{l} (\omega^2 - \omega_z^2) \{(1 + G_v/2) \sin(\omega T_d) - (G_v/2) \sin[\omega(T_s + T_d)]\} - \\ 2\zeta_z \omega_z \omega \{(1 + G_v/2) \cos(\omega T_d) - (G_v/2) \cos[\omega(T_s + T_d)]\} \end{array} \right)}{\pi z_1 m [(\omega_z^2 - \omega^2)^2 + (2\zeta_z \omega_z \omega)^2]} \quad (5.38)$$

For the high- $Q$  case ( $\zeta_z \approx 0$ ), Equations (5.37) and (5.38) are simplified to two simultaneous equations.

$$(\omega^2 - \omega_z^2) \{(1 + G_v/2) \sin(\omega T_d) - (G_v/2) \sin[\omega(T_s + T_d)]\} = 0 \quad (5.39)$$

$$z_1 = \frac{4F_o}{\pi m} \left\{ \frac{(1 + G_v/2) \cos(\omega T_d) - (G_v/2) \cos[\omega(T_s + T_d)]}{\omega^2 - \omega_z^2} \right\} \quad (5.40)$$

The limit-cycle frequency is given implicitly by Equation (5.39). During a period of the limit cycle, at least one sample period must be spent pulling up on the plate and one spent pulling down. Several solutions for  $\omega$  are mathematically possible, but at most one solution satisfies the constraint  $T \geq 2T_s$ . The amplitude,  $z_1$ , is found by substituting the value for  $\omega$  in Equation (5.40).

For the undamped case, a minimum compensation gain,  $G_{v,\min}$  exists which gives a bounded displacement.

$$G_{v,\min} = \frac{2}{\sin[\omega_z(T_s + T_d)] / \sin(\omega_z T_d) - 1} \quad (5.41)$$

For  $G_v < G_{v,\min}$ , the plate oscillates at the resonant frequency with increasing amplitude, eventually hitting the limit stops. If the sampling rate is much larger than the resonant frequency,  $G_{v,\min} \approx 2T_d/T_s$ . Any sampled-data system will have a maximum delay equal to at least the sampling period, so use of  $2 - z^{-1}$  compensation ( $G_v = 2$ ) will not stabilize the system. Figure 5.16 is a plot of  $G_{v,\min}$  versus the ratio of sampling frequency to resonant frequency, with the sampling delay set to  $1.5 T_s$ . The  $f_s/f_z$  ratio must be greater than about 10 to stabilize the system using a practical compensation gain value. For the testbed measurements,  $f_s/f_z = 21.1$ ,  $G_{v,\min} = 3.52$ , and  $G_v = 4$ . Larger values of compensation

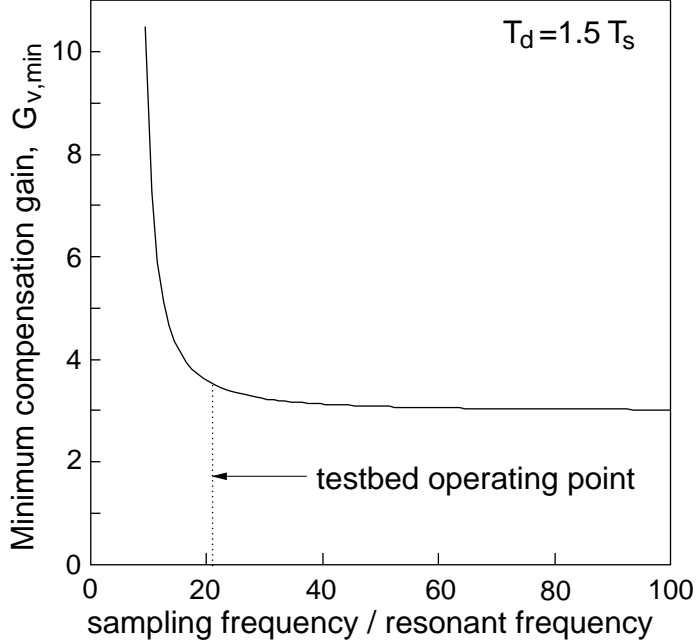


Figure 5.16: Minimum lead-compensation gain for stability,  $G_{v,\min}$ , versus the ratio of sampling frequency to resonant frequency,  $f_s/f_z$ . The sampling delay,  $T_d$ , is set to  $1.5T_s$ .

gain require a larger actuator size or higher driving voltage. Fabrication constraints limit the size of the actuators. Large voltages require special circuitry and increase switching noise.

We find the sampling delay for the testbed system by examining the implementation of the position-sensing circuit. The position sensor voltage is demodulated by subtracting the values sampled at times  $T_s/3$  and  $5 T_s/6$  after the rising clock edge. The comparator output,  $y(t)$ , is given by

$$y(t) = \text{sgn} \left[ V_{\text{sense}} \left( nT_s - \frac{2 T_s}{3} \right) - V_{\text{sense}} \left( nT_s - \frac{T_s}{6} \right) \right] \quad (5.42)$$

where  $n$  is an integer specifying the clock cycle. Assuming the sensor voltage is linearly varying with time between samples, the displacement is observed at approximately  $5 T_s/12$  before the comparator switches. If we also neglect the nonlinearity of the position sensor, a simple relation between the comparator output and displacement results.

$$y(t) = \text{sgn} \left[ \Delta z \left( nT_s - \frac{5 T_s}{12} \right) \right] \quad (5.43)$$

The displacement can cross the reference value just before or right after the observation,

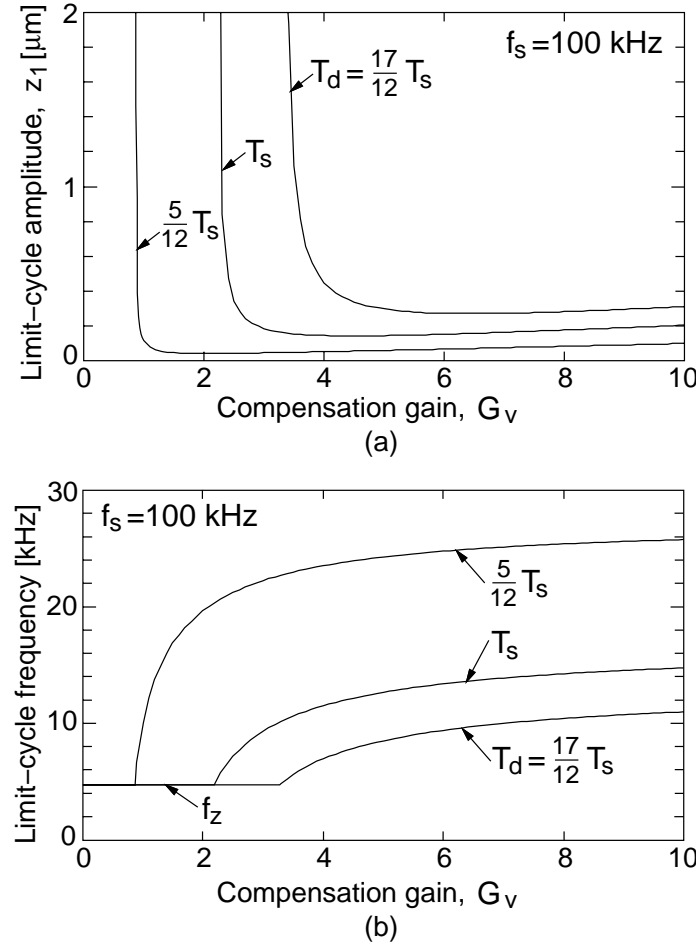


Figure 5.17: Limit cycle amplitude and frequency versus lead-compensation gain,  $G_v$ , with  $T_d = 5/12T_s, T_s, 17/12T_s$ .  $f_s = 100$  kHz,  $F_o = 116$  nN,  $f_z = 4.71$  kHz,  $Q = 50000$ . (a) Amplitude,  $z_1$ . (b) Frequency,  $\omega$ .

providing bounds on the delay,  $T_d$ .

$$\frac{5}{12}T_s \leq T_d \leq \frac{17}{12}T_s \quad (5.44)$$

Noise at the comparator input can increase the bounds, but will be neglected. Using these extreme values of  $T_d$ , maximum and minimum bounds for limit-cycle frequency and amplitude can be calculated.

The displacement limit-cycle amplitude and frequency are plotted versus lead-compensation gain in Figure 5.17. Parameters are set to emulate the testbed operating in a vacuum with a sampling frequency of 100 kHz. Other system parameter values are<sup>5</sup>.  $F_o =$

<sup>5</sup>We assume a nominal polysilicon film thickness of 2 μm in calculating these parameters, so the resonant

116 nN,  $f_z = 4.71$  kHz, and  $Q = 50000$ . Curves for three different sampling delay values are shown: minimum delay ( $5 T_s/12$ ), maximum delay ( $17 T_s/12$ ), and an intermediate delay ( $T_s$ ). The curves where  $T_d$  is set to the maximum and minimum delay provide bounds on the amplitude and frequency of the limit cycle. For compensation values below  $G_{v,\min}$ , the plate oscillates at the resonant frequency,  $f_z$ , until it hits the limit stops. The amplitude rapidly decreases when  $G_v$  is increased above  $G_{v,\min}$ . Compensation gain values above 5 keep the limit-cycle amplitude between 59 nm and 311 nm. An optimal value for the lead-compensation gain is around  $G_v = 6.4$ , which minimizes the upper bound on amplitude. As  $G_v$  is increased further, the frequency approaches its maximum value of  $\omega = 1/\pi/(2T_d + T_s)$ . The value of limit-cycle frequency can not reach the Nyquist frequency,  $f_s/2$ , because of the non-zero sampling delay.

Limit-cycle amplitude and frequency are plotted in Figure 5.18 with the sampling rate increased to 1 MHz. The limit-cycle frequency values are ten times larger, and the amplitude about 100 times smaller than the values in Figure 5.17. However, lead compensation gain above about 4 is still necessary to ensure a bounded limit cycle. The optimum value for  $G_v$  is now 5.6, its value decreasing slightly with increasing sampling rate.

Effects of sampling frequency and damping on the limit cycle are illustrated in Figure 5.19. When the system is mechanically underdamped, the change in amplitude with sampling rate is  $-40dB/decade$ . An overdamped system exhibits a  $-20dB/decade$  change of amplitude with  $f_s$ , as shown by the  $\zeta_z = 100$  case in Figure 5.19(a). At low sampling rates, the amplitude decreases linearly with increasing damping. The amplitude is insensitive to the damping factor at high sampling rates. Limit-cycle frequency increases linearly with sampling rate, except in a transition region where the system is near critical damping. The sampling rate and damping factor affect the point at which the transition from a dominant one-pole limit-cycle response to a two-pole response occurs. The dotted line on Figure 5.19(b) separates the two regions. The displacement waveform approaches a sawtooth pattern with frequency  $f_s/4$  when a large damping factor is combined with a low sampling rate.

### 5.5.3 Non-Zero External Force

---

frequency value is somewhat different from the value of 3.7 kHz stated in chapter chp:results.

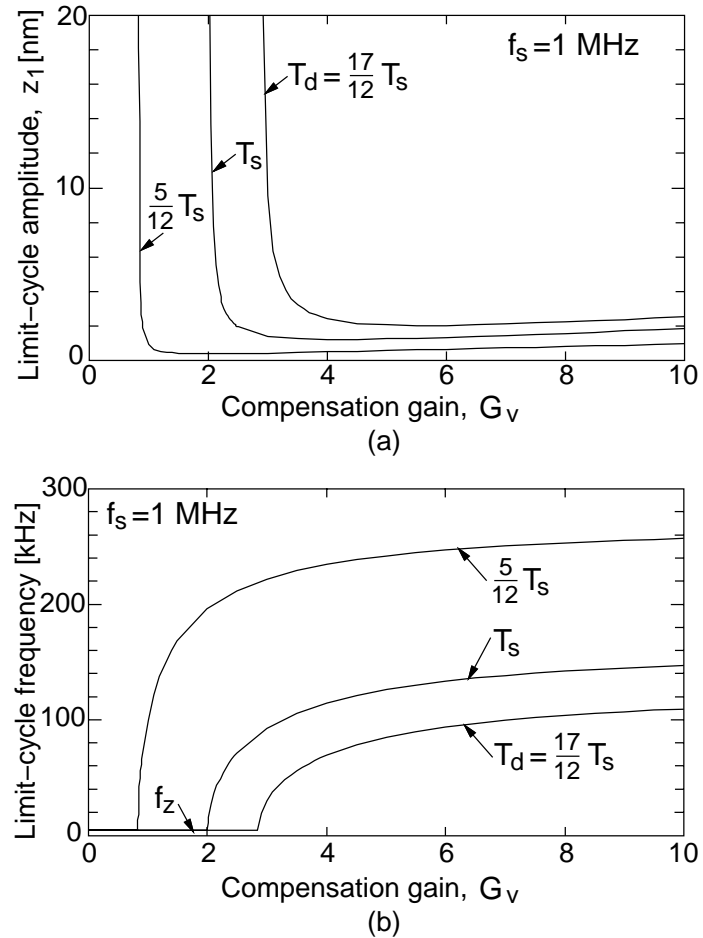


Figure 5.18: Limit cycle amplitude and frequency versus lead-compensation gain,  $G_v$ , with  $T_d = 5/12T_s, T_s, 17/12T_s$ .  $f_s = 1$  MHz,  $F_o = 116$  nN,  $f_z = 4.71$  kHz,  $Q = 50000$ . (a) Amplitude,  $z_1$ . (b) Frequency,  $\omega$ .

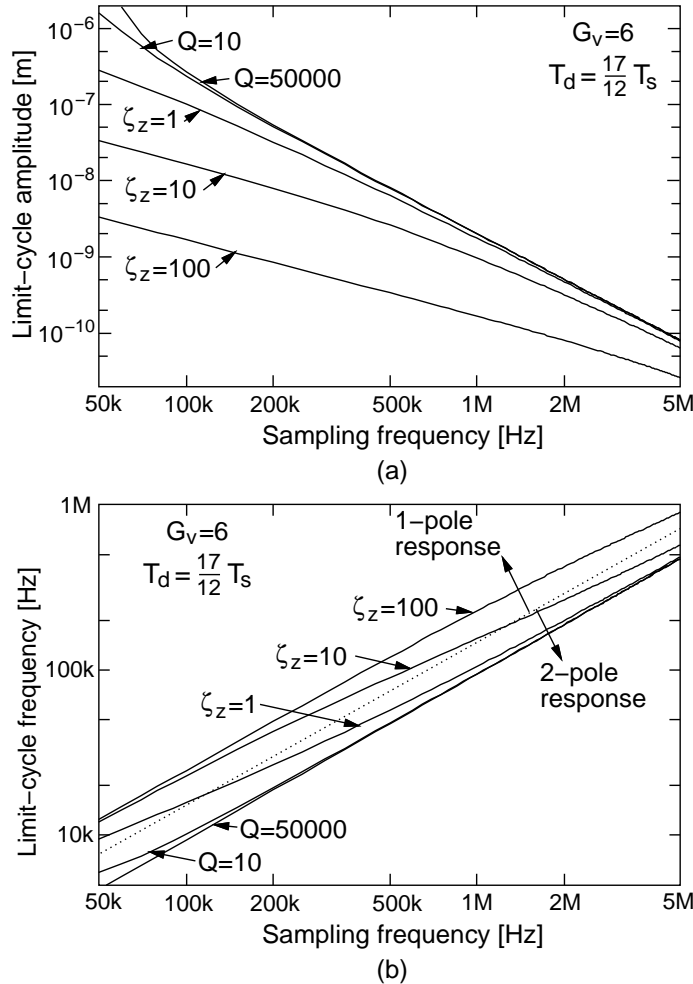


Figure 5.19: Limit cycle amplitude and frequency versus sampling frequency,  $f_s$  with various damping factors.  $T_d = 17/12 T_s$ ,  $G_v = 6$ ,  $F_o = 116$  nN,  $f_z = 4.71$  kHz. (a) Amplitude,  $z_1$ . (b) Frequency,  $\omega$ .

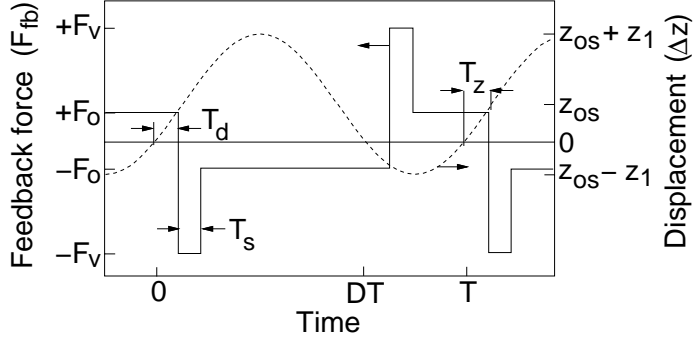


Figure 5.20: Limit-cycle waveforms of linearized feedback force with compensation (solid line), and vertical plate displacement (dashed line). The external force is balanced by feedback with duty cycle,  $D$ .

The analysis in sections 5.5.1 and 5.5.2 assume that the external force was zero. Gravity, accelerating fields, the position sensors, and non-zero position reference signals produce forces acting on the plate, which the feedback force must balance. In this section, we will investigate the effect of external and offset forces on the limit cycle.

The first step is to determine the fundamental components of the displacement and quantizer output. If a steady-state limit cycle exists, the duty cycle of the digital feedback is adjusted so the sum of forces acting on the plate is zero. Feedback with duty cycle,  $D$ , is shown in Figure 5.20. The displacement limit cycle is offset by  $z_{os}$  and delayed  $T_z$  from the position reference crossing.

$$\Delta z = z_{os} + z_1 \sin [\omega(t - T_z)] \quad (5.45)$$

where  $z_1$  is the limit cycle amplitude. The time reference is set such that  $\Delta z(t = 0) = 0$  and  $\Delta z(t = DT) = 0$ . By solving these equations, the offset and delay are found.

$$z_{os} = -\frac{z_1 \sin(2\pi D)}{\sqrt{2[1 - \cos(2\pi D)]}} \quad (5.46)$$

$$T_z = \frac{1}{\omega} \tan^{-1} \left[ -\frac{\sin(2\pi D)}{1 - \cos(2\pi D)} \right] \quad (5.47)$$

Equations (5.46) and (5.47) are substituted into (5.45), giving the displacement in terms of the duty cycle.

$$\Delta z = \frac{z_1 [-\sin(2\pi D) + \sin(\omega t) - \sin(\omega t - 2\pi D)]}{\sqrt{2[1 - \cos(2\pi D)]}} \quad (5.48)$$

The duty cycle is found by equating the average feedback force and the external

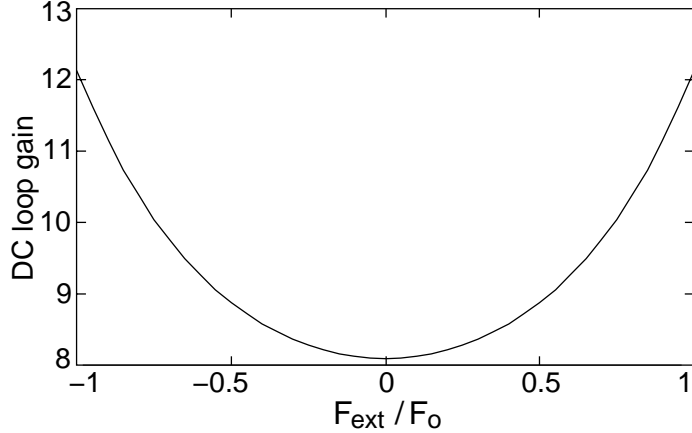


Figure 5.21: DC loop gain versus external force normalized to the full-scale force.

force,  $F_{\text{ext}}$ .

$$D = \frac{1}{2} \left( 1 + \frac{F_{\text{ext}}}{F_o} \right) \quad (5.49)$$

As an intermediate result of this analysis, we can estimate the dc loop gain. First, we recognize that the closed-loop gain equals the displacement offset divided by the external force.

$$\frac{z_{\text{os}}}{F_{\text{ext}}} = \frac{H_z(0)}{1 + L(z_1, 0)} \quad (5.50)$$

We arrive at the expression for dc loop gain by combining Equations (5.50), (5.46) and (5.49) and rearranging terms.

$$L(z_1, 0) = \frac{2F_{\text{ext}} \cos(0.5\pi F_{\text{ext}}/F_o)}{\pi k_z z_1 \sin(\pi F_{\text{ext}}/F_o)} + 1 \quad (5.51)$$

where  $k_z$  is the spring constant for vertical displacement. The loop gain value is a minimum when  $F_{\text{ext}} = 0$  and maximum when  $|F_{\text{ext}}| = F_o$ .

$$\frac{2F_o}{\pi k_z z_1} + 1 \leq L(z_1, 0) \leq \frac{F_o}{k_z z_1} + 1 \quad (5.52)$$

Nominal parameter values for the testbed in air are  $F_o = 0.12 \mu\text{N}$ ,  $k_z = 0.42 \text{ N/m}$ , and  $z_1 = 25 \text{ nm}$ . Figure 5.21 is a plot of loop gain of the testbed versus normalized external force. The loop gain value lies between 8.1 and 12.1, depending on the external force. A much higher loop gain is desirable to reduce nonlinear effects in microsensor and microcontroller applications. The loop gain increases with decreasing spring constant and increasing sampling frequency. The effect of dc loop gain on acceleration signal to noise ratio will be discussed in section 5.6.2.

Now, we turn our attention to determining the amplitude and phase of the quantizer output. The first harmonic output from the quantizer,  $y_1(t)$ , is found using the Fourier analysis method of section 5.5.1.

$$y_1(t) = -\frac{2}{\pi} e^{-j\omega T_d} [\sin(\omega t) - \sin(\omega t - 2\pi D)] \quad (5.53)$$

When  $D = 0.5$ , this equation simplifies to the  $F_{\text{ext}} = 0$  case, given by Equation (5.32). Inspecting the phase of Equations (5.48) and (5.53), we see that the delay of the first harmonic of the displacement and quantizer output differ by  $T_d$ , independent of duty cycle.

The quantizer describing function consists of a gain term with delay  $T_d$ .

$$H_q(z_1, \omega) = \frac{2\sqrt{2[1 - \cos(2\pi D)]}}{\pi z_1} e^{-j\omega T_d} = \frac{4}{\pi z_1} \cos\left(\frac{\pi F_{\text{ext}}}{2F_o}\right) e^{-j\omega T_d} \quad (5.54)$$

If we increase the magnitude of the external force, the fundamental component of the feedback force decreases in amplitude. The amplitude is a maximum at a 50 % duty cycle, where  $F_{\text{ext}} = 0$ . The phase of the quantizer describing function is not affected by external force, so we can still use Equation (5.39) to calculate the limit-cycle frequency (assuming high- $Q$  operation). We include the effects of external force on limit-cycle amplitude by reducing the right side of Equation (5.40) by a factor of  $\cos(0.5\pi F_{\text{ext}}/F_o)$ .

$$z_1 = \frac{4F_o \cos(0.5\pi F_{\text{ext}}/F_o)}{\pi m} \left\{ \frac{(1 + G_v/2) \cos(\omega T_d) - (G_v/2) \cos[\omega(T_s + T_d)]}{\omega^2 - \omega_z^2} \right\} \quad (5.55)$$

In general, we desire to reduce the limit-cycle amplitude in order to minimize nonlinear effects of position. The largest value of limit-cycle amplitude occurs for zero external force, so the effect of external force can be neglected in a worst-case analysis.

#### 5.5.4 Feedback Nonlinearity With Position

Figure 5.22 illustrates the effect of position nonlinearity on the feedback force. The force is applied by parallel-plate actuators, which have an inverse-square dependence on the plate spacing.

$$F_{\text{fb}}(t, \Delta z) = H_{\text{pp}}(\Delta z) F_{\text{fbo}}(t) = \begin{cases} +F_{\text{fbo}}(t)/(1 - \Delta z/z_o)^2 & ; \text{upper actuator} \\ -F_{\text{fbo}}(t)/(1 + \Delta z/z_o)^2 & ; \text{lower actuator} \end{cases} \quad (5.56)$$

where  $z_o$  is the reference spacing between the plates,  $F_{\text{fbo}}(t)$  is the linearized force, and  $H_{\text{pp}}(\Delta z)$  is the parallel-plate nonlinearity term. The reference position is assumed to be centered between the upper and lower actuators. A first-order approximation for the parallel-plate nonlinearity term is valid when displacements are small compared to the reference

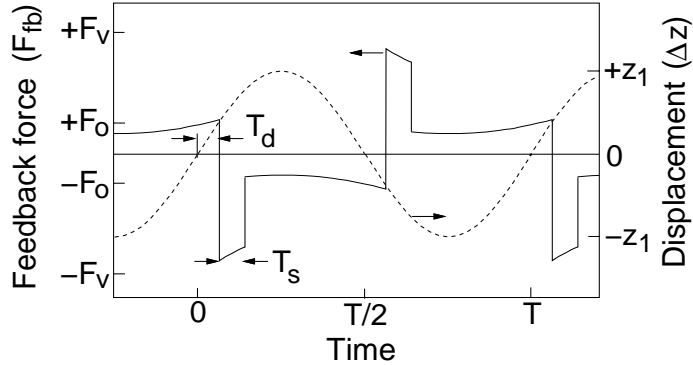


Figure 5.22: Limit-cycle waveforms of nonlinear feedback force with compensation (solid line), and vertical plate displacement (dashed line).

gap.

$$H_{\text{pp}}(t) \approx \begin{cases} 1 + (2z_1/z_o) \sin(\omega t) & ; \text{upper actuator} \\ 1 - (2z_1/z_o) \sin(\omega t) & ; \text{lower actuator} \end{cases} \quad (5.57)$$

where  $\Delta z$  is given by Equation (5.48) with the external force set to zero.

We can derive a describing function which models the quantizer and the actuator nonlinearity together. The compensation is introduced later as a multiplicative term in the expression for loop gain. The limit cycle generated when the quantizer output is passed through the parallel-plate nonlinearity is given by  $H_{\text{pp}}(t)y(t)$ . Fourier coefficients of  $H_{\text{pp}}(t)y(t)$  are calculated using the analysis method from section 5.5.1.

$$A_m = \frac{1}{T} \left\{ \int_{T_d}^{T/2+T_d} \left[ 1 - \frac{2z_1}{z_o} \sin(\omega t) \right] e^{-jm\omega t} dt - \int_{T/2+T_d}^{T+T_d} \left[ 1 + \frac{2z_1}{z_o} \sin(\omega t) \right] e^{-jm\omega t} dt \right\} \quad (5.58)$$

We compare the first-harmonic component with the sinusoidal displacement, providing us with a quantizer describing function which includes the parallel-plate nonlinearity.

$$H_q(z_1, \omega) = \frac{4}{\pi z_1} e^{-j\omega T_d} - \frac{2}{z_1} \quad (5.59)$$

The nonlinearity produces an additional first-harmonic component of the feedback which is in phase with the plate displacement. Limit-cycle amplitude and frequency are found by setting the loop gain to  $-1$ , and solving the resulting simultaneous equations iteratively.

$$L(z_1, \omega) = \frac{F_o \left[ (4/\pi/z_1)e^{-j\omega T_d} - 2/z_o \right] \left[ 1 + G_v(1 - e^{-j\omega T_s})/2 \right]}{m(-\omega^2 + j2\zeta_z \omega_r \omega + \omega_r^2)} = -1 \quad (5.60)$$

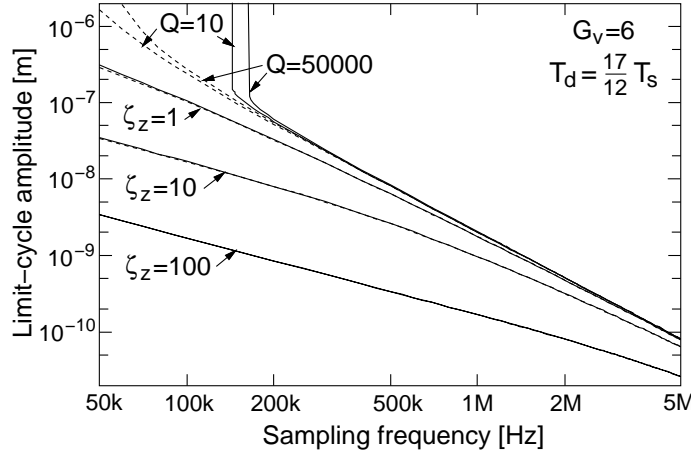


Figure 5.23: Limit cycle amplitude and frequency versus sampling frequency,  $f_s$ , with various damping factors. Actuator nonlinearity is included in the calculations.  $T_d = 17/12T_s$ ,  $G_v = 6$ ,  $F_o = 116$  nN,  $f_z = 4.71$  kHz. (a) Amplitude,  $z_1$ . (b) Frequency,  $\omega$ .

Equations (5.61) and (5.62) are simplified expressions for the mechanically underdamped case ( $\zeta_z \approx 0$ ).

$$(\omega^2 - \omega_z^2) \left\{ \left( 1 + \frac{G_v}{2} \right) \sin(\omega T_d) - \frac{G_v}{2} \sin[\omega(T_s + T_d)] + \frac{\pi G_v z_1}{4 z_o} \sin(\omega T_s) \right\} = 0 \quad (5.61)$$

$$\begin{aligned} z_1 &= \left[ \frac{4F_o \{(1 + G_v/2) \cos(\omega T_d) - (G_v/2) \cos[\omega(T_s + T_d)]\}}{\pi m(\omega^2 - \omega_z^2)} \right] \times \\ &\quad \left[ 1 + \frac{2F_o [(1 + G_v/2) - (G_v/2) \cos(\omega T_s)]}{z_o m(\omega^2 - \omega_z^2)} \right]^{-1} \end{aligned} \quad (5.62)$$

The effect of actuator nonlinearity on the limit-cycle amplitude is illustrated in Figure 5.23. Data represented by the solid lines includes the actuator nonlinearity in the calculations. The dashed lines are the linear curves plotted previously in Figure 5.19. In the underdamped cases, the sampling frequency must be much larger than the values predicted by linear theory to avoid instability. When the system is overdamped, including nonlinearity in the calculations modifies the results by no more than about 10%.

## 5.6 Noise Analysis

### 5.6.1 Brownian Noise

Brownian noise analysis is important in force sensors and accelerometers, where the noise force directly affects the sense signal. In contrast, equivalent Brownian noise position does not limit the performance of closed-loop micropositioners. Feedback nulls the position error, so the equivalent Brownian noise position is reduced from its open-loop value by the effective loop gain. In the testbed  $\Sigma\text{-}\Delta$  loop, limit-cycles, caused by the high-frequency force-feedback pulses, are the primary source of chatter in the plate. Therefore, we will focus our attention on the equivalent Brownian noise acceleration of the testbed.

Brownian noise was discussed in section 3.6.3.3, where we found that it is often greater than circuit noise in a single-mode surface microsystem. In the multi-mode testbed, a Brownian noise source is associated with each vibrational mode. Noise from the  $z$ ,  $\theta$ , and  $\phi$  modes couples to the signal outputs that control each corner of the plate; the noise associated with higher modes can be neglected. Using solutions analogous to Equation (3.232), we find that the noise contributions from the  $z$ ,  $\theta$ , and  $\phi$  modes are

$$\overline{f_z^2} = 4k_B T (2\zeta_z m \omega_z) \Delta f \quad (5.63)$$

$$\overline{\tau_\theta^2} = 4k_B T (2\zeta_\theta I_\theta \omega_\theta) \Delta f = K_{B\theta} L_y^2 \overline{f_z^2} \quad (5.64)$$

$$\overline{\tau_\phi^2} = 4k_B T (2\zeta_\phi I_\phi \omega_\phi) \Delta f = K_{B\phi} L_x^2 \overline{f_z^2} \quad (5.65)$$

where  $\overline{\tau_\theta^2}$  and  $\overline{\tau_\phi^2}$  are the Brownian noise torque about the  $x$ -axis and  $y$ -axis, respectively. We have made the assumption that damping coefficients of the rotational modes are given by Equations (3.34) and (3.35). Since the plate is perforated with many holes, the rotational damping will be comparable to the vertical damping, and cannot be neglected. Equivalent Brownian noise acceleration for the three modes is

$$\overline{a_{eq,z}^2} = 4k_B T \left( \frac{2\zeta_z \omega_z}{m} \right) \Delta f \quad (5.66)$$

$$\overline{a_{eq,\theta}^2} = 4k_B T \left( \frac{2\zeta_\theta \omega_\theta}{I_\theta} \right) \Delta f = \left( \frac{144 K_{B\theta}}{L_y^2} \right) \overline{a_{eq,z}^2} \quad (5.67)$$

$$\overline{a_{eq,\phi}^2} = 4k_B T \left( \frac{2\zeta_\phi \omega_\phi}{I_\phi} \right) \Delta f = \left( \frac{144 K_{B\phi}}{L_x^2} \right) \overline{a_{eq,z}^2} \quad (5.68)$$

where  $\overline{a_{eq,\theta}^2}$  and  $\overline{a_{eq,\phi}^2}$  are the equivalent Brownian-noise angular acceleration.

The external modes of force and torque acting on the testbed are extracted by adding or subtracting the actuator force signals.

$$\begin{bmatrix} F_z \\ \tau_\theta \\ \tau_\phi \end{bmatrix} = \begin{bmatrix} 1 & 1 & 1 & 1 \\ L_{ay} & L_{ay} & -L_{ay} & -L_{ay} \\ -L_{ax} & L_{ax} & L_{ax} & -L_{ax} \end{bmatrix} \begin{bmatrix} F_{ur} \\ F_{ul} \\ F_{ll} \\ F_{lr} \end{bmatrix} \quad (5.69)$$

where the actuators are located at  $|x|=L_{ax}$  and  $|y|=L_{ay}$  from the center of the plate. The noise from each mode referred to the actuators is correlated. When each mode is extracted from the actuator force signals, only the noise from that mode is present; the other modal noise contributions are cancelled. For example, if all four actuator forces are summed, the correlated noise from the rotational modes is cancelled, resulting in a total noise force of  $\overline{f_z^2}$ . Similarly, the total noise torques are  $\overline{\tau_\theta^2}$  and  $\overline{\tau_\phi^2}$ , when referred to  $\tau_\theta$  and  $\tau_\phi$ , respectively. We can substitute the testbed parameter values given in Table A.1 into Equations (5.66) through (5.68) to calculate the Brownian noise in air. The resulting testbed equivalent Brownian noise acceleration is 3.7 milli-G and the equivalent noise angular acceleration is approximately 190 Hz/s (68400°/s<sup>2</sup>), assuming a 50 Hz signal bandwidth.

The noise force can be referred to the individual actuator inputs by defining the four actuator forces as functions of  $F_z$ ,  $\tau_\theta$ , and  $\tau_\phi$ . However, the testbed system is over-constrained, so we would need an extra equation to invert Equation (5.69). Instead, we will analyze the situation in our acceleration experiments<sup>6</sup>, where we have deactivated the lower-right actuator to eliminate the extra constraint. Then, the actuator forces, in terms of the modal forces and torques, are

$$\begin{bmatrix} F_{ur} \\ F_{ul} \\ F_{ll} \\ F_{lr} \end{bmatrix} = \frac{1}{2} \begin{bmatrix} 1 & 0 & -1/L_{ax} \\ 0 & 1/L_{ay} & 1/L_{ax} \\ 1 & -1/L_{ay} & 0 \\ 0 & 0 & 0 \end{bmatrix} \begin{bmatrix} F_z \\ \tau_\theta \\ \tau_\phi \end{bmatrix} \quad (5.70)$$

and the equivalent actuator noise forces when only the three actuators are operating are

$$\overline{f_{eq,ur}^2} = \frac{1}{2} \left( \overline{f_z^2} + \frac{\overline{\tau_\phi^2}}{L_{ax}^2} \right) = \frac{\overline{f_z^2}}{2} \left[ 1 + K_{B\phi} \left( \frac{L_x}{L_{ax}} \right)^2 \right] \quad (5.71)$$

---

<sup>6</sup>See section 6.8 for the experimental results.

$$\overline{f_{eq,ul}^2} = \frac{1}{2} \left( \frac{\overline{\tau_\theta^2}}{L_{ay}^2} + \frac{\overline{\tau_\phi^2}}{L_{ax}^2} \right) = \frac{\overline{f_z^2}}{2} \left[ K_{B\theta} \left( \frac{L_y}{L_{ay}} \right)^2 + K_{B\phi} \left( \frac{L_x}{L_{ax}} \right)^2 \right] \quad (5.72)$$

$$\overline{f_{eq,ll}^2} = \frac{1}{2} \left( \overline{f_z^2} + \frac{\overline{\tau_\theta^2}}{L_{ay}^2} \right) = \frac{\overline{f_z^2}}{2} \left[ 1 + K_{B\theta} \left( \frac{L_y}{L_{ay}} \right)^2 \right] \quad (5.73)$$

Since Brownian noise from all three modes is balanced by the actuator feedback, noise on a single signal of a quadrant is larger than the noise on the sum of all four signals,  $\overline{f_z^2}$ . In a 50 Hz bandwidth, the values of equivalent actuator noise acceleration are  $\sqrt{\overline{f_{eq,ur}^2}}=7.13$  milli-G,  $\sqrt{\overline{f_{eq,ul}^2}}=9.13$  milli-G, and  $\sqrt{\overline{f_{eq,ll}^2}}=6.80$  milli-G; all are larger than  $\sqrt{\overline{f_z^2}}$ .

## 5.6.2 Sigma-Delta Quantization Noise

### 5.6.2.1 Sampled-Data Representation

We will use the single-loop representation in Figure 5.24(a) to analyze quantization noise in the testbed. A sampled-data version of the loop is shown in Figure 5.24(b). The micromechanical mass-spring-damper and the sampling switch are approximated by a second-order z-transform,  $H(z)$ .

$$H(z) = \frac{K_n z^{-1}}{1 - \alpha z^{-1} + \beta z^{-2}} \quad (5.74)$$

where  $\alpha$  and  $\beta$  are fixed coefficients, determined from the second-order mechanical transfer function, and  $K_n$  is the loop gain normalization factor. Based on the limit-cycle analysis developed earlier, The high-gain nonlinear quantizer enforces a loop gain value of  $-1$  at the Nyquist rate,  $f_s/2$ . This loop-gain approximation is valid for overdamped systems and for underdamped systems that are compensated and sampled at a frequency much higher than the resonant frequency. The comparator in Figure 5.24(b) is modeled as an added source of white noise with a total mean square noise given by [90]

$$\overline{e_q^2}_{TOT} = \frac{\Delta^2}{12} \quad (5.75)$$

where  $\Delta$  is the difference in the two quantizer output levels. Quantization noise is limited in bandwidth to the Nyquist rate, so the noise power in a frequency interval  $\Delta f$  is

$$\overline{e_q^2} = \frac{\overline{e_q^2}_{TOT}}{f_s/2} = \left( \frac{\Delta^2}{6f_s} \right) \Delta f \quad (5.76)$$

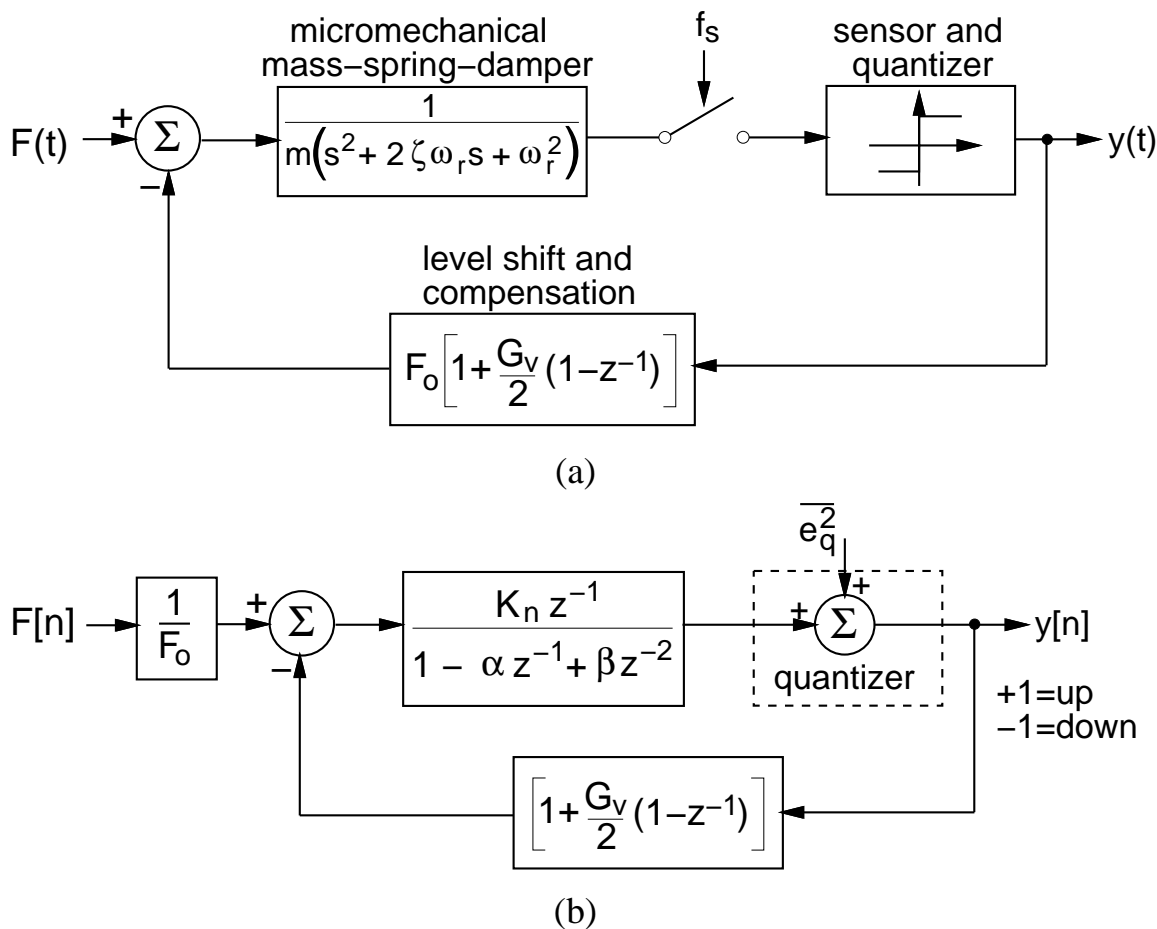


Figure 5.24: Single-loop representation of the testbed. (a) Continuous-time block diagram.  
 (b) Sampled-data version of (a).

### 5.6.2.2 Equivalent Output-Referred Quantization Noise

We derive the equivalent noise acceleration by first referring the quantization noise to the output,  $y[n]$  (see Figure 5.24(b)). The transfer function,  $Y(z)/E_q(z)$ , of the noise input to the output is

$$\frac{Y(z)}{E_q(z)} = \frac{1}{1 + H(z)H'_{\text{fb}}(z)} \quad (5.77)$$

where  $H'_{\text{fb}}(z)$  is the normalized z-transform in the feedback path, equal to

$$H'_{\text{fb}}(z) = 1 + G_v \left( \frac{1 - z^{-1}}{2} \right) \quad (5.78)$$

Combining Equations (5.74), (5.77), and (5.78), we get

$$\frac{Y(z)}{E_q(z)} = \frac{1 - \alpha z^{-1} + \beta z^{-2}}{1 + C z^{-1} + D z^{-2}} \quad (5.79)$$

where  $C \equiv K_n - \alpha + K_n G_v / 2$ , and  $D \equiv \beta - K_n G_v / 2$ .

We now use Equation (5.79), and make the substitution  $z = e^{j\omega T_s}$ , to obtain the equivalent output-referred noise,  $\overline{e_y^2}$ :

$$\begin{aligned} \overline{e_y^2} &= \left| \frac{Y(e^{j\omega T_s})}{E_q(e^{j\omega T_s})} \right|^2 \overline{e_q^2} \\ &= \frac{[1 - \alpha \cos(\omega T_s) + \beta \cos(2\omega T_s)]^2 + [\alpha \sin(\omega T_s) - \beta \sin(2\omega T_s)]^2}{[1 + C \cos(\omega T_s) + D \cos(2\omega T_s)]^2 + [C \sin(\omega T_s) + D \sin(2\omega T_s)]^2} \overline{e_q^2} \end{aligned} \quad (5.80)$$

If the signal bandwidth is much less than the sampling frequency ( $\omega T_s \ll 1$ ), which should be the case for an oversampled converter, we can approximate Equation (5.80) by

$$\overline{e_y^2} \approx \left( \frac{1 - \alpha + \beta}{1 + K_n - \alpha + \beta} \right)^2 \overline{e_q^2} \quad (5.81)$$

At low frequencies, the equivalent output-referred noise is independent of frequency. The lack of noise shaping is a consequence of the constant low-frequency gain of the mechanical mass-spring-damper. If the signal bandwidth extends beyond the mechanical transfer-function poles, then the approximation breaks down and the frequency terms in Equation (5.80) must be included in the noise calculation.

The coefficients,  $\alpha$  and  $\beta$ , are found directly from the impulse response of the second-order mechanical system. The mechanical transfer function can be factored such that

$$\begin{aligned} H(s) &= \frac{1}{s^2 + 2\zeta\omega_n s + \omega_n^2} \\ &= \frac{1}{(s + a_1)(s + a_2)} \end{aligned} \quad (5.82)$$

where the roots,  $-c_1$  and  $-c_2$ , are given by

$$c_1 = \zeta\omega_n - \omega_n\sqrt{\zeta^2 - 1} \quad (5.83)$$

$$c_2 = \zeta\omega_n + \omega_n\sqrt{\zeta^2 - 1} \quad (5.84)$$

For an overdamped system ( $\zeta > 1$ ), the impulse response is

$$h(t)|_{\zeta>1} = \frac{1}{2\omega_o} (e^{-a_1 t} - e^{-a_2 t}) u(t) \quad (5.85)$$

where  $\omega_o \equiv \omega_n\sqrt{\zeta^2 - 1}$ . The corresponding sampled-data impulse response is

$$h[n]|_{\zeta>1} = \frac{1}{2\omega_o} (\alpha_1^n - \alpha_2^n) u[n] \quad (5.86)$$

where  $\alpha_1 = e^{-a_1 T_s}$  and  $\alpha_2 = e^{-a_2 T_s}$ . We take the z-transform of Equation (5.86) and get

$$H(z)|_{\zeta>1} = \left( \frac{\alpha_1 - \alpha_2}{2\omega_o} \right) \frac{z^{-1}}{(1 - \alpha_1 z^{-1})(1 - \alpha_2 z^{-1})} \quad (5.87)$$

Finally, the coefficients in the denominator are matched to solve for  $\alpha$  and  $\beta$ , yielding

$$\alpha|_{\zeta>1} = \alpha_1 + \alpha_2 = e^{-\zeta\omega_n T_s} (e^{\omega_o T_s} + e^{-\omega_o T_s}) \quad (5.88)$$

$$\beta|_{\zeta>1} = \alpha_1 \alpha_2 = e^{-2\zeta\omega_n T_s} \quad (5.89)$$

For  $\omega_o \ll f_s$  and moderate damping,  $\alpha \approx 2$  and  $\beta \approx 1$ ; in this case, the mechanical system behaves like an ideal sampled-data double integrator. A relatively low sampling rate or large damping produces a lossy single-pole mechanical response below the Nyquist frequency, where  $\alpha \approx e^{-\omega_n T_s/(2\zeta)}$  and  $\beta$  can be neglected.

An approximate value for the normalization factor can be determined by first finding the dc loop gain,  $L(z)|_{z=1}$ .

$$\begin{aligned} L(z)|_{z=1} &= \left[ \frac{-K_n (1 + 0.5G_v(1 - z^{-1})) z^{-1}}{1 - \alpha z^{-1} + \beta z^{-2}} \right] \Big|_{z=1} \\ &= \frac{-K_n}{1 - \alpha + \beta} \end{aligned} \quad (5.90)$$

For the overdamped case, we obtain

$$\begin{aligned} L(z)|_{z=1} &\simeq \frac{-K_n}{1 - e^{-c_1 T_s}} \\ &\approx \frac{-K_n}{c_1 T_s} \end{aligned} \quad (5.91)$$

Since the loop transfer function has a pole at  $\omega=c_1$ , the gain at the Nyquist frequency will be  $-1$  if  $K_n=\pi$ .

A similar analysis can be performed for the underdamped case ( $\zeta < 1$ ); the resulting  $\alpha$  and  $\beta$  coefficients are

$$\alpha|_{\zeta<1} = 2e^{-\zeta\omega_n T_s} \cos(\omega_o T_s) \quad (5.92)$$

$$\beta|_{\zeta<1} = \beta|_{\zeta>1} = e^{-2\zeta\omega_n T_s} \quad (5.93)$$

and the normalization factor (for  $\zeta \ll 1$ ) is  $K_n=\pi^2$ .

### 5.6.2.3 Equivalent Quantization Noise Acceleration

We find the equivalent noise acceleration by referring the equivalent output noise to the force input, and scale by  $1/m$ , and get

$$\overline{a_{eq,q}^2} = \left( \frac{F_o}{m} \right)^2 \overline{e_y^2} \quad (5.94)$$

Combining Equations (5.81), (5.88), (5.89) and (5.94), we obtain the equivalent input-referred noise acceleration in terms of the quantization noise. For an overdamped system,

$$\overline{a_{eq,q}^2} \simeq \left( \frac{F_o}{m} \right)^2 \left( \frac{\omega_n}{2\pi\zeta f_s} \right)^2 \overline{e_q^2} \quad (5.95)$$

where we have used the oversampling approximation ( $\omega T_s \ll 1$ ). The total noise acceleration is found by integrating Equation (5.95) over the signal frequency band,  $f=0$  to  $f_o$ , yielding

$$\overline{a_{q,TOT}^2}|_{\zeta>1} \simeq \left( \frac{F_o}{m} \right)^2 \left( \frac{\Delta^2}{12} \right) \frac{2f_n^2 f_o}{\zeta^2 f_s^3} \quad (5.96)$$

where  $f_n = \omega_n/2\pi$ . Doubling the sampling frequency results in a 9 dB noise reduction, as expected for a first-order  $\Sigma\Delta$  loop; however, reducing the signal bandwidth by half results in only a 3 dB noise reduction, because the noise spectral density is constant. Lowering the resonant frequency or increasing the damping will also reduce the input-referred noise. The damping dependence on quantization noise is reversed from that of the Brownian noise, for  $\zeta>1$ .

Equivalent input-referred noise acceleration for a mechanically underdamped system is

$$\overline{a_{q,eq}^2} \simeq \left( \frac{F_o}{m} \right)^2 \left( \frac{\omega_n}{\pi f_s} \right)^4 \overline{e_q^2} \quad (5.97)$$

Again, we assume  $\omega T_s \ll 1$ . Integrating the noise spectral density from  $f=0$  to  $f_o$ , we obtain the total noise acceleration.

$$\overline{a_{q,\text{TOT}}^2} |_{\zeta < 1} \simeq \left( \frac{F_o}{m} \right)^2 \left( \frac{\Delta^2}{12} \right) \frac{f_n^4 f_o}{(f_s/2)^5} \quad (5.98)$$

The quantization noise acceleration is reduced by 15 dB/octave increase in the sampling rate, which matches the performance of the conventional second-order  $\Sigma$ - $\Delta$  loop. As in the overdamped case, the noise is reduced by 3 dB/octave decrease in the signal bandwidth. The noise is insensitive to the mechanical quality factor, but there is a noise reduction of 12 dB/octave due to a decrease in the resonant frequency.

The testbed mechanical parameters for operation in air are  $m=0.47 \mu\text{g}$ ,  $\zeta_z=12$ , and  $f_{n,z}=3.7 \text{ kHz}$ , corresponding to real poles at 150 Hz and 88 kHz. The non-dominant pole is above the sampling frequency of 50 kHz and does not affect the noise shaping. Assuming a full-scale feedback force of  $\pm 293 \text{ nN}$ , ( $\pm 64 \text{ G}$ ) and a signal bandwidth of 50 Hz, and plugging these values into Equation (5.96), we calculate a value of 10.1 milli-G for total equivalent quantization noise acceleration<sup>7</sup>.

### 5.6.3 Equivalent Noise Force from Interconnect Resistance

Another source of equivalent noise force arises from interconnect resistance, which adds thermal noise to the electrostatic actuator voltages. This noise is present on feedback actuators, sensor capacitors, and open-loop actuators (such as the testbed's comb drives). Electrostatic force generated by these elements is proportional to the square of the applied voltage.

$$F = \gamma V_a^2 \quad (5.99)$$

where  $\gamma$  is a proportionality constant with units of N/V<sup>2</sup>. Equivalent noise acceleration due to an interconnect resistance,  $R$ , is

$$\overline{a_{R,\text{eq}}^2} = 4kT R \left( \frac{2\gamma V_a}{m} \right)^2 f_o \quad (5.100)$$

The total equivalent noise force from interconnect is found by summing the contributions from each actuator and sensor capacitor. For the testbed, the values for  $\gamma$  and the applied voltage are:

---

<sup>7</sup>These values assume that all four actuators are operating. In our acceleration measurements, we operate only three of the four actuators at the plate's corners. Then, the full-scale acceleration is  $\pm 48 \text{ G}$  and the total equivalent quantization noise acceleration is 7.5 milli-G.

upper actuator:	$\gamma_u = 1.70 \text{ nN/V}^2$
	$V_{a,u} = 7.15 \text{ V}$
lower actuator:	$\gamma_l = 2.45 \text{ nN/V}^2$
	$V_{a,l} = 3.56 \text{ V}$
sensor capacitor:	$\gamma_s = 18.3 \text{ nN/V}^2$
	$V_{a,s} = 0.3 \text{ V}$

Using a worst-case resistance value of  $35 \text{ k}\Omega$  and assuming a 50 % duty cycle between the upper and lower actuators, we calculate an equivalent noise acceleration of 0.05 milli-G in a 50 Hz bandwidth.

#### 5.6.4 Total Noise Acceleration for the Testbed

Brownian noise ( $\overline{a_{z,\text{TOT}}^2}$ ), quantization noise ( $\overline{a_{q,\text{TOT}}^2}$ ), electronic noise ( $\overline{a_{e,\text{TOT}}^2}$ ) and interconnect noise ( $\overline{a_{R,\text{TOT}}^2}$ ) contribute to the total equivalent noise acceleration of the testbed.

$$\overline{a_{\text{TOT}}^2} = \overline{a_{z,\text{TOT}}^2} + \overline{a_{q,\text{TOT}}^2} + \overline{a_{e,\text{TOT}}^2} + \overline{a_{R,\text{TOT}}^2} \quad (5.101)$$

With the exception of electronic noise, values of these noise contributions have been calculated in the preceding sections. Electronic noise is primarily generated from the unity-gain buffer, discussed in sections 3.6.1.3 and 3.6.3.2. As shown in Figure 3.41, the diode shot noise current dominates the buffer noise at the 50 kHz sampling rate. Since the reference capacitors in our experiments are disconnected, the rms voltage signal into each buffer is around 0.1 V. Using Equation (3.195), we calculate a total noise voltage of  $0.52 \mu\text{V}/\sqrt{\text{Hz}}$ , which is equivalent to a noise acceleration of 0.35 milli-G in a 50 Hz bandwidth. Noise from each buffer is uncorrelated, so the total noise contribution from the electronics is 0.7 milli-G.

We substitute the values for noise into Equation (5.101) and obtain the testbed equivalent noise acceleration in a 50 Hz bandwidth,

$$\begin{aligned} \sqrt{\overline{a_{\text{TOT}}^2}} &= \left[ \underbrace{(3.7 \text{ milli-G})^2}_{\text{Brownian noise}} + \underbrace{(10.1 \text{ milli-G})^2}_{\text{quantization noise}} + \underbrace{(0.7 \text{ milli-G})^2}_{\text{electronic noise}} + \underbrace{(0.05 \text{ milli-G})^2}_{\text{interconnect noise}} \right]^{1/2} \\ &= 10.8 \text{ milli-G} \end{aligned}$$

The total noise is dominated by quantization noise, with the Brownian noise being about 7 times less significant and the other noise contributions being negligible.

## Chapter 6

# Testbed Experimental Results

### 6.1 Introduction

In this section, we present our experimental results for the micromechanical testbed. We will first discuss the die samples used in the testing, followed by a description of the experimental setup. We have performed characterization of the testbed in air using  $\Sigma\text{-}\Delta$  control of the three modes. Open-loop and closed-loop step response of the plate are compared with simulation. The  $\Sigma\text{-}\Delta$  bitstreams can be combined to produce an acceleration output. Accelerometer functionality is verified by measuring the response to a 1 Hz external vibration input. Static acceleration measurements provide the sensitivity and signal-to-noise ratio, and show mode-coupling of the noise. Last, testing results at low pressure are presented, where the existence of bounded limit cycles is confirmed.

### 6.2 Experimental Setup

We have tested the device in air on a wafer probe-station using the custom assembly shown in Figure 6.1. The assembly consists of a zero-insertion-force (ZIF) socket on a printed-circuit board, bolted onto an aluminum chuck. On the bottom-side of the printed-circuit board, signals are routed to 44-pin edge connectors, while the top side is a solid ground plane. Coaxial cables from the edge connectors provide a general interconnection scheme that can be used for many projects. However, the position-sense outputs would be capacitively loaded by the coaxial cable, limiting the bandwidth to less than 1 MHz. For these signals, external buffers are placed close to the testbed chip, on a daughter board

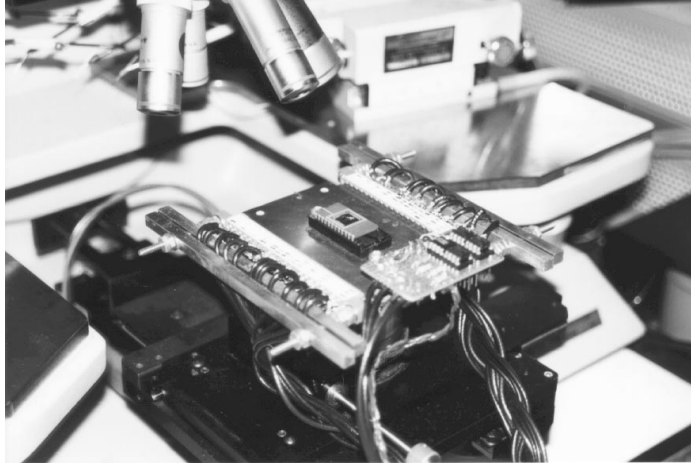


Figure 6.1: Custom mounting assembly for testing on the wafer probe-station. The testbed DIP is located in the center of the photograph.

attached to the printed-circuit board. Direct wiring to the external buffers reduces the load capacitance to less than 10 pF.

A custom probe card, shown in Figure 6.2, was made for testing devices in our vacuum probe-station. A printed-circuit board with a ground plane is used to route signals through a metal end-cap that seals the vacuum chamber, and out to the edge connectors. The connectors are compatible with the coaxial-cable assembly used in testing on the wafer probe-station.

The experimental test setup is shown in Figure 6.3. The external electronics are housed in a card-cage with most connections made via front-panel BNC connectors. Circuit schematics and the card-cage layout are given in appendix A.2.

### 6.3 Position-Sensor Characterization

One period of the position sensor waveform, for various reference input values, is shown in Figure 6.4. Tungsten contacts connecting the reference capacitor to the bridge are disconnected, due to HF attack during the microstructure release. The resulting imbalance in the capacitive divider produces a peak-to-peak sensor offset voltage of  $-103$  mV. The interconnect leading off-chip has a capacitance value of about 10 pF, limiting the risetime to 424 ns. A source-follower circuit drives the signal off-chip, adding a dc offset of  $-0.81$  V. Photocurrent in the diode at the input to the buffer causes the dc bias to shift more negative

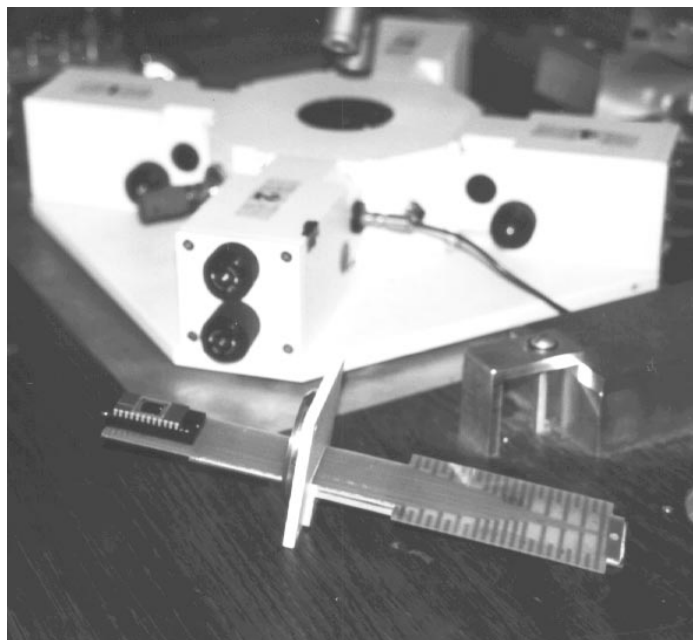


Figure 6.2: Custom probe card for testing in the vacuum probe-station (shown in the background).

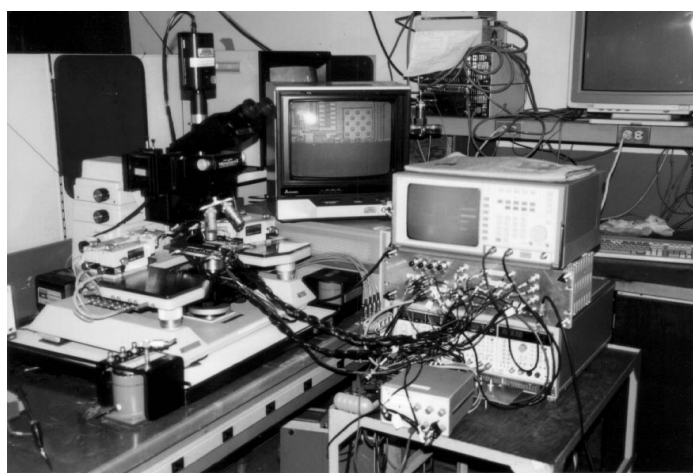


Figure 6.3: Photograph of the experimental test setup.

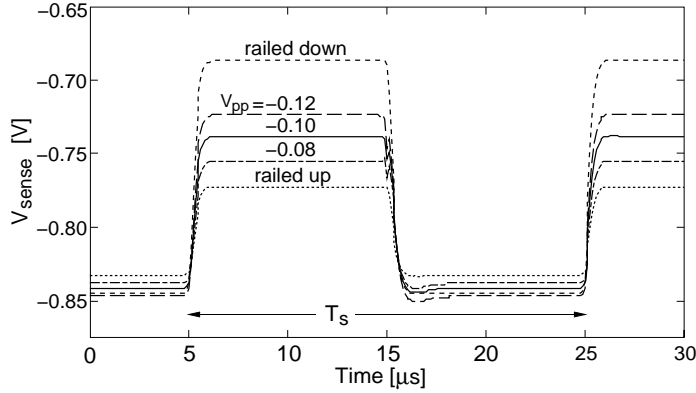


Figure 6.4: One period of the modulated sensor voltage, for various position reference input values.

when the device is exposed to light. The asymmetric current-voltage diode characteristic is responsible for the output dc bias shift with increasing signal amplitude.

Vertical displacement of the plate is measured by counting fringes using laser interferometry between the top plate and underlying substrate surfaces. Each fringe occurs at multiples of a half wavelength of the He-Ne laser (316.4 nm). In previous work, interferometry with a monochromatic infrared source has been used to measure parallelism of bulk-machined surfaces [96]. The present laser interference technique is used to obtain video confirmation of closed-loop tracking of vertical position and tilt to within  $\pm 25$  nm and  $\pm 0.03^\circ$ , respectively.

Measured and calculated values of peak-to-peak sensor output voltage versus displacement are compared in Figure 6.5. Sensitivity of the position sensor is  $42 \text{ mV}/\mu\text{m}$  at zero displacement. Displacement measurement error is  $\pm 25$  nm; sensor output error is  $\pm 1 \text{ mV}$ . The measured sensor output values are fitted to Equation (3.178), using  $|V_m| = 0.3 \text{ V}$ ,  $C_{svo} = 41.4 \text{ fF}$ ,  $C_{sf} = 4.0 \text{ fF}$ ,  $C_r = 6.8 \text{ fF}$ , and  $C'_p = 173 \text{ fF}$ . Interconnect overlap and fringe capacitance account for the reference and fixed sense capacitance. The effective parasitic capacitance value is about 17 times less than the layout value, demonstrating the benefit of the driven shield. As discussed in section 3.6.1.3, most of the parasitic capacitance is due to the diode junction capacitance.

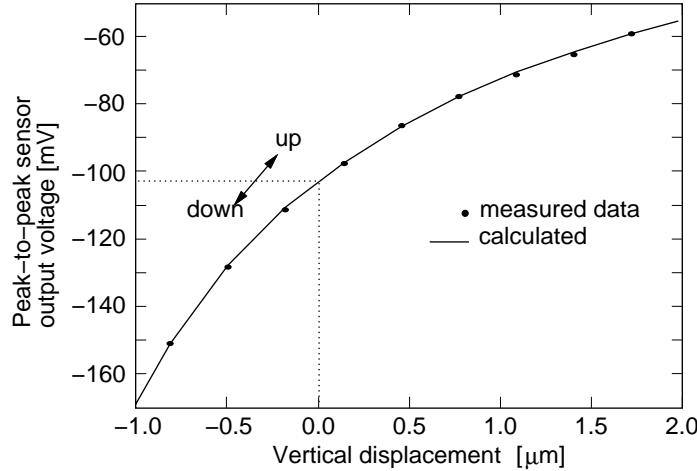


Figure 6.5: Measured and calculated peak-to-peak sensor voltage versus displacement.

## 6.4 Capacitive Feedthrough

Capacitive feedthrough between the electrostatic actuators and position sensors can give rise to errors on the sensor outputs. Table 6.1 gives the measured feedthrough between actuators and the sensor in the lower-left quadrant, where each measurement is made with one actuator driven by a 4-V peak-to-peak square wave and the rest grounded<sup>1</sup>. Voltage feedthrough between actuators and the sense line is a maximum of  $-61$  dB, with the closest actuators contributing the most feedthrough. Unfortunately, feedthrough to the sensors in the upper quadrants is much larger. In these cases, the sensor high-impedance lines crossover the actuator interconnect, creating a  $90 \mu\text{m}^2$  overlap, corresponding to a capacitance of about  $3 \text{ fF}$ , and a feedthrough of  $-38$  dB. For  $10 \text{ V}$  of actuation voltage, the sensor feedthrough is  $130 \text{ mV}$ , which is significant when compared with the signal amplitude.

Since the actuator voltage can only switch at the beginning of a sampling period, the position signal and closed-loop control should not be affected. In practice, however, the feedthrough must settle before the signal is sampled. An example waveform of the demodulation output voltage, in Figure 6.6, illustrates the effects of feedthrough during closed-loop operation. Only one actuator voltage waveform is shown; however, feedthrough

<sup>1</sup>The measured feedthrough value for the upper-left, pull-up actuator is omitted, because the actuator was inadvertently connected to the substrate through a built-in pin-1 connection of the DIP package. We did not correct this problem until after measurements had been taken, however, the feedthrough value should be close to that of the upper-left, pull-down actuator.

actuator location	feedthrough [mV]	[dB]
lower-left, pull-up	3.51	-61
lower-left, pull-down	0.95	-72
left comb-drive	0.64	-76
upper-left, pull-down	0.50	-78
right comb-drive	0.11	-91
upper-right, pull-down	0.10	-92
upper-right, pull-up	0.09	-93
lower-right, pull-up	0.07	-95
lower-right, pull-down	0.05	-98

Table 6.1: Measured peak-to-peak feedthrough between different actuators and the lower-left testbed sensor. The actuator drive is a 4 V p-p square wave.

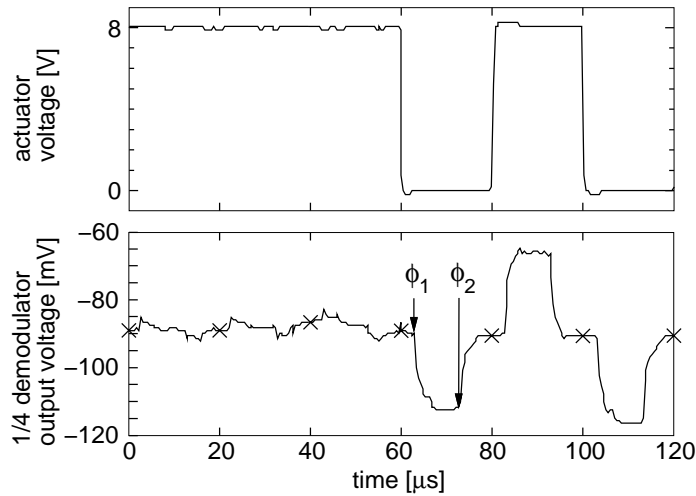


Figure 6.6: Waveforms of an actuator voltage and the demodulator output voltage during closed-loop operation with  $f_m = 50$  kHz. Cross-marks are placed at times when the comparator is strobed. (The demodulator voltage is scaled to correspond to the peak-to-peak sensor output voltage.)

results from the interconnect overlap capacitance of four different actuators. In Figure 6.6, the actuators do not switch for the first  $60 \mu\text{s}$ , so only residual feedthrough from the external sample-and-hold circuitry is evident. When the actuator voltage switches states, the 8 V step feeds through to the sensor input, and shows up in the demodulator output. During phase  $\phi_1$ , the sensor voltage with feedthrough is sampled, producing a large spike at the demodulator output. After phase  $\phi_2$ , the feedthrough is canceled, to first order. The comparator samples the position signal at the times denoted by the cross-marks in Figure 6.6. Operating the testbed above 50 kHz adds more noise to the position signal during actuator switching, because the sample-and-hold cannot accurately acquire the large feedthrough steps. An improvement to the existing electronics would require withholding the  $\phi_1$ -sampled signal from the demodulator output amplifier until the  $\phi_2$ -sampled signal is available. As an alternative control scheme, the sense and feedback cycles could be time multiplexed, at the cost of decreasing the sampling rate.

## 6.5 Open-Loop Step Response

Comb-drive levitation force is used to find the open-loop step response at atmospheric pressure. We applied a 30 Hz square-wave voltage with amplitudes ranging from 1 V to 7 V to the combs on both sides of the plate, and measured the demodulator output voltage waveforms shown in Figure 6.7. With no levitation force applied, the demodulator output voltage from the lower-left sensor is around  $-0.485$  V, corresponding to a displacement of 380 nm down from the reference position. The plate is slightly tilted, because the lower-right sense pad (the non-working sensor) has a larger offset voltage than the other sense pads. The average plate displacement is around  $-310$  nm. At this position, the restoring force of the suspension balances the electrostatic force from the sense capacitors.

Risetime and falltime measurements from Figure 6.7 are tabulated in Table 6.2. The risetime decreases with increasing step height, presumably from a decrease in damping with increasing gap. If we assume that the position dependence of the electrostatic force is important, then we expect to observe shorter falltimes than risetimes, because the offset force increases during the falling (pull-down) step. However, this is not what the measured results indicate; instead, the falltimes are relatively long. In this case, the effects of position dependence are assumed to be negligible compared to the damping effects. When the displacement step is kept small, the risetime approximately equals the falltime, as expected.

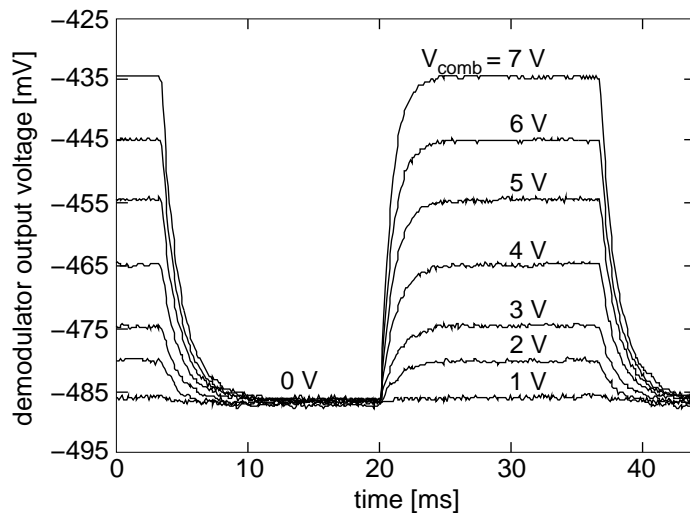


Figure 6.7: Open-loop responses to 30 Hz square-wave levitation force varying in amplitude from 1 V to 7 V.

$V_{\text{comb}}$ [V]	lower $\Delta z$ [nm]	upper $\Delta z$ [nm]	risetime [ms]	falltime [ms]
2	-312	-295	2.8	2.6
3	-312	-275	2.8	2.7
4	-312	-240	2.5	3.0
5	-312	-197	2.2	3.0
6	-312	-157	2.0	3.0
7	-312	-110	1.8	3.0

Table 6.2: Open-loop risetime and falltime measurements.

During the rising (pull-up) step, the position dependence of the offset force approximately cancels that of the comb-drive force, resulting in a net force that is independent of position. The risetime and falltime measurements correspond to damping factors between 9 and 16. Open-loop measurements with larger displacements have not been measured, because of lateral comb-drive instability at higher applied voltages.

One other open-loop measurement was made by exciting the parallel-plate feedback actuators with a small square-wave voltage. In this measurement, the displacement is centered around  $\Delta z=0$ , and the risetime and falltime are both equal to 2.3 ms, corresponding to a damping factor of 12.

The damping factor for a  $360 \mu\text{m} \times 380 \mu\text{m}$  solid plate is very large,  $\xi_z = 463$ , due to the squeeze film of air between the plate and substrate. The testbed plate is not solid, however. Instead, it is perforated with 580,  $4 \mu\text{m}$ -square holes, spaced  $16 \mu\text{m}$  apart, and four,  $64 \mu\text{m} \times 24 \mu\text{m}$  slots, included to allow room for external probing and manipulation. The holes reduce the squeeze-film damping to about 1/30 times the value for a solid plate. In the simulations presented in this chapter, damping is approximated as a constant value of 16 in air. Although there is a damping dependence on position, we have not needed to add these effects to match simulations to our closed-loop measurements.

## 6.6 Comb-Drive Levitation Force

The comb drives on each side of the plate have 39 fingers, which are  $2 \mu\text{m}$  wide and have  $2 \mu\text{m}$  spacing between adjacent fingers. The stationary and movable fingers overlap by  $10 \mu\text{m}$ , and are suspended above the substrate by  $z_o=2.2 \mu\text{m}$ . A two-dimensional finite-element solution of the total comb-drive levitation force, using the Maxwell<sup>TM</sup> [52] electrostatic field solver, gives

$$F_{\text{comb}} = 1.284 \alpha (1 - 1.596 \Delta z) V_{\text{comb}}^2 [\text{nN/m}] \quad (6.1)$$

where  $F_{\text{comb}}$  and  $V_{\text{comb}}$  are the comb-drive force and voltage, respectively, and  $\Delta z$  is given in units of  $\mu\text{m}$ . We have included a fitting factor,  $\alpha$ , to account for differences between the two-dimensional model and any three-dimensional effects or mismatches in the actual geometrical parameters. The spring force is

$$F_{\text{os}} + F_{\text{comb}} = (0.25 \text{ N/m}) \Delta z \quad (6.2)$$

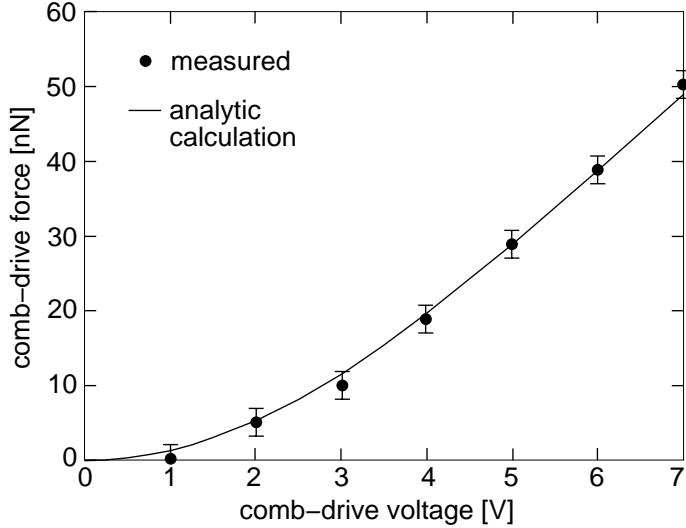


Figure 6.8: Comb-drive levitation force versus comb-drive voltage. Points are calculations from measured data and the line is the best-fit analytic calculation.

where the measured parallel-plate offset force<sup>2</sup>,  $F_{os}$ , is  $-77$  nN at  $\Delta z = 0.31$   $\mu\text{m}$ . We combine Equation (6.1) and (6.2) to get

$$F_{\text{comb}} = \frac{1.37 V_{\text{comb}}^2}{1 + 0.00756 V_{\text{comb}}^2} [\text{nN}] \quad (6.3)$$

where  $\alpha = 0.73$  is selected as a best fit to measured data. A comparison between the measured comb-drive force and Equation (6.3) is made in Figure 6.8. Comb levitation force is measured by differencing the total spring force before and after the comb-drive voltage is applied. The error bars reflect the  $\pm 1$  mV uncertainty in the demodulation output voltage measurement. The fitted finite-element calculations and measured data are in good agreement, demonstrating the linear dependence of comb-drive force on vertical position. In contrast, if there was no position dependence, the comb-drive force would rise much more steeply with increasing applied voltage.

## 6.7 Closed-Loop Step Response

Plots of simulated and measured closed-loop response to an 150 Hz square-wave position reference input are given in Figure 6.9. Operation is at atmospheric pressure without

---

<sup>2</sup>The exact dependence of the offset force on displacement has not been determined, because the plate tilt and broken sensor complicate the analysis. For these calculations, we assume that the offset force behaves like a parallel-plate capacitor force.

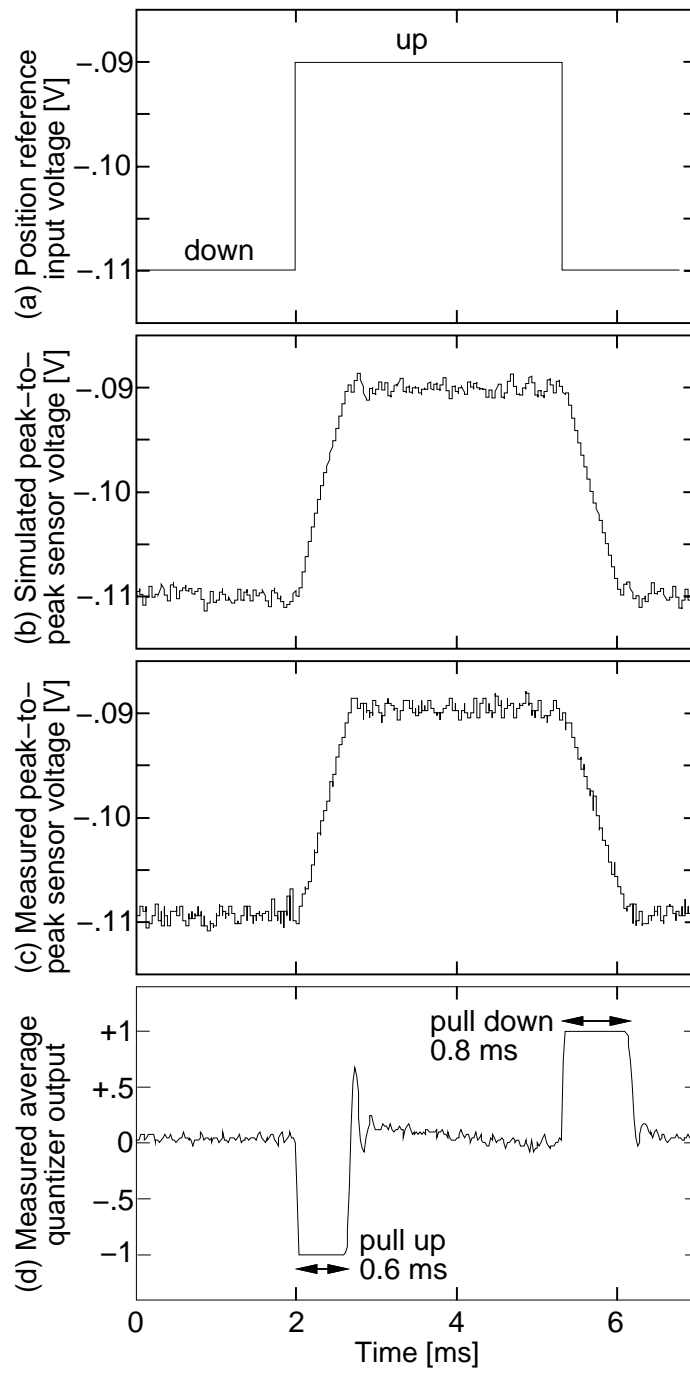


Figure 6.9: Closed-loop response to an 150 Hz square-wave position reference input. (a) Position reference input voltage,  $V_{\text{ref}}$ . (b) Simulated peak-to-peak sensor voltage waveform,  $V_{pp}$ . (c) Measured  $V_{pp}$  waveform. (d) Measured quantizer output, averaged over 1024 sweeps and normalized to  $\pm 1$ .

feedback compensation, and with a sampling rate of 50 kHz. Simulated results are generated by using a commercially available program for simulating dynamic systems[11]. Excellent agreement between the measured and simulated peak-to-peak sensor voltage waveforms is obtained. Limit-cycle oscillations, seen in the single-sweep waveform when the position is locked to the reference, have an amplitude of approximately 25 nm. Total open-loop equivalent Brownian noise position in air is 50 times smaller than the limit-cycle amplitude value. The average quantizer output, plotted in Figure 6.9(d), is near zero for both of the controlled plate positions. The actuator force magnitude increases as the actuator gap is reduced, so average quantizer output does not vary linearly with position.

## 6.8 Accelerometer Testing

The testbed is not specifically designed as an accelerometer, however its sigma-delta digital outputs do provide a measure of external acceleration. An ac acceleration test is performed by manually shaking the device up and down, first along the z-axis and then along a lateral axis. The motion is roughly sinusoidal with a 3 inch amplitude and 1.6 Hz frequency, providing an acceleration amplitude of 0.8 G. Figure 6.10 displays the spectrum of one digital bitstream, which is low-pass filtered and measured with an HP3561 dynamic signal analyzer. Along the z-axis, the measured signal is approximately 1.1 G, based on the full-scale feedback force of 860 nN. No cross-axis signal is detected. The noise floor of about  $-50$  dB is quantization noise passed by the simple one-pole RC filter and aliased to lower frequencies by the dynamic signal analyzer. External angular acceleration about the x-axis and y-axis is also detectable, but no quantitative results are available.

Static acceleration performance is tested in air, with  $f_s = 50$  kHz and  $G_v = 0$ . The digital bitstreams are passed through a  $\text{sinc}^3$  finite-impulse-response (FIR) filter, decimated by 500, and combined to provide an acceleration output with a signal bandwidth of 50 Hz.

In the static testing, four changes are made to the ideal testbed system. First, the lower-right feedback actuators are grounded, leaving three quadrants in closed-loop operation. Using this configuration, we avoid the over-constrained system created when feedback exists on all four corners of the plate. Second, the spring attached to the lower-right corner of the plate was accidentally broken prior to this test, so the suspension is no longer symmetric. Third, the feedback voltage levels are set to 3.56 V for the pull-down actuator and 7.15 V for the pull-up actuator to compensate for the sensor pull-down force.

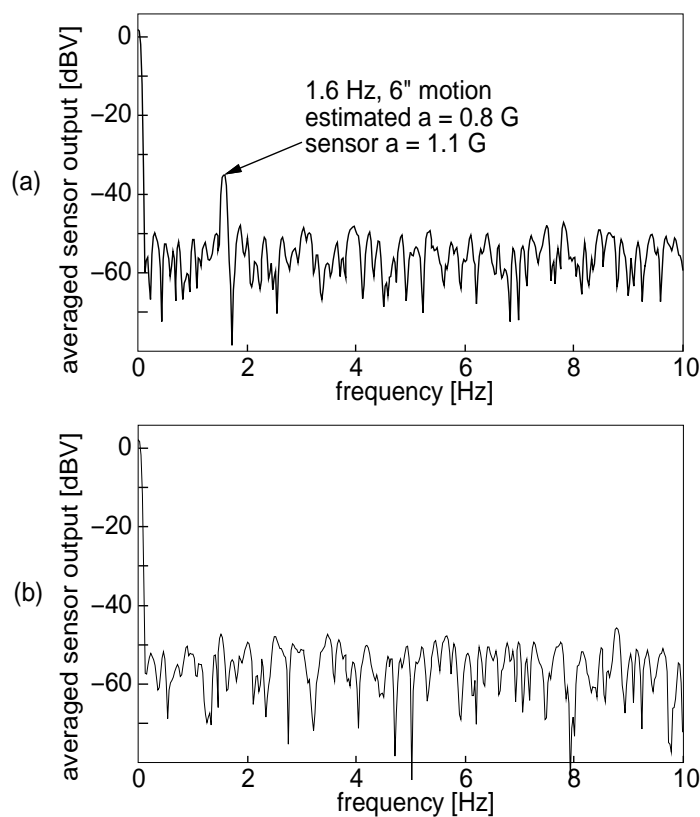


Figure 6.10: Spectrum of one digital bitstream, showing the  $\approx 1$  G acceleration signal at 1.6 Hz. (a) manual shaking along z-axis. (b) manual shaking along lateral axis.

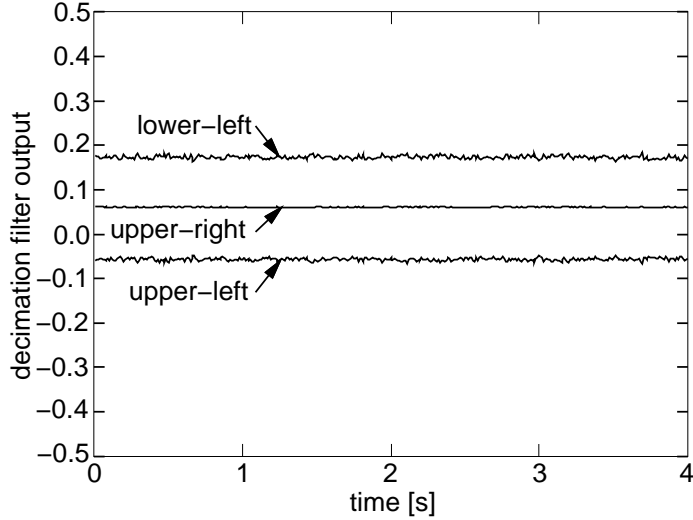


Figure 6.11: Averaged output signals from the three working channels, with the device tilted 90° from horizontal.

Fourth, we adjusted the position references such that the pulse density of the feedback force for all three quadrants is approximately 50%. Precise adjustment of the dc feedback levels is difficult because small changes in the position reference settings produce large shifts in the pulse density and changes in one quadrant couple to the other quadrants. Adequate position settings are:  $\Delta z_{ur} = 0.27 \mu\text{m}$ ,  $\Delta z_{ul} = 0.54 \mu\text{m}$ , and  $\Delta z_{ll} = 0.25 \mu\text{m}$ , where the subscripts denote the quadrant (for example, “ul” is upper-left).

An example of the acceleration waveforms from each channel is given in Figure 6.11, where the device is tilted on its side. Full-scale swing of the feedback force is normalized and centered around zero. Signals from the two left quadrants have about 5 times more noise than the upper-right signal. Some interesting mode-coupling effects are seen in the testbed, which would not exist in a single-axis accelerometer design. An enlargement of the signals, in Figure 6.12(a), illustrates that the noise of the left-channel signals is correlated and has a constant spectral density. The equivalent actuator noise accelerations are  $\sqrt{a_{eq,ur}^2} = 11$  milli-G,  $\sqrt{a_{eq,ul}^2} = 50$  milli-G, and  $\sqrt{a_{eq,ll}^2} = 55$  milli-G. We believe that correlated noise originates from the rotational noise torque of the plate, discussed in section 5.6.1. Since the lower-right spring is cut, the actual modes differ from the  $z$ ,  $\theta$ , and  $\phi$  modes assumed in the Brownian noise calculations. The measured noise of the two left channels is about 6 times larger than the calculated equivalent Brownian noise acceleration. By summing these two signals, much of the correlated noise is canceled, producing the lower waveform shown in Figure 6.12(b).

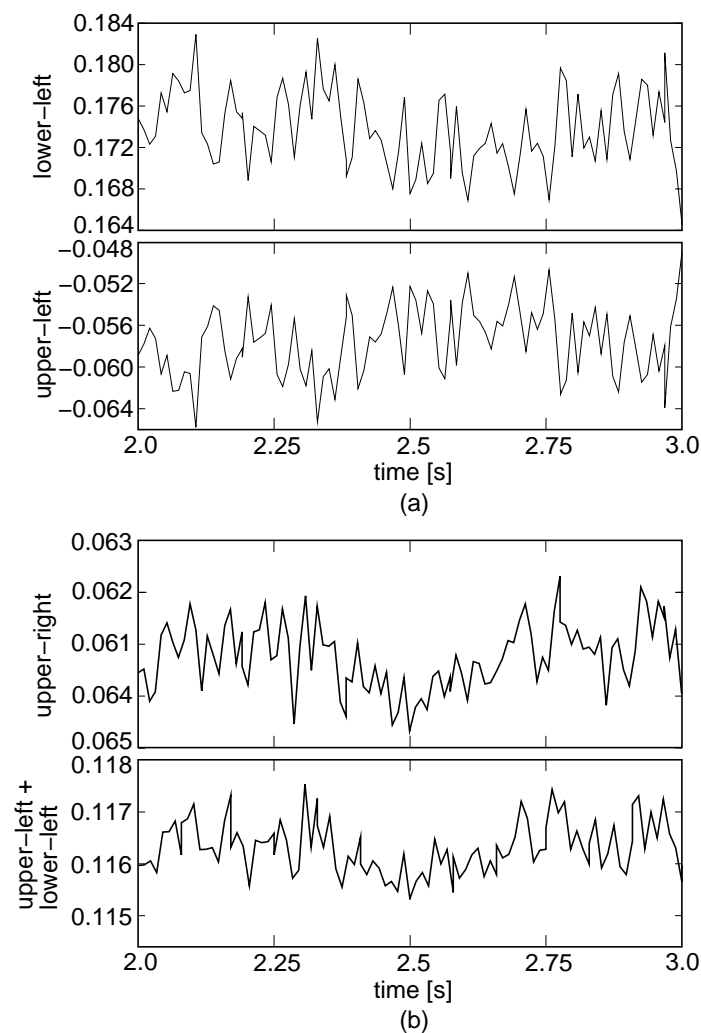


Figure 6.12: Enlargement of the averaged output signals from Figure 6.11. (a) Comparison of the left-channel signals. (b) Comparison of the upper-right signal and the sum of the left-channel signals.

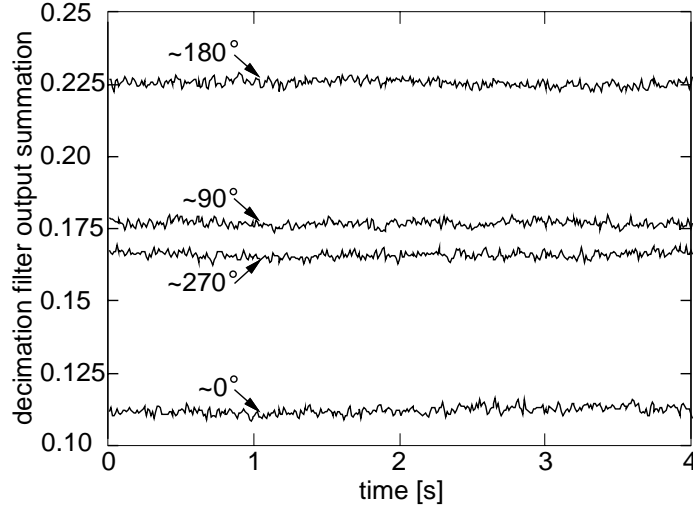


Figure 6.13: Accelerometer signals for differing tilt angles. The tilt angles are off by  $3.5^\circ$ .

The signal from the upper-right channel (the upper waveform in Figure 6.12(b)) has a correlation to the summed waveform; this noise arises from coupling between the left and right sides. Although this noise can be canceled by subtracting a weighted combination of the two waveforms in Figure 6.12(b), the resulting signal would not yield the total z-axis acceleration.

We have chosen to sum all three channels to obtain the total external acceleration signal. Examples of acceleration signals for differing tilt angles are given in Figure 6.13. From the discrepancy between the results at a  $90^\circ$  tilt and a  $270^\circ$  tilt, we estimate that the actual tilt angle is off by  $3.5^\circ$ . We correct for the tilt error and fit the sensor offset and amplitude to generate the 2-G tilt test results in Figure 6.14. The rms error is 31 milli-G, with a maximum measured error of 71 milli-G. The full-scale range is 55 G, however, we have not tested the acceleration sensing outside of the  $\pm 1$  G range. Measured noise acceleration is  $-86 \text{ dB}/\sqrt{\text{Hz}}$ , referenced to the full-scale range of 55 G (0 dB). The previously reported noise value of  $-90 \text{ dB}/\sqrt{\text{Hz}}$  [97] is obtained by using a weighted sum of the three quadrant signals. In the 50 Hz bandwidth, the measured noise floor is 19 milli-G (-69 dB), about 5 times larger than the Brownian noise calculated in section 5.6.1. The measured noise acceleration is close to the value of quantization noise calculated in section 5.6.4<sup>3</sup>. Quantization noise is dominant, with noise from the rotational modes coupling into the

<sup>3</sup>The quantization noise calculation in section 5.6.4 assumed four actuators are in operation. For three actuators in operation, the total noise acceleration value is 8.5 milli-G.

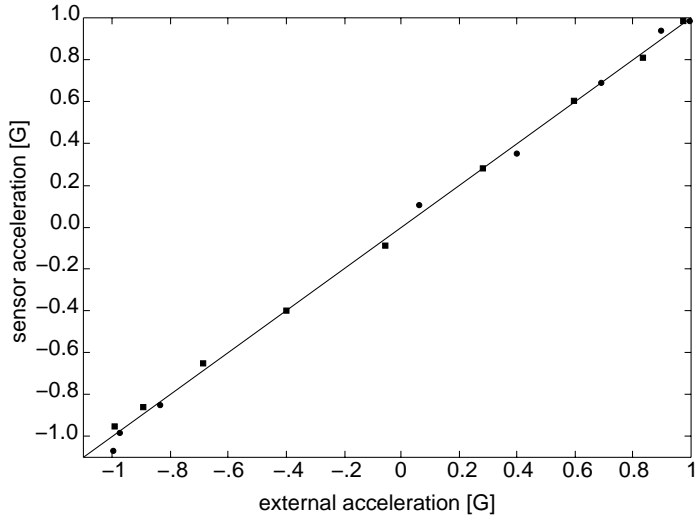


Figure 6.14: Accelerometer tilt test results, displaying sensor acceleration output versus external acceleration input.

acceleration output signal and increasing the measured noise value.

## 6.9 Underdamped Operation at Low Pressure

Underdamped system dynamics are investigated by placing the testbed in a vacuum probe-station. Our experiments are constrained to sampling frequencies up to 100 kHz and compensation gain up to 4, because of external circuit limitations. Three of the four feedback channels are activated; the fourth channel has its actuators grounded to avoid the over-constrained instability.

Measured peak-to-peak sensor voltage waveforms are compared with simulation and theoretical results in Figure 6.15, with  $f_s = 100$  kHz and  $G_v = 4$ . Each column of waveform data is taken at three different pressure values, 10 T, 1 T, and 0.1 T, corresponding to estimated<sup>4</sup> quality factors of 2.4, 24, and 240. Simulation results qualitatively match the measured waveform frequency and amplitude. The maximum limit-cycle amplitude given by the theoretical model is also in agreement with the measured data. As the pressure is decreased, damping also decreases, and the limit-cycle amplitude increases. In the P = 0.1 T

---

<sup>4</sup>Squeeze-film damping, given by Equation (3.30), is proportional to air viscosity, which is proportional to pressure. In our estimation of Q values, we assume that Q is proportional to  $1/P$  and  $\zeta_z = 16$  in air at 760 T. However, as indicated in section 3.3, the gas should no longer be treated as a viscous fluid at pressures below 25 T. Therefore, the actual Q values in our experiment may be higher than those stated.

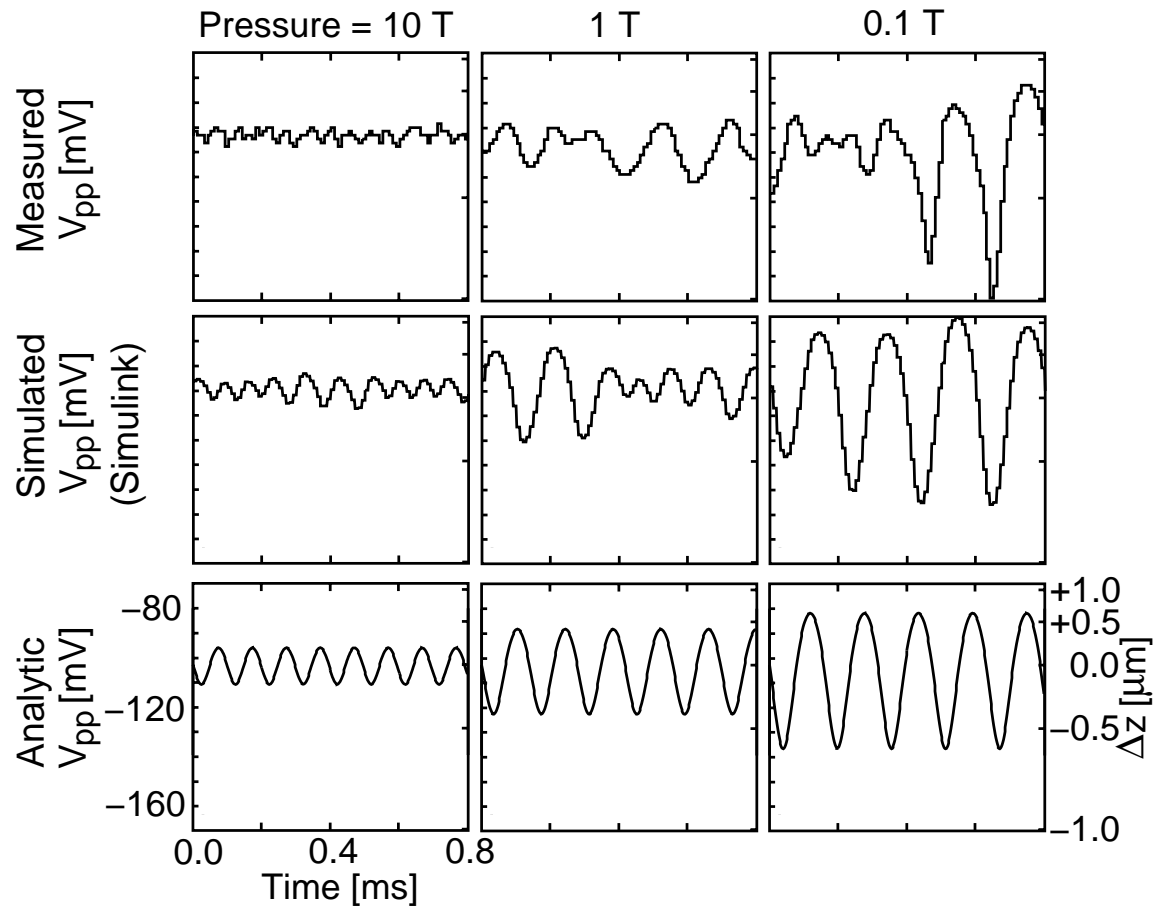


Figure 6.15: Measured, simulated, and theoretical peak-to-peak sensor voltage waveforms during underdamped operation at three different pressure values: 10 T, 1 T, and 0.1 T. The y-axis scales are only supplied once to avoid clutter ( $V_{pp}$  in mV on the left, and  $\Delta z$  in  $\mu\text{m}$  on the right).

case, actuator nonlinearity and added force from the sensor capacitors distorts the feedback force, and is responsible for the larger measured limit-cycle amplitude than the theoretical value. With lead compensation  $G_v < 3$ , the underdamped system is unstable and rails to the limit stops, as predicted by the theory.

# Chapter 7

## Conclusions

In this thesis, we have demonstrated that a complex surface microsystem, the micromechanical testbed, can be modeled with lumped-parameter components that are incorporated into system-level simulation tools, such as SPICE and MATLAB. We have developed analytic models for several components — mass-spring-dampers, parallel-plate and comb-drive electrostatic actuators, and capacitive position sensors — that are used in a broad class of surface Microsystems.

The MEMS engineer can use the spring-constant equations in section 3.4 for design of fixed-fixed, crab-leg, folded, and serpentine suspensions. Linear spring constants for almost any other suspension made from slender beams can be derived using the energy method. Implementation of the mechanical equations of motion and the actuator and sensor capacitor models in HSPICE and MATLAB represents a first generation of system modeling.

In chapter 2, we presented theory and experimentally demonstrated a novel form of post-process micromechanical assembly by welding and fusing polysilicon and aluminum structures. Fuses are used as temporary supports for structures, and to configure suspension stiffness. Demonstrated applications include adjustment of the mechanical response in accelerometers and frequency trimming of resonators. Clean, reliable cutting of  $2 \mu\text{m}$ -wide  $\times$   $12 \mu\text{m}$ -long  $\times$   $2 \mu\text{m}$ -thick polysilicon fuses is obtained by passing about 260 mA of current through the fuse. Cutting of more than four fuses in parallel requires careful matching of low-resistance interconnect. Welding structures provide a relatively large lateral force, on the order of  $\mu\text{N}$ 's, which can be used to actively align elements and to pre-stress springs. We have fabricated designs for two welding applications: narrow-gap comb-finger actuators

for increased drive capability, and frequency trim of fixed-fixed resonators.

In chapter 6, we demonstrated digital control of a micromechanical plate for vertical and angular motion. Although the parallel-plate actuator force is highly nonlinear with position and voltage, the  $\Sigma\text{-}\Delta$  feedback successfully controls plate position to the mechanical limit stops. Since the maximum sampling rate of the testbed is 100 kHz, accuracy of the position control is limited to  $\pm 25$  nm in air. Every doubling of the sampling rate results in a 12dB decrease in the plate chatter. Higher frequency circuitry ( $f_s > 2$  MHz) is necessary to reduce the displacement amplitude below the Brownian noise level of the testbed, which is 0.46 nm in air.

Quantization noise dominates the equivalent noise acceleration of the testbed operating with a sampling frequency of 50 kHz. We have detected correlated quantization noise on the testbed's  $\Sigma\text{-}\Delta$  bitstreams, after filtering to a 50 Hz bandwidth. Multi-axis accelerometers and gyroscopes will require proper filtering to remove these extra sources of noise. We have shown experimentally that the integrated testbed can be operated at high- $Q$ , lowering the Brownian noise floor for digital MEMS applications. A limit-cycle model successfully predicts the behavior of the high- $Q$  system. Other types of micromechanical  $\Sigma\text{-}\Delta$  loops, for example, with pulsed feedback or analog compensation, can be analyzed using the limit-cycle theory. Appropriate sampling frequency and compensation can be designed into future systems to obtain a specified maximum limit-cycle amplitude. At higher sampling rates and high- $Q$  operation, the position-sensor electronic noise limits the acceleration sensitivity. We conclude from our comparison of position-sensing methods that voltage sensing using a unity-gain buffer is superior to displacement-current sensing using a transresistance amplifier. High-frequency modulation of the position signal reduces  $1/f$  noise from the buffer input diode and transistors to negligible levels. Further improvements in acceleration sensitivity will require reductions in thermal noise of the buffer and the following gain stage.

## 7.1 Future Work

This thesis provides an overview of generic surface microsystem components, but much more work is necessary to create a viable system simulation tool that meets the needs of the MEMS engineer. Eventually, a library of MEMS macro-models for each process technology will exist, which both novices and experts can use to design microsystems right

the first time.

Producing good MEMS models is the key to efficient and useful simulations. Model accuracy can be improved by including higher-order effects, such as axial and shear stress in the spring constant equations. The utility of existing models can be increased by extending their range of applicability. For example, flexure models can be extended to include large deflections and rotations. As another example, parallel-plate electrostatic actuator models should include effects of plate rotation and detailed fringe-field corrections. Development of new models will allow simulation of a wider range of microsystem designs. Experimental verification of models is extremely important and will remain a worthwhile research area for several years. Drop-in test structures for characterization of micromechanical materials, processes, and components must be designed and standardized. With standard tests and models, the MEMS community can share and compare design information easily.

Algorithms for extracting the mechanical equations of motion and model parameters from layout are needed to automate the design process. Once a one-to-one correspondence between models and layout is made, further research will lead to programs that synthesize microsystems from design specifications.

It remains a challenge to reach the surface-micro-accelerometer performance level of  $50 \mu\text{G}$  in a 1 kHz bandwidth<sup>1</sup>, representing the Brownian noise limit for a  $0.5 \mu\text{g}$  mass with a 1 kHz resonant frequency and a  $Q$  of 80000. The micromechanical  $\Sigma\Delta$  architecture used in the testbed is a good candidate for the task. If high-speed, low-noise electronics are used, the Brownian noise limit at  $Q = 80000$  is attainable. Control of all mechanical modes with resonant frequencies inside the electrical bandwidth of the system is desirable, and may create a limitation on arbitrary reduction of the fundamental resonant frequency and arbitrary increase of the sampling rate. Eventually, the use of multi-mode control of microstructures will lead to the development of multi-axis accelerometers, angular accelerometers, and gyroscopes.

---

<sup>1</sup>This value for the Brownian noise limit is calculated in section 3.6.3.3.

# Bibliography

- [1] J. M. Gere and S. P. Timoshenko. *Mechanics of Materials*, chapter 7, pp. 412–413. Wadsworth, Belmont, 2nd ed., 1984.
- [2] R. J. Roark and W. C. Young, *Formulas for Stress and Strain*, McGraw-Hill, New York, New York, 5th ed., 1975.
- [3] Meta-Software, Inc., 1300 White Oaks Road, Campbell, California. *HSPICE User's Manual*, h9007 ed., 1991.
- [4] P. Osterberg, H. Yie, X. Cai, J. White, and S. D. Senturia, “Self-consistent simulation and modeling of electrostatically deformed diaphragms,” In *Proceedings*, IEEE Micro Electro Mechanical Systems Workshop, Oiso, Japan, January 1994, pp. 28–32.
- [5] J. R. Gilbert, P. M. Osterberg, R. M. Harris, D. O. Ouma, and S. D. Senturia, “Implementation of memcad system for electrostatic and mechanical analysis of complex structures from mask descriptions,” In *Proceedings*, IEEE Micro Electro Mechanical Systems Workshop, Fort Lauderdale, Florida, February 1993, pp. 207–212.
- [6] M. A. Shulman, M. Ramaswamy, M. L. Heytens, and S. D. Senturia, “An object-oriented material-property database architecture for microelectromechanical cad,” In *Technical Digest*, 6th Inter. Conf. on Solid-State Sensors and Actuators (Transducers '91), San Francisco, California, June 1991, pp. 486–489.
- [7] B. P. Johnson, S. Kim, S. D. Senturia, and J. White, “Memcad capacitance calculations for mechanically deformed square diaphragm and beam microstructures,” In *Technical Digest*, 6th Inter. Conf. on Solid-State Sensors and Actuators (Transducers '91), San Francisco, California, June 1991, pp. 494–497.
- [8] Y. Zhang, S. B. Crary, and K. D. Wise, “Pressure sensor design and simulation using the caemens-d module,” In *Technical Digest*, IEEE Solid-State Sensor and Actuator Workshop, Hilton Head Island, South Carolina, June 1990, pp. 32–35.
- [9] G. K. Ananthasuresh, S. Kota, and Y. Gianchandani, “A methodical approach to the design of compliant micromechanisms,” In *Technical Digest*, Solid-State Sensor and Actuator Workshop, Hilton Head Island, South Carolina, June 1994, pp. 189–192.
- [10] J. G. Korvink, J. Funk, G. Wachutka, and H. Baltes, “Seses: A comprehensive mems modeling system,” In *Proceedings*, IEEE Micro Electro Mechanical Systems Workshop, Oiso, Japan, January 1994, pp. 22–27.

- [11] B. Gogoi, R. Yuen, and C. H. Mastrangelo, "The automatic synthesis of planar fabrication process flows for surface micromachined devices," In *Proceedings*, IEEE Micro Electro Mechanical Systems Workshop, Oiso, Japan, January 1994, pp. 153–157.
- [12] The MathWorks, Inc., Natick, Massachusetts. *MATLAB User's Guide*, 1992.
- [13] R. T. Howe, "Surface micromachining for microsensors and microactuators," *J. Vac. Science and Tech.*, **B6**:1809–1813, 1988.
- [14] R. T. Howe and R. S. Muller, "Polycrystalline and amorphous silicon micromechanical beams: annealing and mechanical properties," *Sensors and Actuators*, **4**:447–454, 1983.
- [15] H. Guckel, D. W. Burns, C. R. Rutigliano, D. K. Showers, and J. Uglow, "Fine-grained polysilicon and its application to planar pressure transducers," In *Technical Digest*, 4th Inter. Conf. on Solid-State Sensors and Actuators (Transducers '87), Tokyo, Japan, June 1987, pp. 277–282.
- [16] H. Guckel, J. J. Sniegowski, T. R. Christenson, , and F. Raissi, "The application of fine-grained, tensile polysilicon to mechanically resonant transducers," *Sensors and Actuators*, **A21**(1–3):346–351, February 1990.
- [17] R. T. Howe, "Resonant microsensors," In *Technical Digest*, 4th Inter. Conf. on Solid-State Sensors and Actuators (Transducers '87), Tokyo, Japan, June 1987, pp. 843–848.
- [18] J. J. Sniegowski, H. Guckel, and T. R. Christenson, "Performance characteristics of second generation polysilicon resonating beam force transducers," In *Technical Digest*, IEEE Solid-State Sensor and Actuator Workshop, Hilton Head Island, South Carolina, June 1990, pp. 9–12.
- [19] C. Linder and N. F. de Rooij, "Investigations on free-standing polysilicon beams in view of their application as transducers," *Sensors and Actuators*, **A23**(1–3):1053–1059, April 1990.
- [20] W. C. Tang, T.-C. H. Nguyen, and R. T. Howe, "Laterally driven polysilicon resonant microstructures," In *Proceedings*, IEEE Micro Electro Mechanical Systems Workshop, Salt Lake City, Utah, February 1989, pp. 53–59.
- [21] R. L. Alley, G. J. Cuan, R. T. Howe, and K. Komvopoulos, "The effect of release-etch processing on surface microstructure stiction," In *Technical Digest*, IEEE Solid-State Sensor and Actuator Workshop, Hilton Head Island, South Carolina, June 1992, pp. 202–207.
- [22] C. H. Mastrangelo and C. H. Hsu, "A simple experimental technique for the measurement of the work of adhesion of microstructures," In *Technical Digest*, IEEE Solid-State Sensor and Actuator Workshop, Hilton Head Island, South Carolina, June 1992, pp. 208–212.
- [23] G. T. Mulhern, D. S. Soane, and R. T. Howe, "Supercritical carbon dioxide drying of microstructures," In *Proceedings*, 7th Inter. Conf. on Solid-State Sensors and Actuators (Transducers '93), Yokohama, Japan, June 1993, pp. 296–299.

- [24] N. Takeshima, K. J. Gabriel, M. Ozaki, J. Takahashi, H. Horiguchi, and H. Fujita, “Electrostatic parallelogram actuators,” In *Technical Digest*, 6th Inter. Conf. on Solid-State Sensors and Actuators (Transducers ’91), San Francisco, California, June 1991, pp. 63–66.
- [25] C. H. Mastrangelo and G. S. Saloka, “A dry-release method based on polymer columns for microstructure fabrication,” In *Proceedings*, IEEE Micro Electro Mechanical Systems Workshop, Fort Lauderdale, Florida, February 1993, pp. 77–81.
- [26] G. K. Fedder and R. T. Howe, “Thermal assembly of polysilicon microstructures,” In *Proceedings*, IEEE Micro Electro Mechanical Systems Workshop, Nara, Japan, February 1991, pp. 63–68.
- [27] G. K. Fedder, J. C. Chang, and R. T. Howe, “Thermal assembly of polysilicon microstructures with narrow comb-drive,” In *Technical Digest*, IEEE Solid-State Sensor and Actuator Workshop, Hilton Head Island, South Carolina, June 1992, pp. 63–68.
- [28] H. Guckel and D. W. Burns, “Integrated transducers based on blackbody radiation from heated polysilicon filaments,” In *Technical Digest*, 3rd Inter. Conf. on Solid-State Sensors and Actuators (Transducers ’85), Philadelphia, Pennsylvania, June 1985, pp. 364–366.
- [29] Y. C. Tai, C. H. Mastrangelo, and R. S. Muller, “Thermal conductivity of heavily doped lpcvd polycrystalline silicon films,” *J. Appl. Phys.*, **63**(5):1442–1447, March 1988.
- [30] C. H. Mastrangelo, *Thermal applications of microbridges*, PhD thesis, Dept. of Electrical Engineering and Computer Sciences, University of California at Berkeley, Berkeley, California, December 1990.
- [31] M. W. Judy, R. T. Howe, Y.-H. Cho, and A. P. Pisano, “Self-adjusting microstructures,” In *Proceedings*, IEEE Micro Electro Mechanical Systems Workshop, Nara, Japan, February 1991, pp. 51–56.
- [32] L. S. Fan and R. S. Muller, “As-deposited low strain lpcvd polysilicon,” In *Technical Digest*, IEEE Solid-State Sensor and Actuator Workshop, Hilton Head Island, South Carolina, June 1988, pp. 55–59.
- [33] P. Krulevitch, T. D. Nguyen, G. C. Johnson, R. T. Howe, H. R. Wenk, and R. Gronsky, “Lpcvd polycrystalline silicon thin films: the evolution of structure, texture and stress,” In *Proceedings*, volume 202, Materials Research Society Fall Meeting, Boston, Massachusetts, 1990.
- [34] K. S. J. Pister, *Hinge polysilicon structures with integrated CMOS thin film transistors*, PhD thesis, Dept. of Electrical Engineering and Computer Sciences, University of California at Berkeley, Berkeley, California, September 1992. Refer to page 20.
- [35] C. H. Mastrangelo, J.H.-J. Yeh, and R. S. Muller, “Electrical and optical characteristics of vacuum-sealed polysilicon microlamps,” *IEEE Trans. on Electron Devices*, **ED-39**(6):1363–1375, June 1992.

- [36] D. W. Greve, "Programming mechanism of polysilicon resistor fuses," *IEEE Trans. on Electron Devices*, **ED-29**(4):719–807, April 1982.
- [37] R. E. Jones, Jr. and S. P. Wesolowski, "Electrical, thermoelectric, and optical properties of strongly degenerate polycrystalline silicon films," *J. Appl. Phys.*, **56**(6):3278–3281, September 1984.
- [38] J. Y. W. Seto, "The electrical properties of polycrystalline silicon films," *J. Appl. Phys.*, **46**(12):5247–5254, December 1975.
- [39] N. C.-C. Lu, L. Gerzberg, C.-Y. Lu, and J. D. Meindl, "A conduction model for semiconductor-grain-boundary-semiconductor barriers in polycrystalline-silicon films," *IEEE Trans. on Electron Devices*, **ED-30**(2):137–149, February 1983.
- [40] F. Llewellyn Jones, *The Physics of Electrical Contacts*, Clarendon Press, Oxford, 1957.
- [41] D. H. Pontius, W. B. Smith, and P. P. Budenstein, "Filamentation in silicon-on-sapphire homogeneous thin films," *J. Appl. Phys.*, **44**(1):331–340, January 1973.
- [42] K. Kato, T. Ono, and Y. Amemiya, "A physical mechanism of current-induced resistance decrease in heavily doped polysilicon resistors," *IEEE Trans. on Electron Devices*, **ED-29**(8):137–149, August 1982.
- [43] P. W. Chapman, O. N. Tufte, J. D. Zook, and D. Long, "Electrical properties of heavily doped silicon," *J. Appl. Phys.*, **34**(11):3291–3295, November 1963.
- [44] C. J. Glassbrenner and G. A. Slack, "Thermal conductivity of silicon and germanium from 3°k to the melting point," *Physical Review*, **134**(4A):1058–1069, May 1964.
- [45] A. W. Adamson. *Physical Chemistry of Surfaces*, chapter 2. John Wiley & Sons, New York, New York, 5th ed., 1990.
- [46] R. C. Weast and M. J. Astle, editors, *CRC Handbook of Chemistry and Physics*, Chemical Rubber Publishing Co., Boca Raton, Florida, 62nd ed., 1981.
- [47] D. W. Greve, "The microstructure of programmed n<sup>+</sup> pn<sup>+</sup> polycrystalline silicon antifuses," *J. Appl. Phys.*, **54**(6):3278–3281, June 1983.
- [48] Y. C. Tai and R. S. Muller, "Fracture strain of lpcvd polysilicon," In *Technical Digest*, IEEE Solid-State Sensor and Actuator Workshop, Hilton Head Island, South Carolina, June 1988, pp. 6–9.
- [49] K. S. J. Pister, M. W. Judy, S. R. Burgett, and R. S. Fearing, "Microfabricated hinges," *Sensors and Actuators*, **A33**(3):249–256, 1992.
- [50] T. Hirano, T. Furuhata, K. J. Gabriel, and H. Fujita, "Operation of sub-micron gap electrostatic comb-drive actuators," In *Technical Digest*, 6th Inter. Conf. on Solid-State Sensors and Actuators (Transducers '91), San Francisco, California, June 1991, pp. 873–876.

- [51] M. W. Judy, *Micromechanisms using sidewall beams*, PhD thesis, Dept. of Electrical Engineering and Computer Sciences, University of California at Berkeley, Berkeley, California, May 1994.
- [52] Ansoft Corp., 4 Station Square, 660 Commerce Court Building, Pittsburgh, Pennsylvania. *Maxwell Solver User's Manual, Electrostatic Package*, 4.31 ed., 1991.
- [53] Hibbit, Karlsson & Sorenson, Inc., 1080 Main Street, Pawtucket, Rhode Island. *ABAQUS User's Manual*, 5.2 ed., 1992.
- [54] W. C. Tang, *Electrostatic comb drive for resonant sensor and actuator applications*, PhD thesis, Dept. of Electrical Engineering and Computer Sciences, University of California at Berkeley, Berkeley, California, November 1990.
- [55] L. Meirovitch. *Analytical Methods in Vibrations*, chapter 2, pp. 47–51. Macmillan Publishing Co., Inc., New York, 1967.
- [56] F. R. Archibald, “Load capacity and time realtions for squeeze films,” *Trans. of the ASME*, **78**:29–35, 1956.
- [57] W. E. Langlois, “Isothermal squeeze films,” *Quarterly of Applied Mathematics*, **XX**(2):131–150, July 1962.
- [58] M. H. Sadd and A. K. Stiffler, “Squeeze film dampers: amplitude effects at low squeeze numbers,” *Journal of Engineering for Industry, Transactions of the ASME*, **B97**:1366–1370, November 1975.
- [59] X. Zhang and W. C. Tang, “Viscous air damping in laterally driven microresonators,” In *Proceedings*, IEEE Micro Electro Mechanical Systems Workshop, Oiso, Japan, January 1994, pp. 199–204.
- [60] Y.-H. Cho, A. P. Pisano, and R. T. Howe, “Viscous damping model for laterally oscillating microstructures,” *J. of Microelectromechanical Systems*, **3**(2):81–87, June 1994.
- [61] Y.-H. Cho, B. M. Kwak, A. P. Pisano, and R. T. Howe, “Slide film damping in laterally driven microstructures,” *Sensors and Actuators*, **A40**(1):31–39, January 1994.
- [62] J. B. Starr, “Squeeze-film damping in solid-state accelerometers,” In *Technical Digest*, IEEE Solid-State Sensor and Actuator Workshop, Hilton Head Island, South Carolina, June 1990, pp. 44–47.
- [63] V. M. McNeil, M. J. Novack, and M. A. Schmidt, “Design and fabrication of thin-film microaccelerometers using wafer bonding,” In *Technical Digest*, 7th Inter. Conf. on Solid-State Sensors and Actuators (Transducers '93), Yokohama, Japan, June 1993, pp. 822–825.
- [64] W. Yun, R. T. Howe, and P. R. Gray, “Surface micromachined, digitally force-balanced accelerometer with integrated CMOS detection circuitry,” In *Technical Digest*, IEEE Solid-State Sensor and Actuator Workshop, Hilton Head Island, South Carolina, June 1992, pp. 21–25.

- [65] C.-J. Kim, A. P. Pisano, R. S. Muller, and M. G. Lim, "Polysilicon microgripper," In *Technical Digest*, IEEE Solid-State Sensor and Actuator Workshop, Hilton Head Island, South Carolina, June 1990, pp. 48–51.
- [66] H. Guckel, J. J. Sniegowski, T. R. Christenson, S. Mohney, and T. F. Kelly, "Fabrication of micromechanical devices from polysilicon films with smooth surfaces," *Sensors and Actuators*, **20**:117–122, November 1989.
- [67] L. S. Fan, Y.-C. Tai, and R. S. Muller, "Integrated movable micromechanical structures for sensors and actuators," *IEEE Trans. on Electron Devices*, **ED-35**(6):724–730, June 1988.
- [68] R. S. Muller and T. I. Kamins. *Device Electronics for Integrated Circuits*, chapter 8. John Wiley & Sons, New York, New York, 2nd ed., 1986.
- [69] C. Keller and M. Ferrari, "Milli-scale polysilicon structures," In *Technical Digest*, Solid-State Sensor and Actuator Workshop, Hilton Head Island, South Carolina, June 1994, pp. 202–207.
- [70] A. P. Pisano and Y.-H. Cho, "Mechanical design issues in laterally-driven microstructures," In *Technical Digest*, 5th Inter. Conf. on Solid-State Sensors and Actuators (Transducers '89), Montreux, Switzerland, June 1989, pp. 1060–1064.
- [71] Y.-H. Cho and A. P. Pisano, "Optimum structural design of micromechanical crab-leg flexures with microfabrication constraints," In *Proceedings*, ASME Winter Annual Meeting, Dallas, Texas, November 1990.
- [72] S. P. Timoshenko and J. N. Goodier. *Theory of Elasticity*, chapter 10, pp. 309–313. McGraw-Hill, New York, New York, 3rd ed., 1970.
- [73] Z. L. Zhang and N. MacDonald, "An rie process for submicron, silicon electromechanical structures," In *Technical Digest*, 6th Inter. Conf. on Solid-State Sensors and Actuators (Transducers '91), San Francisco, California, June 1991, pp. 520–523.
- [74] V. P. Jaeklin, C. Linder, and N. F. de Rooij, "Optical microshutters and torsional micromirrors for light modulator arrays," In *Proceedings*, IEEE Micro Electro Mechanical Systems Workshop, Fort Lauderdale, Florida, February 1993, pp. 124–127.
- [75] H. H. Woodson and J. R. Melcher. *Electromechanical Dynamics, Part I: Discrete Systems*, chapter 3, pp. 63–79. John Wiley & Sons, New York, New York, 1968.
- [76] P. Osterberg, R. K. Gupta, J. R. Gilbert, and S. D. Senturia, "Quantitative models for the measurement of residual stress, poisson ratio and young's modulus using electrostatic pull-in of beams and diaphragms," In *Technical Digest*, Solid-State Sensor and Actuator Workshop, Hilton Head Island, South Carolina, June 1994, pp. 184–188.
- [77] T. C. Edwards, *Foundations for microstrip circuit design*, John Wiley & Sons, New York, New York, 1983.

- [78] K. C. Gupta, R. Garg, and R. Chadha. *Computer-Aided Design of Microwave Circuits*, chapter 3, pp. 47–67. Artech House, Dedham, Massachusetts, 1981.
- [79] M. A. R. Gunston. *Microwave transmission-line impedance data*, chapter 3, pp. 43–44. Van Nostrand Reinhold, New York, New York, 1972.
- [80] W. C. Tang, M. L. Lim, and R. T. Howe, “Electrostatic comb drive levitation and control method,” *J. of Microelectromechanical Systems*, **1**(4):170–178, March 1992.
- [81] J. Kung, H. Lee, and R. T. Howe, “A digital readout technique for capacitive sensor applications,” *IEEE J. Solid-State Circuits*, **23**:972–977, August 1988.
- [82] J. T. Kung, *Integrated Capacitive Sensors Using Charge-Redistribution Sense Techniques*, PhD thesis, Dept. of Electrical Engineering and Computer Science, Massachusetts Institute of Technology, Cambridge, Massachusetts, June 1992.
- [83] W. Yun, *A surface micromachined accelerometer with integrated CMOS detection circuitry*, PhD thesis, Dept. of Electrical Engineering and Computer Sciences, University of California at Berkeley, Berkeley, California, December 1992.
- [84] P. R. Gray and R. G. Meyer, *Analysis and design of analog integrated circuits*, John Wiley & Sons, Inc., New York, New York, 3rd ed., 1993.
- [85] B. R. Chawla and H. K. Gummel, “Transistion region capacitance of diffused p-n junctions,” *IEEE Trans. on Electron Devices*, **ED-18**(3):178–195, March 1971.
- [86] T. B. Gabrielson, “Mechanical-thermal noise in micromachined acoustic and vibration sensors,” *IEEE Trans. on Electron Devices*, **ED-40**(5):903–909, May 1993.
- [87] C. T.-C. Nguyen and R. T. Howe, “Quality factor control for micromechanical resonators,” In *Technical Digest*, Int. Electron Devices Meeting, San Francisco, California, December 1992, pp. 505–508.
- [88] W. Henrion, L. DiSanza, M. Ip, S. Terry, and H. Jerman, “Wide dynamic range direct digital accelerometer,” In *Technical Digest*, IEEE Solid-State Sensor and Actuator Workshop, Hilton Head Island, South Carolina, June 1990, pp. 153–157.
- [89] Y. DeCoulon, T. Smith, J. Hermann, M. Chevroulet, and F. Rudolf, “Design and test of a precision servoaccelerometer with digital output,” In *Technical Digest*, 7th Inter. Conf. on Solid-State Sensors and Actuators (Transducers '93), Yokohama, Japan, June 1993, pp. 832–835.
- [90] J. C. Candy and G. C. Temes. *Oversampling Delta-Sigma Data Converters*, pp. 1–29. IEEE Press, New York, New York, 1992. Paper title: ”Oversampling Methods for A/D and D/A Conversion”.
- [91] J. C. Candy and O. J. Benjamin, “The structure of quantization noise from sigma-delta modulation,” *IEEE Trans. Commun.*, **COM-29**:1316–1323, September 1981.

- [92] J. Bustillo, G. K. Fedder, C. T.-C. Nguyen, and R. T. Howe, "Process technology for the modular integration of cmos and polysilicon microstructures," *Microsystems Technologies*, 1, October 1994.
- [93] L.-L. Lin, R. T. Howe, and A. P. Pisano, "A passive, in situ micro strain gauge," In *Proceedings*, IEEE Micro Electro Mechanical Systems Workshop, Fort Lauderdale, Florida, February 1993, pp. 201–206.
- [94] The MathWorks, Inc., Natick, Massachusetts. *SIMULINK User's Guide*, 1992.
- [95] J. K. Roberge. *Operational Amplifiers*, pp. 217–242. John Wiley & Sons, Inc., New York, New York, 1975.
- [96] J. H. Jerman, "A miniature fabry-perot interferometer with a corrugated silicon diaphragm support," In *Technical Digest*, IEEE Solid-State Sensor and Actuator Workshop, Hilton Head Island, South Carolina, June 1990, pp. 140–144.
- [97] G. K. Fedder and R. T. Howe, "Integrated testbed for multi-mode digital control of suspended microstructures," In *Technical Digest*, Solid-State Sensor and Actuator Workshop, Hilton Head Island, South Carolina, June 1994, pp. 145–150.

## Appendix A

# Testbed Technical Information

Information in the appendices (and elsewhere in this thesis) will be accessible on the World Wide Web (WWW) through a hypertext viewer, such as Mosaic, by specifying the Universal Resource Locator (URL) for the Berkeley Sensor & Actuator Center home page, “<http://nitride.eecs.berkeley.edu>”. From that location, browse to find the link to my research information (look for ”Gary Fedder”). Good luck!

### A.1 Testbed Parameter Data

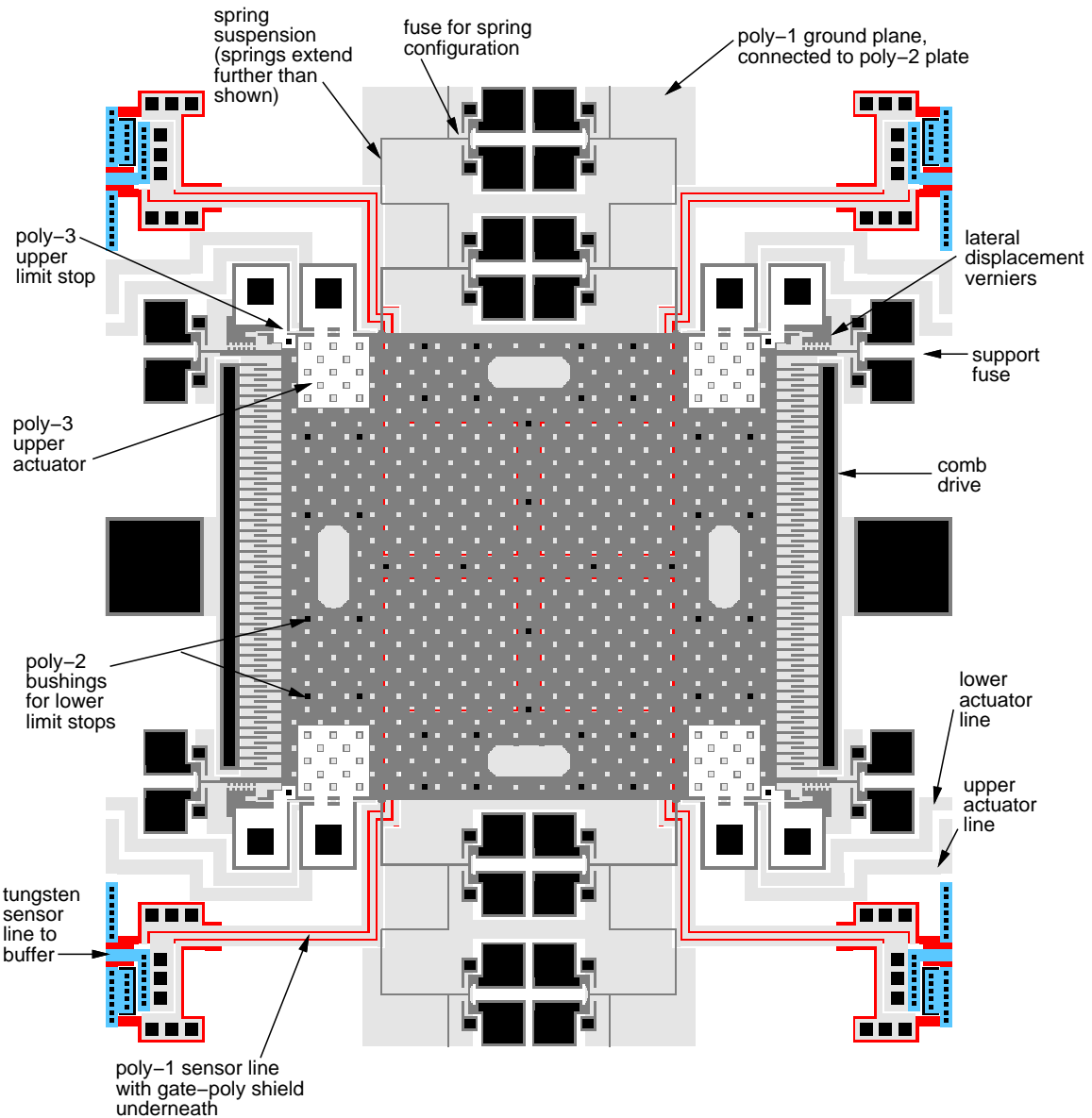
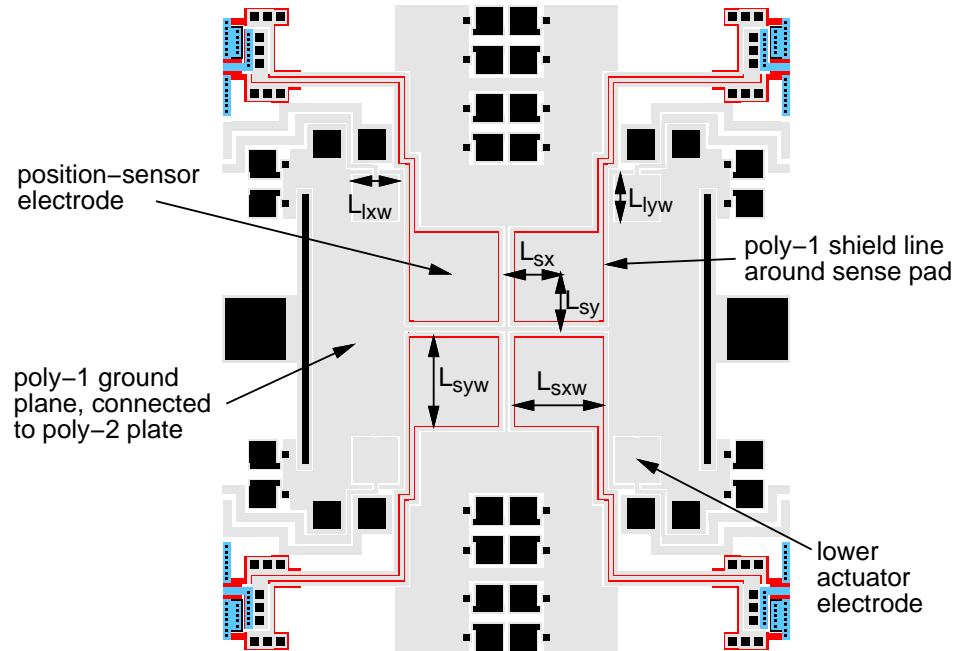


Figure A.1: Layout of the testbed's micromechanical plate and springs.

### Poly-1 Layout:



### Poly-2 and Poly-3 Layout:

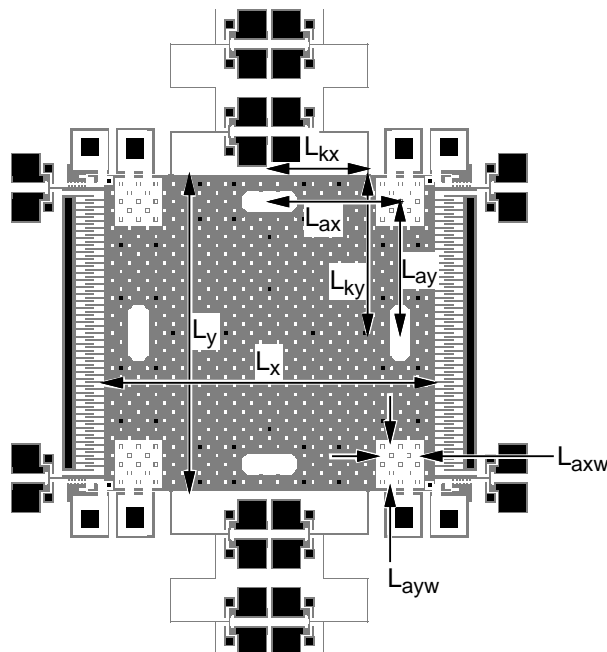


Figure A.2: Testbed layout dimensions. Dimensional values are given in Table A.1.

parameter	value	description
$t$	1.6 $\mu\text{m}$	plate thickness
$z_o$	2.2 $\mu\text{m}$	fabricated air-gap between plate and substrate
$z_{ao}$	2.7 $\mu\text{m}$	fabricated air-gap between plate and upper actuators
$L_x$	380 $\mu\text{m}$	$x$ -axis plate dimension
$L_y$	360 $\mu\text{m}$	$y$ -axis plate dimension
$L_{kx}$	113 $\mu\text{m}$	spring distance from plate's $x$ -axis
$L_{ky}$	180 $\mu\text{m}$	spring distance from plate's $y$ -axis
$L_{sxw}$	100 $\mu\text{m}$	sensor electrode width in $x$ direction
$L_{syw}$	100 $\mu\text{m}$	sensor electrode width in $y$ direction
$L_{sx}$	60 $\mu\text{m}$	sensor distance from plate's $x$ -axis
$L_{sy}$	60 $\mu\text{m}$	sensor distance from plate's $y$ -axis
$L_{lxw}$	52 $\mu\text{m}$	lower-actuator electrode width in $x$ direction
$L_{lyw}$	52 $\mu\text{m}$	lower-actuator electrode width in $y$ direction
$L_{uxw}$	54 $\mu\text{m}$	upper-actuator electrode width in $x$ direction
$L_{uyw}$	54 $\mu\text{m}$	upper-actuator electrode width in $y$ direction
$L_{ax}$	150 $\mu\text{m}$	actuator distance from plate's $x$ -axis
$L_{ay}$	150 $\mu\text{m}$	actuator distance from plate's $y$ -axis

Table A.1: Testbed geometric parameters.

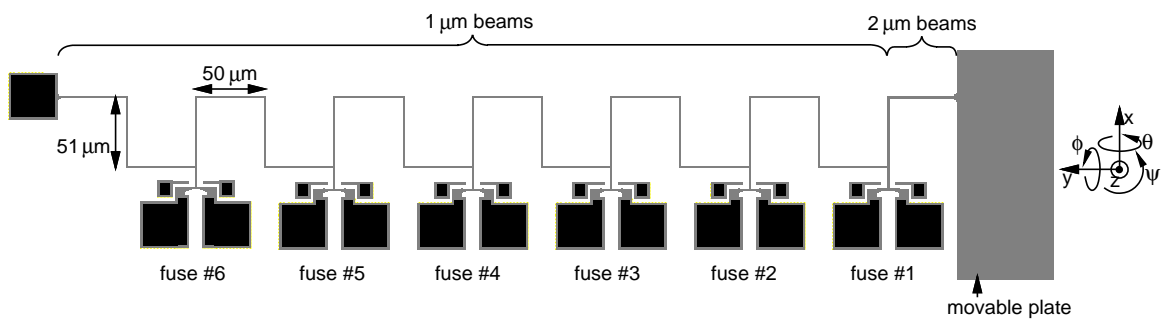


Figure A.3: Layout of one serpentine spring, showing the 6 fuses that can be cut to set the spring constant.

configuration number	fuses cut	$k_z$ [N/m]	$k_x$ [N/m]	$k_y$ [N/m]
1	none	0.455	1.64	3.72
2	#1	0.249	0.282	0.946
3	#1,#2	0.0576	0.0520	0.489
4	#1,#2,#3	0.0205	0.0170	0.328
5	#1,#2,#3,#4	0.00937	0.00746	0.247
6	#1,#2,#3,#4,#5	0.00501	0.00390	0.198
7	#1,#2,#3,#4,#5,#6	0.00357	0.00260	0.169

(a)

spring configuration number						
1		2		3		4
mode	$f_r$ [Hz]	mode	$f_r$ [Hz]	mode	$f_r$ [Hz]	mode
$z$	17200	$\theta$	2860	$\theta$	1670	$x$
$\theta$	17900	$z$	3680	$x$	1670	$z$
$\phi$	18800	$\phi$	3700	$z$	1760	$\phi$
$x$	29800	$x$	3900	$\phi$	1880	$\theta$
$y$	44800	$y$	7140	$\psi$	4640	$\psi$
$\psi$	68100	$\psi$	8110	$y$	5120	$y$
P	80000	P	69400	LS	42800	VS
P	110000	VS	75500	VS	45200	LS
						29200

spring configuration number						
5		6		7		
mode	$f_r$ [Hz]	mode	$f_r$ [Hz]	mode	$f_r$ [Hz]	
$x$	631	$x$	456	$x$	372	
$z$	708	$z$	517	$z$	436	
$\phi$	820	$\phi$	633	$\phi$	556	
$\theta$	1030	$\theta$	909	$\theta$	854	
$\psi$	2780	$\psi$	2400	$\psi$	2170	
$y$	3640	$y$	3260	$y$	3000	
VS	15900	VS	11000	VS	8950	
LS	21100	LS	15500	LS	12100	

(b)

Table A.2: Testbed spring configurations. (a) Static spring constants (four-spring suspension), calculated from linear finite-element analysis (linear and nonlinear finite-element results agree to 4 significant digits). (b) System resonant frequencies, calculated from linear finite-element analysis. Refer to Figure A.3 for definitions of the axes and rotation angles. In the “P” mode, the plate is bending. Springs vibrate laterally in the “LS” mode, and vertically in the “VS” mode.

capacitor name	symbol	capacitance when $\Delta z = 0$	width $\times$ length	spacer gap
sense	$C_s$	41.4 fF	100 $\mu\text{m} \times 100 \mu\text{m}$	2.2 $\mu\text{m}$
reference	$C_r$	40.7 fF	100 $\mu\text{m} \times 100 \mu\text{m}$	2.2 $\mu\text{m}$
lower actuator	$C_{\text{down}}$	10.8 fF	52 $\mu\text{m} \times 52 \mu\text{m}$	2.2 $\mu\text{m}$
upper actuator	$C_{\text{up}}$	9.2 fF	54 $\mu\text{m} \times 54 \mu\text{m}$	2.7 $\mu\text{m}$

Table A.3: Capacitance definitions, dimensions and calculated values. Plate displacement,  $\Delta z$ , is defined relative to the fabricated spacer gap of 2.2  $\mu\text{m}$ . Calculated capacitance values are derived from a combination of parallel-plate, interconnect and etch hole capacitance.

Pin #	Description
1	$V_{dd}$ (+4 V) (pin is connected to package base)
2	Upper-left pull-down actuator
3	Left comb drive
4	Lower-left pull-down actuator
5	Lower-left pull-up actuator
6	Upper-left position sensor output
7	Lower-left position sensor output
8	Test structure position sensor output
9	Test structure direct position sensor output (not source follower)
10	GND
11	p-channel triode bias voltage (not used)
12	$V_{ss}$ (-2.5 V)
13	$I_b$ (80 $\mu\text{A}$ )
14	$V_{dd}$ (+4 V)
15	$V_{m+}$ (modulation voltage to reference capacitor)
16	Upper-left pull-up actuator
17	Lower-right position sensor output
18	Upper-right position sensor output
19	Right comb drive
20	Lower-right pull-down actuator
21	Lower-right pull-up actuator
22	Upper-right pull-down actuator
23	Upper-right pull-up actuator
24	$V_{m-}$ (modulation voltage to sense capacitor, that is the plate mass)

Table A.4: Pin assignments for working testbed chip in a 24-pin dual-inline package.

## A.2 External Testbed Electronics

### A.2.1 Schematics

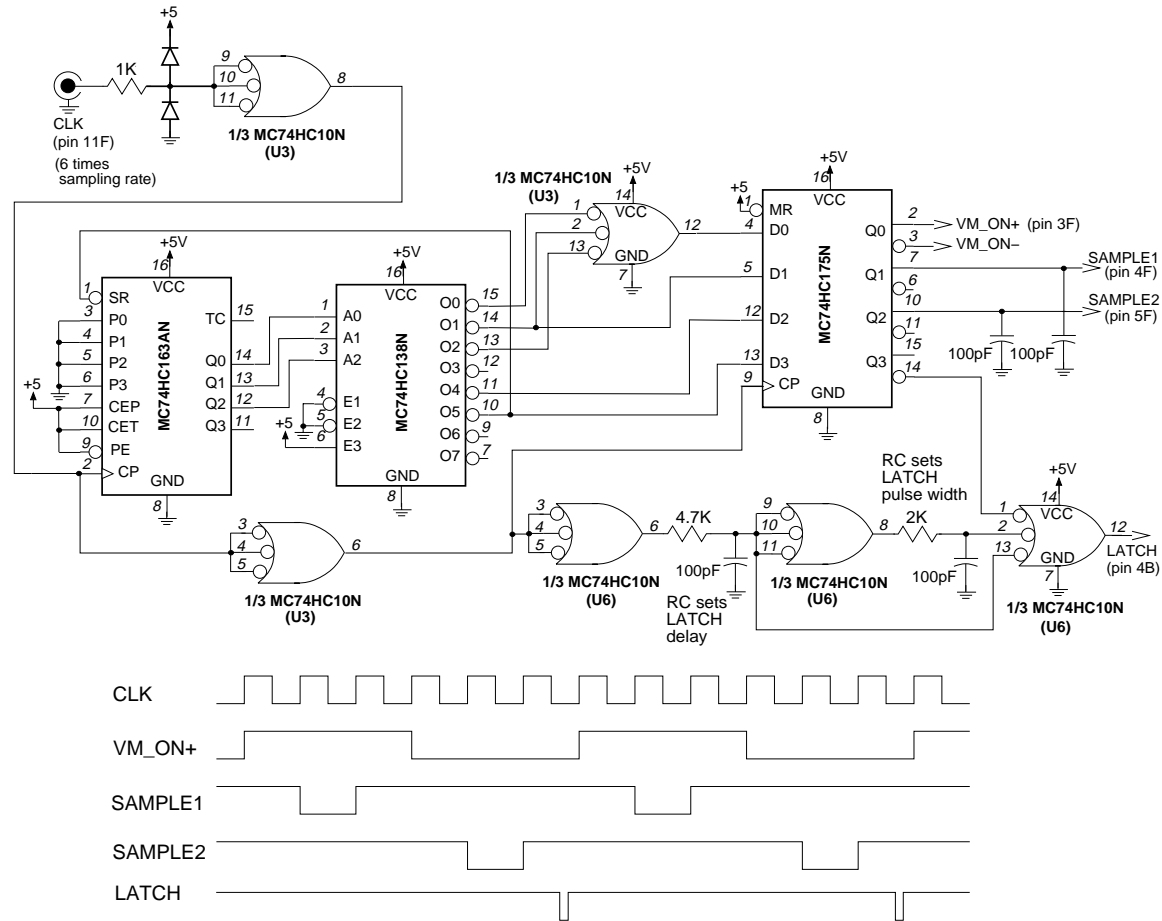


Figure A.4: Timing board, schematic #1: digital control logic

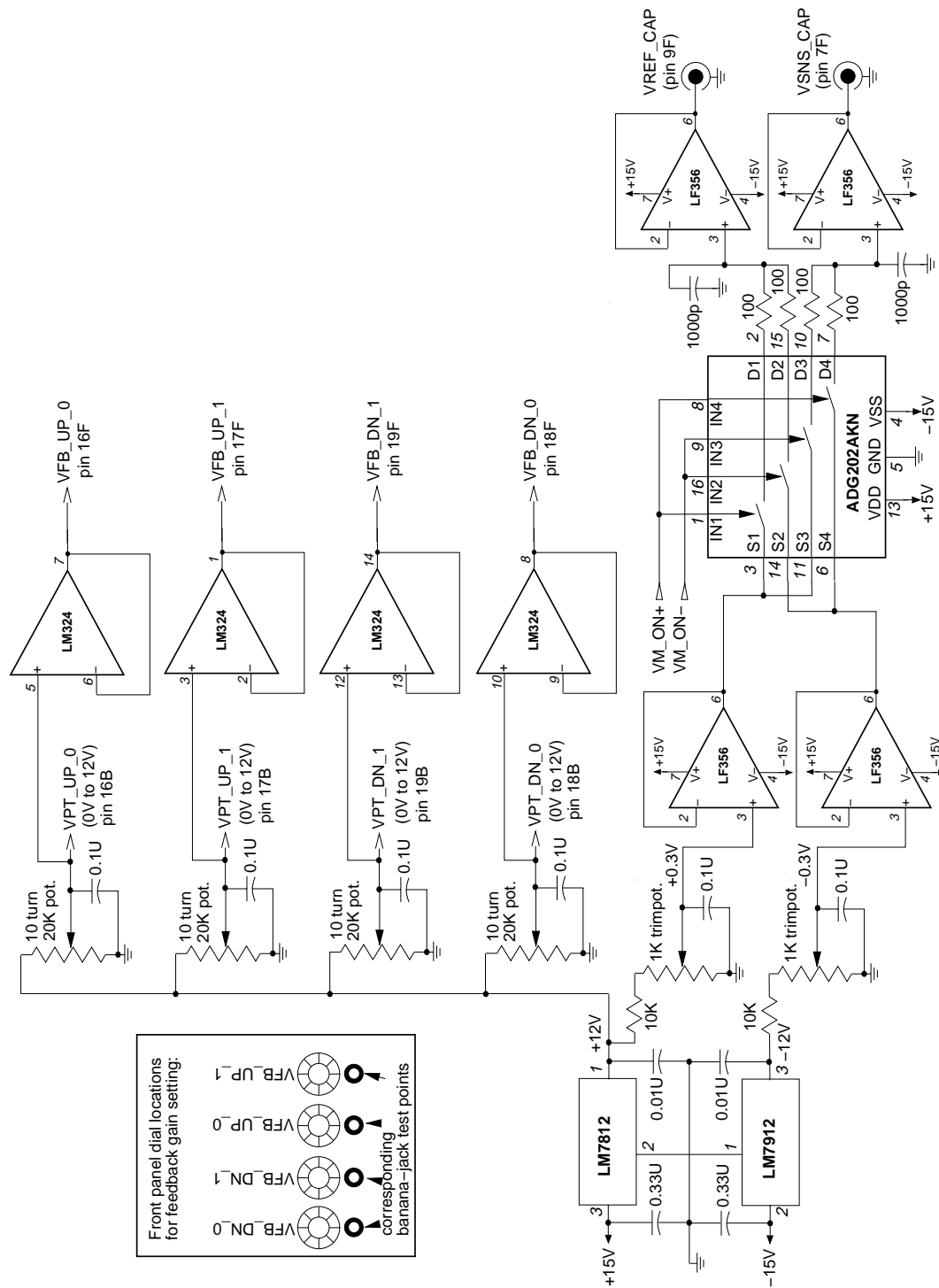


Figure A.5: Timing board, schematic #2: voltage references and balanced modulation source.

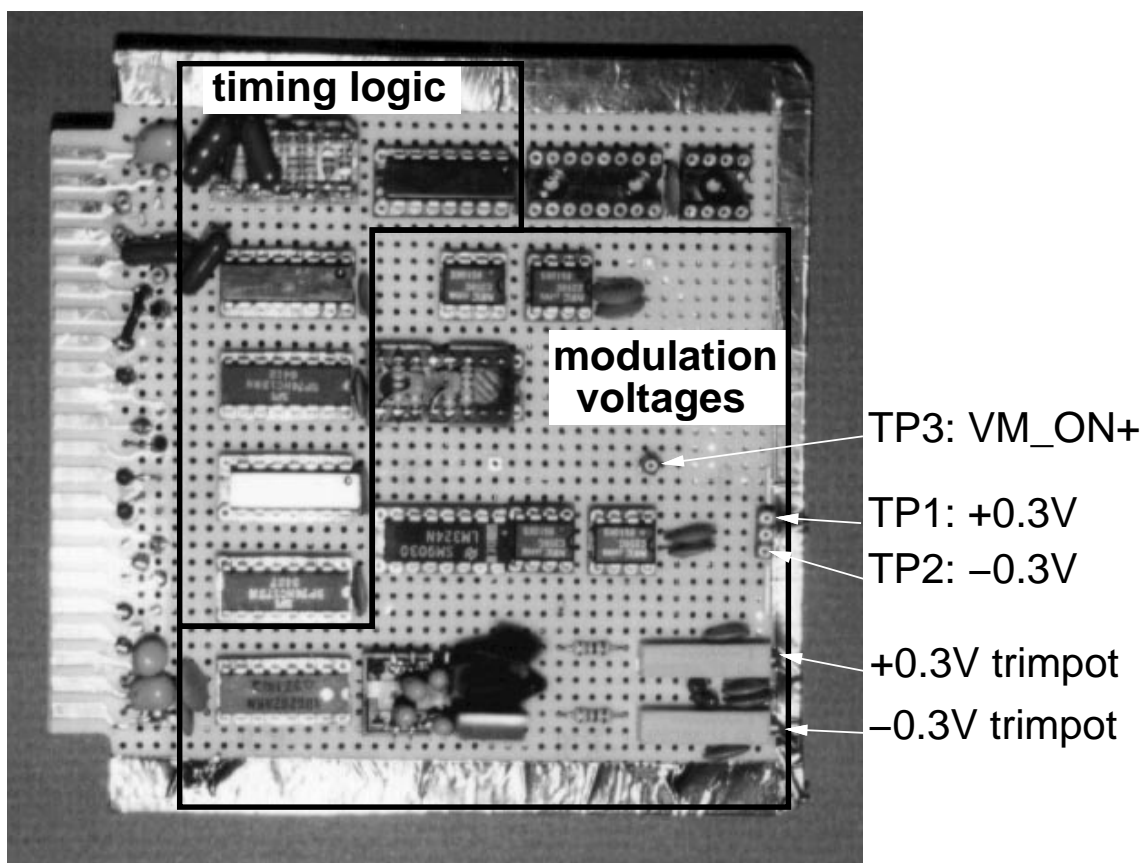


Figure A.6: Photograph of the timing board, identifying the functional blocks and test points.

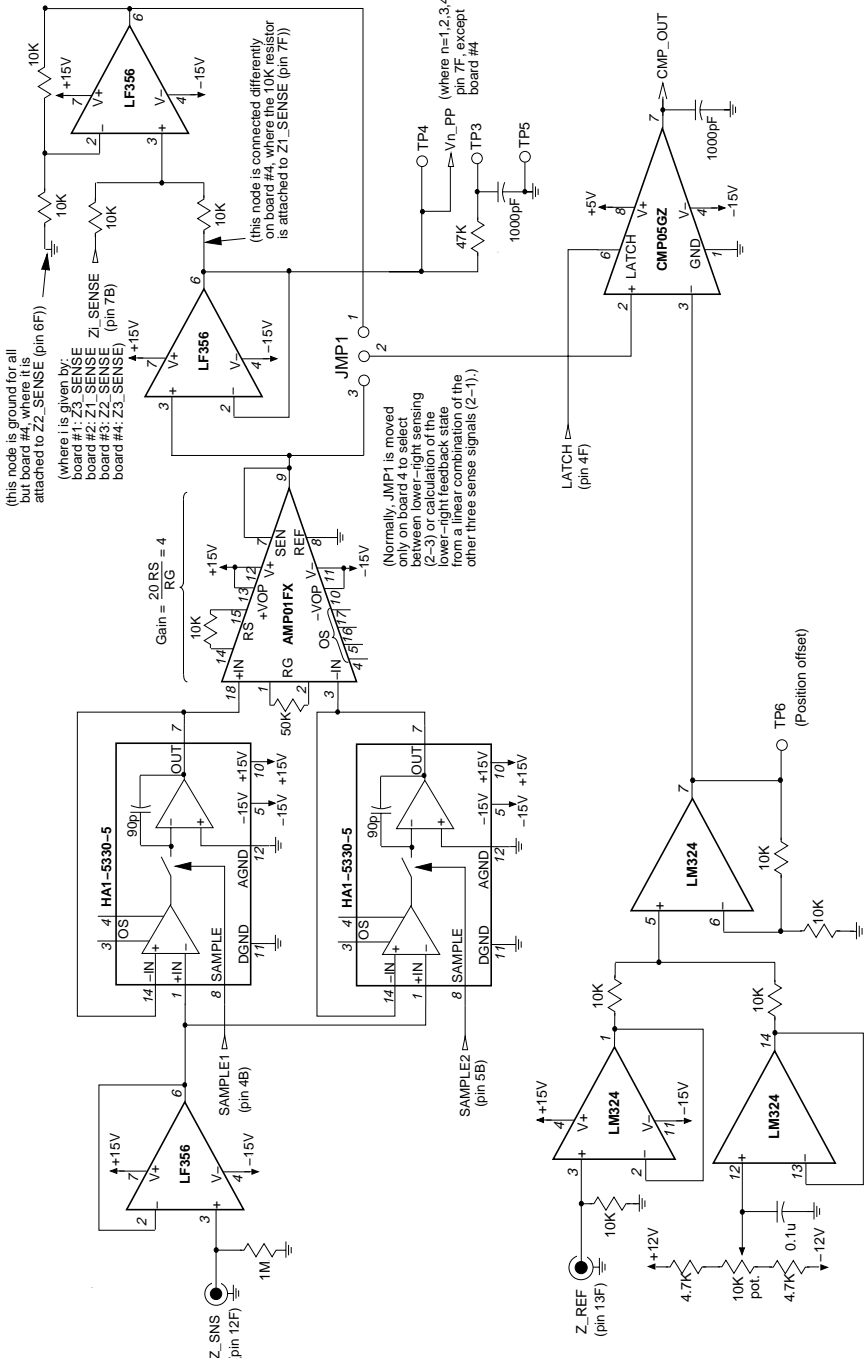


Figure A.7: Feedback board, schematic #1: input demodulator (1 of 4). The feedback boards are assigned as follows. Board 1 takes upper-right channel input. Board 2 takes upper-left channel input. Board 3 takes lower-left channel input. Board 4 takes lower-right channel input, or calculates lower-right channel feedback from the other three channels, dependent on the jumper JMP1.

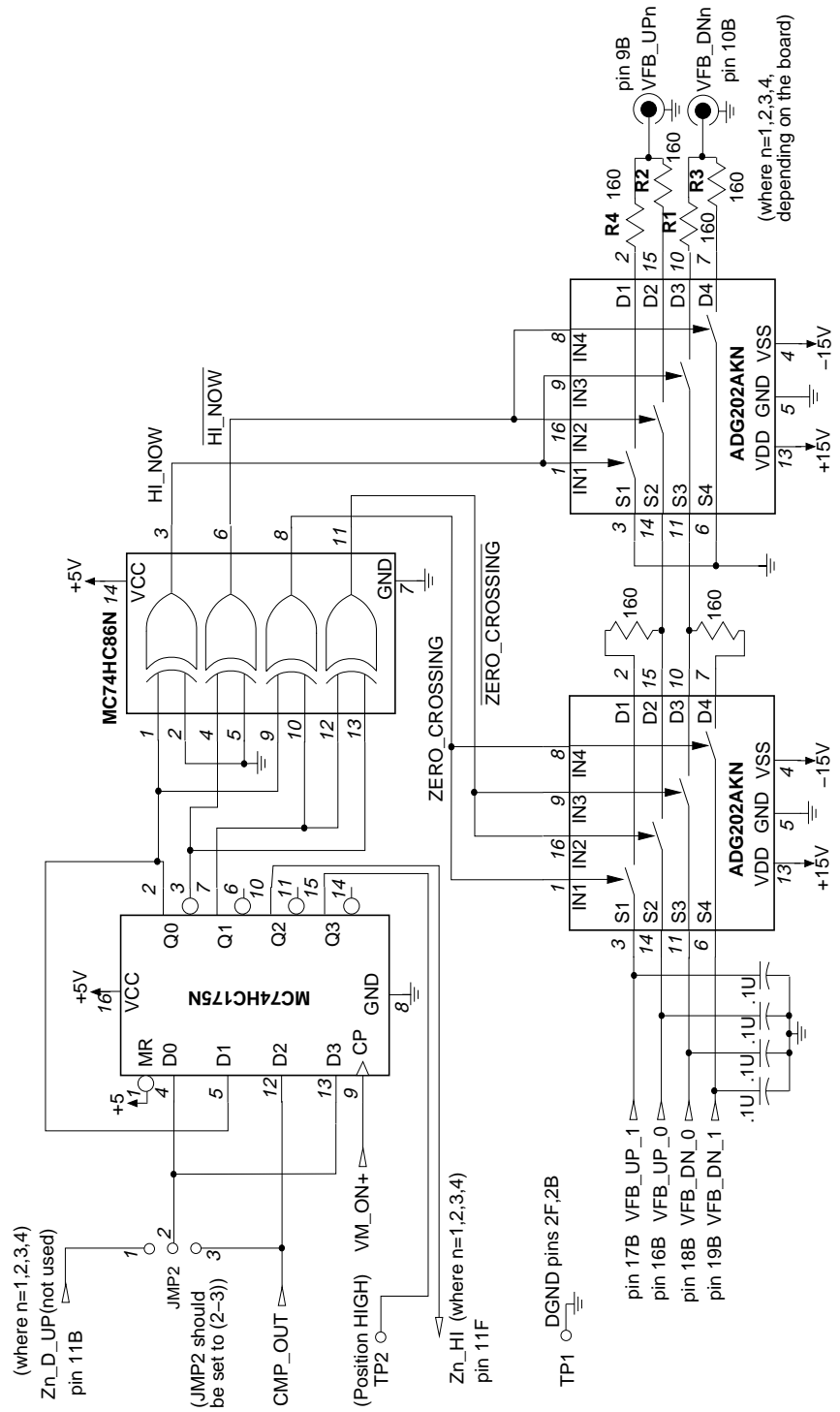


Figure A.8: Feedback board, schematic #2: feedback logic (1 of 4).

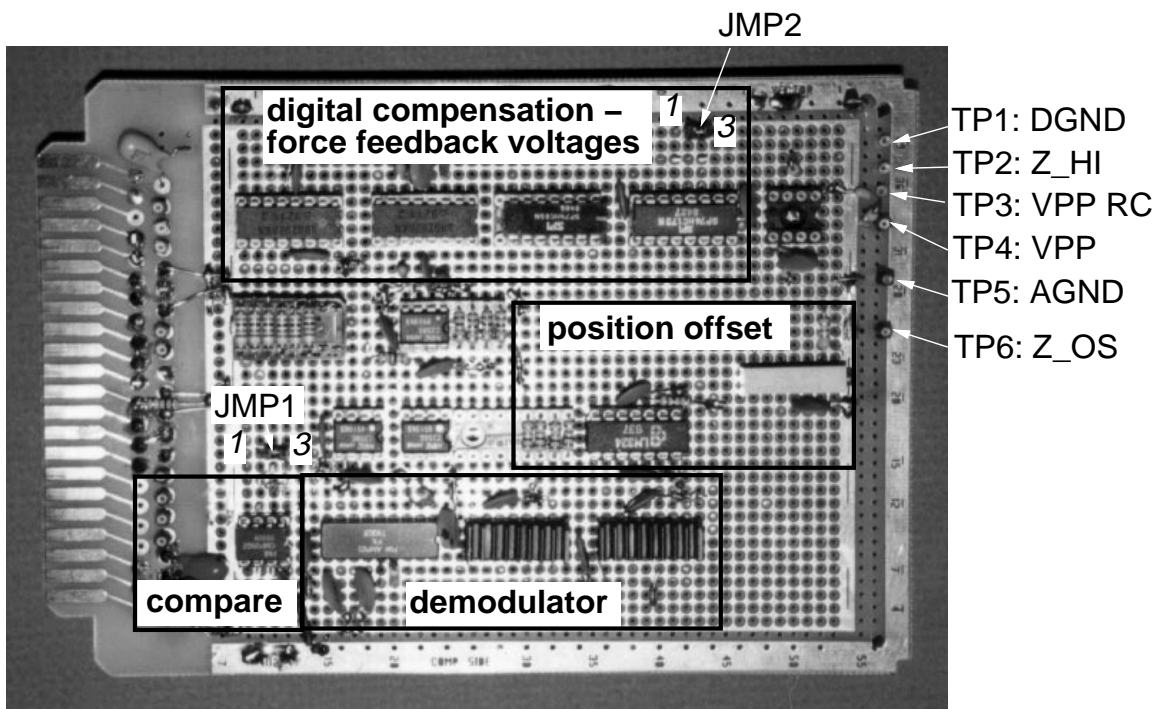


Figure A.9: Photograph of one of the feedback boards (board #2), identifying the functional blocks and test points.

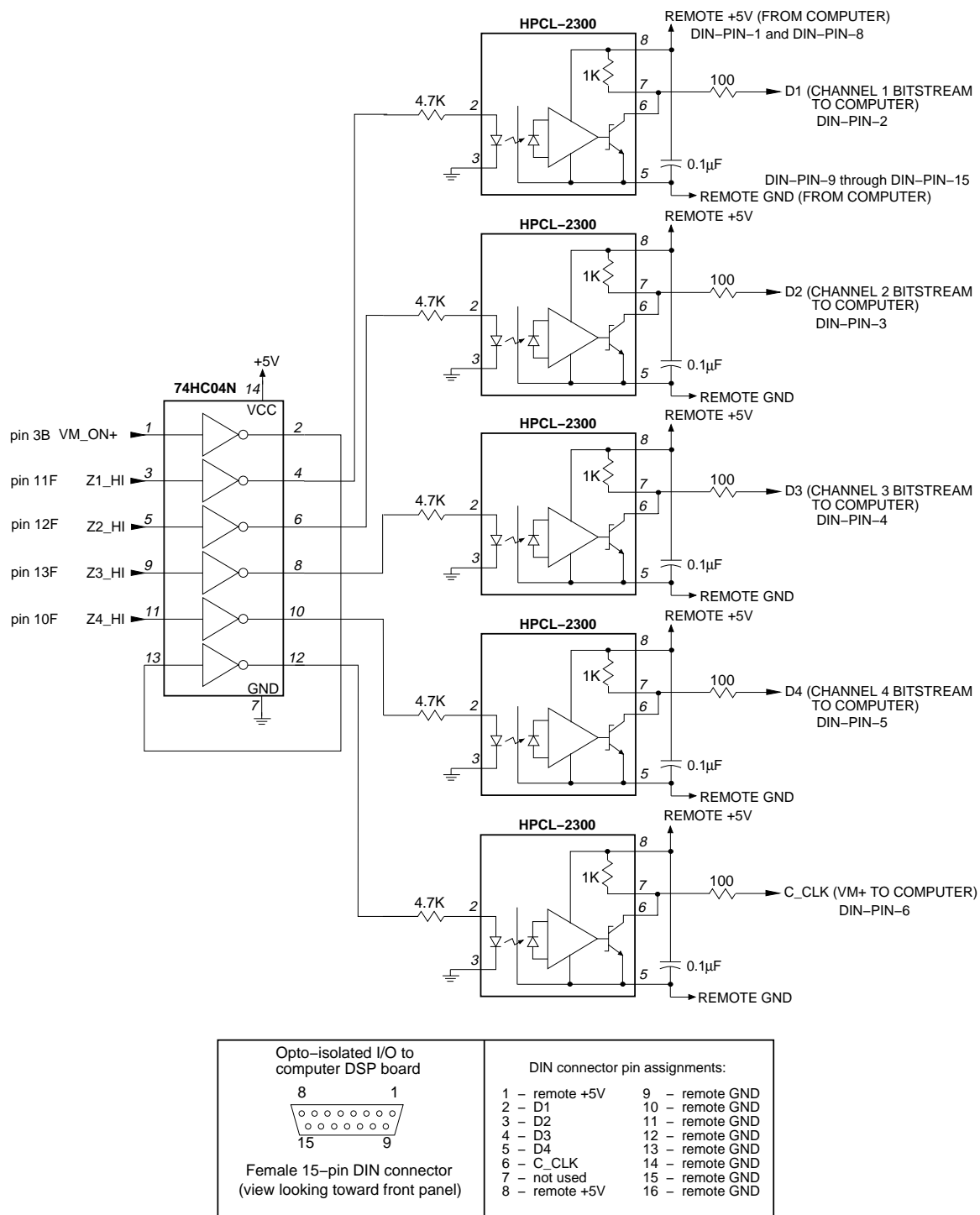


Figure A.10: Schematic of the opto-isolation board.

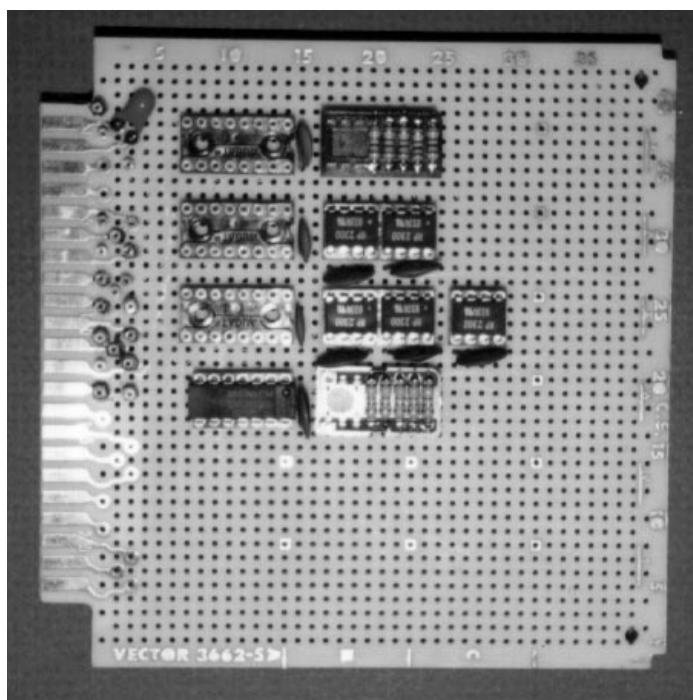


Figure A.11: Photograph of the opto-isolation board.

### A.2.2 Card-Cage Layout

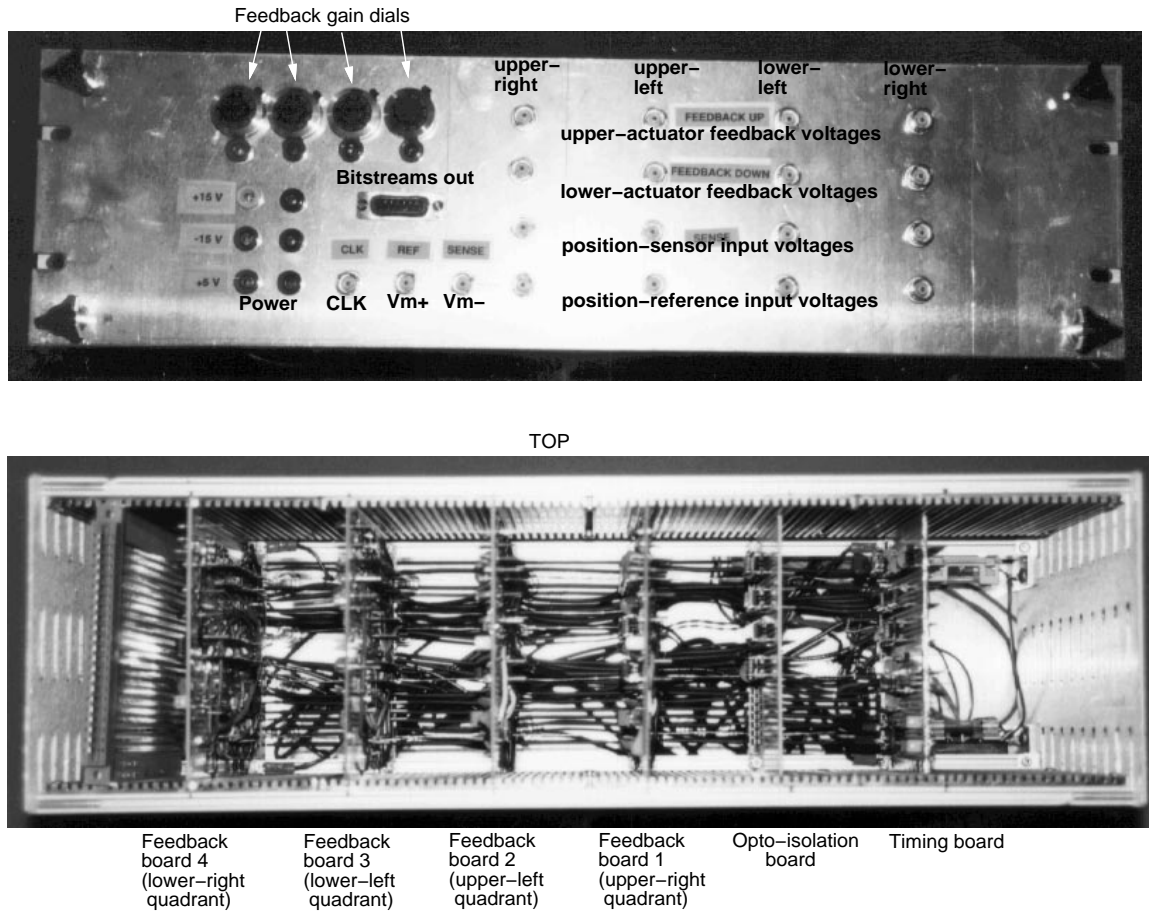


Figure A.12: External electronics, housed in a standard card cage. (a) Front view. (b) Rear view. Most connections are made via front-panel BNC connectors. The opto-isolated bitstreams are available from a 9-pin DIN connector. Dials on the front-panel are used to set feedback gains. Power is supplied through banana-jacks.

Pin #	Timing Board		Opto-isolation Board		Feedback Board	
	Front	Back	Front	Back	Front	Back
1	+5 V	+5 V	+5 V	+5 V	+5 V	+5 V
2	DGND	DGND	DGND	DGND	DGND	DGND
3	VM_ON+	VM_ON+		VM_ON+		VM_ON+
4	SAMPLE1	LATCH			LATCH	SAMPLE1
5	SAMPLE2					SAMPLE2
6	AGND	AGND	REMOTE GND	REMOTE GND	Brd 1,2,3: AGND	AGND
			GND	GND	Brd 4: V2_PP	AGND
7	VSNS_CAP	AGND	REMOTE +5 V	D1	Brd 1: V1_PP	V3_PP
					Brd 2: V2_PP	V1_PP
					Brd 3: V3_PP	V2_PP
					Brd 4: V1_PP	V3_PP
8	AGND	AGND	D2	D3	AGND	AGND
9	VREF_CAP	AGND	C_CLK	D4	DGND	VFB_UP
10	VFB_DN	DGND	Z4_HI	Z1_D_UP	DGND	VFB_DN
11	CLK	DGND	Z1_HI	Z2_D_UP	Brd 1: Z1_HI	Z1_D_UP
					Brd 2: Z2_HI	Z2_D_UP
					Brd 3: Z3_HI	Z3_D_UP
					Brd 4: Z4_HI	Z4_D_UP
12	DGND	DGND	Z2_HI	Z3_D_UP	Z_SNS	AGND
13	DGND	DGND	Z3_HI	Z4_D_UP	Z_REF	AGND
14	DGND	DGND			DGND	DGND
15	+12 V	-12 V			+12 V	-12 V
16	VFB_UP_0	VPT_UP_0				VFB_UP_0
17	VFB_UP_1	VPT_UP_1				VFB_UP_1
18	VFB_DN_0	VPT_DN_0				VFB_DN_0
19	VFB_DN_1	VPT_DN_1				VFB_DN_1
20	+15 V	+15 V			+15 V	+15 V
21	AGND	AGND			AGND	AGND
22	-15 V	-15 V			-15 V	-15 V

Table A.5: Backplane assignments. Pin 1 is located at the top of the card cage. The pins are noted on schematics as "1F" for pin 1-front, etc.

### A.2.3 Test Setup

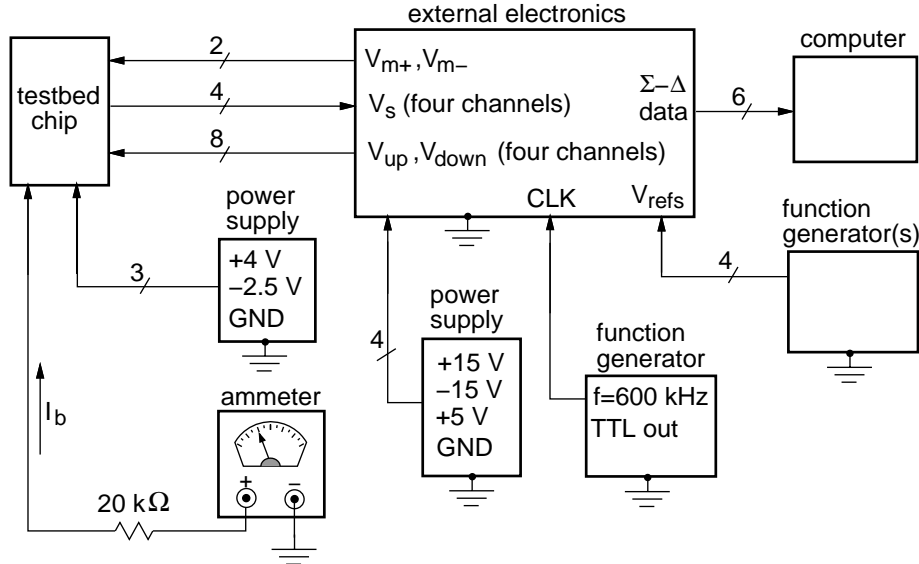


Figure A.13: Schematic of the experimental test setup.

In addition to the custom electronics, several other pieces of equipment are required, including

- $\pm 15\text{ V}$  power supplies, rated 0.6 A, for external analog electronics
- $+5\text{ V}$  power supply, rated 0.1 A, for external digital electronics
- $+4\text{ V}$  and  $-2.5\text{ V}$  power supplies, for  $V_{dd}$  and  $V_{ss}$  to the chip
- 600 kHz square-wave generator, TTL output, for timing clock ( $f_m=100\text{ kHz}$ )
- ammeter, for monitoring chip bias current
- one or more function generators for position reference inputs,  $V_{ref}$ 's
- computer interface for digital bitstream filtering and storage

## Appendix B

# HSPICE Input Files

Information in the appendices (and elsewhere in this thesis) will be accessible on the World Wide Web (WWW) through a hypertext viewer, such as Mosaic, by specifying the Universal Resource Locator (URL) for the Berkeley Sensor & Actuator Center home page, “<http://nitride.eecs.berkeley.edu>”. From that location, browse to find the link to my research information (look for ”Gary Fedder”). Good luck!

### B.1 CMOS Unity-Gain Buffer HSPICE File

Buffer with pmos current mirror load 7/27/94

```
* There are four different input arrangements:
* 1) DC/AC input - to determine gain, bandwidth and offset
*           (dc vtest -0.3 0.3 0.02)
*           (ac dec 10 10k 1G)
* 2) Square wave input - to determine risetime, offset and gain
*           (tran 1n 100n)
* 3) AC input with series cap. - to determine input capacitance
*           (ac dec 10 10k 1Meg)
* 4) Capacitor divider input - actual sensor operation conditions
*           (tran 1u 100u)
*
* differential-pair (buffer) output load capacitance (for #1,2,3 tests)
*   (use cshield for #4 test instead)
.param cout=3p
.param rout=100k
* source-follower output load capacitance
```

```

.param coutb=10p
* shield capacitance
.param cshield=3p
* reference capacitance
.param cref=45f
* variable sense capacitance
.param csense=200f
* fixed sense capacitance
.param csfixed=100f
* fixed parasitic capacitance to ground
.param cparasitic=10f

*****
* 1,2) uncomment for DC, AC, or Square wave input
vtest 3 0 dc 0 ac 0.1 pulse(-0.02 0.02 0 .1u .1u 5u 10u)
*****
* 3) uncomment for AC input with series capacitor
*vtest 64 0 dc 0 ac 0.1
*citest 64 3 10f
*****
* 4) uncomment for Capacitor Divider input
*rinput 63 3 1
*rshield 65 7 1
*****
*
* Power supplies
*
vdd 20 0 dc 4.0
vss 10 0 dc -2.5
*****
*
* Capacitor divider section (only connected for test #4 )
*
* balanced modulation voltages
vtest1a 60 0 dc 0 pulse(0 0.3 0 0.1u 0.1u 5u 10u)
vtest1b 61 0 dc 0 pulse(0 -0.3 5u 0.1u 0.1u 5u 10u)
etest1 30 0 vol='v(60)+v(61)'
etest2 31 0 vol='-'v(30)'
*
* capacitive divider
cupper 30 63 cref
clower 63 32 csense
clowerfix 63 32 csfixed
cpar 63 0 cparasitic

```

```
cshld      65 63 cshield
*
* interconnect resistance to upper plate (can neglect)
rlower     31 32 100k
*
*****
* big resistors to provide dc path to ground for simulator
rdummy1    63 0 10000x
rdummy2    65 0 10000x
rdummy3    0 3 10000x
*****
*
* input diode
* (comment out to find buffer input capacitance w/o diode junction cap)
d1 0 3 diode1
*****
*
* Output load capacitance
cout1 7 0 cout
rout1 7 0 rout
coutb 9 0 coutb
*****
*
* Current reference
*
iref 0 2 dc 80u
m8a 2 2 10 10 mn_4um w=100u l=4u
+ AD=1000.OP PD=120.OU AS=1000.OP PS=120.OU
m8b 2 2 10 10 mn_4um w=100u l=4u
+ AD=1000.OP PD=120.OU AS=1000.OP PS=120.OU
*****
*
* Buffer
*
* Input diff pair
m1a 4 3 8 8 mn_4um w=100u l=4u
+ AD=700.OP PD=47.3U AS=1000.OP PS=120.OU
m1b 4 3 8 8 mn_4um w=100u l=4u
+ AD=700.OP PD=47.3U AS=1000.OP PS=120.OU
m2a 7 7 8 8 mn_4um w=100u l=4u
+ AD=700.OP PD=47.3U AS=1000.OP PS=120.OU
m2b 7 7 8 8 mn_4um w=100u l=4u
+ AD=700.OP PD=47.3U AS=1000.OP PS=120.OU
```

```

* Drain isolation
m3 6 5 4 4 mn_4um w=100u l=4u
+ AD=1000.OP PD=120.OU AS=700.OP PS=47.3U
m4 5 5 7 7 mn_4um w=100u l=4u
+ AD=1000.OP PD=120.OU AS=700.OP PS=47.3U

* Load transistors
m5 6 6 20 20 mp_8um w=100u l=8u
+ AD=1000.OP PD=120.OU AS=1000.OP PS=120.OU
m6 5 6 20 20 mp_8um w=100u l=8u
+ AD=1000.OP PD=120.OU AS=1000.OP PS=120.OU

* Diff pair current source
m7a 8 2 10 10 mn_4um w=100u l=4u
+ AD=1000.OP PD=120.OU AS=1000.OP PS=120.OU
m7b 8 2 10 10 mn_4um w=100u l=4u
+ AD=1000.OP PD=120.OU AS=1000.OP PS=120.OU

* Source follower buffer
m10a 20 7 9 9 mn_4um w=50u l=4u
+ AD=500.OP PD=22.OU AS=500.OP PS=70.OU
m10b 20 7 9 9 mn_4um w=50u l=4u
+ AD=500.OP PD=22.OU AS=500.OP PS=70.OU
m9a 9 2 10 10 mn_4um w=50u l=4u
+ AD=500.OP PD=22.OU AS=500.OP PS=70.OU
m9b 9 2 10 10 mn_4um w=50u l=4u
+ AD=500.OP PD=22.OU AS=500.OP PS=70.OU

*****
* MOS Models are modified from the Orbit 2um models
* kp, vto, gamma, and lambda are from MICS cmos25-run data
*****


.model diode1 d level=3 l=9e-6 w=15e-6 cj=5.3e-3 is=1 xw=1e-6

.model mn_4um nmos level=2 capop=0 acm=0
+ vto=0.56 kp=33u gamma=0.55 phi=0.6
+ lambda=0.043 rdc=10.0 rsc=10.0
+ ld=0.22u xj=0.25u tox=500.0e-10 nsub=2.3e+16
+ uo=619.0 ucrit=2.6e+04 uexp=0.106
+ neff=1.000 delta=1.4 nfs=1.38e+12
+ rsh=4.0 pb=0.8
+ cj=4.06e-04 mj=0.443 cjsw=4.44e-10 mjsw=0.291
+ cgdo=2.5e-10 cgso=2.5e-10 cgbo=2.5e-10

```

```

+ vmax=6.84e+4
+ nss=1.0e+12 tpg=1.0
*
.model mp_4um pmos level=2
+ vto=-0.56 kp=17u gamma=0.55 phi=0.6
+ lambda=0.046 rdc=100.0 rsc=100.0
+ ld=0.16u xj=0.25u tox=500.0e-10 nsub=0.79e+16
+ uo=257.0 ucrit=2.4e+04 uexp=0.270
+ neff=1.001 delta=0.0 nfs=1.1e+12
+ rsh=4.0 pb=0.71
+ cj=2.30e-04 mj=0.410 cjsw=2.20e-10 mjsw=0.1
+ cgdo=2.5e-10 cgso=2.5e-10 cgbo=2.5e-10
+ vmax=4.50e+4
+ nss=1.0e+12 tpg=-1.0
*
.model mp_8um pmos level=2
+ vto=-0.56 kp=17u gamma=0.55 phi=0.6
+ lambda=0.023 rdc=100.0 rsc=100.0
+ ld=0.16u xj=0.25u tox=500.0e-10 nsub=0.79e+16
+ uo=257.0 ucrit=2.4e+04 uexp=0.270
+ neff=1.001 delta=0.0 nfs=1.1e+12
+ rsh=4.0 pb=0.71
+ cj=2.30e-04 mj=0.410 cjsw=2.20e-10 mjsw=0.1
+ cgdo=2.5e-10 cgso=2.5e-10 cgbo=2.5e-10
+ vmax=4.50e+4
+ nss=1.0e+12 tpg=-1.0
*
.options acct chgtol=1e-16 post
.op

* 1a) uncomment for DC analysis
*.dc vtest -2.5 2.5 .05

* 1b,3,4) uncomment for AC analysis
.ac dec 10 10k 20meg sweep coutb lin 2 10f 10pf

* 2,4) uncomment for AC analysis
*.tran 0.2u 30u

.end

```

## B.2 Testbed HSPICE File

Mechanical simulation of microactuator system with buffer 8/20/94

```
*****
***** PARAMETERS *****
*****
* All entered parameters are in mks units.
* Scale factors are used to scale up units used in internal calculations.

* step-generator position-reference input value (target sensor vpp)
.param vref_z=56m

* initial conditions for displacement and rotation
.param z_ic=-2n
.param phi_ic=0.5u
.param theta_ic=-0.3u

.param z_scale=1e6
.param phi_scale=1e6
.param theta_scale=1e6
.param cap_scale=1e-12
.param cref=40.25f

***** material parameters *****
* dimensions of plate: Lx, Ly, Lz
.param lx=380e-6
.param ly=360e-6
.param lz=1.6e-6

* distance from center of plate to springs: Lkx, Lky
.param lkx=113e-6
.param lky=180e-6

* distance from center of plate to center of sensors: s_xc, s_yc
* sensor electrode size: s_xw, s_yw
.param s1_xc=60e-6
.param s1_yc=60e-6
.param s1_xw=100e-6
.param s1_yw=100e-6

.param s2_xc=-60e-6
.param s2_yc=60e-6
.param s2_xw=100e-6
.param s2_yw=100e-6
```

```
.param s3_xc=-60e-6
.param s3_yc=-60e-6
.param s3_xw=100e-6
.param s3_yw=100e-6

.param s4_xc=60e-6
.param s4_yc=-60e-6
.param s4_xw=100e-6
.param s4_yw=100e-6

* distance from center of plate to center of lower actuators: ab_xc, ab_yc
* sensor electrode size: ab_xw, ab_yw
.param ab1_xc=150e-6
.param ab1_yc=150e-6
.param ab1_xw=52e-6
.param ab1_yw=52e-6

.param ab2_xc=-150e-6
.param ab2_yc=150e-6
.param ab2_xw=52e-6
.param ab2_yw=52e-6

.param ab3_xc=-150e-6
.param ab3_yc=-150e-6
.param ab3_xw=52e-6
.param ab3_yw=52e-6

.param ab4_xc=150e-6
.param ab4_yc=-150e-6
.param ab4_xw=52e-6
.param ab4_yw=52e-6

* distance from center of plate to center of upper actuators: at_xc, at_yc
* sensor electrode size: at_xw, at_yw
.param at1_xc=150e-6
.param at1_yc=150e-6
.param at1_xw=54e-6
.param at1_yw=54e-6

.param at2_xc=-150e-6
.param at2_yc=150e-6
.param at2_xw=54e-6
.param at2_yw=54e-6
```

```
.param at3_xc=-150e-6
.param at3_yc=-150e-6
.param at3_xw=54e-6
.param at3_yw=54e-6

.param at4_xc=150e-6
.param at4_yc=-150e-6
.param at4_xw=54e-6
.param at4_yw=54e-6

* distance from poly1 to poly2 = z0
.param z0=2.2e-6

* distance from poly2 to poly3 = z0t
* air gap of upper actuator is negative by convention.
* This is compensated by setting bot_or_top=-1 in the ppc subckt.
.param z0t=-2.7e-6

* spring constant = k = spring
.param kz=0.25

* viscosity of air = 1.83e-5 Pa-s
.param viscosity='1.83e-5'

* etch-hole form factor for damping (zeta_z=12 in air)
.param bf_z='0.02'
.param bf_theta='0.02'
.param bf_phi='0.02'

* etch-hole form factor for capacitance
.param alpha_s='1.0'
.param alpha_l='1.0'
.param alpha_u='0.964'

* dielectric constant of air
.param ep='1.'

* Flexure resistance (ohms)
* about 22kohms in testbed suspension
.param r_flexure='22e3'

* Feedback voltage levels (no compensation)
.param v_up0='5.0'
```

```

.param v_dn0='5.0'

* Logic high and low voltages
.param vdd='2.5'
.param vss='-2.5'

***** CALCULATIONS *****
***** IMPORTANT *****
* All parameters associated with moments are scaled by *
* 1/Ly^2 for x-axis (theta) and 1/Lx^2 for y-axis (phi)*
***** 

.param f_scale='cap_scale*z_scale*z_scale'
.param c_scale='z_scale/cap_scale'
.param x_scale='z_scale/phi_scale'
.param y_scale='z_scale/theta_scale'
.param mt_scale='theta_scale/z_scale/ly/ly'
.param mp_scale='phi_scale/z_scale/lx/lx'

* mass = m = bm
* density = 2330 kg/m^3
.param mass='2330*lx*ly*lz'

* squeeze film damping coefficient = c
* Ks = fitting factor for square plate = 0.425
* Use Lx as longer side of plate
* assume damping independent of position
.param damp='0.425*viscosity*lx*ly*ly/z0/z0/z0'

* scaled moment about x-axis or y-axis = J
.param moment='mass/12'

* scaled damping coefficient for moment about x-axis or y-axis = B
.param z_damp='bf_z*damp'
.param theta_damp='bf_theta*damp'
.param phi_damp='bf_phi*damp'

* torsional spring constant about x-axis = ktheta
.param ktheta='kz*lky*lky/ly/ly'

* torsional spring constant about y-axis = kphi

```

```

.param kphi='kz*lkx*lkx/lx/lx'
* gravitational force
.param fg=-z_scale*9.8*mass'

* External forces for testing circuit
.param f_ext='0.0'
.param mphi_ext='0.0'
.param mtheta_ext='0.0'

***** MAIN CIRCUIT *****

* Sum of forces and moments
v_z_ext fz fat4_z f_ext
v_theta_ext mtheta mat4_theta mtheta_ext
v_phi_ext mphi mat4_phi mphi_ext

***** mechanical system *****
*
* Mechanical subcircuit models a second-order system (mass-spring damper)
* subckt nodes: x1 <force node> <displacement node> mech
* input parameters: pm=mass, pb=damping factor, pk=spring constant
* pscale=scale factor
*
xz fz dz mech pm=mass pb=z_damp pk=kz pscale=z_scale
xtheta mtheta theta mech
+ pm=moment pb=theta_damp pk=ktheta pscale=theta_scale
xphi mphi phi mech pm=moment pb=phi_damp pk=kphi pscale=phi_scale

***** sensor positions z1, z2, z3, z4 *****
*
*      y ^
*          |
*          |
*          |
*          -----
*          |           |
*          |   z2       z1   |
*          |           |
*          |           | -----> x
*          |           | theta rotation about x-axis
*          |   z3       z4   | phi rotation about y-axis
*          |           | Use right-hand rule for rotation direction

```

```

*
* -----
* in general: zi = z +/- Ly theta +/- Lx phi

***** Parallel-Plate Sensors *****
* Cs1 - output v(31)
cs1_ref 29 31 cref
x_s1 31 30 fs1_z 0 ms1_theta 0 ms1_phi 0
+ dz theta phi ppc xc=s1_xc yc=s1_yc zco=z0 xw=s1_xw yw=s1_yw

* Cs2 - output v(32)
cs2_ref 29 32 cref
x_s2 32 30 fs2_z fs1_z ms2_theta ms1_theta ms2_phi ms1_phi
+ dz theta phi ppc xc=s2_xc yc=s2_yc zco=z0 xw=s2_xw yw=s2_yw

* Cs3 - output v(33)
cs3_ref 29 33 cref
x_s3 33 30 fs3_z fs2_z ms3_theta ms2_theta ms3_phi ms2_phi
+ dz theta phi ppc xc=s3_xc yc=s3_yc zco=z0 xw=s3_xw yw=s3_yw

* Cs4 - output v(34)
cs4_ref 29 34 cref
x_s4 34 30 fs4_z fs3_z ms4_theta ms3_theta ms4_phi ms3_phi
+ dz theta phi ppc xc=s4_xc yc=s4_yc zco=z0 xw=s4_xw yw=s4_yw

***** Parallel-Plate Actuators *****
x_ab1 62 30 fab1_z fs4_z mab1_theta ms4_theta mab1_phi ms4_phi
+ dz theta phi ppc xc=ab1_xc yc=ab1_yc zco=z0 xw=ab1_xw yw=ab1_yw
x_ab2 64 30 fab2_z fab1_z mab2_theta mab1_theta mab2_phi mab1_phi
+ dz theta phi ppc xc=ab2_xc yc=ab2_yc zco=z0 xw=ab2_xw yw=ab2_yw
x_ab3 66 30 fab3_z fab2_z mab3_theta mab2_theta mab3_phi mab2_phi
+ dz theta phi ppc xc=ab3_xc yc=ab3_yc zco=z0 xw=ab3_xw yw=ab3_yw
x_ab4 68 30 fab4_z fab3_z mab4_theta mab3_theta mab4_phi mab3_phi
+ dz theta phi ppc xc=ab4_xc yc=ab4_yc zco=z0 xw=ab4_xw yw=ab4_yw

x_at1 61 30 fat1_z fab4_z mat1_theta mab4_theta mat1_phi mab4_phi
+ dz theta phi ppc xc=at1_xc yc=at1_yc zco=z0t xw=at1_xw yw=at1_yw
+ bot_or_top=-1
x_at2 63 30 fat2_z fat1_z mat2_theta mat1_theta mat2_phi mat1_phi
+ dz theta phi ppc xc=at2_xc yc=at2_yc zco=z0t xw=at2_xw yw=at2_yw
+ bot_or_top=-1
x_at3 65 30 fat3_z fat2_z mat3_theta mat2_theta mat3_phi mat2_phi
+ dz theta phi ppc xc=at3_xc yc=at3_yc zco=z0t xw=at3_xw yw=at3_yw
+ bot_or_top=-1
x_at4 67 30 fat4_z fat3_z mat4_theta mat3_theta mat4_phi mat3_phi

```

```

+ dz theta phi ppc xc=at4_xc yc=at4_yc zco=z0t xw=at4_xw yw=at4_yw
+ bot_or_top=-1

***** Timing Circuitry *****
* Modulation voltages, modulation duty cycle will be small.
* Vm+ = v(29), Vm- = v(28)
* modulation frequency = 50 kHz
vmod1a 71 0 dc 0 pulse(0 0.3 0 .1u .1u 10u 20u)
vmod1b 72 0 dc 0 pulse(0 -0.3 10u .1u .1u 10u 20u)
evmod1 29 0 vol='v(71)+v(72)'
evmod2 28 0 vol='-v(29)'
*
* testbed suspension resistance
r_series 28 30 r_flexure
*
* Sample/Hold clocks
* vpp = v_sense(t=clk1)-v_sense(t=clk2)
* actuator output clocked out on clk3
vclk1 clk1 0 dc 0 pulse(0 vdd 2.5u .1u .1u 5u 20u)
vclk2 clk2 0 dc 0 pulse(0 vdd 12.5u .1u .1u 5u 20u)
vclk3 clk3 0 dc 0 pulse(0 vdd 0 .1u .1u 5u 20u)

***** Position-Reference Inputs *****
* Reference position inputs v(39),v(40),v(41),v(42)
vref1 39 0 dc 0 pulse(0 vref_z 200u .1u .1u 5m 10m)
vref2 40 0 dc 0 pulse(0 vref_z 200u .1u .1u 5m 10m)
vref3 41 0 dc 0 pulse(0 vref_z 200u .1u .1u 5m 10m)
vref4 42 0 dc 0 pulse(0 vref_z 200u .1u .1u 5m 10m)

***** Position-Sense Circuitry *****
* Node 61 produces a voltage pulse when z1 is negative, C is large,
* so use top actuators
* Node 62 produces a voltage pulse when z1 is positive, C is small,
* so use bottom actuators
* similar logic holds for the other quadrants
xsense1 31 39 61 62 clk1 clk2 clk3 sensor v_up=v_up0 v_dn=v_dn0
xsense2 32 40 63 64 clk1 clk2 clk3 sensor v_up=v_up0 v_dn=v_dn0
xsense3 33 41 65 66 clk1 clk2 clk3 sensor v_up=v_up0 v_dn=v_dn0
xsense4 34 42 67 68 clk1 clk2 clk3 sensor v_up=v_up0 v_dn=v_dn0

*****
***** SUBCKT's *****
*****
```

```
*****
***** Sense ckt *****
.subckt sensor sense_in ref_in top bottom clk1 clk2 clk3
+ v_up=vdd v_dn=vdd
* Comparators (linear below 10^(-15) V)
* Position strobed when Vm+ = -0.3 V, Vm- = 0.3 V
* so if v(1)>v(2), then the plate is below the reference
* and the top actuator is activated

* Unity-gain buffer
* nodes are: sense_in=buffer input, z_buf=buffer output
xbuffer z_buf sense_in buffer vos=6m
ez_in z_buffer 0 z_buf 0 1
*
* Sample signal
xsamp1 zsamp1 z_buffer clk1 sample
xsamp2 zsamp2 z_buffer clk2 sample
*
* Instrumentation amplifier
* Vpp = v(zsamp1) - v(samp2)
e_ampl v_pp 0 zsamp1 zsamp2 1
*
* position comparator
* positive z_hi means plate is above reference
xcomp_pos v_pp ref_in z_hi compare
xcomp_neg ref_in v_pp z_low compare
*
* latch signal on next sample cycle
xlatch top2 bot2 z_low z_hi clk3 latch
*
* activate either the top or bottom actuator
* output through second-order smoothing filter to help
* with convergence
ea_top top3 0 vol='v_up*v(top2)/vdd'
ea_bot bot3 0 vol='v_dn*v(bot2)/vdd'
xtop top3 top smooth
xbot bot3 bottom smooth
.ends sensor

***** S/H *****
.subckt sample out in phi_in
gs1 in out vcr pwl(1) phi_in 0 0.5v,100x 2.0v,1.0
csamp out 0 0.01u
```

```

.ic v(out) 0
.ends sample

***** latch *****
.subckt latch out_p out_m in_p in_m stb
xnand1 in_p stb 6 nand
xnand2 in_m stb 7 nand
xnand3 6 out_m1 out_p1 nand
xnand4 7 out_p1 out_m1 nand
*
* clean up digital output signals by sending through a comparator
vmids vmid 0 'vdd/2'
xdig_p out_p1 vmid out_p compare cmp_pl=0.025m cmp_pc=0.1n cmp_low=0
xdig_m vmid out_p1 out_m compare cmp_pl=0.025m cmp_pc=0.1n cmp_low=0
.ends latch

***** comparator *****
*
.subckt compare in_p in_m out_p cmp_pl=0.25m cmp_pc=1n
+ cmp_hi=vdd cmp_low=vss
ez_less 1 0 pwl(1) in_p in_m -1u,cmp_low 1u,cmp_hi
rb in_p 0 10
rf in_p 1 1x
cb in_p 0 1f
xsMOOTH 1 out_p smooth pl=cmp_pl pc=cmp_pc
.ends compare

***** nand gate *****
.subckt nand 1 2 n_out
e_nand n_out1 0 nand(2) 1 0 2 0
+ -2.5 2.5v
+ 0.0 2.5v
+ 0.25 2.4
+ 0.5 2.25
+ 2.0 0.25v
+ 2.25 0.1v
+ 2.5 0.0v
xnout n_out1 n_out smooth
.ends nand

***** ppc *****
.subckt ppc 1 2 fz2 fz1 mt2 mt1 mp2 mp1 z_in theta phi
+ xc=0 yc=0 zco=2 xw=1 yw=1 bot_or_top=1

```

```

***** fixed scale factors *****
* x_scale = z_scale/phi_scale
* y_scale = z_scale/theta_scale
* f_scale = z_scale*zscale*cap_scale
* c_scale = z_scale/cap_scale
* mt_scale = theta_scale/z_scale/lx/lx
* mp_scale = phi_scale/z_scale/ly/ly

* z_in, zc, and z force (fz) scaled by z_scale
* theta and theta moment (mt) scaled by theta_scale
* phi and phi moment (mp) scaled by phi_scale
* capacitance scaled by cap_scale

* x,y in mks units
* positive force pulls up, negative force pulls down

xcap 1 2 cap 0 tvc
* zc = z +/- Lx theta +/- Ly phi
* "Top" z position will actually be negative. This is compensated by
*           setting bot_or_top=-1 in ppc subckt.
ez zc 0 vol=
+ 'bot_or_top*(v(z_in)+zco*z_scale+yc*y_scale*v(theta)-xc*x_scale*v(phi))',
v_dz zc dzc 'bot_or_top*zco*z_scale'
r_dz dzc 0 1x
ec cap 0 vol='8.854e-12*c_scale*ep*xw*yw/v(zc)'
efz fz2 fz1
+ vol=-bot_or_top*v(cap)*f_scale*(v(1)-v(2))*(v(1)-v(2))/2./v(zc),
emt mt2 mt1 fz2 fz1 'yc*mt_scale'
emp mp2 mp1 fz1 fz2 'xc*mp_scale'
.ends

***** tvc *****
* Time varying capacitor (tvc) subcircuit
* C is connected to nodes 1 and 2.
* C(t) = v(3,4)
.subckt tvc 1 2 3 4

* e1: generate non-linear voltage so, I = d/dt [C(v3-v4) * V]
e1 5 0 vol='v(3,4)*v(1,2)'
* c1: linear capacitance
c1 6 0 cap_scale
* v1: Ammeter to measure current into capacitor
v1 5 6 dc 0
* Drive the current through c1 back into the circuit

```

```

f1 1 2 v1 1
.ends tvc

***** smooth *****
.subckt smooth in out pl=0.1m pc=0.4n pr=1k
* second-order smoothing filter
*  $H(s) = 1/(LC s^2 + RC s + 1)$ 
* damping factor = 0.5 R / sqrt(L/C) = 1
* wn = 1/sqrt(LC) => 318 kHz (L=.25m, C=1n)
ef_in n1 0 in 0 1
r_in n1 n2 pr
l_in n2 n3 pl
c_in n3 0 pc
e1 out 0 n3 0 1
.ends

***** mech *****
.subckt mech f_in x_out pm=1 pb=1 pk=1 pscale=1
* f=v(f_in), z=v(x_out)
* f comes in scaled up by pscale (in micro Newtons)
* z comes out scaled up by pscale (in microns)

xin f_in force smooth
L1 force xr 'pscale*pm'
r1 xr xinit 'pscale*pb'
c1 xinit 0 '1./pk/pscale'
ez x_out1 0 vol='v(xinit)/pk'
rout x_out1 0 1x
ez_clip x_out 0 pw1(1) x_out1 0 -2,-2 2,2
.ends mech

***** MODELS *****

* include CMOS unity-gain buffer subcircuit
.include 'buffer.subckt'

***** MODELS *****

*.model diode d level=3 l=9e-6 w=15e-6 cj=5.3e-3 is=1 xw=1e-6
.model diode d

.model mn_4um nmos level=2 capop=0 acm=0

```

```

+ vto=0.56 kp=33u gamma=0.55 phi=0.6
+ lambda=0.043 rdc=10.0 rsc=10.0
+ ld=0.22u xj=0.25u tox=500.0e-10 nsub=2.3e+16
+ uo=619.0 ucrit=2.6e+04 uexp=0.106
+ neff=1.000 delta=1.4 nfs=1.38e+12
+ rsh=4.0 pb=0.8
+ cj=4.06e-04 mj=0.443 cjsw=4.44e-10 mjsw=0.291
+ cgdo=2.5e-10 cgso=2.5e-10 cgbo=2.5e-10
+ vmax=6.84e+4
+ nss=1.0e+12 tpg=1.0
*
.model mp_4um pmos level=2
+ vto=-0.56 kp=17u gamma=0.55 phi=0.6
+ lambda=0.046 rdc=100.0 rsc=100.0
+ ld=0.16u xj=0.25u tox=500.0e-10 nsub=0.79e+16
+ uo=257.0 ucrit=2.4e+04 uexp=0.270
+ neff=1.001 delta=0.0 nfs=1.1e+12
+ rsh=4.0 pb=0.71
+ cj=2.30e-04 mj=0.410 cjsw=2.20e-10 mjsw=0.1
+ cgdo=2.5e-10 cgso=2.5e-10 cgbo=2.5e-10
+ vmax=4.50e+4
+ nss=1.0e+12 tpg=-1.0
*
.model mp_8um pmos level=2
+ vto=-0.56 kp=17u gamma=0.55 phi=0.6
+ lambda=0.023 rdc=100.0 rsc=100.0
+ ld=0.16u xj=0.25u tox=500.0e-10 nsub=0.79e+16
+ uo=257.0 ucrit=2.4e+04 uexp=0.270
+ neff=1.001 delta=0.0 nfs=1.1e+12
+ rsh=4.0 pb=0.71
+ cj=2.30e-04 mj=0.410 cjsw=2.20e-10 mjsw=0.1
+ cgdo=2.5e-10 cgso=2.5e-10 cgbo=2.5e-10
+ vmax=4.50e+4
+ nss=1.0e+12 tpg=-1.0
*
*****
***** CONTROL CARDS *****
*****
*
.ic
+ v(dz)='z_ic*z_scale' v(xz.xinit)='z_ic*kz*z_scale'
+ v(phi)='phi_ic*phi_scale' v(xphi.xinit)='phi_ic*kphi*phi_scale'
+ v(theta)='theta_ic*theta_scale'

```

```

+ v(xtheta.xinit)='theta_ic*ktheta*theta_scale'
+ v(xz.xr)='z_ic*kz*z_scale'
+ v(xphi.xr)='phi_ic*kphi*phi_scale'
+ v(xtheta.xr)='theta_ic*ktheta*theta_scale'
+ v(xsense1.6)=vdd v(xsense1.7)=vdd
+ v(xsense2.6)=vdd v(xsense2.7)=vdd
+ v(xsense3.6)=vdd v(xsense3.7)=vdd
+ v(xsense4.6)=vdd v(xsense4.7)=vdd
+ v(61)=vdd v(62)=0 v(63)=vdd v(64)=0 v(65)=vdd v(66)=0 v(67)=vdd v(68)=0
+ v(70)=0

.options acct
+ chgtol=1e-16 absi=1e-15 absv=1e-9
+ dvdt=0 imax=20 rmin=1e-12
+ lvltim=3 post
+ probe ingold=1 co=132

.tran 1u 1m uic

.print v(fz) v(mphi) v(mtheta) v(dz) v(phi) v(theta) v(30)
.print v(fab1_z) v(fab2_z) v(fab3_z) v(fab4_z)
+ v(fat1_z) v(fat2_z) v(fat3_z) v(fat4_z)
.print v(31) v(32) v(33) v(34) v(fs1_z) v(fs2_z) v(fs3_z) v(fs4_z)
.print v(x_s1.dzc) v(x_s2.dzc) v(x_s3.dzc) v(x_s4.dzc)
+ v(xsense1.v_pp) v(xsense2.v_pp) v(xsense3.v_pp) v(xsense4.v_pp)

.probe v(fz) v(mphi) v(mtheta)
.probe v(dz) v(phi) v(theta)
.probe v(fs1_z) v(fs2_z) v(fs3_z) v(fs4_z)
.probe v(fab1_z) v(fab2_z) v(fab3_z) v(fab4_z)
.probe v(fat1_z) v(fat2_z) v(fat3_z) v(fat4_z)
.probe v(x_s1.dzc) v(x_s2.dzc) v(x_s3.dzc) v(x_s4.dzc)
*.probe v(x_at1.dzc) v(x_at2.dzc) v(x_at3.dzc) v(x_at4.dzc)
*.probe v(x_ab1.dzc) v(x_ab2.dzc) v(x_ab3.dzc) v(x_ab4.dzc)
.probe v(30) v(31) v(32) v(33) v(34)
.probe v(61) v(63) v(65) v(67)
.probe v(xsense1.v_pp) v(xsense2.v_pp) v(xsense3.v_pp) v(xsense4.v_pp)
.end

```

## Appendix C

# MICS Fabrication Process

Information in the appendices (and elsewhere in this thesis) will be accessible on the World Wide Web (WWW) through a hypertext viewer, such as Mosaic, by specifying the Universal Resource Locator (URL) for the Berkeley Sensor & Actuator Center home page, “<http://nitride.eecs.berkeley.edu>”. From that location, browse to find the link to my research information (look for ”Gary Fedder”). Good luck!

The following listing is the process flow for the Modular Integration of CMOS and Polysilicon Microstructures, called “MICS”. This flow reflects the status of the MICS process when the integrated-testbed system was fabricated, in the fall of 1993. Up-to-date information about MICS is available from the Berkeley Sensor & Actuator Center. Notes are included with the process outline to document the results from the integrated-testbed run. We have included dates with the flow to give an idea of the time it takes to finish a microstructure process; this run took a little over two months to complete.

### MICS BACKEND PROCESS (3 SENSOR POLY)

Version 2.0  
 (08-27-93)

J. Bustillo, G. K. Fedder, C. T.-C. Nguyen, and R. T. Howe  
 1 or 2 um substrate gap, 2um thickness, In Situ Doped poly-Si

0.0-30.0 standard Baseline CMOS through and including Contact Etch

---

31.0 TiN/TiSi<sub>2</sub> Formation - Wed Sept 22 1993

- 
- 31.1 a) 20 sec 25/1 HF dip just before titanium metallization
  - b) measure PSG oxide loss

---

31.2 Titanium Metallization: target = 350A  
CPA: pressure = 20 mTorr Ar, power = 2 kW,  
track speed = 60 cm/s  
Ti thickness on as200 = 200-285A (thinner than expected)  
4-point probe on Ti monitor 1 (over bare Si): 37 ohm/sq  
4-point probe on Ti monitor 2 (over oxide): 84 ohm/sq

---

31.3 RTA for TiN / TiSix Formation  
Heatpulse1: time = 30 sec, temp. = 600 C, flow = 2 slpm N2  
Wafer ends up silver, instead of usual golden  
color after anneal.  
4-point probe on Ti monitor 1 (over bare Si): 14 ohm/sq

---

31.4 Self Aligned Ti Strip  
a) Soak wafers in 3:1 NH4OH:H2O2 for 12 min, agitated  
b) check for lack of continuity in field region  
c) add 5 min if field not clear

---

31.5 Check for field Ti shorts using I-V probe

---

31.6 RTA for TiSi2 and Rc reduction  
Heatpulse1: time = 30 sec, temp. 850 C, flow = 2 slpm N2  
4-point probe on Ti monitor 1 (over bare Si): 5 ohm/sq

---

31.7 Titanium Nitride deposition: target = 650A  
CPA: p = 20 mTorr (Ar/N2=50/50), Pdc = 2 kW, speed = 30 cm/s  
TiN thickness measured with as200 = 200A  
(thinner than expected)  
inspect: some source contacts on cmos30-3 are gold/brown,  
whereas all other contacts are white/gold.  
No graininess.  
4-point probe on Ti monitor 1 (over bare Si): 5 ohm/sq  
4-point probe on TiN monitor 3 (over bare Si): 20 kohm/sq

---

31.8 TiN Anneal  
SVANNEAL: tylan14, 20min @ 600C in N2 (15 min ramp from 400C)  
2 hr ramp down to 375C  
inspect: no graininess, contacts are maize/gold  
4-point probe on Ti monitor 1 (over bare Si): 5 ohm/sq

---

32.0 Tungsten Metallization: target = 5000-6000 A total

---

\*\* option 1: (available in the Microlab and used for cmos30-2)

32.1 First tungsten deposition - Thu Sept 23 1993  
 CPA, 2.0kW, 20mT (Ar=100%), 16 cm/min

32.2 First tungsten stress relief anneal  
 RTA: 30sec @ 900C in Ar

32.3 Second tungsten deposition  
 CPA, 2.0kW, 20mT (Ar=100%), 16 cm/min

32.2 Second tungsten stress relief anneal  
 RTA: 30sec @ 900C in Ar

inspect: film quality is specular, no graininess in contacts.  
 4-point probe on Ti monitor 1 (over bare Si): 0.4 ohm/sq

---

\*\* option 2: (preferred process due to reduced film stress)

CVD: hydrogen reduction process at Stanford CIM

32.1 Tungsten deposition

- a) nucleation layer: SiH<sub>4</sub> reduction (T<sub>f</sub>=1000A)
  - b) bulk deposition: H<sub>2</sub> reduction (T<sub>f</sub>=5000A)
- 

33.0 Metal Photo Mask: CMF (emulsion-cf)

- a) Photo Module 1.0: thick g-line PR
  - b) align to POLY-CPG
- 

34.0 Tungsten / Titanium Nitride Etch

---

34.1 Etch Module 1.0: Tungsten Etch

---

34.2 Etch inspect:

- a) should see oxide color
  - b) test for lack of continuity in the field
  - c) check for stringers at gate poly vernier and TX gates
- nanospec: field tox after W etch, in angstroms

T	R	B	L	C	mean	sigma
cmos30-2:	12202	11855	11930	12066	11590	-> 11929 +/- 231

---

34.3 PR strip: a) module 3.0 - no SP clean!

- b) PRS-2000, 10 min, at 50C (needed)

- c) acetone soak (if needed) (didn't need)
- 

35.0 Sintering and Test:

---

35.1 Acetone rinse for 30 min, DI rinse, blow dry  
(didn't do this)

---

35.2 SINTV: tylan14, 400 C for 20 min. in forming gas.  
(used SINTV instead of SINT400, because of higher  
forming gas flow. This may help inhibit tungsten  
oxidation while loading/unloading tube)

---

35.3 CMOS device testing of Vt's, and contacts (N+, P+, CPG)

---

36.0 Std. Tungsten clean: Acetone rinse for 30 min. + DI rinse  
in sink7. Blow dry with N2 gun.  
Also, clean NITCTRL1 and NITCTRL2 in sink6.  
(didn't do this, instead used:  
mti: acetone strip program ran twice to clean wafers  
sink8: DI rinse to 12 Mohm)

---

37.0 CMOS Passivation - Tue Sep 28 1993

---

37.1 LTO Deposition: tylan20, VDOLTOC, target = 3500-5000 Å  
Flows (sccm): SiH4 = 60, PH3 = 0, O2 = 90  
Temp = 400 C, pressure = 300 mT  
time = 25 min (review previous DR on wand)  
Include NITCTRL1 and NITCTRL2 and a tox ctrl.  
nanospec: passivation PSG thickness, in angstroms  
T R B L C mean sigma  
NITCTRL1: 4598 4697 4482 4448 4558 -> 4557 +/- 98  
inspect: lots of ~1um hillocks have formed on tungsten

---

37.2 RTA LTO Densification  
Heatpulse1: time = 30 sec, temp = 900 C, flow = 2.0 slpm Ar  
nanospec: passivation PSG thickness, in angstroms  
T R B L C mean sigma  
NITCTRL1: 4476 4592 4343 4364 4444 -> 4444 +/- 99  
nanospec: oxide thickness in field  
cmos30-2: 16778 16448 16640 16766 16533 -> 16633 +/- 144

---

37.3 Low Stress Nitride Deposition:  
tylan18, BSLOW.1, target=1750 Å  
Flows (sccm): DCS = 100, NH3 = 25, T = 835 C, P = 140 mT  
time = 54 min (review previous DR on wand)  
Include NITCTRL1 (not NITCTRL2) and thickness ctrls. (Si).  
nanospec, prog2 R.I.=2.2: passivation nitride thickness

T R B L C mean sigma

NITCTRL1: 2486 2504 2517 2493 2464 -> 2493 +/- 20

---

38.0 Inter CMOS-ustructure Contact Mask: SNT (chrome-df)  
 - Wed Sep 29 1993  
 a) Photo Module: 1.0: thick g-line PR  
 b) align to POLY-CPG

---

39.0 Nitride Passivation Etch - Thu Sep 30 1993  
 Etch Module 2.0: Nitride Etch  
 (had to use tegal instead of lam1, which was down)  
 tegal: 150mT, 200W, 80 sccm SF6, 1min 45sec etch  
 nanospec: oxide thickness in field left

T	R	B	L	C	mean	sigma
cmos30-2:	16913	16364	16459	16828	16466	-> 16606 +/- 247

---

40.0 Oxide Passivation Etch  
 a) Etch Module 4.0: Oxide Etch  
 b) check for continuity in CMOS gate poly  
 It took 2 min to etch.

---

41.0 PR strip: see module 1.0

---

42.0 uStructure Poly1 Deposition: target = 3000 Å

---

42.1 Standard clean: a) sink6: SP clean, DI rinse  
 b) 10 sec 10:1 HF dip, DI rinse  
 (reduced dip time to avoid undercutting PSG)  
 (used 15 sec 5:1 BHF dip instead)  
 inspect: Exposed tungsten pads for contact testing  
 etched away in the pirahna.

---

42.2 Phosphorous-doped polysilicon deposition:  
 tylan16, DOPLY16A  
 time = 1hr 50min (check DR on wand), temp.= 610 C +/- 6 C,  
 P = 375 mT, SiH4 = 100 sccm, PH3 = 1.0 sccm  
 Include etching controls: PLY1CTRL1, PLY1CTRL2  
 nanospec: SP1 polysilicon thickness

T	R	B	L	C	mean	sigma
PLY1CTRL1:	3023	3009	3016	3032	3042	-> 3024 +/- 13

4-point probe on PLY1CTRL1: 263 ohm/sq

---

43.0 uStructure Poly1 Mask: SP1 (emulsion-cf) - Fri Oct 1 1993  
 a) Photo Module 2.0: standard i-line PR

(I used 2um g-line PR)

b) align to SNT layer

---

44.0 Poly1 Etch

Etch Module 3.0: Poly Etch

7sec SF6, 36sec Cl2 + 10sec overetch Cl2

nanospec, prog2 R.I.=2.2: nitride thickness left

T	C	B	L	R	mean	sigma
NITCTRL1:	2340	2324	2216	2225	2264	-> 2274

---

45.0 PR strip: see module 1.0

(include PSG1CTRL1 and PSG1CTRL2)

---

46.0 Sacrificial PSG Deposition: - Mon Oct 4 1993

---

46.1 Standard clean: a) sink6: SP clean, DI rinse

---

46.2 Sacrificial PSG Deposition: tylan20, VDOLTOC, target = 2 um

Flows (sccm): SiH4 = 60, PH3 = 10.3, O2 = 90,

time: 2 hrs (check DR on wand), p=300mT, T=450C

Include etching controls: PSG1CTRL1 (near load), PSG1CTRL3,  
and PSG2CTRL2 (near pump)

nanospec: sacrificial PSG1 thickness

T	C	B	L	R	mean	sigma
PSG1CTRL1:	22268	22846	22719	22396	22344	-> 22515 +/- 253
PSG1CTRL2:	21349	22821	22580	21975	22114	-> 22168 +/- 572

---

47.0 RTA for Sacrificial PSG Densification

Heatpulse1: time = 30 sec, temp = 900 C, flow = 2.0 slpm Ar

(also do PSG1CTRLs)

nanospec: densified sacrificial PSG1 thickness

T	R	B	L	C	mean	sigma
PSG1CTRL2:	22391	21701	21676	22187	21874	-> 21966 +/- 313

---

48.0 Dimple Photo Mask: SD1 (same as SD2) (chrome-df)

a) Photo Module 2.0: standard i-line PR  
(used 1um g-line instead)

b) align to SP1 layer

---

49.0 Dimple Formation

Timed wet etch in 5:1 BHF. (Check E.R. with PSG TW)

2min 20sec, fresh 5:1 BHF

target dimple depth = 1.0um (or half the SACOX thickness)

inspect: Dimples present. Can't measure since there's

no process monitor. Color looks OK (not like poly).

---

50.0 PR strip: see module 1.0

---

51.0 uStructure Anchor Photo Mask: SG1 (chrome-df) - Tue Oct 5 1993  
 a) Photo Module 1.0: thick g-line PR  
 b) align to SP1 layer

---

52.0 Thick Oxide Etch

a) Etch Module 4.0: Oxide Etch  
 b) check for continuity in uStructural Poly1  
 Etch took 3 min 30 sec  
 inspect: contacts are white/green/rose, depending on wafer position, iv shows conduction between 250 to 1.5kohm

---

53.0 PR strip: see module 1.0

---

54.0 uStructure Poly2 Deposition: - Wed Oct 6 1993

---

54.1 Standard clean: a) sink6: SP clean, DI rinse  
 b) 10 sec 10:1 HF dip, DI rinse  
 (reduced dip time due to exposed PSG)

---

54.2 uStructure Poly2 Deposition -  
 tylan16, DOPLY16A, target=2.0um,  
 time = 12 hrs (check DR on wand), temp.= 610 C +/- 6 C,  
 p= 375 mT, SiH4 = 100 sccm, PH3 = 1.0 sccm  
 Include etching controls: PLY2CTRL1, PLY2CTRL2  
 tylan16 was inadvertently acked at 9 hrs 18 min dep time  
 I decided to pull wafers out at this time.  
 nanospec: SP2 polysilicon thickness

T	R	B	L	C	mean	sigma
PLY2CTRL1:	16085	16445	16024	16052	16048	-> 16131 +/- 177

---

55.0 PSG Oxide Mask Deposition - target = 0.5 um

tylan20, VDOLTOC  
 Flows (sccm): SiH4 = 60, PH3 = 10.3, O2 = 90, p=300mT, T=450C  
 time = 25 min (check DR on wand)  
 Include etching controls: PSG2CTRL1 and PSG2CTRL2  
 nanospec: PSG thickness (non-erodible mask for SP2 etch)

T	R	B	L	C	mean	sigma
PSG2CTRL1:	4681	4625	4384	4660	4564	-> 4583 +/- 120

---

56.0 RTA Polysilicon stress relief anneal  
 Heatpulse1: time = 60 sec, temp = 900 C, flow = 2.0 slpm Ar  
 inspect: poly looks uniform, no bubbles

---

57.0 uStructure Poly2 Mask: SP2 (emulsion-cf)  
 a) Photo Module 2.0: standard i-line PR (must use i-line)  
 b) align to SP1 layer

---

58.0 Oxide Etch  
 Etch Module 4.0: Oxide Etch  
 59 sec to endpoint + 15 sec overetch  
 inspect: I was worried about the 1um lines, since  
 they looked eroded to 0.5um due to the illusion of PR  
 over the oxide mask. It turns out the lines  
 were fine. There was still PR over the larger  
 oxide areas so I went ahead with the lam4 etch on faith.

---

59.0 Structural Poly2 Etch - Thu Oct 7 1993  
 Etch Module 3.0: Poly Etch  
 7 sec SF6, 4 min Cl2 + 1 min 20 sec overetch  
 inspect: 1um lines look fine, poly stringers etched.  
 nanospec: sacrificial PSG1 thickness left  

T	C	B	L	R	mean	sigma
PSG1CTRL1:	21579	21670	21307	21026	20897	-> 21296
PSG1CTRL3:	22051	22382	22347	21549	21683	-> 22002

=====

#### SOG Planarization Module

---

60.0 uStructural Planarization - Fri Oct 8 1993

---

60.1 Standard clean: a) sink8: SP clean, DI rinse  
 b) sink6: SP clean, DI rinse

---

60.2 Planarization 1st Dielectric (PLAD1)  
 PSG Deposition: tylan20, VDOLTOC, target = 0.7um  
 Flows (sccm): SiH4 = 60, PH3 = 10.3, O2 = 90,  
 time = 39 min (check DR on wand), P=300mT, T=450C  
 include PSG1CTRL1 through PSG1CTRL3  
 nanospec: pre-SOG PSG thickness  

T	C	B	L	R	mean	sigma
PLAD1CTRL1:	7352	7297	7219	7253	7072	-> 7239 +/- 106

=====

## 60.3 Planarization 2nd Dielectric (PLAD2) - 10/08/93

SOG Application: Allied Signal Accuglass 512

warmed to ambient for 60min prior to use.

a) dehydration bake at 120C (approx 60min)

a) 1st coat: spinner1, 3000 rpm, 15 sec

b) hot plate bakes: 1 min @ 90C, 1 min @ 150C, 1 min @ 250C

c) 2nd coat: spinner1, 3000 rpm, 15 sec

d) hot plate bakes: 1 min @ 90C, 1 min @ 150C, 1 min @ 250C

nanospec: SOG index of refraction (Nf) and thickness (Tf)

	T	C	B	L	R	mean
--	---	---	---	---	---	------

SOG1CTRL1: Nf 1.313 1.369 1.353 1.430 1.362 -&gt; 1.365

SOG1CTRL1: Tf 9080 8876 8943 8934 8948 -&gt; 8956 / 75

## 60.4 SOG cure: tylan14, SVANNEAL, 60 min at 425C in N2

(10' ramp up, 5' stab, 60' cure, 10' ramp dwn, 400C idle)

nanospec: SOG index of refraction (Nf) and thickness (Tf)

	T	C	B	L	R	mean
--	---	---	---	---	---	------

SOG1CTRL1: Nf 1.359 1.364 1.369 1.357 1.346 -&gt; 1.359

SOG1CTRL1: Tf 8518 8329 8423 8401 8446 -&gt; 8423 / 69

## 60.5 SOG Etch Back: Etch Module 5.0 - Mon Oct 11 1993

SOG Etch Back  
Technics-C Plasma Etcher

P (mT) 260 (non-regulated)

RF (W) 100

SF6 (sccm) 13 (cf = 0.28)

He (sccm) 21 (cf = 1.46)

time (min) 5

\* Note: Due to the across-wafer nonuniformity of this system,  
rotate wafers 180 degrees after half the etch time.

nanospec: oxide/SOG thickness after etchback

	T	C	B	L	R	mean
--	---	---	---	---	---	------

PLAD1CTRL1: 4970 4944 4901 4678 4808 4860 / 119

SOG1CTRL1: 2665 2392 2326 2279 2193 2371 / 180

PSG loss during EB = 7239 - 4860 = 2379A ER = 476 A/min

SOG loss during EB = 8367 - 2371 = 5996A ER = 1199 A/min

## 61.0 Sacrificial PSG2 Deposition: target = 2 um - Thu Oct 14 1993

## 61.1 Standard clean: a) sink6: SP clean, DI rinse

- 
- 61.2 Sacrificial PSG2 Deposition:  
 tylan20, VDOLTOC, target = 2 um  
 Flows (sccm): SiH4 = 60, PH3 = 10.3, O2 = 90,  
 time = 2 hrs (check DR on wand), P=300mT, T=450C  
 Include etching controls: PSG3CTRL1 and PSG3CTRL2  
 inspect: all wafers look fine, some small 1um PSG "bubbles"  
 in field, probably there from before dep.  
 comb finger gaps look clear, can see PSG sidewalls
- 
- 62.0 Sacrificial PSG2 Densification  
 Heatpulse1: time = 30 sec, temp = 900 C, flow = 2.0 slpm Ar  
 (also include PSG1CTRLs and PSG3CTRLs)  
 inspect: same bubbles in field, comb finger gaps are now dark  
 on all wafers. All wafers have brown streaks in field,  
 where the SOG still exists. The streaks are radial  
 out from the center, from the SOG spin. This brown  
 color did not show up until after the RTA.  
 Occasional trenches had long cracks in the SOG.  
 nanospec: densified sacrificial PSG2 thickness  

T	R	B	L	C	mean	sigma
PSG3CTRL1:	20192	19983	19570	20214	19627	-> 19917 +/- 305
PSG1CTRL1:	50253	49833	48501	50356	48288	-> 49446 +/- 983
PSG1CTRL3:	50817	49603	48655	50987	48724	-> 49757 +/- 1111
- 
- 63.0 Dimple Photo Mask: SD3 (chrome-df) - Mon Oct 18 1993  
 a) Photo Module 1.0: double thick g-line PR (2um-thick)  
 b) align to SP2 layer
- 
- 64.0 Dimple Formation  
 Timed wet etch in 5:1 BHF. 2 min 20 sec (Check E.R. with PSG TW)  
 target dimple depth = 1.0um (or half the PSG2 thickness)  
 nanospec: sacrificial PSG2 thickness for dimples (after etch)  

T	R	B	L	C	mean	sigma
PSG3CTRL1:	10899	11037	10937	11577	10256	-> 10941 +/- 470
so dimple depth is about 19917 - 10941 = 8976 A						
- 
- 64a.0 Back Side PSG etch (this is not a "standard" MICS process step)  
 a) Spin on 2um g-line PR, hardbake  
 b) 14 min, 5:1 BHF etch (until backside dewets in water)
- 
- 65.0 PR strip: see module 1.0
- 
- 66.0 uStructure Anchor Photo Mask: SG2 (chrome-df) - Tue Oct 19 1993

- a) Photo Module 3.0: 4-times (4um) thickness g-line PR
  - b) align to SP2 layer
- 

## 67.0 Thick Oxide Etch - PSG2

- a) Etch Module 4.0: Oxide Etch
  - b) check for continuity in uStructural Poly2  
etch time = 6 min 30 sec  
rotate wafers 180 deg after each 1 min etch  
inspect: after 5 min etch, most contacts are etched to white, however, small SG2 contacts have extra SOG.  
The SOG creates round contacts with residual oxide in corners. After 6 min total etch, contacts on all but side dies are clear and conducting on iv.  
Check SP2-SP1 contacts at this time - they're ok.
- 

## 68.0 PR strip: see module 1.0

## 69.0 uStructure Poly3 Deposition: - Wed Oct 20 1993

- 
- 69.1 Standard clean: a) sink6: SP clean, DI rinse
  - b) 15 sec 10:1 HF dip, DI rinse
- 

- 69.2 uStructure Poly3 Deposition -  
tylan16, DOPLY16A, target=1.0um  
time = 6 hrs (check DR on wand), temp.=610 C +/- 6 C,  
P = 375 mT, SiH4 = 100 sccm, PH3 = 1.0 sccm  
Include etching controls: PLY3CTRL1, PLY3CTRL2  
nanospec: second structural polysilicon thickness, PLY3  
T R B L C mean sigma  
PLY3CTRL1: 11799 12104 11664 11697 12049 -> 11863 +/- 202

---

- 70.0 PSG Oxide Mask Deposition - target = 0.5 um - Mon Nov 1 1993  
tylan20, VDOLT0C  
Flows (sccm): SiH4 = 60, PH3 = 10.3, O2 = 90, P=300mT, T=450C  
time = 20 min (check DR on wand)  
Include etching controls: PSG4CTRL1 and PSG4CTRL2  
nanospec: PSG4 thickness (non-erodible mask for PLY3 etch)  
T R B L C mean sigma  
PSG4CTRL1: 3503 3522 3419 3471 3444 -> 3472 +/- 42

---

- 71.0 uStructure Poly3 Definition Mask: SP3 (emulsion-cf)  
- Tue Nov 2 1993
  - a) Photo Module 3.0: 4X thickness g-line PR  
(required because of poor planarization)

(used 3um-thick g-line PR instead)

b) align to SP2 layer

---

72.0 Oxide Etch

- a) Etch Module 4.0: Oxide Etch  
45 sec to endpt + 15 sec overetch
- b) 15 sec. 5:1 BHF dip in sink 8 to remove oxide stringers

---

73.0 Structural Poly3 Etch

- a) Etch Module 3.0: Poly Etch  
7 sec SF6, 170 sec Cl2 to endpt (C), 120 sec overetch
- b) Poly3 stringer removal - technics-c  
SF6 = 13.0, He = 21.0, O2 = 0.0, power = 100 W  
etch time = 0.5 min., inspect, rotate wafers 180 deg.  
etch for additional time = 0.5 min. (if needed)  
(etch required because of poor planarization)  
inspect: the SF6 etch for stringer removal of cmos30-2  
was actually done after the SREL lithography step 77.1  
no poly3 stringers after 30 sec SF6 etch

---

74.0 PR strip: see module 2.0

---

75.0 RTA PSG Densification and Polysilicon stress relief anneal

- Heatpulse1: time = 30 sec, temp = 900 C, flow = 2.0 slpm Ar  
two RTA cycles, so total time is 60 sec

---

76.0 Back Side Etch (not done on cmos30-2)

---

76.1 PR spin, no exposure, hard bake: 60 min @ 120C

---

76.2 repeat 16.2

---

76.3 Etch back side of wafers as follows:

- a) dip off oxide in BHF (PSG3 oxide mask)
- b) wet etch poly-Si (structural poly3)
- c) dip oxide off in BHF (sacrificial PSG2)
- d) wet etch poly-Si (structural poly2)
- e) dip oxide off in BHF (sacrificial PSG oxide)
- f) wet etch poly-Si (ground-plane poly1)
- g) etch nitride in Tegal
- h) etch oxide off in BHF (oxide over W and over capacitor)
- i) wet etch poly-Si (capacitor poly)
- j) etch oxide in BHF (capacitor oxide)
- k) wet etch poly-Si (CMOS gate poly)

1) final dip in BHF until back dewets

---

76.4 PR strip: see module 1.0

---

77.0 uStructure Release

---

77.1 SREL photolithography (optional, and done for cmos30-2)

- a) Photo Module 2.0: std g-line PR
  - b) align to SP2
- 

77.2 a) Wet etch: 10:1 BHF (sink8), or - Mon Nov 8 1993  
concentrated (49%) HF (sink7) - if SREL not used.

(agitate slowly, time: as required)

For cmos30-2, we used 35 min, 5:1 BHF release in total  
darkness (covered with opaque bell jar) to inhibit  
electrochemical etching of polysilicon pads.

- b) DI rinse
- c) SP clean, 10min

We did pirahna clean for 1hr.

- d) DI rinse
- 

77.3 Dry: - Fri Nov 12 1993

- a) methol soak
  - b) supercritical CO<sub>2</sub> drying
- 

frontend: S. Fang/K. Voros

backend: J. Bustillo/G. Fedder/C. Nguyen

---

Backend MICS\_2poly alignment strategy:

---

mask	type	name	aligns to	PR
METAL	emulsion-cf	CMF	POLY_CPG	2.0um g-line
uS CONTACT	chrome-df	SNT	CPG	2.0um g-line
uS POLY1	emulsion-cf	SP1	SNT	std i-line
DIMPLE	chrome-df	SD2/SD1	SP1	std i-line
uS ANCHOR	chrome-df	SG1	SP1	2.0um g-line
uS POLY2	emulsion-cf	SP2	SP1	std i-line
DIMPLE2	chrome-df	SD3	SP2	2.0um g-line

uS ANCHOR2	chrome-df	SG2	SP2	4.0um g-line
uS POLY3	emulsion-cf	SP3	SP2	4.0um g-line
release etch	chrome-df	SREL	SP2	2.0um g-line

assuming 2.0um uStructural design rules, alignment  
should be within +/-1.0um a-w and +/-0.5um at ctr.

---

MICS Backend  
Plasma/RIE Etch Modules  
version 2.0

---

1.0

## Tungsten Etch

## Tegal 701 RIE

SF6 = 80 sccm  
Pin = 200 Watts  
p = 200 mT  
T = 40 C (temperature set at chiller)

\*Note: Set forward power using Bird meter.  
Use matching network in manual mode.

SF6 etch will also clear underlying TiN over field.

---

2.0

## Nitride Etch

## Lam1 AutoEtch 490 Plasma Etch

	step 2	step 4
P (mT)	375	300
RF (W)	250	100
gap (cm)	1.35	2.50
O2 (sccm)	-	5
He (sccm)	50	-
SF6 (sccm)	175	50
time	endpt	10% O/E

---

## 3.0

## Polysilicon Etch

---

Lam4 Rainbow Plasma Etch  
(standard recipe #400)

	step 5	step 7	step 8
P (mT)	400	425	425
RF (W)	200	275	275
gap (cm)	1.00	0.80	0.80
CL2 (sccm)	-	180	180
He (sccm)	-	400	400
SF6 (sccm)	100	-	-
time	7sec	endpt	0/E
CH		C	
delay		15	
norm sec		10	
norm val		5000	
trigger		90	
%		25	

\* Note: HBr etch of structural poly will passivate sidewalls and may leave "grass" when thick poly is etched.  
Use the chlorinated etch process for SP layers.

---

## 4.0

## Oxide Etch

---

Lam2 AutoEtch 590 Plasma Etch

	step 2	step 4
P (Torr)	2.8	3.0
RF (W)	850	700
gap (cm)	0.38	0.40
He (sccm)	120	110
CHF3(sccm)	30	35
CF4 (sccm)	90	30
time	endpt	0/E

\* Note: Overetching SP masking oxide w/ step #4 can cause polymerization and subsequent micromasking of SP layer during the SP etch,

or difficulty making poly-poly contacts at SNT, SG1, or SG2.  
Any overetching should be done with an extension of step #2.

Suggest excluding the overetch step (#4) except for CMOS  
contacts (metal-silicon contacts not affected).

-----

=====

MICS Backend  
Photolithography Modules

=====

1.0                    2X Thick g-line PR (CMF and SD1 layers)

=====

- 1 Dehydrate: VWR Oven for 30 min. @ 120 C
  - 2 HMDS vapor prime
  - 3 Spin g-line resist: KTI 820 (prog. 9),  
target PR = 1.8-2.0um  
30sec @ 1500rpm,  
soft bake: 60sec @ 120 C
  - 4 Expose: GCA2 6200-10X G-line wafer stepper  
or  
GCA1 6200-10X I-line wafer stepper  
4.1 Focus/Exposure Matrix  
4.2 calculate appropriate F/E for thicker PR  
4.3 align to appropriate layer
  - 5 Post exposure bake: 60sec @ 120 C (prog. 4)
  - 6 Develop in MTI-Omnichuck:  
Kodak 932 2:1, 60 seconds. (prog. 1)
  - 7 Develop Inspect (five sites)
  - 8 Descum in Technics-C: O2 plasma, 50 Watts, 1 minute.
  - 9 Hard bake in VWR oven: 60min @ 120 C convection
-

## 2.0 Standard i-line PR (SNT, SP1, SG1, SP2, and SREL layers)

1 Dehydrate: VWR Oven for 30 min. @ 120 C

2 HMDS: Vapor prime

3 Spin I-line resist: Olin-Hunt I-line (prog15)  
25 sec @ 4600 RPM,  
softbake: 60 sec @ 90 C

4 Expose: GCA1 6200-10X I-line wafer stepper,  
align to appropriate layer

5 Post Exposure Bake on Eaton: 60 secs. @ 120 C

6 Develop in MTI-Omnichuck:  
Std. Olin-Hunt I-line (prog. 70)

7 Develop Inspect (five sites)

8 Descum in Technics-C: O2 plasma, 50 Watts, 1 minute.

9 Hard bake in VWR oven: 120 C, 60 min. convection

## 3.0 4X Thick g-line PR (SG2 and SP3 masks)

1 Dehydrate: VWR Oven for 30 min. @ 120 C

2 HMDS vapor prime

3 Spin g-line resist: KTI 820 (prog. 9),  
target PR = 1.8-2.0um  
30sec @ 1500rpm,  
soft bake: 60sec @ 120 C  
\*\* repeat to get 3.6-4.0 um \*\*

4 Expose: GCA2 6200-10X G-line wafer stepper  
(larger depth of focus required)

4.1 Focus/Exposure Matrix  
4.2 calculate appropriate F/E for thicker PR  
4.3 align to appropriate layer

---

5 Post exposure bake: 60sec @ 120 C (prog. 4)

---

6 Develop in MTI-Omnichuck:  
Kodak 932 2:1, 60 seconds. (prog. 1)

---

7 Develop Inspect (five sites)

---

8 Descum in Technics-C: O2 plasma, 50 Watts, 1 minute.

---

9 Hard bake in VWR oven: 60min @ 120 C convection

---

=====

Standard PR Strip Modules

=====

1.0 PR strip: a) technics-c, 300W, O2, 10 min  
b) sink8: 10 min SP clean, DI rinse

---

2.0 PR strip: a) sink8: 10 min SP clean, DI rinse  
(used after SP2 or SP3 etch)

---

3.0 PR strip: a) technics-c, 300W, O2, 10 min - only!  
(used after tungsten etch)

=====

=====